CSDL-T-1036

GUIDANCE, STEERING, LOAD RELIEF AND CONTROL OF AN ASYMMETRIC LAUNCH VEHICLE

by

Frederick W. Boelitz

August 1989

Master of Science Thesis
Massachusetts Institute of Technology

The Charles Stark Draper Laboratory, Inc.
555 Technology Square
Cambridge, Massachusetts 02139

GUIDANCE, STEERING, LOAD RELIEF AND CONTROL OF AN ASYMMETRIC LAUNCH VEHICLE

by

Frederick W. Boelitz
B.S.M.E., University of Massachusetts, (1986)

Submitted in Partial Fulfillment
of the Requirements for the
Degree of

MASTER OF SCIENCE

at the

MASSACHUSETTS INSTITUTE OF TECHNOLOGY

September 1989

Signature of Author 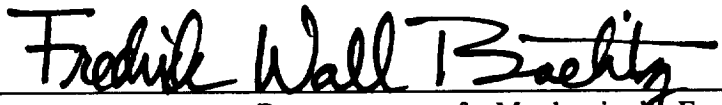
Department of Mechanical Engineering
September 1989

Certified by _____
Professor William K. Durfee
Thesis Advisor, Department of Mechanical Engineering

Approved by 
Gilbert S. Stubbs
CSDL Project Manager

Accepted by _____
Ain A. Sonin
Chairman, Department Graduate Committee

Guidance, Steering, Load Relief and Control of an Asymmetric Launch Vehicle

by

Frederick Wall Boelitz

Submitted to the Department of Mechanical Engineering
in partial fulfillment of the requirements for the
Degree of Master of Science

Abstract

A new guidance, steering, and control concept is described and evaluated for the Third Phase of an asymmetrical configuration of the Advanced Launch System (ALS). The study also includes the consideration of trajectory shaping issues and trajectory design as well as the development of angular rate, angular acceleration, angle of attack, and dynamic pressure estimators.

The Third Phase guidance, steering and control system is based on controlling the acceleration-direction of the vehicle after an initial launch maneuver. Unlike traditional concepts the alignment of the estimated and commanded acceleration-directions is unimpaired by an add-on load relief. Instead, the acceleration-direction steering-control system features a control override that limits the product of estimated dynamic pressure and estimated angle of attack. When this product is not being limited, control is based exclusively on the commanded acceleration-direction without load relief. During limiting, control is based on nulling the error between the limited angle of attack and the estimated angle of attack. This limiting feature provides full freedom to the acceleration-direction steering and control to shape the trajectory within the limit, and also gives full priority to the limiting of angle of attack when necessary.

The flight software concepts were analyzed on the basis of their effects on pitch plane motion. The stability of both the acceleration-direction control mode and the angle of attack control mode was also evaluated. Simulation studies were conducted to evaluate the performance of all the estimators as well as the Phase Three steering, guidance and control concept. Results of the study indicate that the system can effectively steer to the desired trajectory as well as provide fast load relief response.

Acknowledgement

This report was prepared by The Charles Stark Draper Laboratory, Inc. under Task Order 74 from the National Space and Aeronautics Administration Langley Research Center under Contract NAS9-18147 with the National Space and Aeronautics Administration Johnson Space Center.

While working on my Masters Thesis I received help and advice from many people. I would especially like to thank Mr. Gilbert Stubbs, and Mr. Richard Goss for their many hours of assistance. With their help, they made the task of completing my thesis both enjoyable and challenging. I would also like to thank Jeannie Sullivan who spent many hours helping me with the acceleration-direction concept.

Thank you also to my friends Joe, Anthony, Steve, Carolyne, (spring break crew - Ralph, Ronbo, and Pete), Carol, Carole, Margaret, Tony, Mike, Dino, Kelly, Kellie, Kelleye, Jesse, Bob P., Dave, Duncan, and Bob R.

Without all of you, it would have been HELL.

Finally, I would like to thank my family for all their love and encouragement over the years. This thesis is dedicated to you.

Frederick Wall Boelitz

Table of Contents

Chapter **Page**

Chapter **Page**

Chapter Page

Appendix Page

List of Figures

Figure **Page**

Figure **Page**

Figure **Page**

Figure **Page**

Figure **Page**

Figure **Page**

List of Tables

Table **Page**

Chapter One

INTRODUCTION

1.1 Background

This thesis will analyze and evaluate guidance, steering and control concepts for one configuration of an early design of the Advanced Launch System (ALS) being developed by NASA and the US Air Force. The basic launch vehicle design that will be employed in this investigation was proposed by General Dynamics in 1988. The vehicle consists of a 293 ft. long core stage which can have either one or two booster stages of roughly half its length attached in a parallel configuration with the engine nozzles of the core and booster stages at the same longitudinal station. If two booster stages are employed they are attached to the core at diametrically opposite locations so as to achieve symmetry. The single attached booster stage produces an unavoidable asymmetry that must be addressed in the design of the guidance, steering and controls. Both the core and booster stages employ liquid oxygen (LOX) and liquid hydrogen (LH) for propulsion, employing low-cost, non-throttleable engines.

Since the guidance, steering and control problems are most severe for the case of the asymmetrical launch vehicle employing only one booster stage it was decided to use this vehicle configuration as the basis for analysis and evaluation. The flight concepts developed for this configuration should then be applicable to the symmetric configuration employing two booster stages.

1.2 Overview

The guidance, steering, and control system studied for the ALS builds upon the concepts studied previously by Corvin for the single stage to orbit (SSTO) Shuttle II, with some important modifications, additions and innovations.

Both the SSTO and ALS systems were designed to achieve close to an all-weather launch capability and a greater autonomy then is currently possible with the Space Shuttle and many unmanned launch vehicles. The ALS system is similar to the SSTO system in its prelaunch trajectory design and its use of prelaunch doppler radar wind measurements to optimize the atmospheric phases of the boost trajectory. In both systems there are four distinct phases:

(1) Phase One, in which the vehicle rises nearly vertically to clear the launch tower.

(2) Phase Two, in which the vehicle is pitched over rapidly. (in accordance with prelaunch computations)

(3) Phase Three, in which the vehicle is pitched over more slowly. (again in accordance with prelaunch computations, but subject to a load relief constraint on the estimated angle of attack)

(4) Phase Four, in which a predictive-adaptive Powered Explicit Guidance (now employed in the Space Shuttle) determines the direction of the vehicle acceleration in the upper atmosphere and beyond.

The ALS system studied in this thesis differs from the SSTO system studied by Corvin in two important respects. First, in the development of a completely different implementation of Phase Three, and second in the development of control signal estimators that deal with the problems resulting from asymmetry in the ALS vehicle. In addition, an optional implementation of Phase Two was studied. The new features are summarized below:

(1) An optional functionalization of commanded attitude versus time in Phase Two that is designed to achieve a specified angular rate in addition to a specified attitude and angle of attack at the beginning of Phase Three.

(2) The replacement in Phase Three of the SSTO combination of velocity direction steering and angle of attack control with an alternative concept

of an acceleration-direction steering-control system with a control override feature that limits the product of estimated dynamic pressure and estimated angle of attack.

(3) The modification of the prelaunch trajectory design program to generate and store (for in-flight use) the acceleration direction instead of the velocity direction as in the SSTO system.

(4) An angular rate estimator that employs a first order complementary filter to combine (a) a low frequency rate estimate based on measured attitude increments and (b) a high frequency rate estimate based on estimated angular acceleration.

(5) An angular acceleration estimator (for use in the angular rate estimator and angle of attack estimator) that utilizes accelerometer measured velocity increments in combination with measured deflections of all the engines to determine an angular acceleration estimate that is corrected for mismodeling of the magnitudes and points of application of forces acting on the vehicle.

(6) A correction feedback loop in the angular acceleration estimator that computes an acceleration correction signal from the integral of the filtered difference between the estimated angular acceleration and the angular acceleration computed from the back difference of estimated angular rate.

(7) An angle of attack estimator employing a second order complementary filter to combine (a) a low frequency angle of attack estimate based on accelerometer measured velocity increments, measured engine deflections, estimated angular acceleration and estimated dynamic pressure and (b) a high frequency angle of attack estimate based on measured attitude.

(8) A dynamic pressure estimator (for use in the angle of attack estimator) that computes the air density from the estimated altitude and that

utilizes estimated values of earth-relative velocity and angle of attack to estimate the air-relative velocity.

In order to limit the scope of this thesis investigation to a level consistent with the availability of design data and the constraints of time it was decided to describe and evaluate the flight software concepts in terms of pitch plane problems, assuming no yaw or roll motion of the vehicle. Except for the possibility of commanding a zero yaw angle of attack to minimize undesirable aerodynamic torques about the roll axis resulting from vehicle asymmetry, the flight software concepts outlined above should be applicable also to yaw-axis guidance, steering and control.

The flight software concepts will be analyzed and evaluated for their effects on pitch-plane motion first in terms of frequency response characteristics where appropriate and second in terms of transient response characteristics.

Since bending and sloshing characteristics have yet to be determined for the ALS design, the vehicle characteristics will be approximated by a rigid body model.

The transient response evaluations will be based on two Jimsphere-measured wind profiles representing the worst-case variations in the winds over a 3 and 1/2 hour period. The first wind profile will be employed in the prelaunch trajectory design program to determine post launch profiles for commanded attitude and commanded specific force direction. The effects of changes in the winds between the prelaunch trajectory design computations and the subsequent in-flight utilization of these computations will be represented by using the second wind profile for flight simulation.

In both the trajectory design computations and the flight simulation it will be assumed that the Powered Explicit Guidance (PEG) developed for the Space Shuttle takes over some time before the point of booster separation. This guidance technique generates a specific force direction versus time profile that is close to optimal, assuming that aerodynamic forces can be neglected. Subsequent to booster stage separation, an analytical prediction performed by PEG is employed to approximately determine the on-orbit mass that will result from the vehicle state achieved at booster separation.

This thesis study of ALS software concepts is a prelude to a follow-on study that will employ a more comprehensive model of the launch vehicle (including slosh and bending modes) and will investigate the use of predictive adaptive techniques to enhance performance. Conclusions and recommendations of this thesis will relate to the subsequent follow-on investigation.

Chapter Two

DESCRIRTION OF THE VEHICLE AND ITS FLIGHT PHASES

2.1 Physical Configuration of the A.L.S. Vehicle

Figure 2.1 illustrates the minimum-payload asymmetrical configuration of the Advanced Launch System for which the guidance, steering and control concepts will be developed and evaluated in this thesis. As shown in this figure, this configuration consists of a core stage with a single attached booster stage. Both core and booster stages have identical non-throttleable engines employing liquid hydrogen (LH) and liquid oxygen (LOX), with a thrust level of 612,000 lbs per engine. These stages also have identical LH and LOX tanks. The larger number of engines of the booster results in its propellant tanks being drained before those of the core stage. When the booster fuel tanks have been expended the booster stage is separated from the core. Figure 2.1 also shows the following differences between the core and booster stages:

(1) The core stage has a length of 293 ft, compared to the booster length of 161 ft.

(2) The upper portion of the core contains the payload bay. The diameter of the payload bay is larger than the diameter of the lower portion of the core, whose diameter equals that of the booster.

(3) The inertial measurement unit (IMU) is located in the lower portion of the core below the LH tank.

(4) All seven booster engines, their servos, and their fuel distribution lines are housed in a Booster Recovery Module (BRM). Separation of the BRM occurs approximately twenty seconds after

Core Length	293 ft.
Booster Length	161 ft.
Gross Liftoff Weight	3,782,000 lbs.
Dry Weight	331,000 lbs.

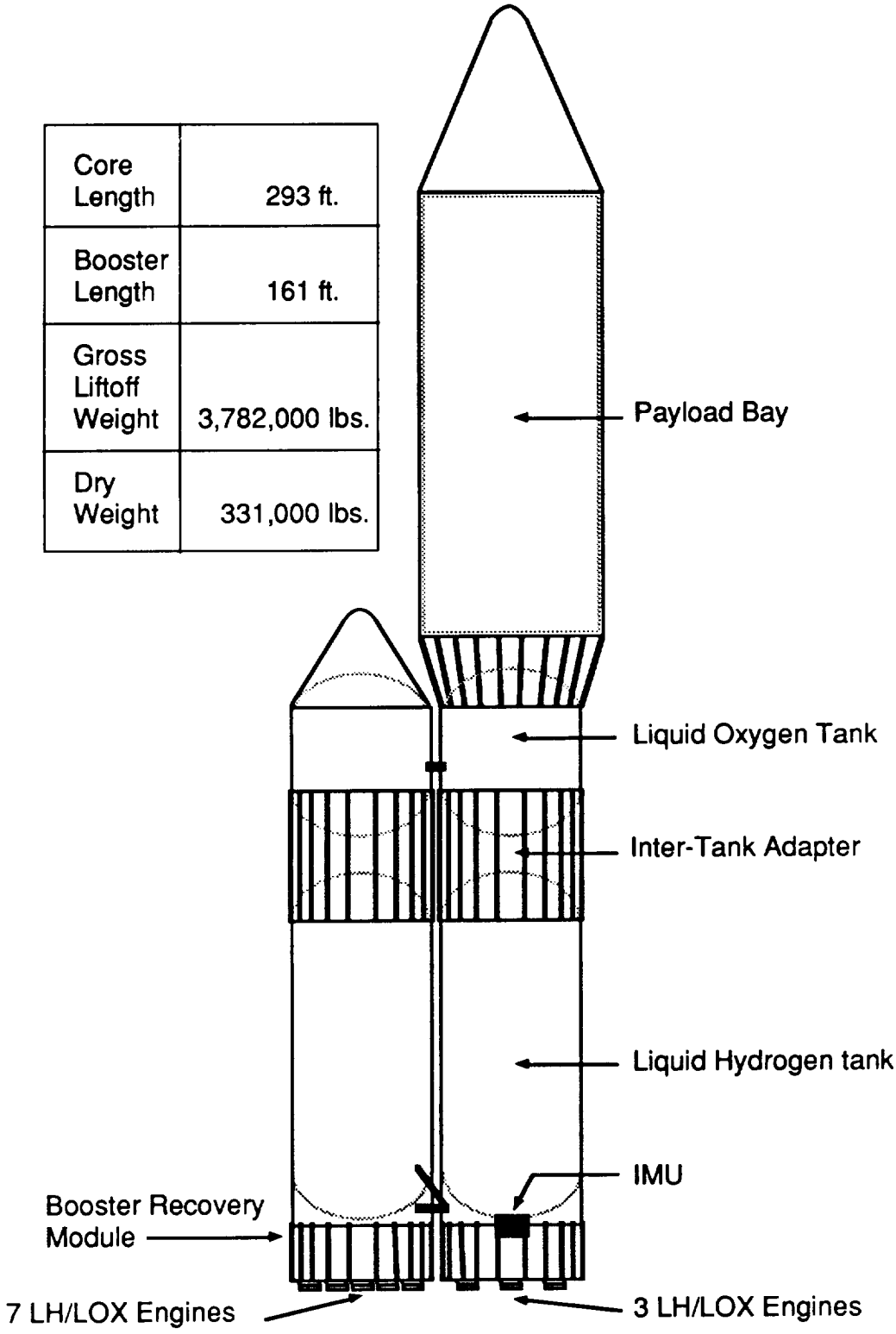

Figure 2.1 A.L.S. General Configuration

core/booster separation and parachutes are used to return the module to Earth. Recovery of the BRM is made at sea. The remaining components of the booster and core stages are not reusable.

(5) The ALS vehicle employs 10 gas generator fixed thrust engines. All of the engines are of the same type and all possess pitch and yaw plane gimballing capability. Table 2.1 is a summary of the physical characteristics of the engines. The vacuum thrust, the propellent flow rate, the cross section area of the engine, and the local atmospheric pressure are used to calculate the thrust generated by the vehicle. In addition because of the asymmetry of the vehicle all engines are installed with a 5° cant as illustrated in Figure 2.2. This provides the vehicle with a wider gimballing margin to help withstand "engine out" possibilities and large wind/gust dispersions.

NAME	SPECIFICATION
Cycle	Gas Generator
Propellants	LOX/LH
Throttling Rage	Fixed
Propellant Flow Rate	1,427 Lbs/sec
Vacuum Thrust	612 KLbs
Weight	6,744 Lbs
Inside Diameter	88.0 in
Length	150 in

Table 2.1 ALS engine data.

The exact location of all ten core and booster engines, and the manner in which individual engine deflections are to be commanded to produce desired attitude changes were not

specified in the design data package employed in this thesis. Therefore, to simplify the analysis it was decided to assume that the vehicle is controlled by two resultant thrust vectors, one for the core engines and one for the booster engines. Both resultant thrust vectors are assumed to be deflected by the same pitch angle, δ, which is computed by the flight control system. The deflection of the two engine thrust vectors can then cause torques on the vehicle which cause it to rotate to its commanded inertial attitude.

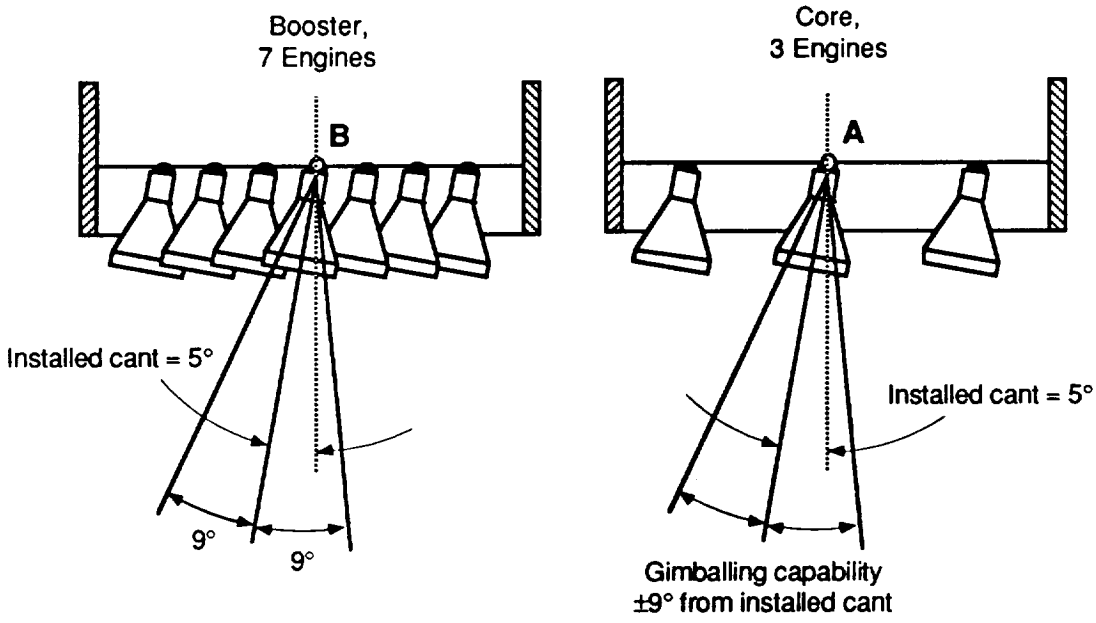

NOTE

1) All 10 engines are installed with a 5° cant.
2) All 10 engines have the same gimballing capability.
3) Resultant thrust vector of core acts through point **A.**
4) Resultant thrust vector of booster acts through point **B.**

Figure 2.2 ALS gimballing and engine cant relationship.

At this point it is appropriate to mention that the asymmetry in the launch vehicle of Figure 2.1 has made it necessary to employ the following operational modes and software design features:

(1) In order to minimize the aerodynamic roll torques, which are magnified by the asymmetry, it was decided to assume a roll orientation that puts the booster stage on top as the vehicle pitches over after liftoff. This orientation makes it possible to null aerodynamic roll torques by nulling the yaw angle of attack.

(2) As a result of vehicle asymmetry it is necessary to allow for appreciable pitch angle of attack values throughout the trajectory, even in the absence of winds. This is because the unequal total thrusts of the booster and core stages make it necessary to deflect the thrust vectors to maintain a near zero pitch rate. This is best illustrated at liftoff where the vehicle is commanded to maintain a 90° pitch attitude. At ignition, the thrust deflections produce an appreciable component of velocity perpendicular to the vehicle's longitudinal axis, with an accompanying no-wind angle of attack in the pitch plane. This is shown in Figure 2.3 where F_{Total} represents the effective sum of the core and booster thrusts for the zero torque condition necessary to maintain the initial 90° attitude. Also shown is the net acceleration applied to the vehicle by the thrust and gravity forces. It can be seen from the figure that the net acceleration vector is at an angle Φ with respect to the vertical. As a result, velocity is immediately developed in this direction and the vehicle acquires an instantaneous angle of attack equal to Φ. Although the aerodynamic pitch moment associated with the angle of attack allows some diminishment of the pitch deflections of the engines, these deflections must never the less be appreciable throughout the endoatmospheric boost phase.

(3) Although no data on the center of pressure position as a function of Mach number and angle of attack was available for this thesis study, it is assumed that there may be greater uncertainties in this position as well as in the aerodynamic force magnitudes for the

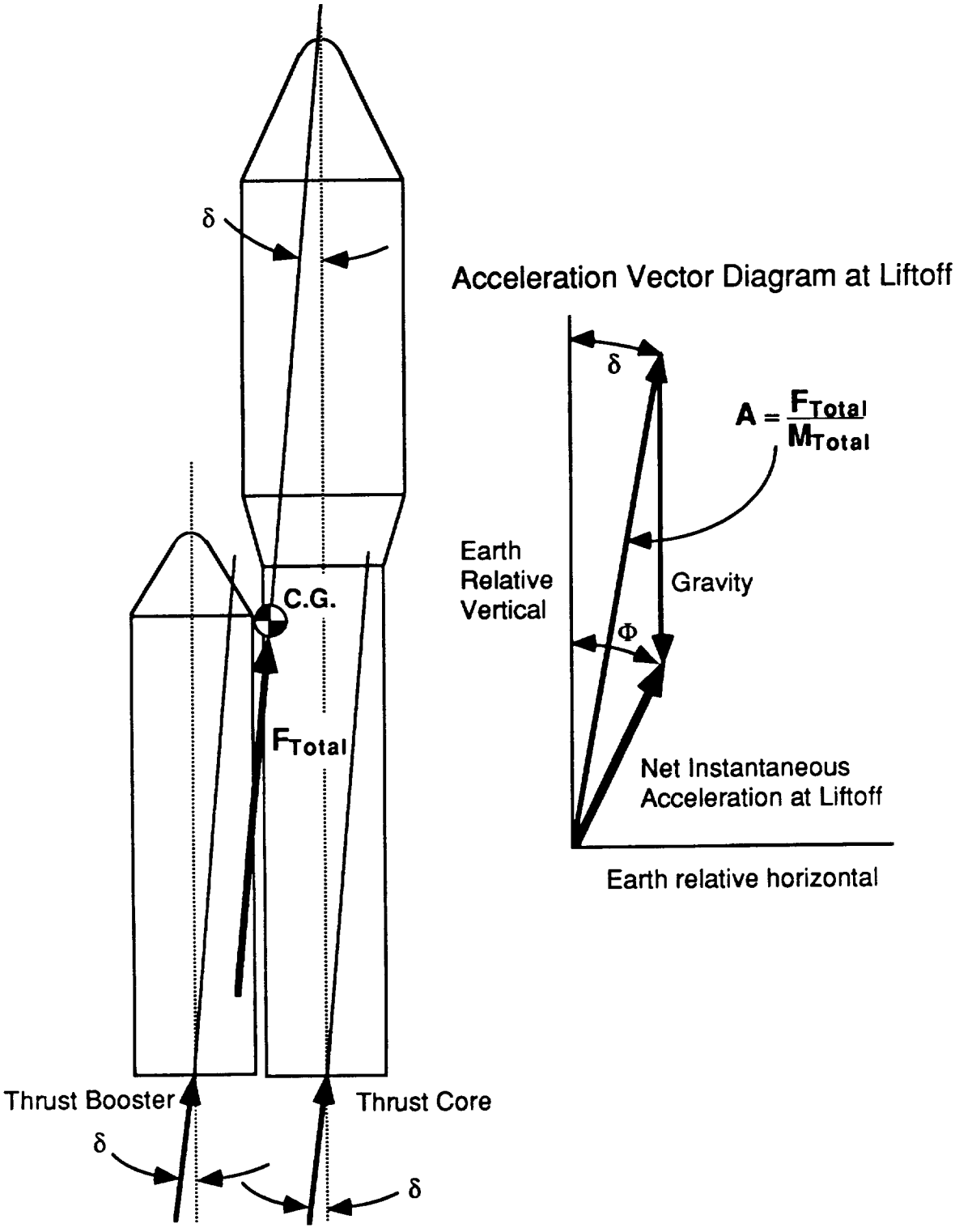

Figure 2.3 Net Acceleration Direction at Liftoff

asymmetrical vehicle. It is assumed that these uncertainties as well as uncertainties in the thrust-produced moments may require a special software feature that estimates the effects of torque mismodelling in order to obtain accurate estimates of angular acceleration, angular velocity and angle of attack for pitch plane control.

2.2 Flight Phases

As shown in Figure 2.4 the ascent profile of the ALS consists of four distinct flight phases which employ different guidance and control modes. The first three of these phases are endoatmospheric. The transition to exoatmospheric flight occurs in the last phase.

It will be noted that these phases are defined corresponding to guidance and control modes rather than the utilization of vehicle stages. The only staging event is the thrust termination and separation of the booster which occurs during Phase Four.

Phase One is characterized by a near vertical rise so that the vehicle may safely clear the launch tower. During this phase the vehicle is commanded to maintain a 90° pitch attitude. Termination of Phase One and transition to Phase Two occurs once the vehicle has reached a height of 400 ft. The next two endoatmospheric flight phases are designed to avoid excessive loads associated with the normal aerodynamic force. Since the magnitude of this force is proportional to the product of the dynamic pressure, Q, times the angle of attack, α, it is customary to constrain the atmospheric boost trajectory to avoid a specified maximum $Q\alpha$. The manner in which this avoidance is carried out has a crucial bearing on the safety and performance of the vehicle in its endoatmospheric boost phases.

Once the launch tower has been cleared in Phase One, Phase Two is initiated. This second phase covers a time period in which the value of the Q has not risen to a value where the $Q\alpha$ limit will significantly constrain attitude control. During this period the vehicle is maneuvered rapidly to achieve an end state that is compatible with the initial requirements of Phase Three. The

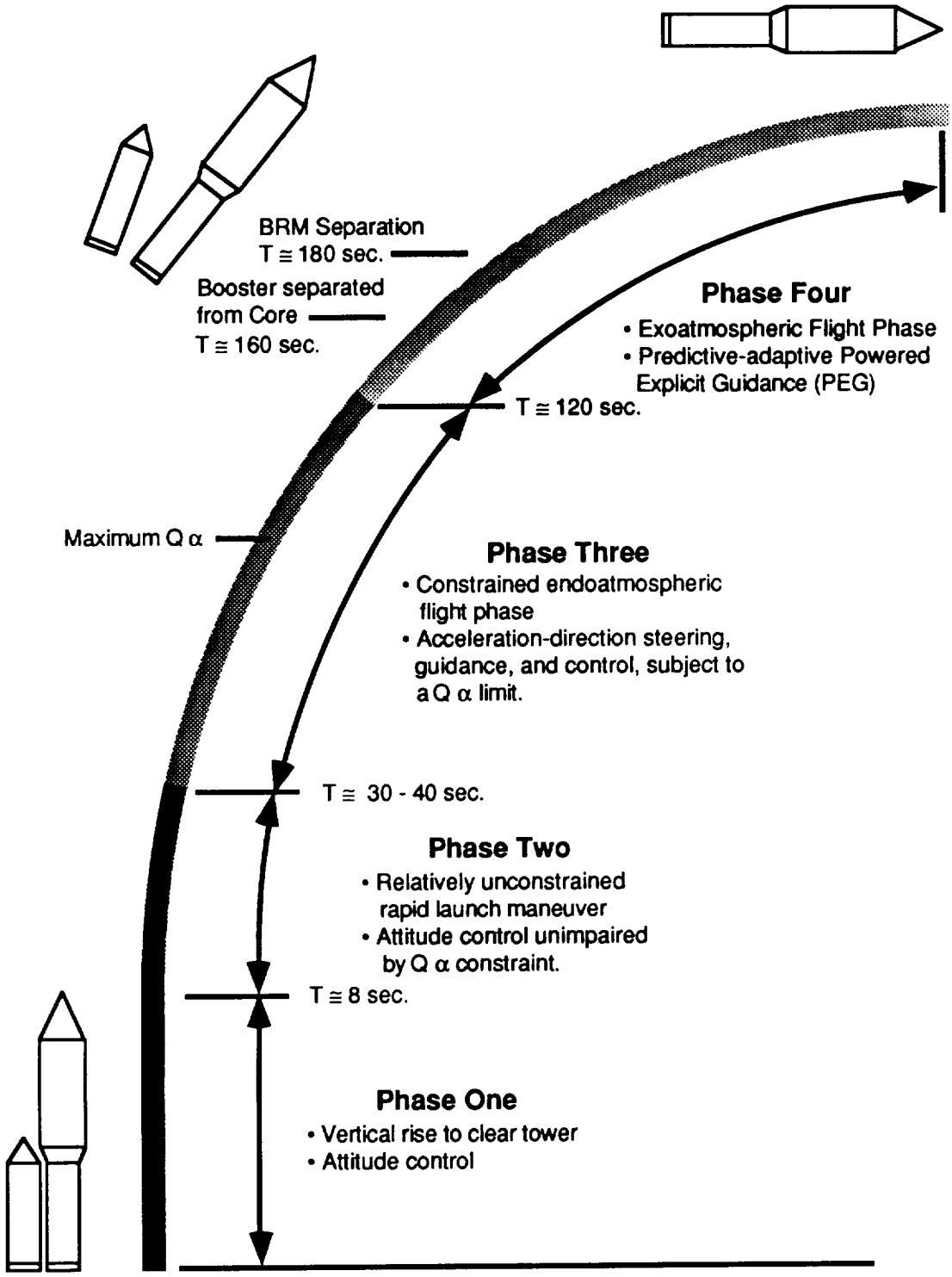

Figure 2.4 ALS Flight Phases.

commanded attitude in Phase Two is generated by an analytical function of time whose parameters are determined prior to launch by a trajectory design program described in Chapter Seven.

Phase Three covers a time period in which Q is sufficiently high that the limit on the $Q\alpha$ product can significantly constrain the boost trajectory. During this phase the vehicle's acceleration direction is controlled subject to the $Q\alpha$ limit. The commanded acceleration direction in Phase Three is obtained from a stored time profile generated prior to launch by the trajectory design program.

Phase Four is defined to begin at the point where the guidance shifts from one of the alternatives in Phase Three to a predictive-adaptive guidance method known as Powered Explicit Guidance (PEG). This method analytically predicts the on-orbit mass in cut-and-try computations which neglect the effects of atmospheric drag. The differing thrust levels before and after staging are taken into account in these computations. The direction of the thrust in each cut-and-try prediction is based on a "linear-tangent guidance law" which then generates the commanded thrust direction for 4 second time intervals between PEG updates.

When PEG takes over at 120 seconds the simulation is simplified by assuming that the thrust is in the commanded direction, with the effects of aerodynamic drag being subtracted from the thrust produced acceleration. The simplified simulation is terminated at the point of booster separation which occurs out of the atmosphere at 160 seconds. At this point the PEG prediction based on no atmosphere provides an accurate prediction of the on-orbit mass.

2.3 Coordinate Frames

To simulate and study the translational and rotational motion of the vehicle during flight four reference frames are defined. They are :

(1) Inertial Earth Centered Reference Frame - **(X, Y, Z)**.

All equations of motion are referred to this non-rotating Earth fixed reference frame. The origin of the frame is at the center of the

Earth with the **Z** axis pointed through the North Pole. The positive **X** axis points through 0 longitude at t=0. The **Y** direction forms a right handed set with **X** and **Z**.

(2) Local Geographic Frame - (**NORTH**, **EAST**, **UZG**).

The origin of this axis is located at the cg of the vehicle. **UZG** points toward the center of the Earth. **NORTH** lies on the plane formed by the **Z** axis and **UZG**. and points toward the North Pole. **EAST** completes right handed frame.

(3) Body Fixed Frame - (**UBX**, **UBY**, **UBZ**).

This frame is fixed to the cg of the vehicle. The **UBX** (roll) coordinate points along the center line of the vehicle. The **UBY** (pitch) coordinate remains perpendicular to pitch plane. **UBZ** completes the right handed set.

(4) Velocity Direction Frame - (**UVX**, **UVY**, **UVZ**).

This frame is fixed to the cg of the vehicle. **UVX** is directed along the Earth relative velocity vector. **UVY** is in the direction of the cross product of the gravity vector and **UVX**. **UVZ** completes the right handed set.

Figure 2.5 illustrates the relationship between the body axes and the local geographic coordinate system. The attitude, heading and bank of the vehicle is defined relative to the Local Geographic coordinate frame and the body frame. The attitude is the only variable of interest since this study is limited to the pitch plane. The bank of the vehicle is set to zero and the heading is determined by the initial launch azimuth. Figure 2.6 shows the relationship between the pitch plane trajectory of the vehicle and its inertial, body, and velocity frames. In relation to the body frame the velocity vector is described by two angles: the angle of attack, α, and the sideslip angle, β. However, for this

study the vehicle is constrained to fly in the trajectory plane assuming zero crosswinds, so that β=0.

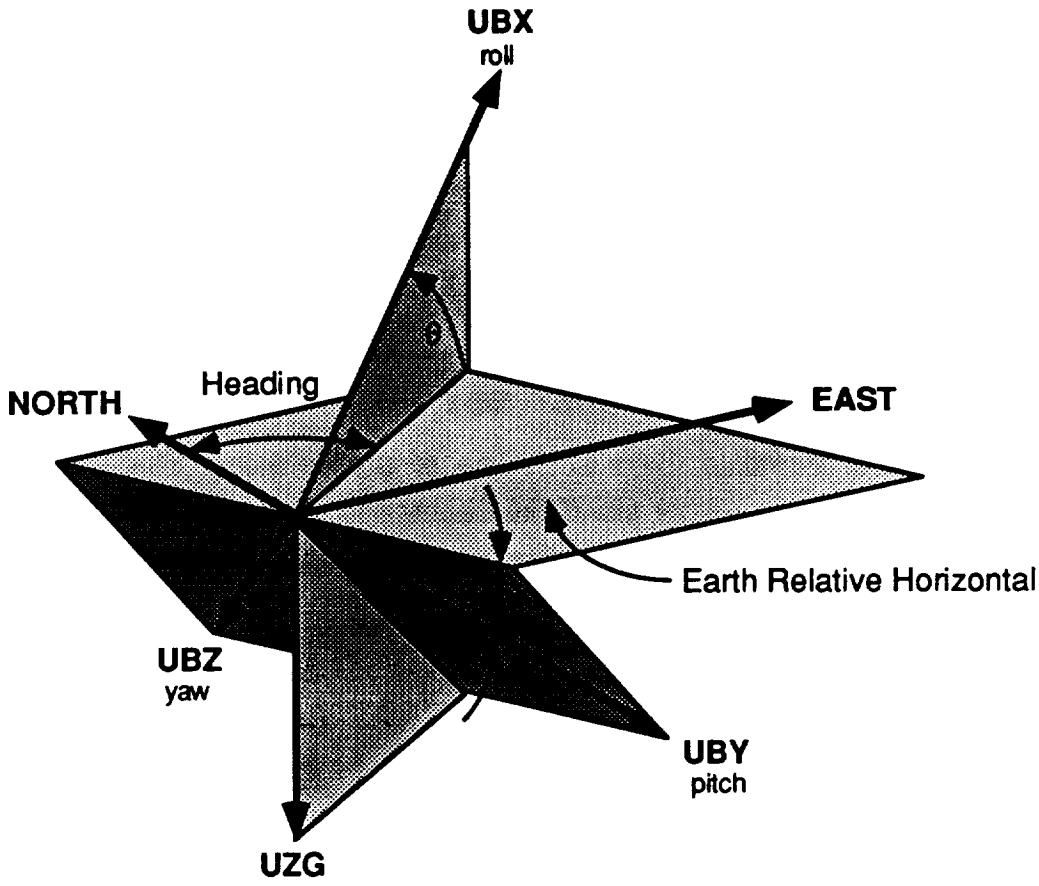

Figure 2.5 Body Frame with Local Geographic Frame

2.4 Constraints

The primary constraint on maneuvering within the atmosphere is the limit on aerodynamic loads which are produced by the normal aerodynamic force, F_n. This force is perpendicular to the centerline of the vehicle and acts at the

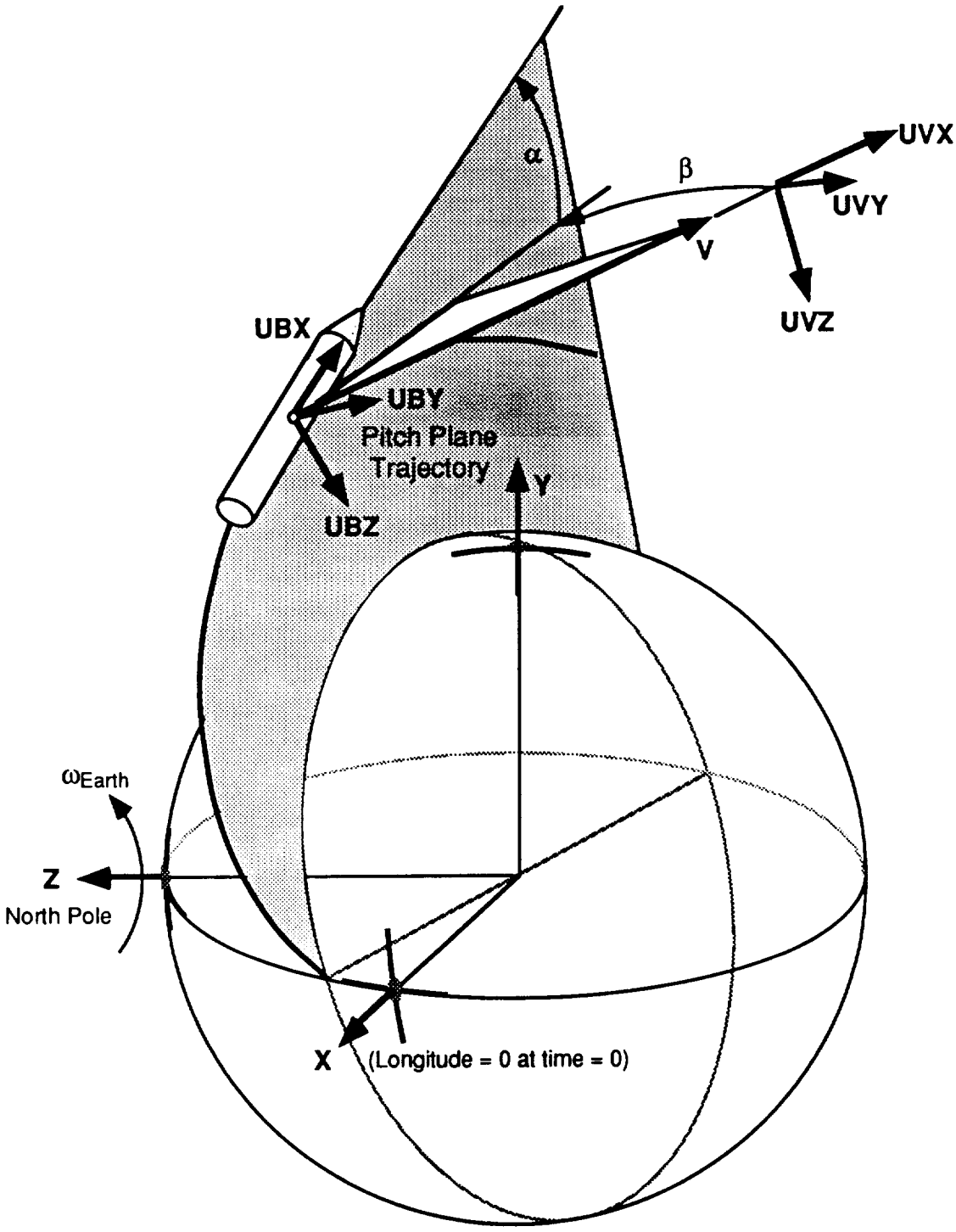

Figure 2.6 Reference Frame Relationships.

center of pressure. As the vehicle accelerates through the atmosphere the aerodynamic force can cause very large bending moments capable of destroying the vehicle. For a vehicle traveling with an air relative velocity V_a, the aerodynamic normal force can be expressed as:

$$F_n = \frac{1}{2} \rho \, V_a^2 \, S \, C_n \tag{2.1}$$

where

ρ = the air density

S = the cross-sectional area of the vehicle

C_n = the aerodynamic normal force coefficient.

The aerodynamic normal force coefficient is a function of Mach number and angle of attack. A simplified aerodynamic model for the the ALS was used based on a linear relationship between C_n and α for a wide range of Mach numbers. Given this linear relationship Equation (2.1) is then expressed as

$$F_n = \frac{1}{2} \rho \, V_a^2 \, S \, C_{n\alpha} \, \alpha \tag{2.2}$$

where

$$C_{n\alpha} = \frac{\partial C_n}{\partial \alpha}$$

The dynamic pressure Q, is defined as

$$Q = \frac{1}{2} \rho \, V_a^2 \tag{2.3}$$

so that the above equation for normal aerodynamic force can be rewritten as

$$F_n \cong S\, Q\, C_{n\alpha}\, \alpha \tag{2.4}$$

To control the normal aerodynamic force, a limit is usually imposed on the product of Q and α. The magnitude of Q is a function of the magnitude of the air-relative velocity of the vehicle, V_a, which increases during flight, and the air density, ρ, which decreases with altitude. The combined effects of the variations in ρ and V_a typically cause Q to maximize midway through Phase Three. In this region of maximum Q, the aerodynamic normal force is most sensitive to variations in angle of attack. A typical dynamic pressure profile for the ALS is illustrated in Figure 2.7.

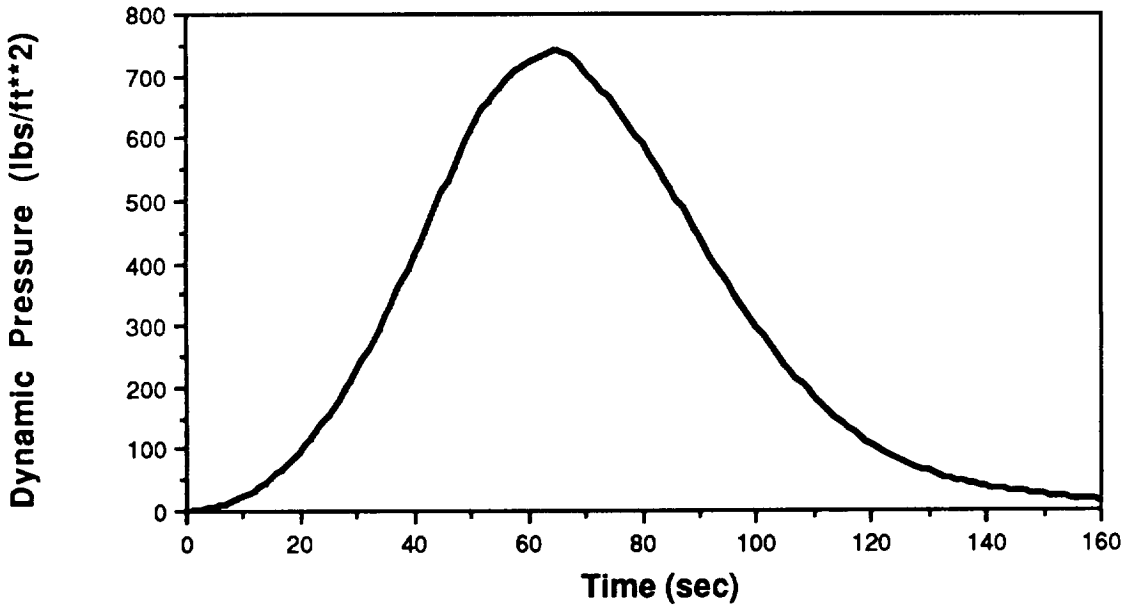

Figure 2.7 ALS Dynamic Pressure Profile.

2.5 Rigid Body Motion

All the steering, guidance and control concepts studied in this thesis are limited to the pitch plane and all roll and yaw motion is assumed to be zero.

As mentioned in the introduction, in the absence of bending and slosh data for this particular ALS design it was decided to employ only a rigid body model of the vehicle in this investigation. The equation of motion for linear acceleration is given by the relationship:

$$\mathbf{F} = m\,\mathbf{A}^{ci} \tag{2.5}$$

where

$\mathbf{F}$ = the vector sum of all forces acting on the vehicle.

m = the total vehicle mass.

$\mathbf{A}^{ci}$ = is the acceleration of the vehicle center of gravity with respect to an inertial frame of reference.

The rotational equation of motion is given by the relationship

$$\mathbf{M} = \dot{\mathbf{H}} \tag{2.6}$$

where

$\mathbf{M}$ = the vector sum of all moments applied to the system about the center of gravity.

and

$\mathbf{H}$ = the centroidal angular momentum vector.

The angular momentum vector is defined by the relationship

$$\mathbf{H} = \mathbf{I}\omega \tag{2.7}$$

where

$\mathbf{I}$ = Inertia matrix about the center of gravity.

ω = The angular rate vector of the vehicle with respect to the inertially fixed Earth Centered Reference Frame.

For the purposes of computing the derivative of $\mathbf{H}$ in Equation (2.6), it is convenient to compute the components of the inertia tensor and the components of the angular rate vector with respect to the vehicle axis system (u_1, u_2, u_3) (the body roll, pitch, and yaw axes respectively). In this system,

$$\mathbf{I} = \begin{bmatrix} I_{11} & I_{12} & I_{13} \\ I_{21} & I_{22} & I_{23} \\ I_{31} & I_{32} & I_{33} \end{bmatrix} \tag{2.8}$$

and

$$\omega = \begin{bmatrix} \omega_1 \\ \omega_2 \\ \omega_3 \end{bmatrix} \tag{2.9}$$

It is assumed in this thesis that the vehicle axis system is approximately a principal axes set -- ie, the products of inertia are sufficiently small so that they can be neglected. With this assumption, the angular momentum vector computed from Equations (2.7), (2.8), and (2.9) is given by

$$\mathbf{H} = \begin{bmatrix} I_{11}\,\omega_1 \\ I_{22}\,\omega_2 \\ I_{33}\,\omega_3 \end{bmatrix} \tag{2.10}$$

Equation (2.6) can now be evaluated from the following relationship

$$\mathbf{M} = \frac{d}{dt}\mathbf{H}\Big|_{\substack{\text{relative to} \\ \text{an inertial} \\ \text{reference frame}}} = \frac{d}{dt}\mathbf{H}\Big|_{\substack{\text{relative to the} \\ \text{body fixed frame}}} + \omega \times \mathbf{H} \tag{2.11}$$

Substituting Equations (2.9) and (2.10) into (2.11),

$$\mathbf{M} = \begin{bmatrix} I_{1\,1}\dot{\omega}_1 - \omega_2\omega_3(I_{22} - I_{33}) \\ I_{2\,2}\dot{\omega}_2 - \omega_3\omega_1(I_{33} - I_{11}) \\ I_{3\,3}\dot{\omega}_3 - \omega_1\omega_2(I_{11} - I_{22}) \end{bmatrix} \tag{2.12}$$

It will be noted that terms involving derivatives of I_{11}, I_{22}, and I_{33} have not been included in the above equations. These derivatives, which are caused by propellant expenditure, are assumed to be negligible. The components of Equation (2.12) represent Euler's Equations of motion. These equations can be solved for the angular accelerations $\dot{\omega}_1$, $\dot{\omega}_2$ and $\dot{\omega}_3$ which can then be integrated by the ALS simulation to provide angular rate and attitude information with respect to the body frame. In vector form, the angular accelerations can be determined by substituting Equation (2.7) into Equation (2.11) and solving for $\dot{\omega}$ to obtain

$$\dot{\omega} = \mathbf{I}^{-1}\mathbf{M} - \mathbf{I}^{-1}\left(\omega \times (\mathbf{I}\,\omega)\right) \tag{2.13}$$

Equation (2.13) can be solved for acceleration and integrated by the ALS simulation.

2.6 Aerodynamic Characteristics

Aerodynamic data were provided to CSDL by the NASA Langley Research Center. Lift and drag coefficients for both the subsonic (0.1 < Mach < 2.0) and supersonic (3.0 < Mach < 10) speed ranges were provided over angles of attack of ± 20°. Subsequently this data was converted to coefficients of normal and axial force so that all forces on the vehicle could be summed in the body frame. Over the entire speed range interference affects between the core and booster stages are neglected.

Because only a discrete matrix of aerodynamic data points is available over the specified ranges of Mach number and angle of attack, a linear interpolation scheme is used to extract the values of aero-coefficients between the data points. This is achieved by first fitting all of the aero coefficients to several third order curves by least squares fits along lines of constant Mach number, and then linearly interpolating between two of the constant Mach curves termed the "Low-Mach" and "High-Mach" curves for given values of α and Mach Number. Appendix C contains a more detailed description of this procedure.

Since this study is limited to the pitch plane, only those aero coefficients affecting motion in the pitch plane are generated in the simulation. Accordingly, all lateral forces are neglected and the vehicle is subjected only to tail and head winds.

2.7 Mass properties

In order to simulate the dynamics of the ALS vehicle an estimation of the moment of inertia in the pitch plane and the location of the center of gravity is required. This is achieved in a subroutine of the main program where the mass properties of the vehicle are updated each control cycle (100 ms) by continually

re-evaluating the remaining masses of core and booster propellant during flight and adjusting the cg location and inertia of the vehicle based upon these fuel mass properties and a pre-launch dry estimate of the vehicle mass properties. An exact description of the ALS is not available and therefore the dry estimate is simplified by using a model based upon several basic geometric solids in aggregate. These solids are further assumed to have masses which are uniformity distributed. The fuel tanks, for example, are modelled as hollow circular cylinders.

The liquid booster stage from aft to forward consists of a Booster Recovery Module (BRM), a liquid hydrogen tank, an inter-tank adapter, a liquid oxygen tank, and a nose cone. All of these components are modelled as hollow cylinders with the exception of the BRM which is modelled as a solid cylinder. In addition, the engine modules on both stages share a common structure or frame. However, because no information is available on the gross mass of each module, both structures are assumed to equal 15% of their respective total engine weights. The lower half of the core stage is modelled similarly to the booster stage, with the exception of the payload bay. Because no specific payload configuration was available the cargo bay was simply modelled as a solid homogeneous cylinder.

The volumes of liquid oxygen (LOX) and liquid hydrogen (LH) in both the core and booster stages are estimated from the total propellant weight at liftoff, and the fuel mixture ratio (FMR) of each engine. Consequently, the amounts of LOX and LH in each vehicle are programmed to drain simultaneously upon engine burnout. The fuel for each vehicle is modelled as a pair of solid cylinders, one on top of the other, running lengthwise along the vehicle with the liquid hydrogen tanks located aft. As liquid propellant is combined and then ignited the inertia model assumes that all of the remaining fuels form homogeneous cylinders at the base of each fuel container. Table 2.2 shows a summary of the dry mass properties of the A.L.S. A more detailed description of the dry inertia model can be found in Appendix A.

Vehicle	X c.g. (ft)	Z c.g (ft)	Pitch Inertia (slug ft^2)
Core	138.0	0.0	56,872,200
Booster	63.5	0.0	16,945,000
TOTAL*	**112.2**	**-11.1**	**98,671,000**

Table 2.2 Summary of Mass Properties.

* Datum located at base of core, see Figure C.2

Chapter Three

ACCELERATION DIRECTION GUIDANCE, STEERING, AND CONTROL

3.1 Introduction

The SSTO Shuttle II system concept investigated by Corvin employed a combination of velocity-direction guidance-steering and angle of attack control. For the ALS an alternative guidance steering and control concept will be considered. This concept employs an acceleration direction guidance-steering algorithm, subject to a control override based on a $Q\alpha$ limit. This alternative concept combines the best features of the Shuttle II approach and the traditional approach of acceleration-direction guidance with add-on load relief. The following chapter will (1) examine the rationale behind the selection of the ALS system concept, (2) describe the application of frequency response analysis to determine values of compensation gains for the two ALS modes and (3) describe a method for implementing the switching of compensation gains.

The ALS, Shuttle II and traditional atmospheric boost phase concepts are special cases of the generic guidance, steering and control system illustrated in Figure 3.1. As shown in this figure, the generic system has three major feedback loops. The innermost loop is the control loop, whose feedback variable is related to the rotational motion of the vehicle. Closed around the control loop is the steering loop whose feedback variable is related to the translational motion of the vehicle. Finally, there is the guidance loop which employs the estimated vehicle state to generate the steering command. As seen from the figure, the guidance can be either closed-loop or open-loop. In the latter case the guidance is based on computations that are performed prior to launch.

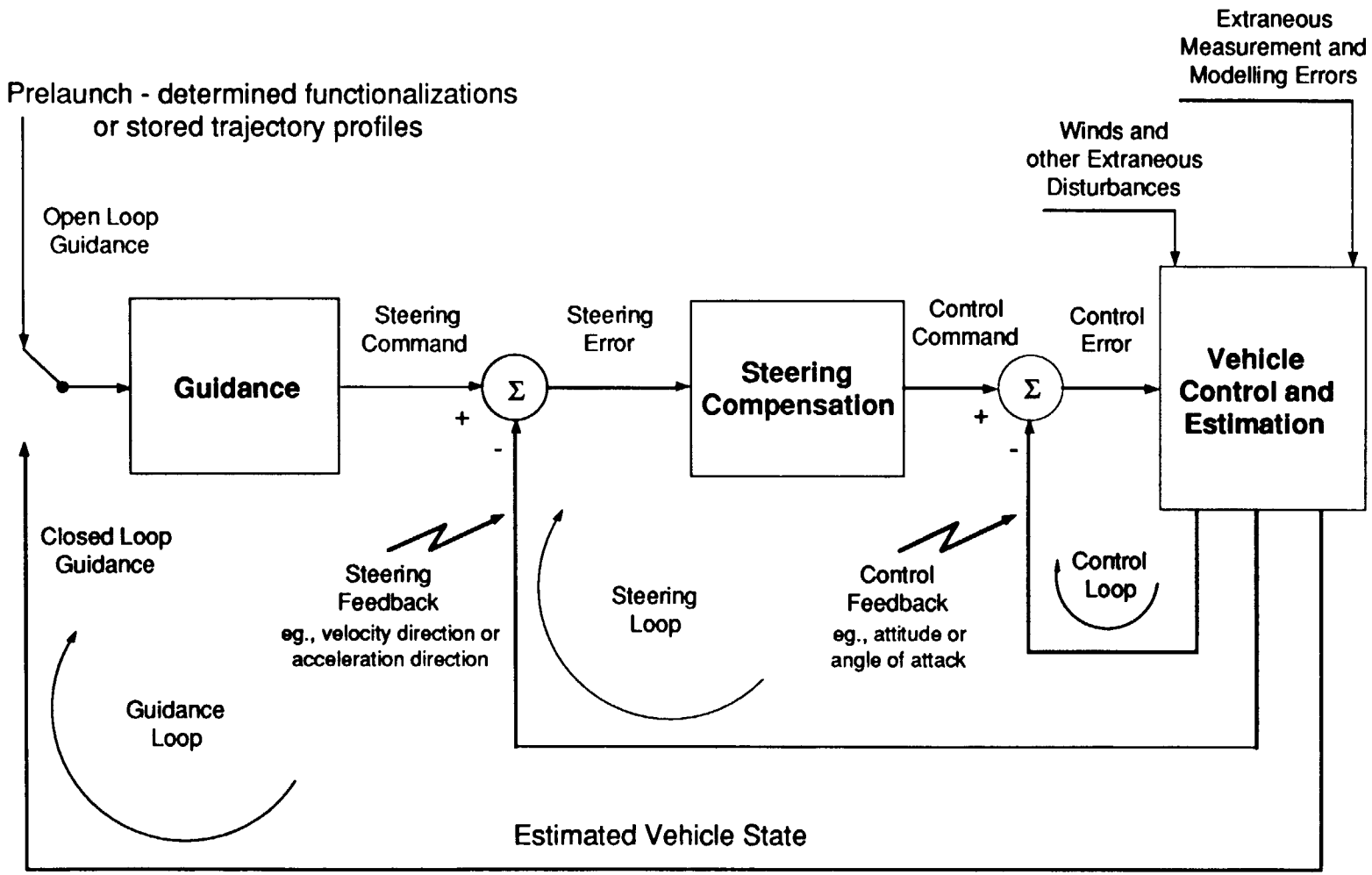

Figure 3.1 Generic block diagram defining guidance, steering and control operations

The block in Figure 3.1 labeled "Vehicle Control and Estimation" is expanded into its component blocks and signal paths in Figure 3.2. The configuration described in the latter figure is common to all of the overall guidance, steering and control concepts that are discussed below. As shown, the control and estimation system consists of five blocks and one primary feedback loop. Two different compensation blocks are present, the first of which is located outside the attitude rate feedback loop, and the second of which modifies the estimated attitude rate error to generate a nozzle deflection command for the engine nozzle servos. Thus, all of the systems achieve attitude control through the deflection of their engines. In addition, the measured engine nozzle deflection is used in conjunction with IMU measurements to generate the necessary estimated feedback variables used for control and steering purposes. One of these estimated signals is the estimated angular velocity of the vehicle.

The traditional approach to guidance, steering and control in the latter portion of atmospheric boost is shown in Figure 3.3. This approach combines the steering and control functions into a single feedback loop which approximately nulls the sum of an add-on load relief signal and the error between the commanded and estimated acceleration directions. The combining of the steering and control loops into a single loop provides a fast response to steering commands; however, the use of add-on load relief to modify the steering-control error has two major disadvantages:

(1) The achievement of both trajectory control and load relief objectives through a linear combination of signals (which often are in conflict) necessitates certain compromises in system design.

(2) The load relief feedback signal can appreciably alter the trajectory in unpredictable ways in the presence of winds, even when the winds are not sufficient to cause aerodynamic forces to come close to their design limits.

Moreover, the control of acceleration direction rather than velocity direction (as in the Shuttle II concept) can result in the accumulation of errors in velocity direction (or flight path angle) and altitude. These errors can be significant in some applications.

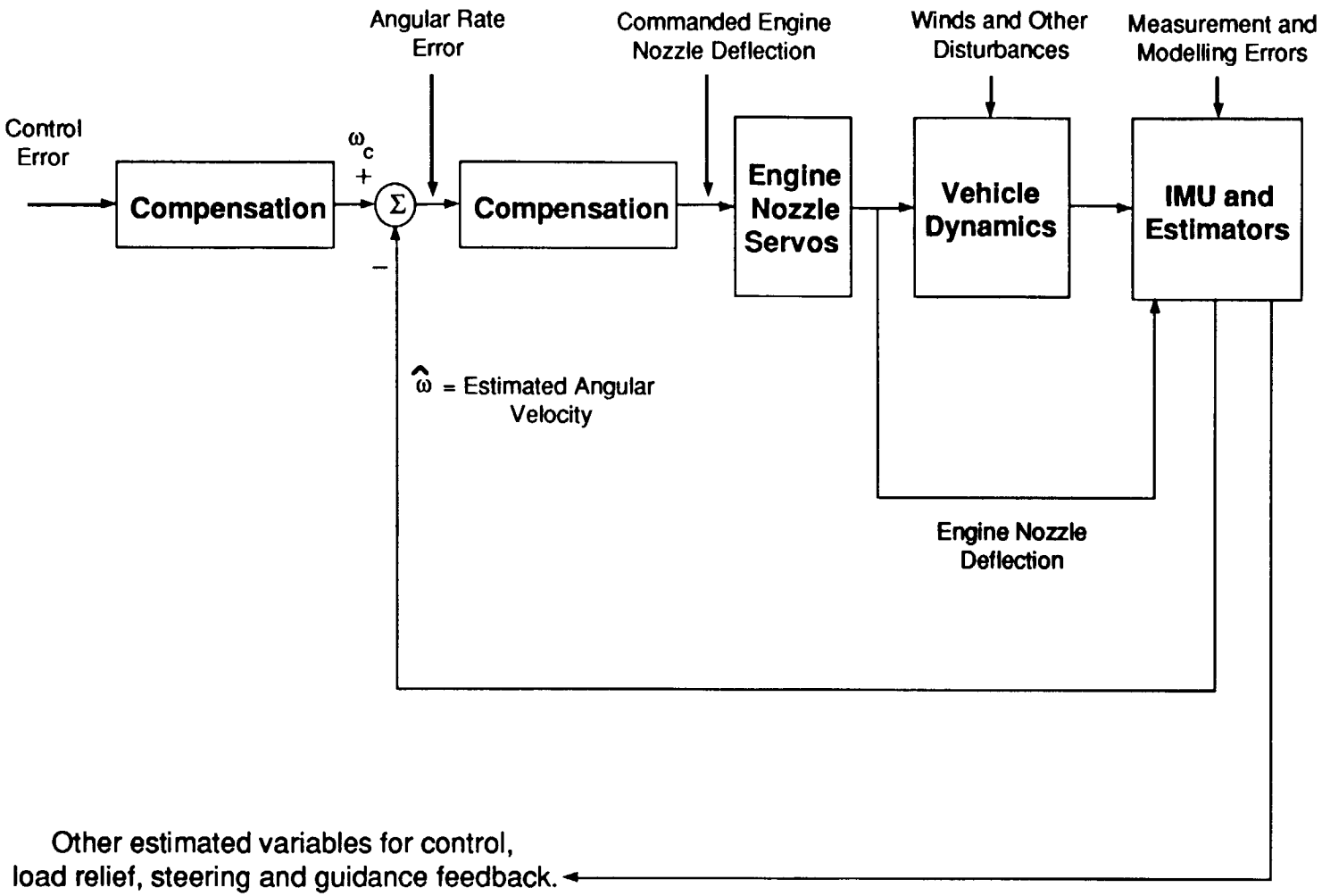

Figure 3.2 Elements of the vehicle control and estimation block in Figure 3.1

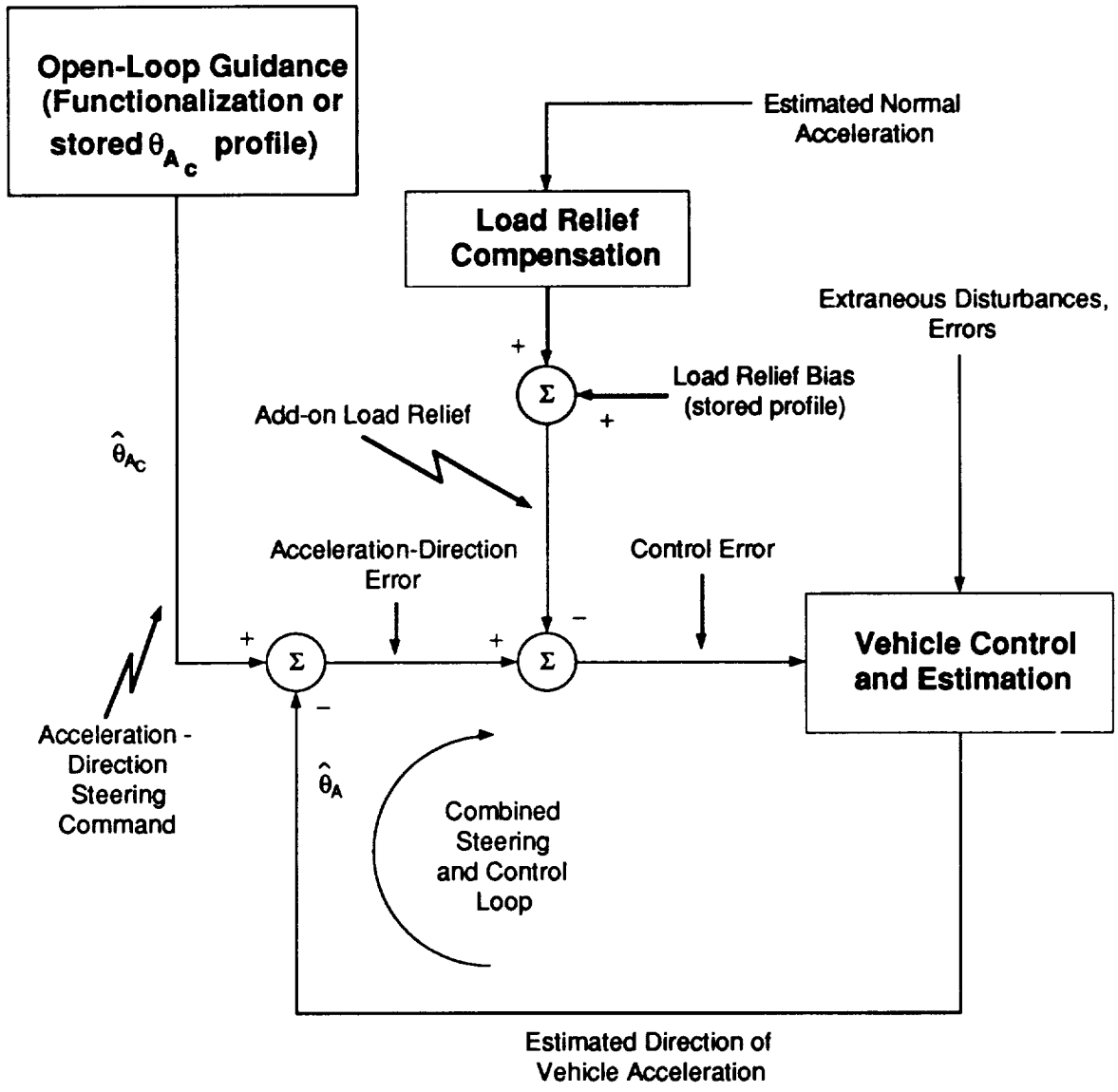

Figure 3.3 Traditional acceleration-direction guidance with combined steering and control loop with add-on load relief.

Some of the disadvantages of the traditional approach are overcome by the alternative of velocity-direction guidance-steering and angle of attack control illustrated in Figure 3.4. In this alternative configuration the load relief function is implemented by feeding back the angle of attack in the inner-loop and by limiting the angle of attack command. As a result, the load relief is not in

conflict with velocity direction control except when that control is affected by the limiting of the angle of attack command. Even when the angle of attack command is limited, the resulting vehicle acceleration is in a direction to null the velocity direction error. Furthermore, since the angle of attack is the only feedback control variable, this concept can provide a better load relief response to wind disturbances than the traditional system concept. Also, the velocity-direction outer steering loop overrides the effects of winds on the angle of attack inner loop, and thereby offers, at least in theory, a more accurate control of both the velocity direction and altitude. The block diagram of Figure 3.4 includes the representation of the predictive-adaptive guidance feedback loop that was considered by Corvin as an option for the Shuttle II system and also considered by Ozaki in an earlier study.[1, 2]

The third alternative, which will be studied for the ALS application, combines some of the features and advantages of the traditional and Shuttle II concepts. This alternative, which is described in Figure 3.5, achieves the fast steering response of the traditional approach while also achieving the fast load relief and other advantages of the Shuttle II approach. As shown in Figure 3.5, the concept for the ALS builds on the traditional concept in its use of a combined steering-control system whose primary input is a commanded direction of the vehicle acceleration. However, unlike the traditional concept, the alignment of the commanded and estimated acceleration directions is unimpaired by an add-on load relief. Instead, the load relief function is performed only when the angle of attack that would be produced by the nulling of the acceleration direction error exceeds a limit derived from a specified $Q\alpha$ limit. As shown in the figure, this is done by utilizing a mode switching logic based on the predicted error-nulling angle of attack, $\alpha_{pred} = \hat{\alpha} + E_A$. This quantity is compared to the $Q\alpha$-determined limit, α_{lim}, in the mode switching logic and the sign of this quantity determines the polarity of the angle of attack

---

[1] Corvin, M.A., " Ascent Guidance for a Winged Boost Vehicle". 1988. Massachusetts Institute of Technology Master of Science Thesis, CSDL Report T- 1002.

[2] Osaki, A.H., "Predictive/Adaptive Steering for the Atmospheric Boost Phase of a Space Vehicle". 1987. Massachusetts Institute of Technology Master of Science Thesis, CSDL Report T-966.

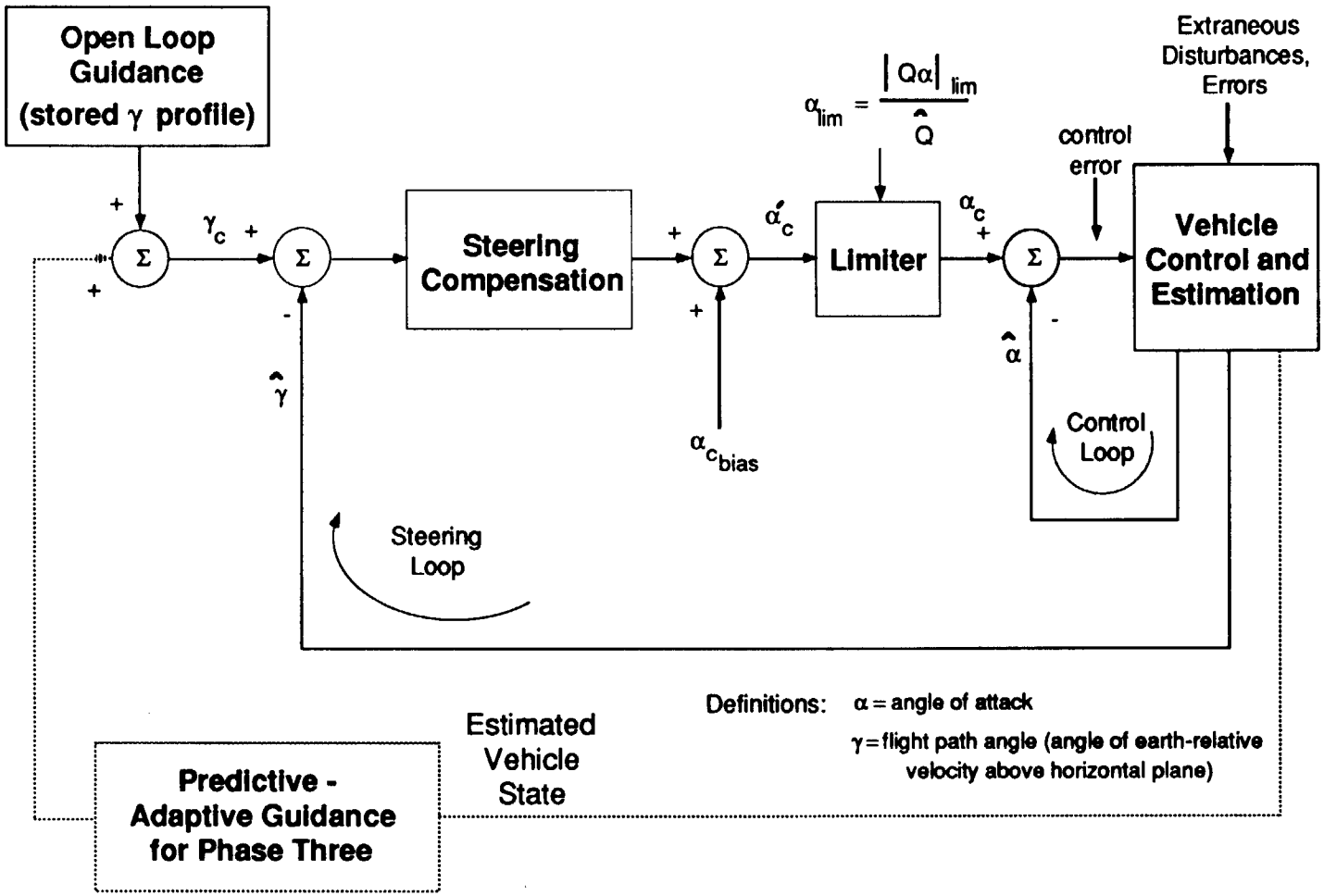

Figure 3.4 SSTO guidance, steering and control system for Phase Three.

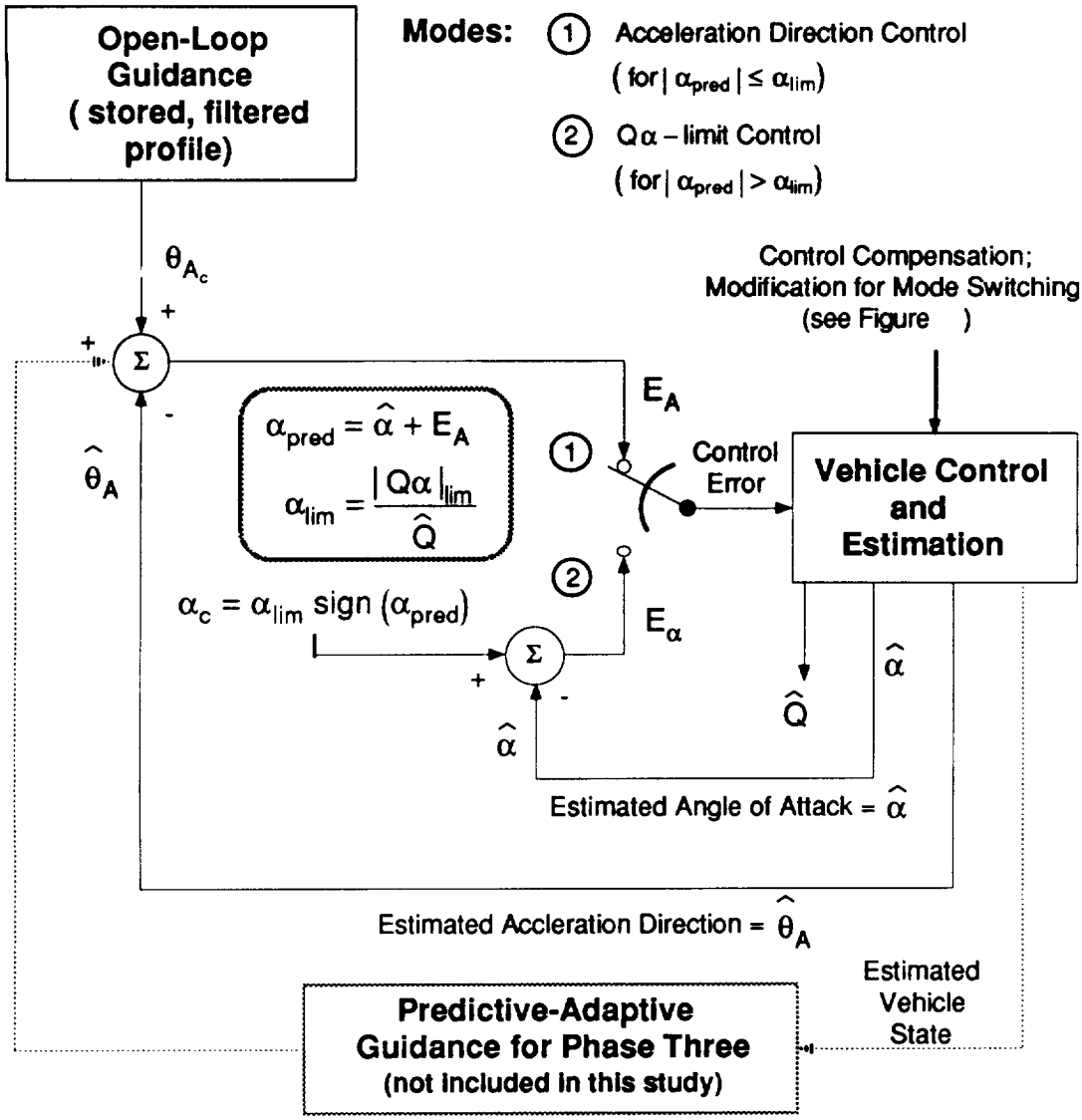

Figure 3.5 Improved acceleration-direction guidance, steering and control for Phase Three of the ALS, with Qα-limit override replacing add-on load relief.

command when in the limiting mode. This Qα limiting feature gives full freedom to the acceleration direction steering and control to shape the boost trajectory within the Qα limit, and also gives full priority to the control of angle of attack when necessary. This basic dual mode concept was first introduced in an

earlier study by Glenn Bushnell.[3] This concept will be expanded for the ALS system. The only possible disadvantage of this approach for the ALS relative to the Shuttle II approach is the fact that in using acceleration direction rather than velocity direction for steering, the ALS method may allow larger errors to accumulate in velocity direction and altitude (relative to the desired trajectory). However, a predictive-adaptive guidance technique which is illustrated as an option in the figure could be designed to achieve desired values of velocity direction at the end of Phase Three. The predictive-adaptive guidance in the ALS application could be designed alternatively for the more important objective of minimizing the aerodynamic loads or maximizing the utilization of propellant in the entire boost operation. The option of predictive-adaptive guidance will not be explored in this thesis.

There are two aspects of the ALS design of Figure 3.5 which require elaboration. One is the design of the various estimators of the ALS system concept. These will be discussed in this chapter and three subsequent chapters. The second aspect is the changing of control compensation parameters and reinitialization of the compensation in switching from one control mode to the other. The need for this compensation feature will be explained in a stability analysis presented later in this chapter, after which the implementation of the parameter switching and reinitialization will be described.

3.2 Estimators for the ALS System

It can be seen from Figures 3.1 and 3.5 that the guidance, steering and control system to be considered for the ALS involves the feedback of three estimated variables. These variables are the estimated acceleration direction, $\hat{\theta}_A$, the estimated angle of attack, $\hat{\alpha}$, and the estimated angular velocity, $\hat{\omega}$. In addition, there are two other estimated variables which are employed in the estimation of the feedback variables. These are the estimated dynamic

---

[3] Bushnell, G.S., "Guidance, Steering and Control of a Three Stage Solid Propellant Boost Vehicle". 1989. Massachusetts Institute of Technology Master of Science Thesis, CSDL Report T-1012.

pressure, (employed in estimating the angle of attack), and the estimated angular acceleration (employed in estimating the angle of attack and the angular velocity). The design of the estimators to generate these variables involves consideration of (a) the reduction of adverse effects of signal errors (e.g., quantization), (b) minimization of the effects of system modelling errors, and (c) the effects of estimator design on speed of response and stability.

The designs of most of the estimators described in this thesis are highly tentative, since the system and signal characteristics which influence the configurations and parameters of these estimators have yet to be finalized for the ALS. This is especially true for the angular velocity, angular acceleration, and angle of attack estimators discussed in Chapters 4 and 5. The signal and system characteristics have the least effect on the design of the dynamic pressure estimator, which is described in Chapter 6.

3.3 Acceleration Direction Estimator

3.3.1 Introduction

The estimator which generates the estimated direction of the vehicle acceleration (excluding gravity) is of primary importance in the design of the acceleration direction guidance, steering, and control algorithm. The design and implementation of this estimator involves the following steps:

(1) Computing the direction of the acceleration vector in body axes from inertial measuring unit (IMU) accelerometer measurements.

(2) Expressing the direction of the measured thrust direction in terms of pitch and yaw angles.

(3) Passing the pitch and yaw angles through first order low-pass filters to generate filtered angles.

(4) Employing the filtered angles to generate a unit vector in body axes representing the filtered acceleration direction.

(5) Comparing the unit filtered-direction vector with the commanded acceleration direction (transformed to body axes) to compute the pitch and yaw errors in acceleration direction.

An important feature of the acceleration direction estimator is step (3), the filtering of the measured acceleration direction. This filtering is necessary to reduce the control signal fluctuations caused by the effects of quantization in the IMU accelerometer signals. In addition, filtering improves the control loop stability by reducing the effects caused by the regenerative feedback of the engine nozzle contribution to the estimated acceleration direction.

The acceleration direction is employed as a feedback variable in both the pitch and yaw loops in the conventional version of acceleration direction guidance, steering and control. However, in the ALS it will be assumed that this direction is employed only in the pitch loop, and that the yaw angle of attack or the sideslip angle is employed as the primary feedback variable for yaw control. As pointed out previously, only the problems of pitch control will be considered in this thesis. The possibility of using the acceleration direction estimator in both pitch and yaw is not precluded by the design described below, which includes both pitch and yaw angles of the acceleration direction vector.

3.3.2 Calculation Procedure

The commanded and estimated acceleration direction angles θ_{Ac} and $\hat{\theta}_A$ in Figure 3.5 are actually represented by unit vectors in the present simulation of the ALS system. Initially the commanded acceleration vector, θ_{Ac}, is computed in the inertial frame and stored as a function of time (see Chapter 7). Later, during actual in-flight simulations this stored acceleration vector is retrieved and transformed into the body axis system. The estimated acceleration direction angle, $\hat{\theta}_A$, is derived from IMU accelerometer measurements employing relationships that will be described in this section. The manner of computing pitch and yaw errors from these vectors will also be described.

The estimated acceleration direction is based on inertial velocity increments measured by the IMU. During each control cycle these inertial measurements are transfered to the body-axis system. These three body-axis increments are:

ΔV_1 = increment in velocity along the vehicle x (roll) axis

ΔV_2 = increment in velocity along the vehicle y (pitch) axis.

ΔV_3 = increment in velocity along the vehicle z (yaw) axis.

These increments are employed as follows to compute the pitch and yaw angles of the measured acceleration-direction vector, designated respectively as β_p and β_y.

$$\beta_p = \tan^{-1} (\Delta V_3/\Delta V_1) \tag{3.1}$$

$$\beta_y = \tan^{-1} (-\Delta V_2/\Delta V_1) \tag{3.2}$$

where the angles are defined positive according to the right handed rule. These two acceleration-direction angles are then sent through a discrete low-pass filter. In the continuous domain this filter has the form

$$\frac{\tilde{\beta}(s)}{\beta(s)} = \frac{1}{\tau_\beta s + 1} \tag{3.3}$$

where τ_β is the filter time constant. Using the Backward Rectangular rule the complex frequency, s, can be approximated in the z-domain by the relationship:

$$s = \frac{1 - z^{-1}}{T} \tag{3.4}$$

where T is the sampling time of the discrete filter. Substituting Equation (3.4) into (3.3) results in the following two difference equations:

$$\tilde{\beta}_p = K_\beta z^{-1} \tilde{\beta}_p + (1 - K_\beta) \beta_p \tag{3.5}$$

$$\tilde{\beta}_y = K_\beta z^{-1} \tilde{\beta}_y + (1 - K_\beta) \beta_y \tag{3.6}$$

where $\tilde{\beta}_p$, $\tilde{\beta}_y$ are the filtered pitch and yaw angles, respectively, and where the constant K_β is computed as

$$K_\beta = \frac{\tau_\beta}{T + \tau_\beta} \tag{3.7}$$

Finally, the unit vector, $\hat{\mathbf{U}}_A$, representing the estimated filtered thrust direction in body axes is computed from

$$\hat{\mathbf{U}}_A = \text{Unit value of} \begin{bmatrix} 1 \\ \tan(\tilde{\beta}_y) \\ \tan(-\tilde{\beta}_p) \end{bmatrix} \tag{3.8}$$

Designating the transformed unit vector representing the commanded acceleration direction as $\mathbf{U}_{Ac}$, the acceleration-direction errors E_{A_p} (pitch) and E_{A_y} (yaw) are computed as follows. First, the cross product between $\mathbf{U}_{Ac}$ and $\hat{\mathbf{U}}_A$ is obtained:

$$C = \hat{\mathbf{U}}_A \times \mathbf{U}_{Ac} \tag{3.9}$$

Then the angle, β_A, between the vectors is computed from

$$\beta_A = \sin^{-1} |C| \tag{3.10}$$

And finally, a vector representing the error angles is computed from

$$\hat{U}_E = \beta_A [\ \text{unit}\ (C)\ ] \tag{3.11}$$

The pitch and yaw error angles E_{A_p} and E_{A_y} are then equal to components of $\hat{U}_E$:

$$E_{A_p} = \hat{U}_{E_2} \tag{3.12}$$

$$E_{A_y} = \hat{U}_{E_3} \tag{3.13}$$

The pitch error E_{A_p} is represented by the symbol E_A in Figure 3.5.

3.4 Approximate Vehicle Transfer Functions Relationships for Stability Analysis

Since the details of the vehicle bending and slosh modes and the characteristics of the engine nozzle servos were unavailable at the initiation of this thesis study, it was decided to represent the ALS by a rigid-body model, assuming lagless engine nozzle servos. These assumptions make it an easy matter to achieve large stability margins. This further justifies the use of approximate dynamic models to adjust the compensation parameters.

The two control modes used in the ALS simulation are illustrated in Figures 3.6 and 3.7. As shown in these figures the compensation design is achieved by breaking the forward control path at the nozzle servo command. It

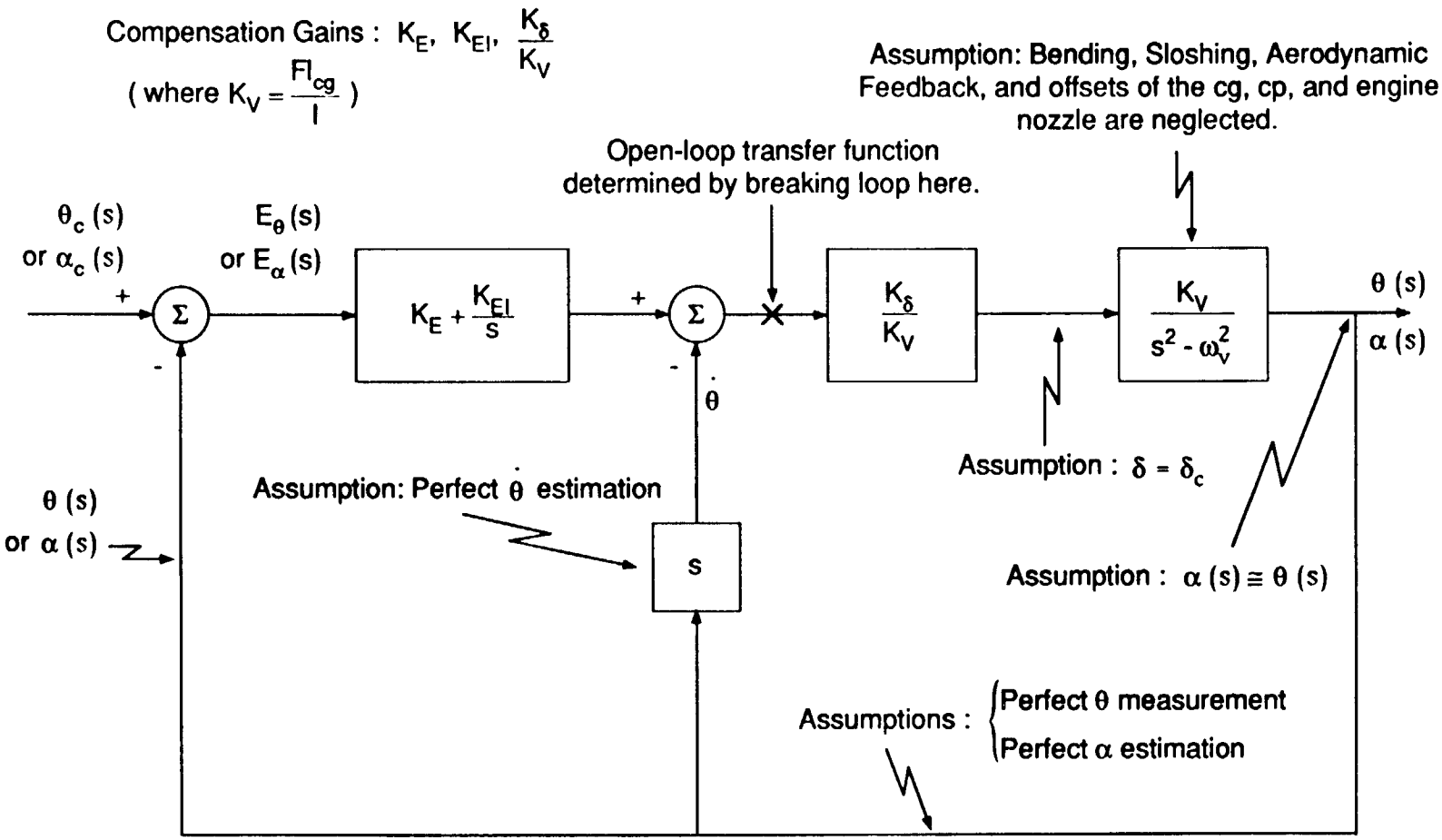

Figure 3.6 Approximate transfer functions for Phase One and Two and for the Qα limit mode in Phase Three.

Compensation Gains : $\tilde{K}_E, \tilde{K}_{EI}, \frac{\tilde{K}_\delta}{K_V}$

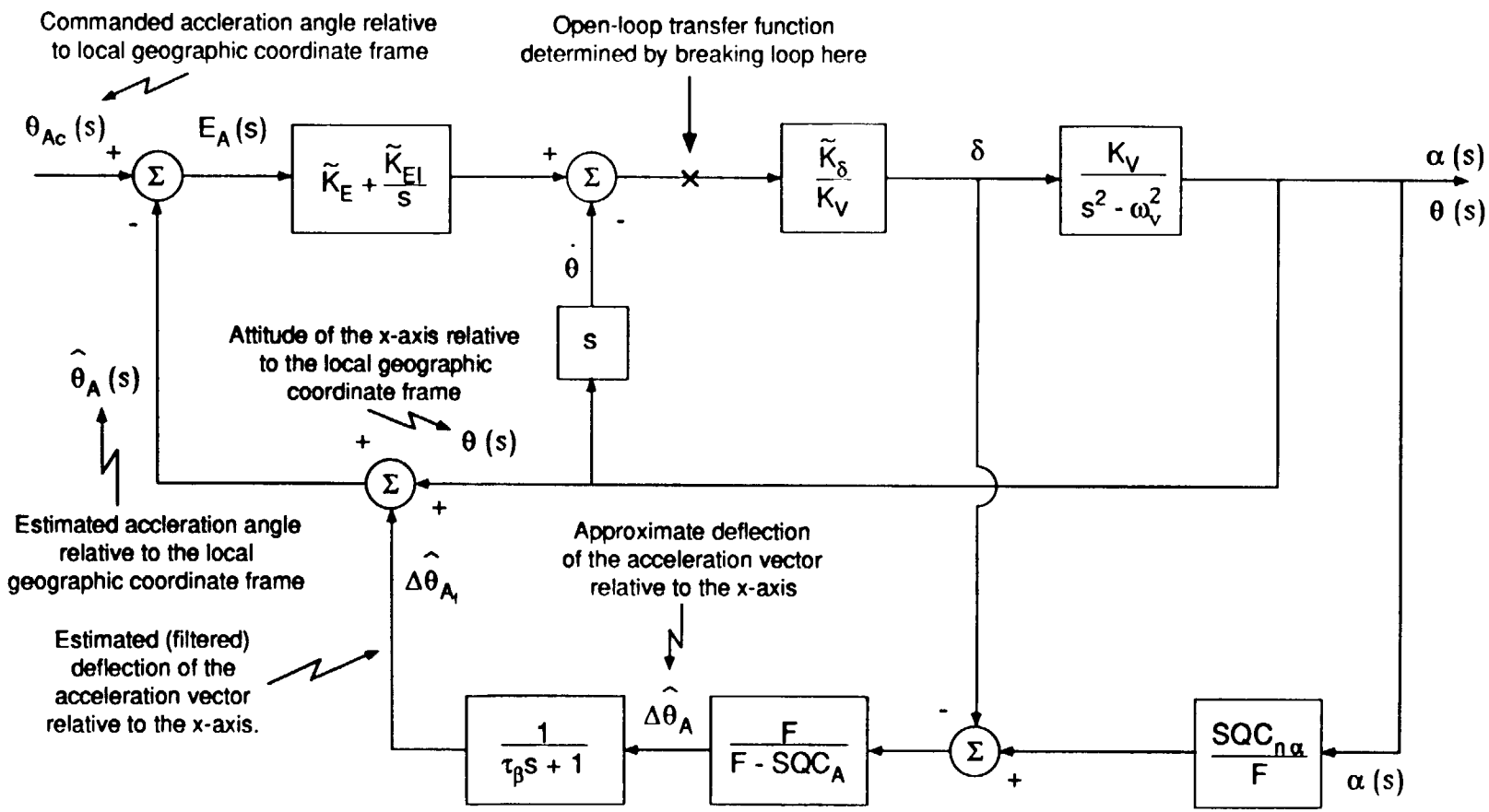

Figure 3.7 Approximate transfer functions for the acceleration-direction mode in Phase Three

was decided to design the compensation parameters to produce a 0 dB open-loop crossover frequency of 3 rad/sec. This crossover frequency was chosen to allow for adequate phase and gain compensation of the bending modes. For the ALS it is assumed that the estimated first and second bending frequencies are 13.8 rad/sec and 17.4 rad/sec, respectively. These bending modes are based on data provide by the Boeing Aerospace Corporation for a vehicle which is similar in design to the system being studied in this thesis. Also, the chosen 0 dB crossover frequency is sufficiently high for rigid body stabilization, being well above the maximum unstable pole frequency.

For the purpose of stability analysis, the following assumptions are made to approximate the vehicle transfer functions:

(1) The transfer function between the attitude, θ, and the engine nozzle deflection, δ, as derived in Appendix D and expressed in Equation (D.13), is

$$\frac{\Delta\theta(s)}{\Delta\delta(s)} = \frac{C5\left\{s + \left\{\frac{C3\,C4}{C5} - (C2 + C1)\right\}\right\}}{\left\{s^3 - (C1 + C2)\,s^2 - C4\,s + C2\,C4\right\}} \tag{3.14}$$

where the incremental signs of Equation (D.31) have been dropped for simplicity. In the vicinity of the chosen 0 dB crossover frequency this transfer function can be approximated as

$$\frac{\theta(s)}{\delta(s)} \cong \frac{C5}{\left(s - \frac{C1}{2} + \sqrt{C4}\right)\left(s - \frac{C1}{2} - \sqrt{C4}\right)} \tag{3.15}$$

where the two poles are based on the approximate relationship of Equation D.37. Since the values of the quantity C1, as listed in Table D.1 of Appendix D are very much smaller than those of C4, this transfer function can be further approximated by the form employed in Figures 3.5 and 3.6:

$$\frac{\theta(s)}{\delta(s)} = \frac{K_v}{s^2 - \omega_v^2} \tag{3.16}$$

where

$$K_v = C5 \tag{3.17}$$

$$\omega_v^2 = C4 \tag{3.18}$$

The first-cut analytical computation of the compensation gains for the two control modes will neglect ω_v, whose maximum value is roughly a factor of three below the chosen 0 dB crossover frequency of 3 rad/sec. However, the computer generated frequency response characteristics and the gain values based on these characteristics will include the effects of ω_v.

(2) It can also be assumed that changes in vehicle attitude in the vicinity of 3 rad/sec do not produce significant changes in the earth-relative velocity direction, as represented by the flight path angle γ. Since the pitch angle of attack in the absence of winds is merely equal to the difference between θ and γ, it can therefore be assumed that

$$\alpha(s) \cong \theta(s) \tag{3.19}$$

in this frequency range.

(3) The representation of the acceleration-direction feedback in Figure 3.7 is simplified by assuming that this feedback is based on the acceleration at the c.g. rather than the acceleration at the IMU which is employed in the simulation studies.

3.5 Nozzle Command Conversion Relationship

As seen in Figures 3.6 and 3.7 the ALS flight controller generates a single nozzle deflection command, δ_c, based on the product of a gain, K_δ/K_v, and the attitude rate error. K_δ is the constant inner loop gain and K_v is the calculated vehicle gain. By dividing K_δ by K_v the total inner loop forward gain is held constant as the vehicle gain varies with time. The nozzle command, δ_c, illustrated in Figures 3.6 and 3.7 is based on the vehicle model illustrated in Figure 3.8 where the nozzle hinge point is located along the roll axis of the vehicle. According to Figure 3.8, the moment generated by a deflection of the thrust vector is given by the expression

$$M = T \sin \delta_o \, x_{cg} \tag{3.20}$$

where T equals the total thrust of the core and booster stages.

For the ALS vehicle an equal pair of nozzle commands (δ_c and δ_b) is required from the flight controller such that the resulting moment due to the core and booster thrusts is equal to the moment calculated from Equation (3.20). From Figure 3.9 the moment generated by the ALS thrust vectors is given by the relationship

$$M = (T_b + T_c) \sin(\delta) \, x_{cg} - T_b \cos(\delta) (D + z_{cg}) - T_c \cos(\delta) \, z_{cg} \tag{3.21}$$

The thrust of the core and booster can be represented as a fraction of the total thrust by the expressions

$$T_b = T \frac{n_b}{n_b + n_c} \qquad \text{and} \qquad T_c = T \frac{n_c}{n_b + n_c} \tag{3.22}$$

where n_b and n_c are the number of operating booster and core engines respectively. Substituting Equation (3.22) into Equation (3.21) results in

$$M = T \sin(\delta)\, x_{cg} - T \cos(\delta) \left\{ \frac{n_b}{n_b + n_c} (D + z_{cg}) + \frac{n_c}{n_b + n_c} z_{cg} \right\} \qquad (3.23)$$

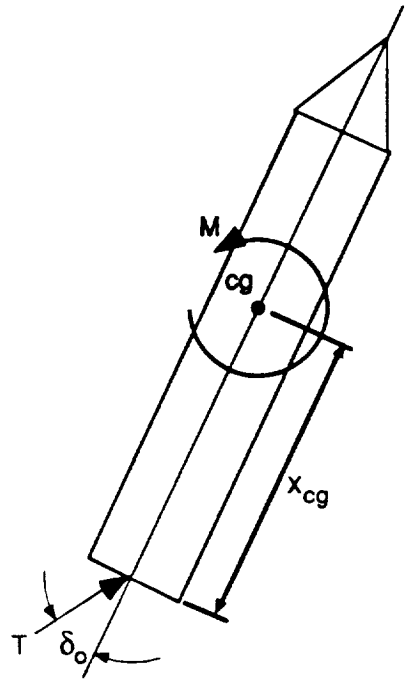

Figure 3.8 Single nozzle deflection configuration.

Define

$$A = \left\{ \frac{n_b}{n_b + n_c} (D + z_{cg}) + \frac{n_c}{n_b + n_c} z_{cg} \right\} \qquad (3.24)$$

Then Equation (3.24) can be written as

$$M = T \sin(\delta)\, x_{cg} - T \cos(\delta)\, A \qquad (3.25)$$

Setting Equation (3.20) equal to Equation (3.25) results in

$$T \sin(\delta)\, x_{cg} - T \cos(\delta)\, A = T \sin(\delta_o)\, x_{cg} \qquad (3.26)$$

As previously mentioned in Chapter 2 the nozzles of the core and booster engines are installed at a fixed cant angle, C. The nozzle deflection as

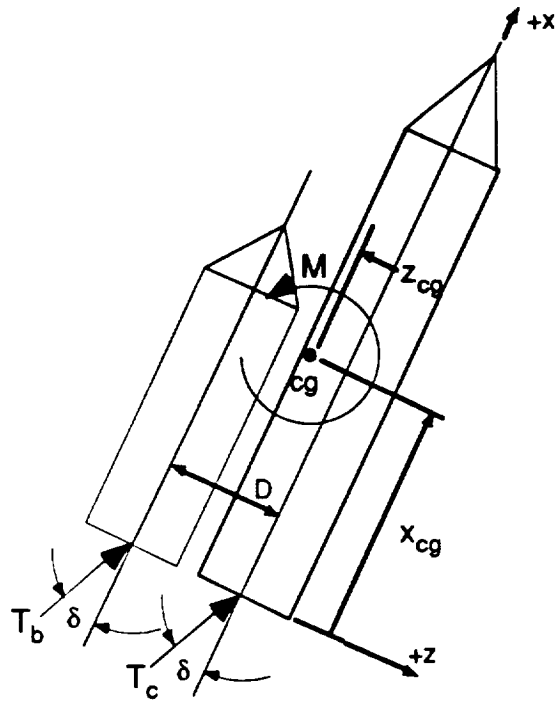

Figure 3.9 Moment generated by ALS nozzle deflections.

defined in Figure 3.9 can therefore be redefined in terms of the installed cant angle by the relationship

$$\delta = (\delta_c + C) \tag{3.27}$$

Substituting Equation (3.27) into (3.26) and eliminating the total thrust, T, results in

$$\tan\ (\delta_c + C) = \frac{A}{x_{cg}} + \frac{\sin\ \delta_o}{\cos\ (\delta_c + C)} \tag{3.28}$$

Assuming that $\cos(\delta_c+C) \equiv 1$, the relationship for the commanded nozzle deflection is given by:

$$\delta_c = \tan^{-1}\left(\frac{A}{x_{cg}} + \sin\delta_o\right) - C \tag{3.29}$$

Further, assuming that the nozzle deflection, δ_o, is small, then the commanded nozzle deflection can be approximated by

$$\delta_c = \delta_o + \delta_{Bias} \tag{3.30}$$

where

$$\delta_{Bias} = \frac{A}{x_{cg}} - C$$

The commanded nozzle defections for both the core and booster is, therefore, a function of the multiplicative gain, K_δ/K_v, as well as an additive bias term, δ_{Bias}. The block diagram for determining the commanded nozzle defection for the ALS simulation is shown in Figure 3.10. In analyzing the stability issues of both the acceleration-direction control mode as well as the Qα limiting control mode, the effects of the additive bias term are neglected. Consequently, δ_{Bias} is not included in either Figure 3.6 or Figure 3.7.

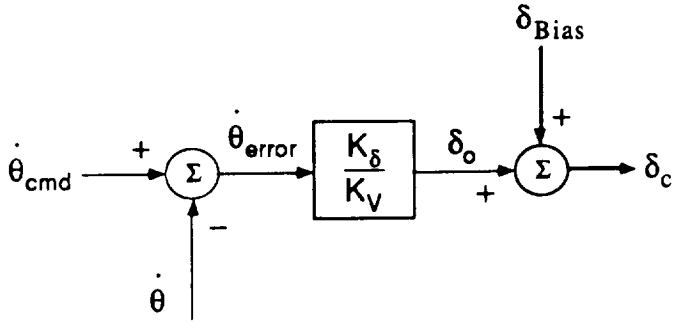

Figure 3.10 ALS nozzle command block diagram.

3.6 Approximate Transfer Functions for the Qα-Limit Mode

Utilizing the above simplifying assumptions along with other assumptions, the approximate transfer function model of the ALS shown in Figure 3.6 can be employed to analyze the critical frequency response near the 0 dB crossover for Phase One, Phase Two and the Qα-limit mode for Phase Three. This transfer function model neglects the effects of sampling, assumes perfect measurements and estimations of feedback variables, and employs the same control compensation gains for the control modes of the three flight phases. An integral-plus-proportional compensation operates on the attitude errors E_θ and E_α, to obtain a signal which is combined with the estimated angular rate. The resulting signal is then multiplied by a proportional gain equal to K_δ/K_V to generate the engine nozzle command.

The open-loop transfer function of Figure 3.6, determined by breaking the inner loop in the forward path, is expressed as follows:

$$G_o(s) \cong \left[K_E + \frac{K_{EI}}{s} + s\right]\left[\frac{K_\delta}{s^2 - \omega_v^2}\right] \tag{3.31}$$

This open-loop function will be employed, with and without the superimposed effects of sampling, in computer studies of the frequency response of this mode. As mentioned previously, first-cut analytical comparisons of the two control modes will neglect the effects of ω_v to simplify the analysis.

3.7 Approximate Transfer Functions for Acceleration Direction Feedback Mode

Employing the same assumptions as in Figure 3.6, a second approximate transfer function model shown in Figure 3.7 can be employed to describe the critical frequency response characteristics for the acceleration-

direction feedback mode of Phase Three. This diagram differs from that of Figure 3.6 in its addition of another feedback variable, the estimated (filtered) deflection of the acceleration vector relative to the x-axis, $\hat{\Delta\theta}_{A_f}$. When this variable is added to the attitude θ of the x-axis relative to the local geographic coordinate frame the estimated acceleration angle $\hat{\theta}_{A_p}$ relative to the local coordinate frame is obtained. This estimated acceleration angle is then subtracted from the commanded acceleration angle θ_{A_c} to generate the acceleration-direction control error E_A.

The derivation of the transfer function relationships for the additional acceleration direction feedback signal $\hat{\Delta\theta}_A$ is as follows. First, it is noted that the acceleration normal to the x-axis in the pitch plane may be approximated by the sum

$$a_{Normal} \cong \frac{-F\delta + SQC_{n\alpha}\alpha}{M} \tag{3.32}$$

and that the net axial acceleration may be expressed as

$$a_{Axial} \cong \frac{F - SQC_a}{M} \tag{3.33}$$

Second, assuming that $a_{Normal} << a_{Axial}$, it is noted that the angle of the acceleration vector relative to the vehicle x-axis in the pitch plane can be approximated by

$$\hat{\Delta\theta}_A \cong \frac{a_{Normal}}{a_{Axial}} \tag{3.34}$$

Substituting Equation (3.33) and (3.32) into Equation (3.34) results in

$$\Delta\hat{\theta}_A \cong \frac{F}{F - SQC_a}\left[-\delta + \left(\frac{SQC_{n\alpha}}{F}\right)\alpha\right] \tag{3.35}$$

Third, approximating the discrete low-pass filter of the acceleration direction estimator by a continuous low-pass filter with a time constant τ_β, the Laplace transform of the additional filtered feedback signal $\Delta\hat{\theta}_{A_f}(s)$ is related to the unfiltered $\Delta\hat{\theta}_A(s)$ by

$$\Delta\hat{\theta}_{A_f}(s) \cong \left[\frac{1}{\tau_\beta s + 1}\right]\Delta\hat{\theta}_A(s) \tag{3.36}$$

The open-loop transfer function of Figure 3.7, determined by breaking the inner loop in the forward path, is expressed as follows

$$\begin{aligned}\tilde{G}_o(s) = \frac{\tilde{K}_\delta}{K_v}\Bigg\{ & s\,\frac{K_v}{s^2 - \omega_v^2} - \left(\frac{F}{F - SQC_a}\right)\left(\frac{1}{\tau_\beta s + 1}\right)\left(\tilde{K}_E + \frac{\tilde{K}_{EI}}{s}\right) \\ & + \left[1 + \left(\frac{1}{\tau_\beta s + 1}\right)\left(\frac{SQC_{n\alpha}}{F - SQC_a}\right)\right]\left[\left(\tilde{K}_E + \frac{\tilde{K}_{EI}}{s}\right)\left(\frac{K_v}{s^2 - \omega_v^2}\right)\right]\Bigg\}\end{aligned} \tag{3.37}$$

This transfer function will be employed to study the effects of compensation gains on the open-loop frequency response, with and without the effects of sampling. However, in order to obtain an insight into the differences between the acceleration-direction control mode and the Qα-limit mode, some further approximations will be introduced. These are described below.

In the vicinity of the 0 dB crossover frequency of 3 rad/sec $\tilde{G}_o(s)$ may be simplified as follows:

First, assuming $\tau_\beta = 5$ seconds,

$$\left[\frac{1}{\tau_\beta s + 1}\right]_{\substack{s = j\omega \\ \omega = 3}} \cong \frac{1}{15.03} \angle -90° + 3.8° \cong \frac{1}{j15} \tag{3.38}$$

or

$$\left[\frac{1}{\tau_\beta s + 1}\right]_{s = j3} \cong \frac{1}{\tau_\beta s} \tag{3.39}$$

Employing the approximation of Equation (3.39) and neglecting ω_v in Equation (3.37), the transfer function becomes

$$\tilde{G}_o(s) \cong \frac{\tilde{K}_\delta}{K_v}\left\{\frac{K_v}{s} - \left[\frac{F}{F - SQC_a}\right]\left[\frac{\tilde{K}_E}{\tau_\beta s} + \frac{\tilde{K}_{EI}}{\tau_\beta s^2}\right]\right.$$
$$\left. + \left[1 + \left(\frac{1}{\tau_\beta s}\right)\left(\frac{SQC_{n\alpha}}{F - SQC_a}\right)\right]\left[\left(\tilde{K}_E + \frac{\tilde{K}_{EI}}{s}\right)\left(\frac{K_v}{s^2}\right)\right]\right\} \tag{3.40}$$

Second, assuming the same value of τ_β = 5 seconds, it can be shown that for close to maximum aerodynamic effects, based on Q = 790 psf, the term enclosed by the first brackets in the third term of Equation (3.40) is approximately unity when $\omega = 3$ rad/sec:

$$\left[1 + \frac{1}{s}\left(\frac{1}{\tau_\beta}\right)\left(\frac{SQC_{n\alpha}}{F - SQC_a}\right)\right]_{s = j3,\ Q = 790\ psf}$$
$$= \left[1 - j\,\frac{0.1095}{3}\right] = [1 - j\ 0.0365] \cong 1 \tag{3.41}$$

Hence, Equation (3.41) can be approximated as

$$\tilde{G}_o(s) \equiv \frac{\tilde{K}_\delta}{K_v}\left\{\frac{K_v}{s} - \left[\frac{F}{F - SQC_a}\right]\left[\frac{\tilde{K}_E}{\tau_\beta s} + \frac{\tilde{K}_{EI}}{\tau_\beta s^2}\right] + \left[\tilde{K}_E + \frac{\tilde{K}_{EI}}{s}\right]\left[\frac{K_v}{s^2}\right]\right\} \tag{3.42}$$

Factoring out K_v/s^2 from Equation (3.42) and rearranging terms, the open-loop transfer function near 3 rad/sec becomes

$$\tilde{G}_o(s) = \frac{\tilde{K}_\delta}{s^2}\left\{ s\left[1 - \left(\frac{\tilde{K}_E}{K_v \tau_\beta}\right)\left(\frac{F}{F - SQC_a}\right)\right] + \tilde{K}_E\left[1 - \frac{\tilde{K}_{EI}/\tilde{K}_E}{K_v \tau_\beta}\left(\frac{F}{F - SQC_a}\right)\right] + \frac{\tilde{K}_{EI}}{s}\right\} \tag{3.43}$$

This open-loop function and the other open-loop function of Equation (3.31) with $\omega_v = 0$ will provide the starting bases in the next section for a first-cut analytical comparison of the problems of compensation gain selection in the two control modes represented by these functions.

3.8 Approximate Analytical Stability Analysis Without Sampling Effects

The purposes of the following approximate analyses are (1) to provide an insight into the aspects that influence the selection of compensation gains for the two control modes of Phase Three and (2) to show how the compensation gains of the two modes must differ because of the role of the engine nozzle deflection in the acceleration direction feedback. The open-loop transfer functions expressed in Equations (3.31) and (3.43) provide useful insights into the effects of compensation gains on stability. These transfer functions will be

examined individually, first considering the case where there is no integral gain and then considering the problem of adjusting the integral gain along with other gains.

Proceeding first to the determination of gains for the Qα-limit mode as represented by Equation (3.31). Assuming that ω_v is zero, and letting the integral gain, K_{EI}, also equal zero, the open-loop transfer function then becomes.

$$G_o(s) = [K_E + s]\frac{K_\delta}{s^2} \tag{3.44}$$

It can be shown that the values of K_E and K_δ required for a phase margin of $\Delta\phi_m$ at a 0 dB crossover frequency are solutions of

$$\tan\ \Delta\phi_m = \frac{\omega_o}{K_E} \tag{3.45}$$

and

$$\left[K_E^2 + \omega_o^2\right]^{1/2}\ \frac{K_\delta}{\omega_o^2} = 1 \tag{3.46}$$

Solving these relationships for a chosen phase margin of 45° yields

$$K_E = \frac{\omega_o}{\tan\ (\Delta\phi_m)} = 3\ \text{sec}^{-1} \tag{3.47}$$

and

$$K_\delta = \frac{\omega_o^2}{\left[K_E^2 + \omega_o^2\right]^{1/2}} = 2.121 \tag{3.48}$$

The next step in this approximate design procedure is to select a value for the integral gain K_{EI}. Using Equation (3.31) and letting $\omega_v = 0$ results in the new open-loop transfer function

$$G_o(s) = \frac{K_\delta}{s^2}\left[s + K_E + \frac{K_{EI}}{s}\right] \tag{3.49}$$

Assuming K_E is unchanged, the effect of introducing K_{EI} is to reduce the phase margin to a value $\Delta\phi_m'$, which is a solution of

$$\tan\left(\Delta\phi_m'\right) = \frac{\omega_o - \dfrac{K_{EI}}{\omega_o}}{K_E} \tag{3.50}$$

Selecting a value of 35° for the new phase margin yields an integration gain of

$$K_{EI} = \omega_o\left[\omega_o - K_E \tan\left(\Delta\phi_m'\right)\right] = 2.698 \text{ sec}^{-2} \tag{3.51}$$

In order to maintain the 0 dB crossover at 3 rad/sec with the added effect of K_{EI} it is necessary to adjust K_δ to satisfy

$$\left[K_E^2 + \left(\omega_o - \frac{K_{EI}}{\omega_o}\right)^2\right]^{1/2} \frac{K_\delta}{\omega_o^2} = 1 \tag{3.52}$$

therefore

$$K_\delta = \frac{\omega_o^2}{\left[K_E^2 + \left(\omega_o - \frac{K_{EI}}{\omega_o} \right)^2 \right]^{1/2}} = 2.458 \text{ sec}^{-2} \tag{3.53}$$

The gain margins based on the above compensation gains for the open-loop function of Equation (3.49) are adequate. The high frequency margin is infinite and the low-frequency margin is 8.7 dB.

Although the above values of the compensation gains will be significantly revised in the subsequent computer studies, these approximate values are useful for comparison with similarly determined values for the acceleration control mode. For the acceleration-direction mode it will be recalled that the open-loop function may be approximated by

$$\tilde{G}_o(s) = \frac{\tilde{K}_\delta}{s^2} \left\{ s \left[1 - \left(\frac{\tilde{K}_E}{K_v \tau_\beta} \right) \left(\frac{F}{F - SQC_a} \right) \right] + \tilde{K}_E \left[1 - \frac{\tilde{K}_{EI}/\tilde{K}_E}{K_v \tau_\beta} \left(\frac{F}{F - SQC_a} \right) \right] + \frac{\tilde{K}_{EI}}{s} \right\} \tag{3.54}$$

Except for the terms in the brackets which multiply s and K_E, this open loop function has the same form as the Qα-limit mode, given by Equation (3.49):

$$G_o(s) = \frac{K_\delta}{s^2} \left[s + K_E + \frac{K_{EI}}{s} \right] \tag{3.55}$$

In fact, both open-loop functions can be expressed in the general form,

$$G_o(s),\ \tilde{G}_o(s) = \frac{1}{s^2}\left[K_1 s + K_2 + \frac{K_3}{s}\right] \tag{3.56}$$

where for the Qα-limit mode,

$$K_1 = K_\delta \tag{3.57}$$

$$K_2 = K_\delta K_E \tag{3.58}$$

$$K_3 = K_\delta K_{EI} \tag{3.59}$$

and for the acceleration-direction mode,

$$K_1 = \tilde{K}_\delta\left[\ 1 - \left(\frac{\tilde{K}_E}{K_v \tau_\beta}\right)\left(\frac{F}{F - SQC_a}\right)\right] \tag{3.60}$$

$$K_2 = \tilde{K}_\delta \tilde{K}_E\left[\ 1 - \left(\frac{\tilde{K}_{EI} / \tilde{K}_E}{K_v \tau_\beta}\right)\left(\frac{F}{F - SQC_a}\right)\right] \tag{3.61}$$

$$K_3 = \tilde{K}_\delta \tilde{K}_{EI} \tag{3.62}$$

Equations (3.57) to (3.62) indicate that only two of the open-loop function coefficients, K_1 and K_2, are affected by the choice of control mode. Furthermore, analysis has shown that only one of these coefficients, K_1, is affected appreciably. Thus, assuming vehicle parameters for a trajectory point where Q is close to a maximum, assuming $\tau_\beta = 5$, assuming $\tilde{K}_E = K_E$, $\tilde{K}_{EI} = K_{EI}$, and $\tilde{K}_\delta = K_\delta$ in Equations (3.60) to (3.62), and substituting the above determined values of K_E, K_{EI}, and K_δ into Equations (3.57) and (3.59), it is found that in going from the Qα-limit mode to the acceleration-direction mode

(1) The value of K1 is reduced by roughly 18% from 2.457 to 2.018 and

(2) The value of K2 is reduced by only about 5% from 7.371 to 6.976.

Using the above values of K1 and K2 for the acceleration-direction control mode along with the original value of K_3 it is found that the 0 dB crossover frequency is reduced from 3 rad/sec to 2.68 rad/sec and that the phase margin is reduced from 35° to 22.9°. This reduction in phase margin is sufficient to suggest that that it may be necessary to change the compensation gains when switching modes.

The compensation gains that would be required in the acceleration-direction control mode to produce the same K_1, K_2, and K_3 values that result from given K_E, K_{EI}, and K_δ values in the Qα-limit mode can be computed by the following approximate procedure. First, assume that the close-to-unity factor in Equation (3.61) is equal to a constant C_o, defined as

$$C_o = 1 - \left(\frac{K_{EI} / K_E}{K_v \tau_\beta}\right)\left(\frac{F}{F - SQC_a}\right) \tag{3.63}$$

Then, employ C_o in Equation (3.61) to solve for $\tilde{K}_E$:

$$\tilde{K}_E = \frac{K_2 / C_o}{\tilde{K}_\delta} \tag{3.64}$$

Next, substitute this expression into Equation (3.60) and solve the resulting relationship for $\tilde{K}_\delta$:

$$\tilde{K}_\delta = K_1 + \left(\frac{K_2}{C_o K_v \tau_\beta}\right)\left(\frac{F}{F - SQC_a}\right) \tag{3.65}$$

Finally, using the value of $\tilde{K}_\delta$ computed from Equation (3.65), compute $\tilde{K}_E$ from Equation (3.64) and compute $\tilde{K}_{EI}$ from Equation (3.62).

Employing the above procedure for the chosen point on the trajectory yields values of

$\tilde{K}_\delta = 2.921$ (as compared to $K_\delta = 2.458$)

$\tilde{K}_E = 2.666$ (as compared to $K_E = 3$)

$\tilde{K}_{EI} = 2.270$ (as compared to $K_{EI} = 2.698$)

These compensation gains result in K1, K2, and K3 values that are within 0.4% of the original values for the Qα-limit mode.

It will be shown in Section 3.10 that the transient produced by changing the compensation gains as the control modes are switched can be minimized by a procedure for reinitializing the control integrator so that the engine nozzle command does not change when the compensation gains are altered. Before proceeding to this method of accommodating the gain changes, the values of the gains required will be determined by a more accurate analysis which includes higher order terms and the effects of digital sampling.

3.9 Approximate Stability Analysis with Sampling Effects

To include the digital sampling effects in the preliminary analysis presented above a control design software package, MATLAB, was utilized. A single sampler was assumed to operate on the engine nozzle command. The frequency response analysis was facilitated by the decision to employ a single sampling period of T=0.1 seconds for the guidance, steering, control, and estimation. The use of the single sampling period for all operations also facilitated the implementation. Although the first cut computation of the compensation gains for both modes neglected ω_v, the following computer

generated analysis includes this effect. As discussed in Appendix D (Equation D.37) the approximate locations of the maximum unstable poles is given by

$$s \cong \frac{C1}{2} \pm \sqrt{C4}$$

This relationship can be further simplified by noting from Table D.1 that the values for C1 throughout Phase Two and Three are in general much smaller than C4. As a result, the first term on the right side of the above equation can be eliminated so that the maximum unstable pole frequency is approximately equal to the square root of C4. As shown in Table D.1, the value of the unstable pole frequency is small during the beginning of Phase Two (t=8 sec) and Phase Four (t=120 sec), but comparatively large during the midpoint of Phase Three.

The peak value of C4, which occurs at approximately 90 seconds after ignition, represents the point in the trajectory when the vehicle is at its most unstable state without control feedback. Typically this period occurs at or near the maximum dynamic pressure when the combined effects of the air-relative velocity of the vehicle and the air-density are most critical. Consequently, the vehicle state at 90 seconds was chosen as the critical operating point at which the control gains would be selected. In this manner, the resulting phase and gain margins should theoretically be acceptable for the remaining points along the trajectory

In applying the sampled data analysis to recompute the compensation gains it was decided to choose these gains to produce an open-loop function whose corresponding closed-loop function yields a peak magnitude close to 5 dB for both control modes at 90 seconds. This criterion necessitates increasing the phase margin to about 40°, increasing the low frequency gain margin to above 12 dB and increasing the 0 dB crossover frequency (ω_c) up to a maximum value of 4.3 rad/sec.

It was found that these frequency response requirements could be met with a single set of three constant control gains for each control mode. These gains are given in Tables 3.1 and 3.2. Employing these gains at various points for both control modes produced the values of phase margin, low frequency gain margin (GM1), high frequency gain margin (GM2), 0 dB crossover

frequency, and peak closed-loop magnitude presented in Tables 3.3 and 3.4. Nichols plots of both the open-loop characteristics at 90 seconds are given for the two control modes in Figures 3.11 and 3.12.

These frequency response characteristics were obtained with an approximate vehicle system which assumed perfect nozzle actuators as well as other simplifications. The inclusion of a nozzle actuator transfer function could significantly reduce the 0 dB crossover frequency, the phase margin, and the high frequency gain margin, and thereby require some adjustments in the compensation gains. Moreover, the inclusion of bending and slosh modes may require not only the adjustment of the three compensation gains but also the addition of one or more compensation filters.

Time (sec)	Phase Margin	Low Freq. Gain Margin (GM1)	High Freq. Gain Margin (GM2)	ω_c	Peak Mag
8	42.530	18.359	15.720	3.845	4.544
66	41.863	14.570	15.725	3.723	4.805
90	41.344	12.651	15.728	3.635	5.019
120	42.156	15.983	15.723	3.776	4.688

Table 3.1 Stability statistics for Qα limiting mode at different critical times in the trajectory.

Name	Value
K_E	2.700
K_{EI}	0.917
K_δ	3.276

Table 3.2 Selected gains for Qα limiting mode.

Time (sec)	Phase Margin	Low Freq. Gain Margin (GM1)	High Freq. Gain Margin (GM2)	ω_c	Peak Mag
8	43.378	19.384	14.673	4.279	4.330
66	42.750	13.707	14.515	4.158	4.735
90	42.610	11.405	14.351	4.092	5.014
120	44.887	16.446	14.191	4.341	4.224

Table 3.3 Stability statistics for acceleration-direction steering mode at different critical times in the trajectory.

Name	Value
$\tilde{K}_E$	2.394
$\tilde{K}_{EI}$	0.794
$\tilde{K}_\delta$	4.390

Table 3.4 Selected gains for acceleration-direction steering mode.

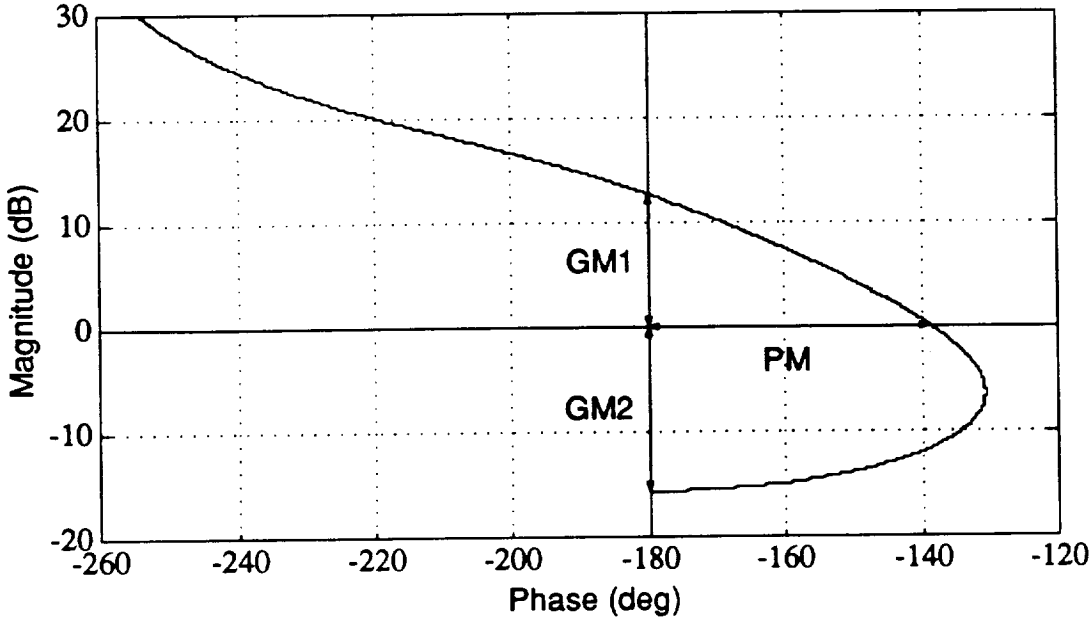

Figure 3.11 Nichols plot for Qα-limiting mode at t=90 sec.

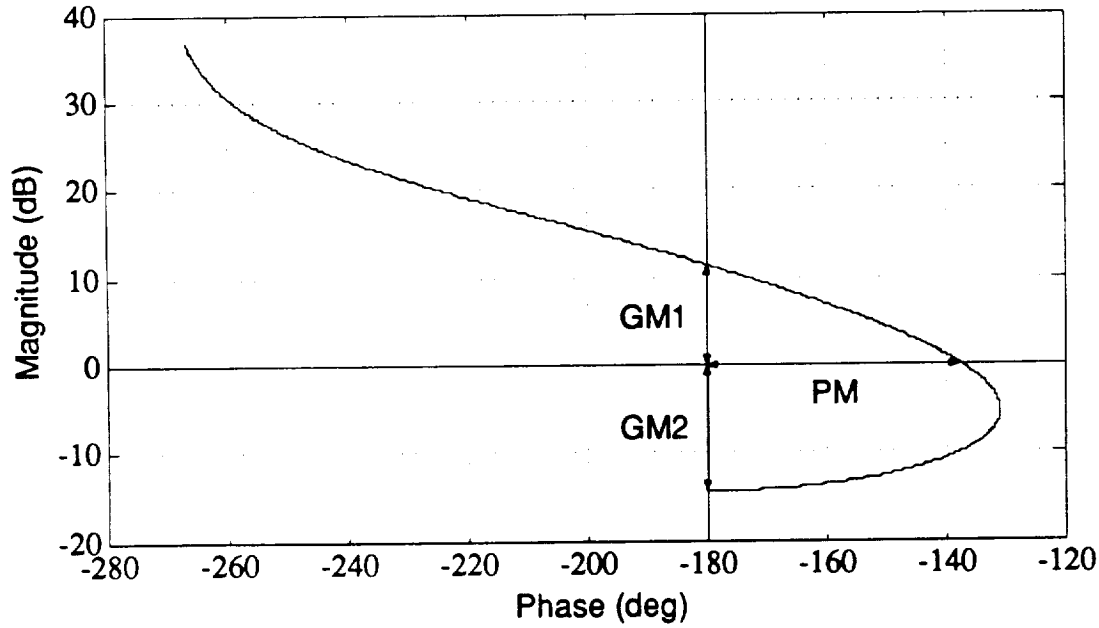

Figure 3.12 Nichols plot for acceleration-direction mode at t=90 sec.

3.10 Control Gain Reset Procedure for Mode Switching

Section 3.8 and 3.9 have shown that the dynamics for the acceleration-direction control mode and the angle of attack (or Qα-limit) control mode are different. Because of this difference, different control gains had to be selected for each mode to achieve the same relative stability margins in both modes.

A problem with having different control gains for each mode is that during switch-over a transient is produced in the commanded nozzle deflection. This transient can be minimized by reinitializing the integrator every time the mode is switched so that the new commanded deflection after switching equals the commanded deflection just before switching. Thus, the integrator must be reinitialized so that

$$\tilde{\delta}_c = \delta_c \tag{3.66}$$

where $\tilde{\delta}_c$ is the commanded nozzle deflection during Qα limiting mode, and δ_c is the commanded nozzle deflection in the acceleration-direction steering mode. Each nozzle deflection command can then be expanded and expressed in terms of its respective gains. For $\tilde{\delta}_c$ this results in

$$\tilde{\delta}_c = \frac{\tilde{K}_\delta}{K_v}\left[-\tilde{K}_{FB}\hat{\omega} + \tilde{K}_E E + \tilde{K}_{EI}\tilde{E}_{INT} \right] \tag{3.67}$$

For δ_c the relationship is

$$\delta_c = \frac{K_\delta}{K_v}\left[-K_{FB}\hat{\omega} + K_E E + K_{EI}E_{INT} \right] \tag{3.68}$$

where

$\tilde{K}_\delta$ and K_δ = The engine deflection gains for Mode 2 and Mode 1, respectively.

K_v = The vehicle gain.

$\tilde{K}_{FB}$ and K_{FB} = The rate feedback gain for Mode 2 and Mode 1, respectively.

$\hat{\omega}$ = The estimated angular rate. (For stability analysis purposes, perfect rate estimation was assumed.)

$\tilde{K}_E$ and K_E = The proportional gain of the Flight Control System (FCS) for Mode 2 and Mode 1 respectively.

E = The commanded error to the FCS. (From Figures 3.6 and 3.7, E can be either E_θ, E_α, or E_A.)

$\tilde{K}_{EI}$ and K_{EI} = The integral gain of the FCS for Mode 2 and Mode 1, respectively.

$\tilde{E}_{INT}$ and E_{INT} = The integrator output for Mode 2 and Mode 1, respectively.

Equating Equations (3.67) and (3.68) and solving for $\tilde{E}_{INT}$ results in the expression

$$\tilde{E}_{INT} = \frac{1}{\tilde{K}_{EI}}\left[\hat{\omega}\left(\tilde{K}_{FB} - K_{FB}\frac{K_\delta}{\tilde{K}_\delta} \right) + E\left(-\tilde{K}_E + K_{FB}\frac{K_\delta}{\tilde{K}_\delta} \right) + K_{EI}\frac{K_\delta}{\tilde{K}_\delta}E_{INT} \right] \quad (3.69)$$

Equation (3.69) provides the value that the control integrator should be reinitialized to, when switching from acceleration-direction mode to Qα–limiting mode. The relationship for switching modes in the opposite direction (ie., Qα–limiting mode to acceleration-direction mode) is obtained by solving Equation (3.69) for E_{INT}.

$$E_{INT} = \frac{1}{K_{EI}}\left[\hat{\omega}\left(K_{FB} - \tilde{K}_{FB}\frac{\tilde{K}_{\delta}}{K_{\delta}} \right) + E\left(-K_{E} + \tilde{K}_{FB}\frac{\tilde{K}_{\delta}}{K_{\delta}} \right) + \tilde{K}_{EI}\frac{\tilde{K}_{\delta}}{K_{\delta}}\tilde{E}_{INT} \right] \quad (3.70)$$

The effect of resetting the control gain during control mode switching is clearly illustrated in Figures 3.13 and 3.14. As shown in Figure 3.13 the control integrator is reset at two points. The first point occurs approximately 34 seconds after ignition and corresponds to a control mode switch from acceleration-direction steering to $Q\alpha$ limiting. Following this control mode reset the vehicle continues to fly under $Q\alpha$ limiting control until approximately 95 seconds after ignition, whereupon the vehicle returns to acceleration-direction steering and the control integrator is again reset. Although the resetting of the control integrator is very small at the first switching point, the second switch point ($t \cong 95$ sec) clearly shows a transient in the value of the integrator output. This transient is necessary to maintain a smooth command to the nozzles during control mode switching. The effect of resetting the integrator upon the commanded nozzle deflection is shown in Figure 3.14. Although the shape of the nozzle command is different once the vehicle has transferred back to acceleration-direction steering, there is no step or discontinuity present at switch over.

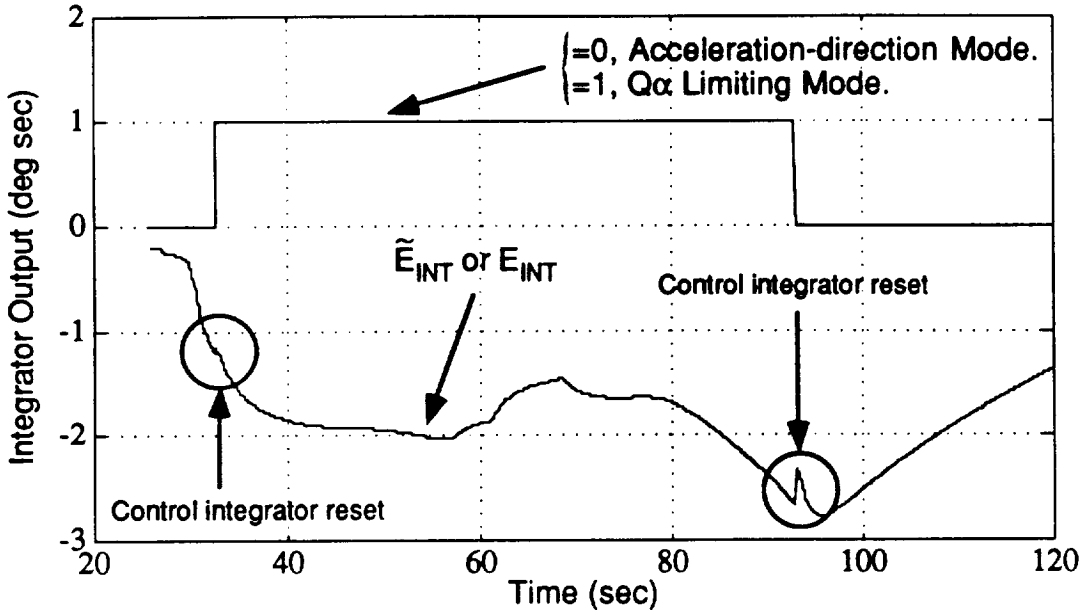

Figure 3.13 Control integrator reset for control mode switching.

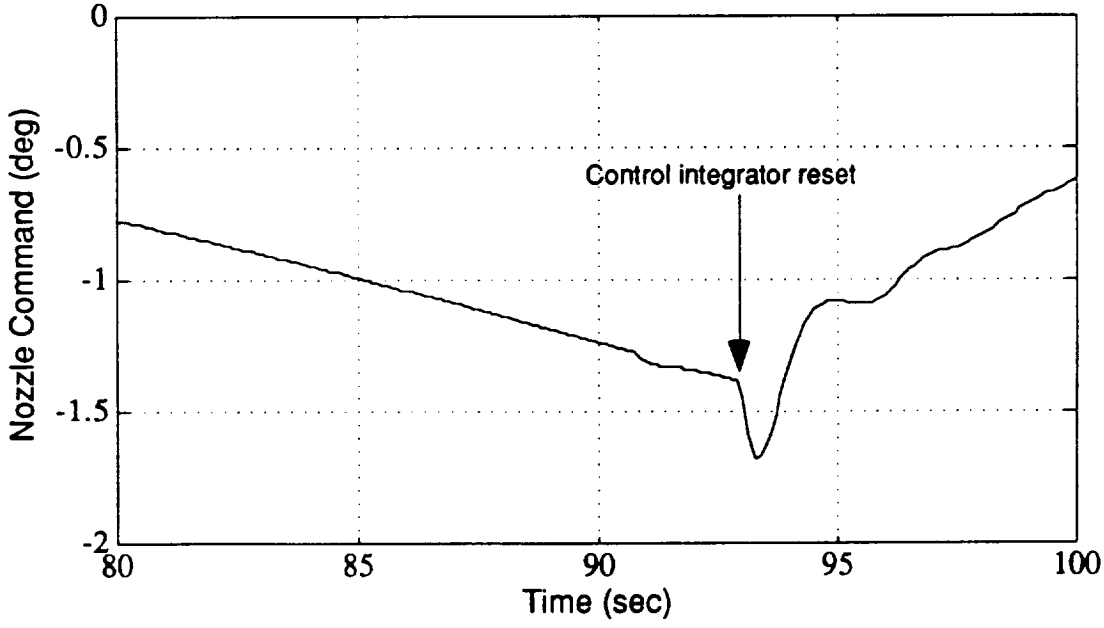

Figure 3.14 Nozzle command during control integrator reset.

Chapter Four

ANGULAR RATE ESTIMATION

4.1 Description

The manner in which the angular rate and other feedback variables are to be generated is dependent on the design of the avionics system which has yet to be fixed for the ALS. For the purposes of this thesis investigation it was decided to assume that the only measurements available for generating feedback variables are (1) the vehicle attitude relative to an inertial reference frame measured by an inertial measurement unit (IMU), (2) the inertial velocity of the vehicle measured by the IMU, and (3) the measured deflections of the engine nozzles. It was further assumed that either a strapdown or a stabilized-platform IMU could be employed, with either high or low performance accelerometers and gyros.

In order to accommodate the wide range of possible IMU characteristics this thesis develops feedback signal estimators that can deal with worst-case levels of noise and/or quantization in the IMU signals. This means in the case of the angular rate feedback signal that it is not sufficient to employ a rate signal that is merely derived from the quotient of attitude change and the control sampling period. This derived rate signal can have unacceptably large fluctuations if the IMU measurements have large quantization or noise levels and/or if there is a short sampling period.

One method for reducing these fluctuations is to employ a complementary filter estimator which utilizes the derived rate signal in combination with an estimated angular acceleration signal. This estimator reduces the effects of quantization and noise in the attitude measurements by employing the low-pass filtering of the derived rate signal to generate an estimator rate signal that is accurate only at low frequencies. This low-frequency signal is augmented by a high-frequency estimated rate signal generated by the low-pass filtering of an angular acceleration estimate. The

effect of the low-pass filtering of the angular acceleration estimate is equivalent to the high-pass filtering of a rate signal based on the integral of angular acceleration. The angular acceleration estimate is based on the IMU-measured velocity increments and the measured engine deflections, with an additional correction for small errors in the modeling of the effects of thrust and aerodynamic forces on angular acceleration. If the quantization and noise levels in the IMU velocity measurements are sufficiently low, this rate estimator can produce lower signal fluctuations than are contained in a derived rate signal.

4.2 The Complementary Filter

A simplified continuous representation of a complementary filter is illustrated in Figure 4.1. With this approach, the high frequency state estimate, $\hat{x}_{high}$, is passed through a high-pass filter while the low frequency state, $\hat{x}_{low}$, is passed through a low-pass filter. The outputs of the two filters are then combined to produce a single state estimate. Each filter attenuates unwanted frequency components. Thus, the low pass filter attenuates high frequency components and the high pass filter attenuates low frequency components. The transfer function for the complementary filter has unity gain with no phase shift. Consequently, in the ideal case where both the low and high frequency estimates are exact, the complementary filter acts as a unity transfer function.

4.3 ALS Rate Estimation

Figure 4.2 shows a simplified continuous signal representation of the ALS angular rate estimator. The low frequency estimate is passed through a low pass filter. The high frequency component is obtained by first estimating the angular acceleration of the vehicle. In effect, this signal is then integrated to produce a high frequency estimate of angular rate and then filtered through a high pass filter. In the actual implementation, the high frequency estimator path combines the integrator and high pass filter to produce the simplified continuous form of the rate estimator shown in Figure 4.3.

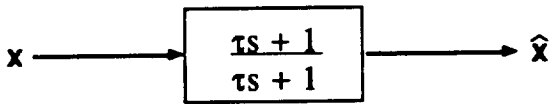

Or equivalently,

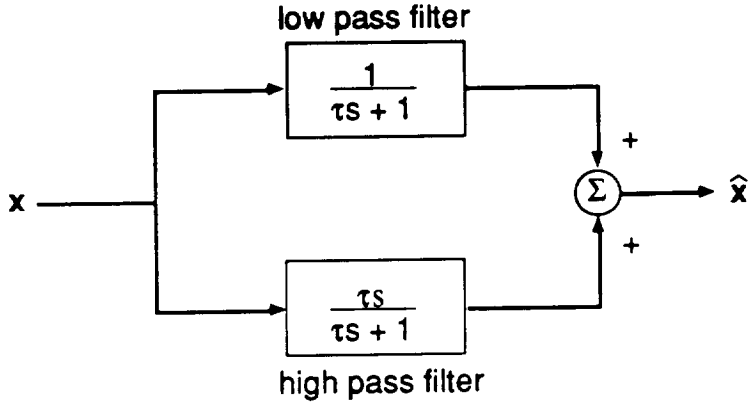

Or equivalently,

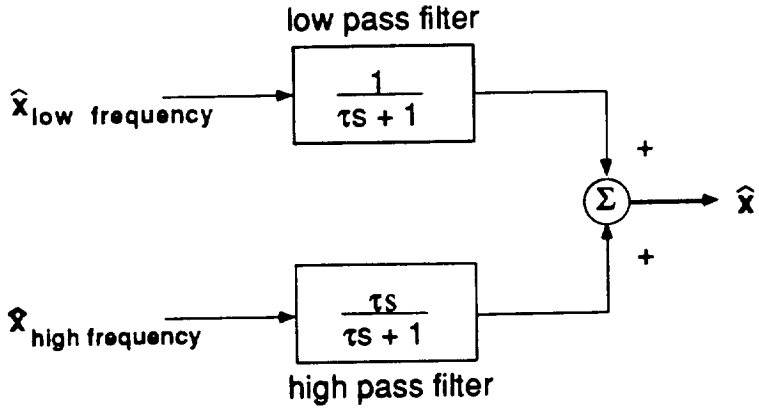

Figure 4.1 Block diagram development of complementary filter.

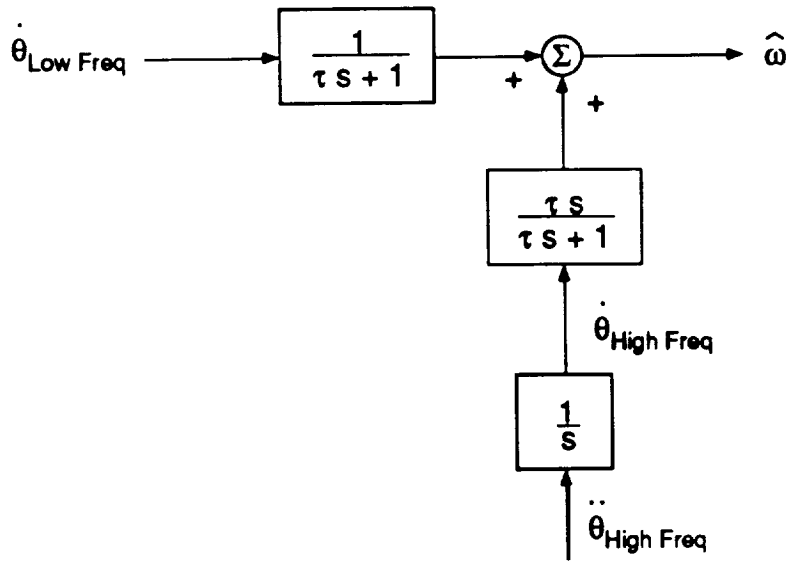

Figure 4.2 Continuous ALS rate estimator

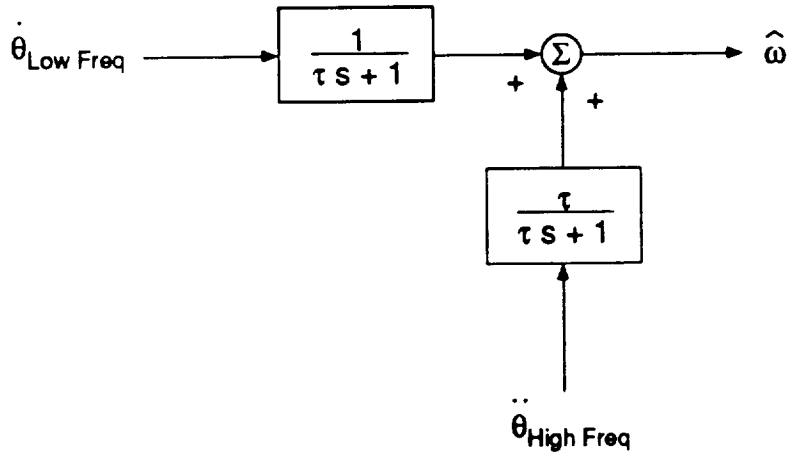

Figure 4.3 Simplified continuous ALS rate estimator.

The accuracies of both the low and high frequency estimates are affected by measurement noise. In addition, the accuracy of the high frequency estimate is affected by errors in the modeling of the vehicle. One category of mismodeling errors that is of particular concern in the case of the ALS is the one that results in constant or slowly varying bias errors in the estimated angular

acceleration. Such a bias can be produced, for example, by an unmodeled offset of a thrust vector as illustrated in the bottom diagram of Figure 4.4. If this offset is ignored, as shown in the top diagram of Figure 4.4, the estimated contribution to angular acceleration of the thrust will be in error by the product of the thrust times the offset divided by the moment of inertia perpendicular to the plane of the offset. This error amounts to a constant bias in the estimated angular acceleration that produces a corresponding bias in the estimated angular rate. As can be seen from Figure 4.3, an acceleration estimate bias, $\hat{\ddot{\theta}}_{Bias}$, would result in a steady state bias in estimated rate of $\tau\hat{\ddot{\theta}}_{Bias}$. To remove the modelling error, an additional feedback loop for acceleration bias correction is added to Figure 4.3. This correction loop which is illustrated in Figure 4.5, is based on a concept developed by James Herner of Autonetics.

As shown in Figure 4.5, the correction for the estimated-acceleration bias is derived from the difference of two acceleration estimates. The first estimate, $\hat{\dot{\omega}}_1$, is the derivative of the estimated angular rate. The second estimate, $\hat{\dot{\omega}}_2$, is the corrected estimate of angular acceleration.

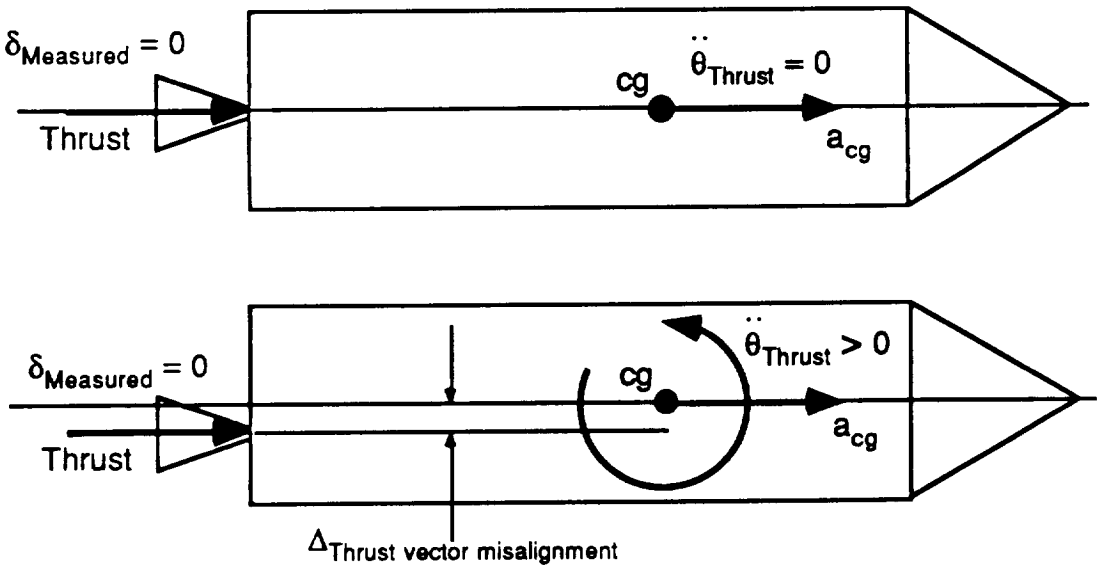

Figure 4.4 Thrust vector misalignment contribution to estimated rate.

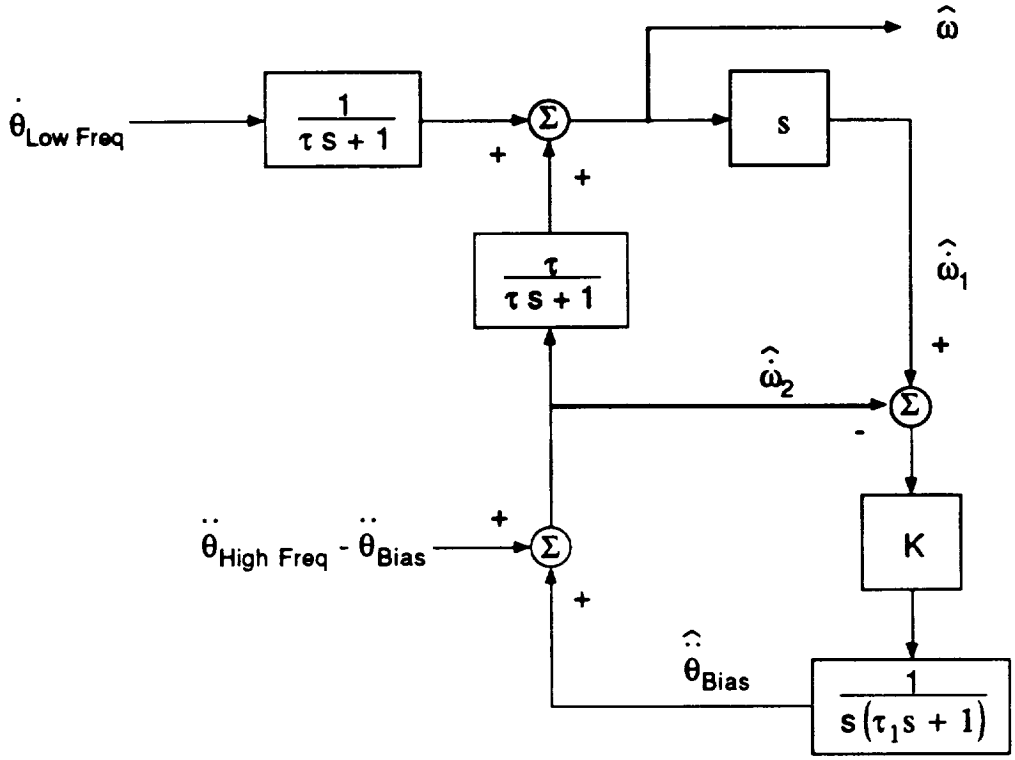

Figure 4.5 Simplified continuous ALS rate estimator with estimated angular acceleration feedback.

By integrating and filtering the error between the two acceleration signals and then feeding the result back as an estimated bias, the estimated angular acceleration is continually driven to null $\hat{\dot{\omega}}_1 - \hat{\dot{\omega}}_2$.

4.4 Digital Complementary Filter

The above discussion of the complementary filter assumes a continuous-signal domain representation for convenience only. Using the bilinear transformation the complex frequency, s, can be approximated in the discrete z-domain by the relationship:

$$s \cong \frac{2}{T}\left(\frac{1 - z^{-1}}{1 + z^{-1}}\right) \tag{4.1}$$

where T is the sampling time of the discrete filter. Substituting Equation 4.1 for s into Figure 4.1 results in the digital filter illustrated in Figure 4.6

For the ALS the measured quantities used to estimate angular rate are the following:

1) The incremental change in attitude over the sampling instant of 0.1 sec. : The change in attitude about the pitch axis, $\Delta\theta_y$, is computed in the following manner assuming a single-rotation-axis maneuver.

   a) The transformation from initial to commanded body axes is computed by:

$$C_{Body}^{Body\ Last} = (C_{Body}^{Inertial})(C_{Body\ Last}^{Inertial})^T \tag{4.2}$$

   where

   $C_{Body}^{Inertial}$ = the direction cosine matrix relating the current transformation from inertial to body coordinates.

   $(C_{Body\ Last}^{Inertial})^T$ = the transpose of the direction cosine matrix relating the transformation from inertial to body coordinates computed at the last sampling period.

   b) It can be shown that for a single-rotation-axis maneuver where the angle of rotation between the present and past commanded orientations is small, the incremental roll, yaw, and pitch components of rotation are given by:

$$\Delta\theta_x = \frac{(C_{23} - C_{32})}{2} \tag{4.3}$$

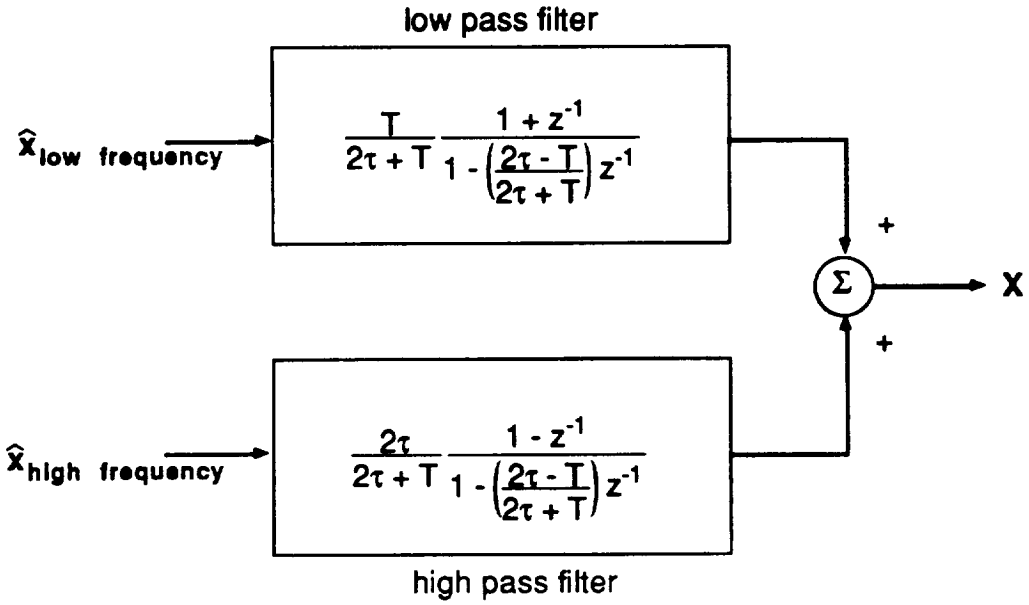

or equivalently

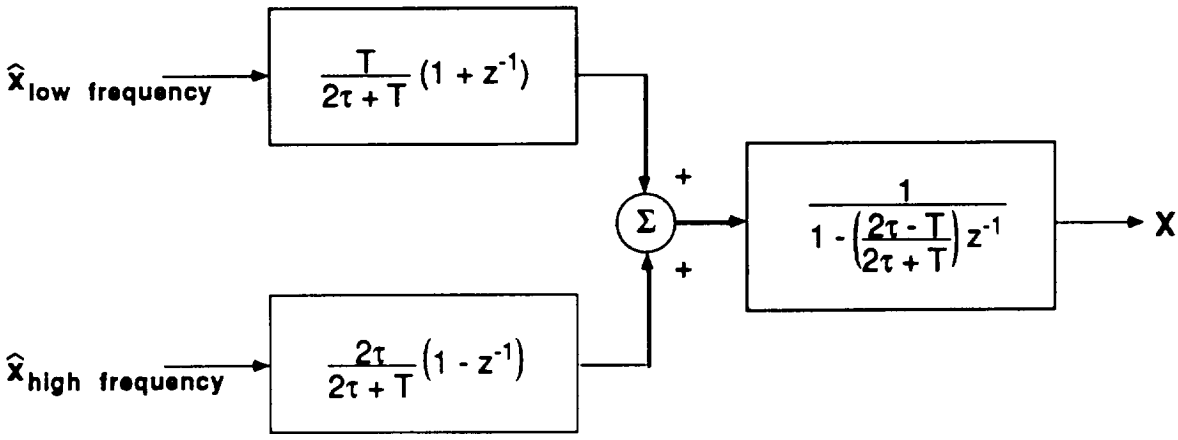

Figure 4.6 Digital Rate Estimator.

$$\Delta\theta_x = \frac{(C_{31} - C_{13})}{2} \tag{4.4}$$

$$\Delta\theta_x = \frac{(C_{12} - C_{21})}{2} \tag{4.5}$$

where $C_{(m,n)}$ is an element of the transformation $C^{\text{Body Last}}_{\text{Bodt}}$, relating past to present body axes. The subscripts m and n represent the row and column locations of each element.[1]

2) The incremental change in velocity over the sampling instant of 0.1 sec. : The incremental change in velocity produced by external forces (not including the effects of gravity) is determined first in inertial axes, based on IMU accelerometer measurements, and then is transformed into body axes using the current inertial to body axes transformation. The resulting incremental velocity vector, ΔV, has components ΔV_x, ΔV_y, and ΔV_z along the roll, pitch, and yaw axes, respectively.

3) The sensed angular deflection of the core and booster nozzles: (The flight computer generates the same nozzle deflection command to both the core and booster, so that δ_y is the pitch axis component of both equivalent nozzles.)

4.5 Low Frequency Angular Rate Estimate

The low frequency estimate of angular rate is computed by dividing the incremental change in attitude over the control cycle by the sampling time, T:

---

[1] Stubbs, G. S.," Final Report, Fiscal Year 1974 Advanced Targeting and Software Design Studies." August 1974. C.S.D.L. Report R-838.

$$\hat{\dot{\theta}}_{\text{Low Frequency}} = \frac{\Delta\theta_y}{T} \tag{4.6}$$

Because the incremental attitude signals are generated from the IMU, these signals are typically corrupted by deterministic, quantization, and noise errors. However, these errors are significantly attenuated by the low pass filter shown in Figure 4.2.

It should be pointed out that the use of derived rate as expressed in Equation (4.6) for the low frequency estimate introduces a time lag of T/2 seconds. This time lag can be removed by the addition of a signal based on the angular acceleration whose estimation is described in the next section. Although this addition would be desirable if stability margins were tight in the final ALS design, it was found that the inclusion of this term did not significantly alter response characteristics for the system being considered in this thesis. Therefore, the simple relationship of Equation (4.6) was utilized in the current simulation studies and is employed in the estimator descriptions presented subsequently in this chapter.

4.6 High Frequency Angular Rate Estimate

The angular acceleration estimate employed to generate the high frequency portion of the angular rate signal is derived from a linear combination of the pitch axis nozzle deflection, and the change in sensed body frame velocity over a control cycle. A general expression for the angular acceleration is defined below.

From Figure 4.7, it is seen that the rigid body equation of motion for angular acceleration of the vehicle in the pitch plane is given by the equation

$$\begin{aligned} I_y\dot{\omega}_y = {} & T_c x_{cg} \sin(\delta_c) + T_b x_{cg} \sin(\delta_b) - T_c z_{cg} \cos(\delta_c) - \\ & T_b (D + z_{cg}) \cos(\delta_b) + F_A (z_{cg} - l_{cpz}) + F_N (l_{cpx} - x_{cg}) \end{aligned} \tag{4.7}$$

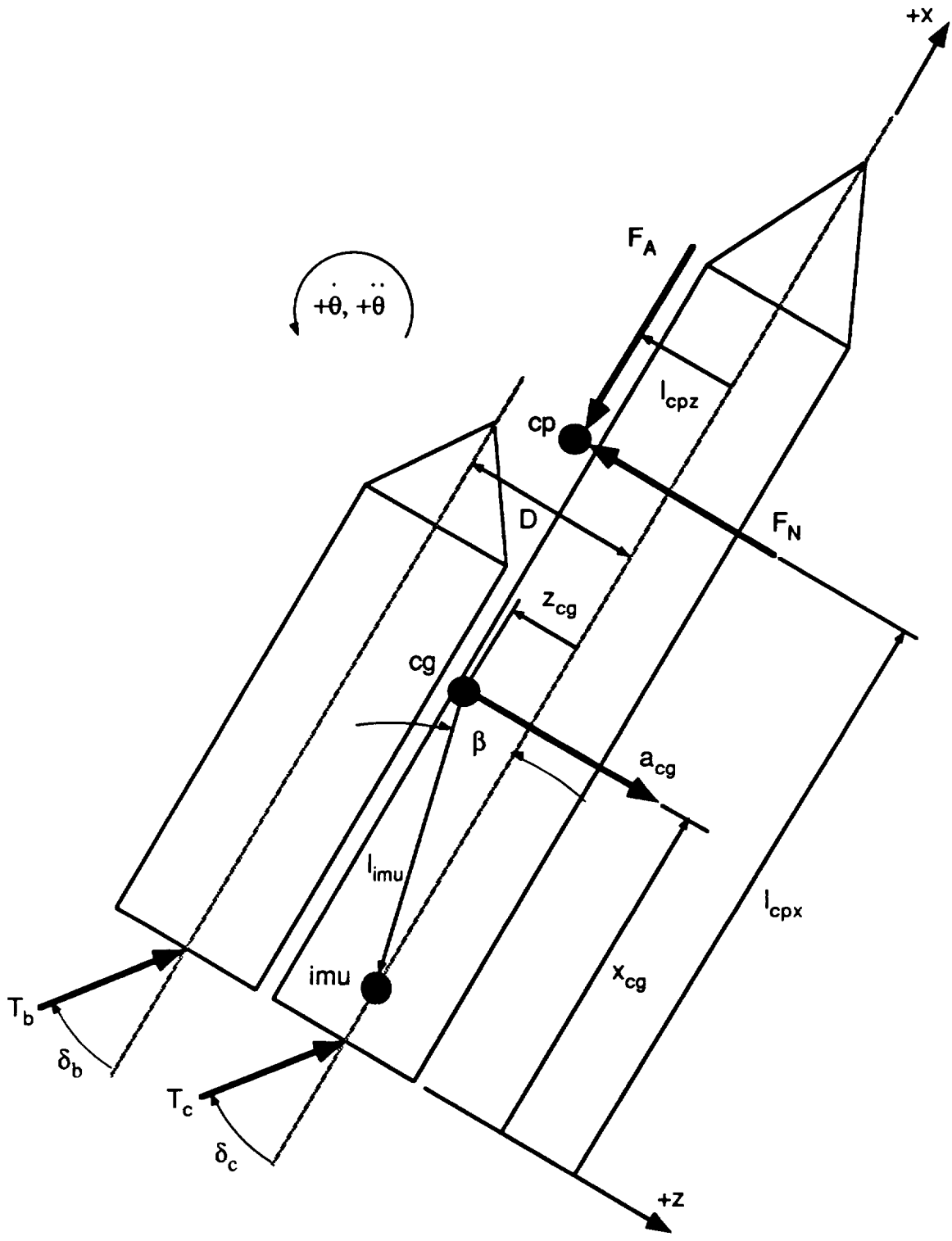

Figure 4.7 Vehicle description for the derivation of estimated high frequency angular rate.

where

I_y	=	Pitch axis moment of inertia.
T_c	=	Core thrust.
T_b	=	Booster thrust.
δ_c	=	Core pitch axis nozzle deflection.
δ_b	=	Booster pitch axis nozzle deflection.
x_{cg}	=	Body x axis center of gravity position.
z_{cg}	=	Body z axis center of gravity position.
D	=	Distance between centerline of core and booster.
l_{cpx}	=	Body x axis distance from the centerline of the core to the center of pressure.
l_{cpz}	=	Body z axis distance from the base of the core to the center of pressure.
F_A	=	Axial aerodynamic force.
F_N	=	Normal aerodynamic force.

A second equation can be written which relates the linear acceleration at the center of gravity along the body z axis to the normal aerodynamic force and the body z axis component of the engine thrusts. That is,

$$ma_{cg} = -F_N + T_c \sin(\delta_c) + T_b \sin(\delta_b) \tag{4.8}$$

The acceleration at the center of gravity can be related to the acceleration as seen at the IMU by the following expression.

$$a_{cg} = a_{imu} + l_{imu}\omega^2 \sin(\beta) - l_{imu}\dot{\omega} \cos(\beta) \tag{4.9}$$

Substituting the expression for a_{cg} given by Equation (4.9) into Equation (4.8) and solving for F_n and then substituting this expression for F_n into Equation (4.7) and solving for $\dot{\omega}$ yields:

$$\dot{\omega}_y = \frac{1}{I_y - m\left(l_{cpx} - x_{cg}\right) l_{imu}} \left(T_c l_{cpx} \sin\left(\delta_c\right) + T_b l_{cpx} \sin\left(\delta_b\right) - T_c z_{cg} \cos\left(\delta_c\right) - T_b\left(D + z_{cg}\right) \cos\left(\delta_b\right) - m a_{imu}\left(l_{cpx} - x_{cg}\right) - m\left(l_{cpx} - x_{cg}\right) l_{imu} \sin\left(\beta\right) \omega_y^2 + F_A\left(z_{cg} - l_{cpz}\right)\right) \tag{4.10}$$

Let

$$K_{1c} = \frac{T_c l_{cpx}}{I_y - m\left(l_{cpx} - x_{cg}\right) l_{imu}} \tag{4.11}$$

$$K_{1b} = \frac{T_b l_{cpx}}{I_y - m\left(l_{cpx} - x_{cg}\right) l_{imu}} \tag{4.12}$$

$$K_2 = \frac{m\left(l_{cpx} - x_{cg}\right)}{I_y - m\left(l_{cpx} - x_{cg}\right) l_{imu}} \tag{4.13}$$

$$K_3 = \frac{m\left(l_{cpx} - x_{cg}\right) l_{imu} \sin\left(\beta\right)}{I_y - m\left(l_{cpx} - x_{cg}\right) l_{imu}} \tag{4.14}$$

$$K_{4c} = \frac{T_c z_{cg}}{I_y - m\left(l_{cpx} - x_{cg}\right) l_{imu}} \tag{4.15}$$

$$K_{4b} = \frac{T_b\left(D + z_{cg}\right)}{I_y - m\left(l_{cpx} - x_{cg}\right) l_{imu}} \tag{4.16}$$

Then Equation (4.10) can be expressed as

$$\dot{\omega}_y = K_{1c} \sin(\delta_c) + K_{1b} \sin(\delta_b) - K_2\, a_{imu} - K_3\, \omega_y^2 - K_{4c} \cos(\delta_c) - K_{4b} \cos(\delta_b) + F_A\, (z_{cg} - l_{cpz}) \tag{4.17}$$

By integrating $\dot{\omega}_y$ over a sampling interval and then dividing by the sampling period, the average angular acceleration is obtained:

$$\frac{1}{T} \int_{t_{n-1}}^{t_n} \dot{\omega}_y \, dt = \ddot{\theta}_{avg} \tag{4.18}$$

where t_n is the present sampling instant and t_{n-1} is the preceding calculation time. Substituting Equation (4.17) into Equation (4.18),

$$\ddot{\theta}_{avg} = \frac{1}{T} \int_{t_{n-1}}^{t_n} K_{1c} \sin(\delta_c)\, dt + \frac{1}{T} \int_{t_{n-1}}^{t_n} K_{1b} \sin(\delta_b)\, dt - \frac{1}{T} \int_{t_{n-1}}^{t_n} K_2\, a_{imu}\, dt - \frac{1}{T} \int_{t_{n-1}}^{t_n} K_3\, \omega_y^2\, dt - \frac{1}{T} \int_{t_{n-1}}^{t_n} K_{4c} \cos(\delta_c)\, dt - \frac{1}{T} \int_{t_{n-1}}^{t_n} K_{4b} \cos(\delta_b)\, dt + \frac{1}{T} \int_{t_{n-1}}^{t_n} F_A\, (z_{cg} - l_{cpz})\, dt \tag{4.19}$$

The integrals on the right side of Equation (4.19) can be approximated by the expressions

$$\frac{1}{T} \int_{t_{n-1}}^{t_n} K_{1c} \sin(\delta_c)\, dt \cong K_{1c} \sin(\delta_c)_{n-1} \tag{4.20}$$

$$\frac{1}{T}\int_{t_{n-1}}^{t_n} K_{1b}\sin(\delta_b)\,dt \cong K_{1b}\sin(\delta_b)_{n-1} \tag{4.21}$$

$$\frac{1}{T}\int_{t_{n-1}}^{t_n} K_{4c}\cos(\delta_c)\,dt \cong K_{4c}\cos(\delta_c)_{n-1} \tag{4.22}$$

$$\frac{1}{T}\int_{t_{n-1}}^{t_n} K_{4b}\cos(\delta_b)\,dt \cong K_{4b}\cos(\delta_b)_{n-1} \tag{4.23}$$

The above relationships are based on the assumption that the nozzle deflection over a sampling period is constant with time. The remaining integrals can be approximated by,

$$\frac{1}{T}\int_{t_{n-1}}^{t_n} K_2\, a_{imu}\,dt \cong K_2\frac{\Delta V_z}{T} \tag{4.24}$$

$$\frac{1}{T}\int_{t_{n-1}}^{t_n} K_3\,\omega_y^2\,dt \cong K_3\left(\hat{\omega}_y^2\right)_{n-1} \tag{4.25}$$

where $\hat{\omega}_y^2$ is the previous estimate of angular rate as computed by the rate estimator. The last term on the right side of Equation (4.19) is the component of axial acceleration due to the axial aerodynamic force and the offset between the center of gravity and the center of pressure. As an open loop calculation this quantity may be difficult to estimate, primarily because the location of the center of pressure (l_{cpz}) may not be accurately known. From a transient point of view, however, it is possible to assume that the axial aerodynamic force will generate an angular acceleration which is slowly varying. This is a good approximation since both the center of gravity and F_a are slowly changing with time. Therefore, the angular acceleration term generated by the axial aerodynamic force is modelled for the moment as an unknown acceleration bias on the system. Substituting Equations (4.20) through (4.25) into (4.19), and renaming the last term on the right side of Equation (4.19) by the term $\mathbf{accel_{bias}}$, results in:

$$\ddot{\theta}_{avg} = K_{1c} \sin(\delta_c)_{n-1} + K_{1b} \sin(\delta_b)_{n-1} - K_2 \frac{\Delta V_z}{T} -$$
$$K_3 \left(\hat{\omega}_y^2\right)_{n-1} - K_{4c} \cos(\delta_c)_{n-1} - K_{4b} \cos(\delta_b)_{n-1} + \mathbf{accel_{bias}} \qquad (4.26)$$

In the actual implementation of the rate estimator the term $\mathbf{accel_{bias}}$ of Equation (4.26) represents not only the effects of the axial aerodynamic force, F_a, acting on a moment arm $x_{cg} - l_{cpz}$, but also the effects of any errors in modelling that combine to produce a slowly varying bias in the estimated value of $\ddot{\theta}_{avg}$. This bias term is estimated and approximately corrected by the addition of an angular acceleration bias estimation (AABE) loop to the estimator. The implementation of this loop will be described in Section 4.7.

To obtain the change in attitude rate over time, Equation (4.26) is multiplied by the digital sampling rate. Thus,

$$\Delta\dot{\theta}_{\text{High Frequency}} = \ddot{\theta}_{avg} T \qquad (4.27)$$

The digital lagless filter illustrated in Figure 4.6 can be implemented by substituting Equation (4.6) for the low frequency estimate and Equation (4.27) as the high frequency estimate. The resulting block diagram is illustrated in Figure 4.8.

4.7 Acceleration Bias Estimate

As discussed in Section 4.3, mismodeling errors in the high frequency estimate of angular acceleration also result in errors in the estimation of angular rate. To eliminate these errors an additional feedback loop was added to the the continuous signal representation of the rate estimator shown in Figure 4.3 which resulted in the new rate estimator illustrated in Figure 4.5. As seen from

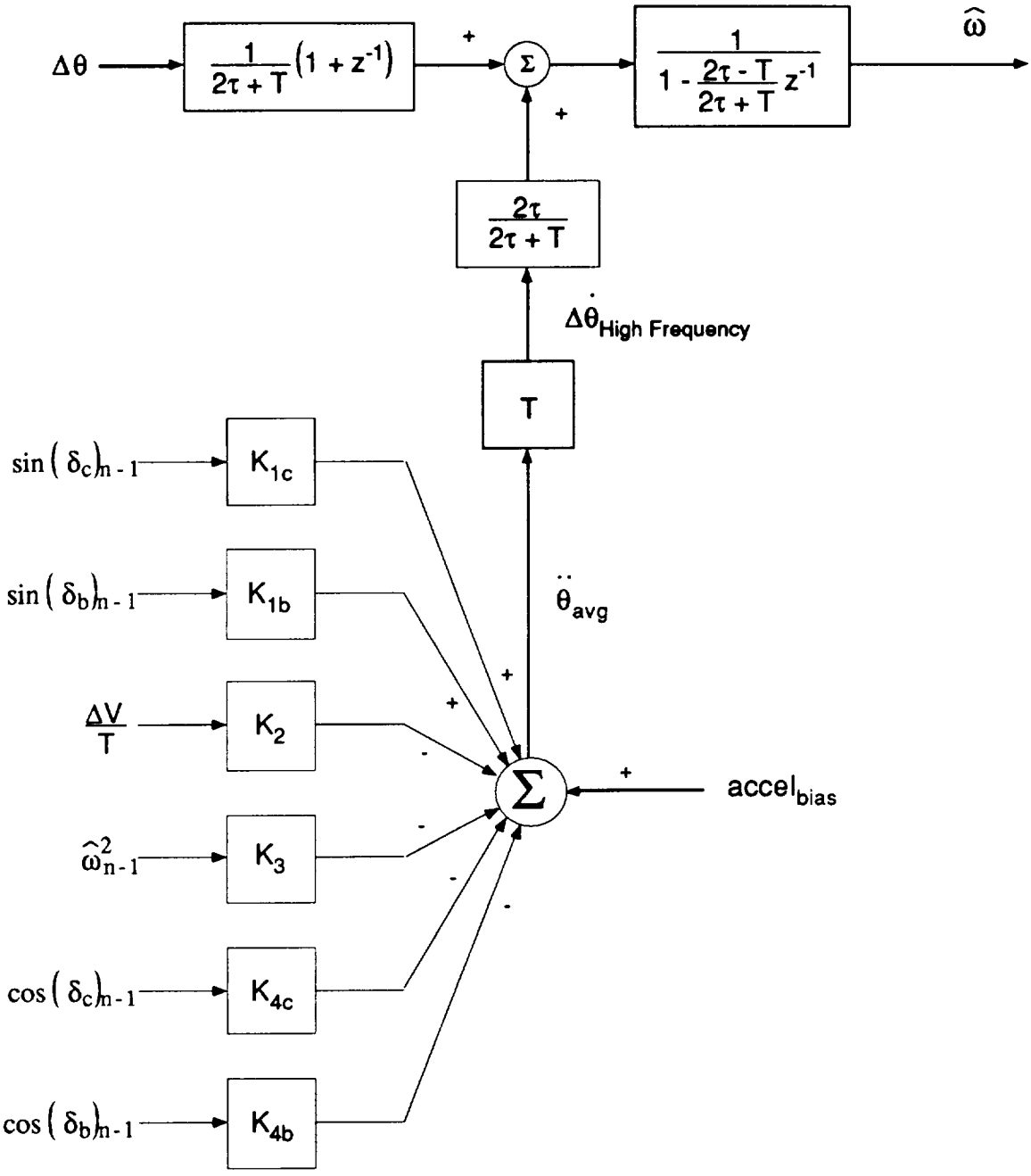

Figure 4.8 Rate estimator without acceleration bias estimation

Figure 4.5 the estimation of unmodeled angular acceleration was computed from the filtered difference of the estimated angular acceleration and the derivative of the estimated angular rate. To emulate this procedure of estimating unmodeled angular acceleration in the discrete signal implementation a similar feedback loop is added to Figure 4.8 as shown in Figure 4.9. As shown in Figure 4.9 the continuous integrator and low pass filter of the angular acceleration loop have been replaced by their equivalent digital implementations. In addition, $\dot{\hat{\omega}}_1$, which was computed in Figure 4.5 as the derivative of the estimated angular rate is now computed as the back difference of the estimated angular rate.

4.8 Frequency Response and Transient Response

4.8.1 General

As seen in Figure 4.8, the rate estimator is a multi-input system. Measured attitude, nozzle deflection, and ΔV signals are combined through a lagless complementary filter to form low and high frequency estimates of the angular rate. Both the low and high frequency estimates are modified by the complementary filter whose time constant, τ, determines its dynamic performance. This time constant represents a relative weighting of the low and high frequency paths. The larger the time constant the lower is the break frequency of the low and high pass filters. For both low and high frequency paths the choice of τ is driven by the considerations of measurement noise, system stability, and steady state error of the estimate.

In addition to the effects caused by the complementary filter the effects of the estimation of angular acceleration bias must also be considered. As shown in Figure 4.9 the estimation of unmodeled angular acceleration is coupled to the estimate of angular rate and vice versa. This occurs as a result of feeding back the estimated unmodeled angular acceleration into the high frequency estimate

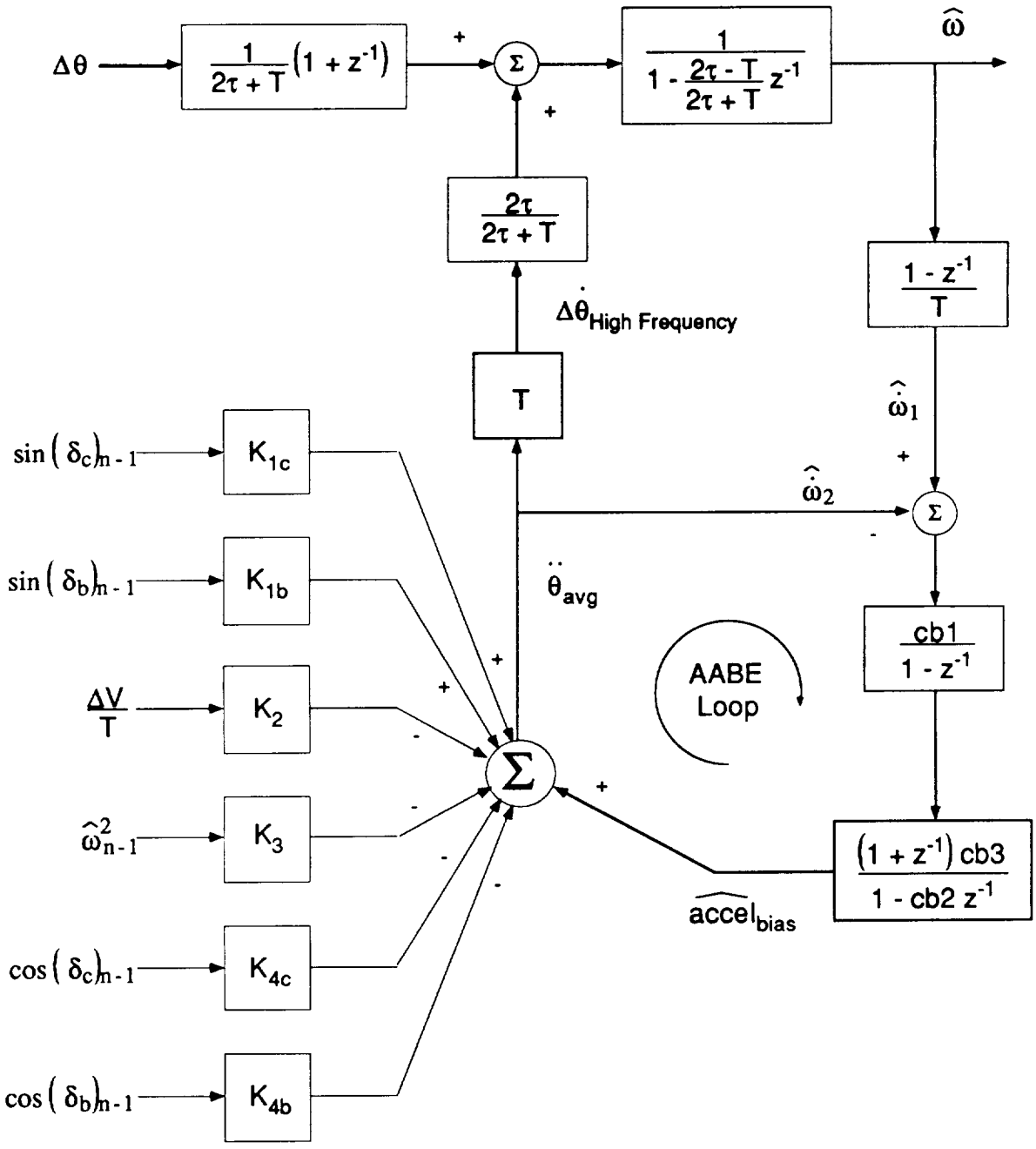

Figure 4.9 Rate estimator with acceleration bias estimation.

of angular rate. The effect of the estimated unmodeled angular acceleration upon the high frequency estimate of angular rate is a function of the filtering dynamics present in the AABE loop. The integral gain of the loop is determined by the two constants cb1, and cb3. The low pass filter time constant is equal to cb2. The choice of the integral gains and filter time constants for the angular acceleration loop is driven by noise, tracking, and stability considerations.

4.8.2 Estimator Transfer Functions

To analyze the frequency response characteristics of the rate estimator an approximate continuous model of the estimator is employed. As shown in Figure 4.10 this is achieved by modifying the inputs to both the low and high frequency paths of the rate estimator. In the high frequency path the components of angular acceleration due to nozzle deflection, and ΔV are replaced by the derivative of the true angular rate. In the low frequency path the true angular rate is employed instead of $\Delta\theta/T$. As a result, the effects of measurement noise and parameter uncertainty are neglected in this estimator model. Lastly, an angular acceleration input disturbance, $\dot{\omega}_b$, is added to the loop to replace the bias in the estimated angular acceleration resulting from errors and omissions in the modelling of the moments produced by engine and aerodynamic forces.

Compared to the system illustrated in Figure 4.9 the simplified continuous block diagram now has only two inputs, ω and $\dot{\omega}_b$. The frequency response of the estimator can be analyzed by treating each input ,ω and $\dot{\omega}_b$ separately and deriving a set of continuous transfer functions in terms of the output quantities $\hat{\omega}$, $\hat{\dot{\omega}}_1$, and $\hat{\dot{\omega}}_b$. Although it is possible to derive a total of six transfer functions, only four are necessary to study the control issues. They are:

$$\frac{\hat{\omega}}{\omega} = \frac{1 + \dfrac{K}{s(\tau_1 s + 1)(\tau s + 1)}}{1 + \dfrac{K}{s(\tau_1 s + 1)(\tau s + 1)}} = 1 \qquad (4.28)$$

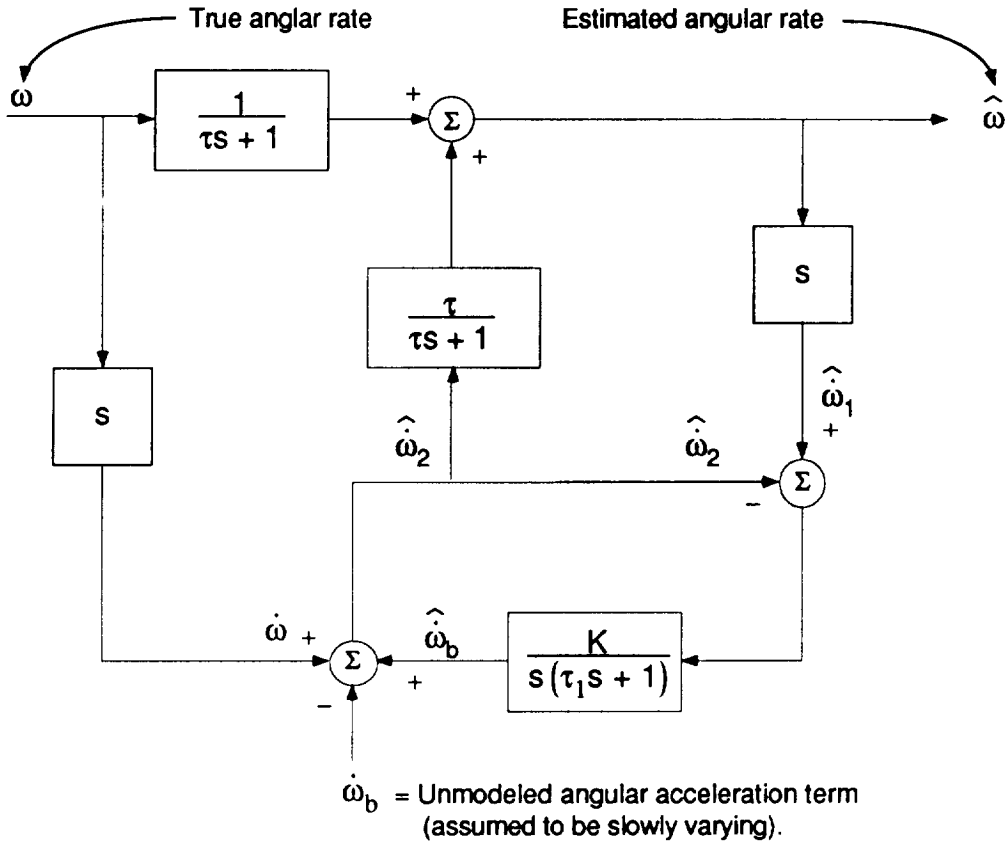

Figure 4.10 Simplified continuous rate estimator design loop.

$$\frac{\hat{\dot{\omega}}_b}{\dot{\omega}_b} = \frac{K}{s(\tau_1 s + 1)(\tau s + 1) + K} \tag{4.29}$$

$$\frac{\hat{\dot{\omega}}_2}{\dot{\omega}_b} = \frac{-s(\tau_1 s + 1)(\tau s + 1)}{s(\tau_1 s + 1)(\tau s + 1) + K} \tag{4.30}$$

$$\frac{\hat{\omega}}{\dot{\omega}_b} = \frac{-\tau s(\tau_1 s + 1)}{s(\tau_1 s + 1)(\tau s + 1) + K} \tag{4.31}$$

The derivation of these transfer functions is described in Appendix E. The continuous signal transfer functions presented in Equations (4.28) through (4.31) are functions of the parameters K, τ_1, and τ. In the actual implementation of the estimator a discrete set of time constants and gains was employed as illustrated in Figure 4.9. The relationships necessary to convert the continuous signal parameters K, and τ_1 to the equivalent discrete signal values of cb1, cb2, and cb3 are presented in Appendix F. The time constant τ is the same in both the discrete and continuous representations. The next two sections will employ the approximate continuous-signal transfer functions to explain the rationale for choosing the values of τ, K and τ_1 and then will examine the frequency response characteristics produced by the values of these parameters chosen for this thesis.

4.8.3 Rate Estimator Coefficients

The choice of τ is influenced by two factors. First, there is the need to filter out the effects of noise and/or quantization in the derived rate $\Delta\theta/T$ which is used for the low frequency estimate of angular rate. This need places a lower limit on the acceptable value of τ and correspondingly places an upper limit on the crossover frequency of the first order complementary filter. Second, there is the need to minimize the effects of uncertainties in the parameters used to generate $\hat{\dot{\omega}}_2$. This need suggests that the time constant τ be no higher than dictated by the first requirement.

The choice of K and τ_2 in the angular acceleration bias estimation (AABE) loop depends upon:

(1) The need to minimize the errors associated with tracking the bias $\dot{\omega}_b$ resulting from mismodeling of the angular acceleration. (A higher value of integral gain, K, will generally improve the tracking capability, however this is also at the expense of the stability of the acceleration feedback loop.)

(2) The need to filter the effects of noise and/or quantization on $\hat{\dot{\omega}}_1$. (As shown in Figure 4.5, $\hat{\dot{\omega}}_1$ is derived from the back difference of the estimated angular rate divided by the sampling time of the rate estimator. This form of differentiation is inherently "noisy" and can adversely affect the estimated unmodeled angular acceleration.)

(3) The need to maintain the stability of the unmodeled angular acceleration feedback loop based upon the open loop transfer function:

$$\frac{K}{s(\tau_1 s + 1)(\tau s + 1)}$$

(4) The need to limit the errors in the estimation of the average angular acceleration, $\hat{\dot{\omega}}_2$. (An accurate measure of the angular acceleration is needed for the estimation of the angle of attack. See Chapter 5.)

4.8.4 Frequency Response Characteristics

The continuous signal gain and filter time constants chosen for the rate estimator and their corresponding discrete signal values are shown in Table 4.1. The resulting frequency response characteristics for the approximate continuous signal transfer function relationships will be examined below in terms of the frequency response characteristics of the transfer functions represented by Equations (4.28) to (4.31).

The significance of the identity relationship of Equation (4.28) is that for the approximate continuous signal model of the estimator, the transfer function between estimated and actual angular rate is unity, independent of the effects of the angular acceleration bias estimator (AABE) loop. Of course, in the actual estimator, where mismodeling produces gain as well as bias errors, the transfer function between estimated and true angular rate will not be unity. However, this function and its effects on ALS stability can be expected to be nearly independent of the dynamics of the AABE loop.

Equations (4.29) to (4.31) define three other transfer functions that relate the estimator variables $\hat{\dot{\omega}}_b$, $\hat{\omega}$, and $\hat{\dot{\omega}}_1$ to the angular acceleration bias term, $\dot{\omega}_b$. The cancellation of this bias term and its effects on the estimated angular

CONTINUOUS	
K	0.50
τ_1	1.2487
τ	0.245
DISCRETE	
τ	0.245
cb1	0.05
cb2	0.923
cb3	0.0385

Table 4.1 Continuous and discrete rate filter constants.

acceleration $\hat{\dot{\omega}}_1$ and estimated angular rate $\hat{\omega}$ is the purpose of the AABE loop. The ability of the AABE loop to achieve this purpose with the selected estimator parameters is indicated by the frequency-response plots of Figures 4.11 through 4.13, representing the functions of Equations (4.29) through (4.31), respectively.

The frequency response of $\hat{\dot{\omega}}_b/\dot{\omega}_b$ shown in Figure 4.11 indicates the ability of the estimated angular acceleration bias estimate, $\hat{\dot{\omega}}_b$, to track variations in the bias $\dot{\omega}_b$. This figure shows that sinusoidal variations in $\dot{\omega}_b$ are well tracked by the bias estimator for frequencies equal to or less than 0.1 rad/sec and that the magnitude of $\hat{\dot{\omega}}_b$ is essentially equal to that of $\dot{\omega}_b$ up to 0.7 rad/sec. However, the phase lag which starts out at roughly 10° at 0.1 rad/sec reaches an unacceptable value of about 120° at 0.7 rad/sec. It may be concluded from these results that the estimator provides acceptable performance out to a

frequency range of about 0.2 rad/sec. Fortunately, the bias to be estimated is expected to vary at a slow rate that the estimator should be capable of tracking.

The effects of the ability of the AABE loop to cancel out low frequency variations in $\dot{\omega}_b$ are shown in Figures 4.12 and 4.13. First, examining Figure 4.12 it is seen that the transfer function relating the estimated angular acceleration $\hat{\dot{\omega}}_1$ to $\dot{\omega}_b$ is well attenuated at low frequencies, having a magnitude of approximately -30 dB at 0.1 rad/sec. Similarly, the transfer function relating the estimated angular rate $\hat{\omega}$ to $\dot{\omega}_b$ is also attenuated at low frequencies, having a magnitude of approximately -25 dB at 0.1 rad/sec.

4.8.5 Quantization Effects

As shown in Figure 4.9, the low and high frequency estimates of angular rate are derived from measured $\Delta\theta$, ΔV, and δ signals.It is presently anticipated that the $\Delta\theta$ and ΔV signals will be provided by a strapdown IMU whose ring laser gyros provide medium to high quality $\Delta\theta$ signals. However, the estimators

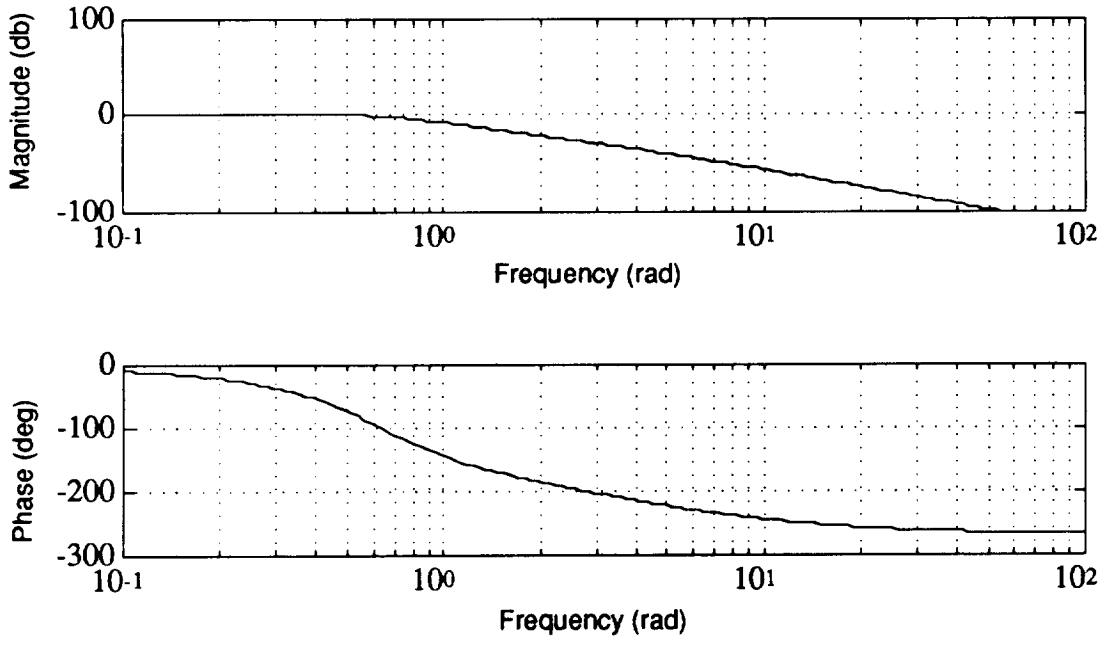

Figure 4.11 Frequency response of $\hat{\dot{\omega}}_b/\dot{\omega}_b$.

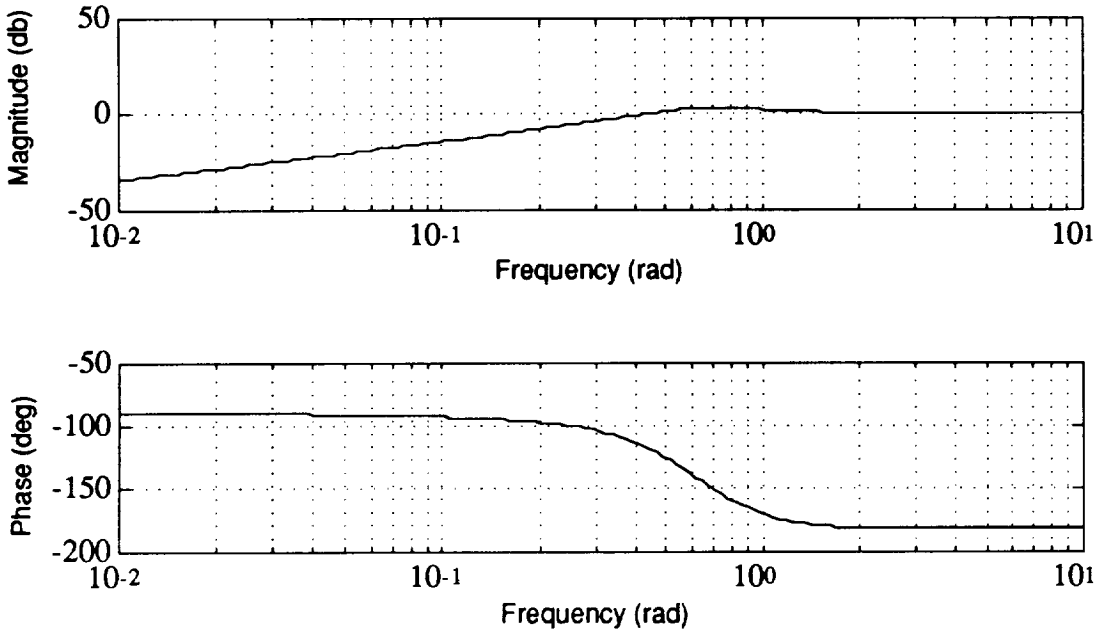

Figure 4.12 Frequency response of $\hat{\dot{\omega}}_2/\dot{\omega}_b$.

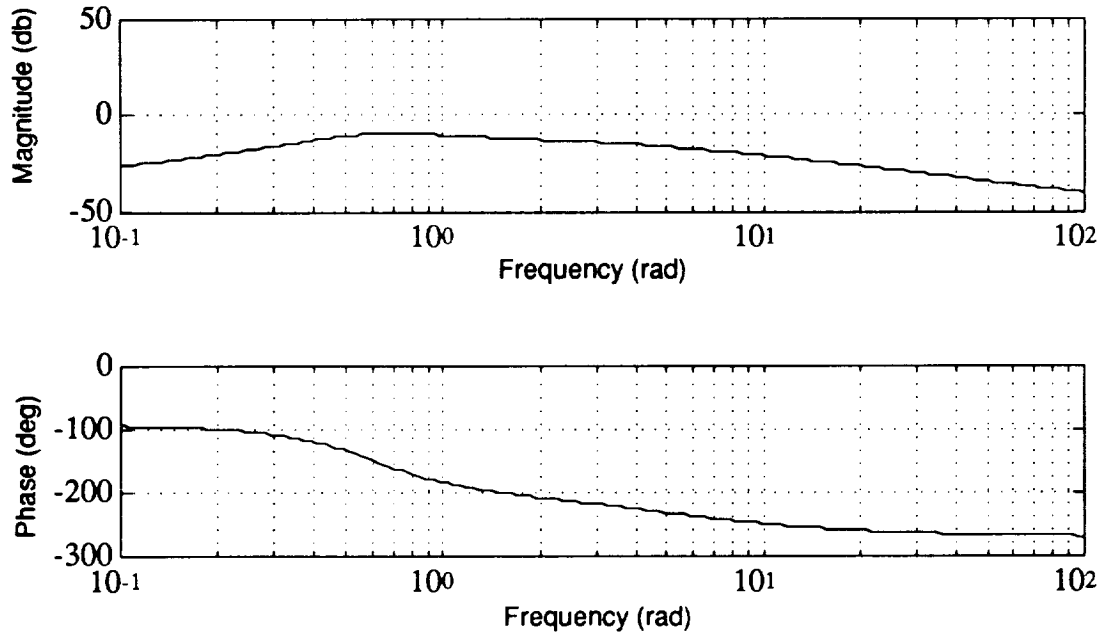

Figure 4.13 Frequency response of $\hat{\omega}/\dot{\omega}_b$.

employed in this thesis study are designed to accommodate also the lower quality $\Delta\theta$ signals that would be generated by the electrical resolvers of a stabilized-platform IMU.

It is assumed that the requirements of ALS guidance and control would be adequately served by ring laser gyros whose primary error source affecting estimator performance is an attitude signal quantization that ranges from 3 arcsec to 11 arcsec. In the case of the stabilized-platfrom IMU it is assumed that the use of resolvers to measure attitude would increase the signal quantization to 110 arcsec. Also, the effects of signal noise which are negligible in the ring laser gyros, can be comparable to the effects of quantization in the case of stabilized-platform IMU resolvers. In this study noise effects were neglected for both IMU types.

The accelerometers of both IMU's types are assumed to have velocity signal quantization as the primary error source affecting estimator performance. The quantization level is assumed to range from 0.0128 ft/sec to 0.032 ft/sec. For the sake of comparison an unacceptably high value of velocity quantization of 0.32 ft/sec is also considered in combination with the maximum attitude quantization of 110 arcsec.

The effects of noise, quantization and other potential error sources in the measurement of the engine nozzle deflection were neglected. The statistical properties of the estimated rate error, $\omega_{true} - \hat{\omega}$, were determined by a no-wind boost simulation for the period from 40 to 60 seconds after liftoff. In each simulation different levels of gyro and accelerometer quantization were employed. The effects of these quantization levels upon the estimated angular rate were determined from a statistical analysis of the simulated variables. This analysis consisted of computing the mean ($\overline{x}$), variance (σ^2), and standard deviation (σ) in the difference between the true rate and estimated rate. The effects of quantization on the estimated angular rate and angular acceleration were computed in simulation runs which used true feedback variables. During each simulation a total of at least 200 data points were taken over a period of 20 seconds. These data points were collected during Phase Three at approximately 40-50 seconds from ignition. The results of the analysis are shown in Table 4.2.

Also presented for comparison in Table 4.2 are values of the standard deviation of the derived angular rate , σ, as computed from

$$\sigma = \frac{\sqrt{2}}{T}\left(\frac{\text{Quant.}}{\sqrt{12}}\right) = \frac{0.408}{T}(\text{Quant.}) = 4.08\,(\text{Quant.})$$

where

derived rate = $\Delta\theta/T$

Quant. = quantization of the measured attitude.

T = sampling period = 0.1 sec.

The data in Table 4.2 indicates the following:

(1) The standard deviation of the estimated angular rate is less than that of the derived rate, as might be expected, except for the cases where the attitude quantization is small (3 arcsec. or 0), in which cases the effects of transient errors in the simulation cause the standard deviation in the estimated rate to be larger than the derived rate.

(2) For the ranges in quantization of 3 arcsec to 11 arcsec for θ, and 0.0128 ft/sec to 0.0320 ft/sec for V, the derived rate signal provides a standard deviation that seems quite adequate to control feedback.

(3) For the increased quantization in θ of 110 arcsec., as might be encountered in a stabilized-platform IMU, the standard deviation of the derived rate may be too high to be acceptable, but the standard deviation of the estimated is lower than that of the derived rate for the lowest quantization of 3 arcsec. Therefore, it appears to be both feasible and desirable to use the estimated angular rate if a stabilized-platform IMU is employed.

(4) The use of accelerometers with the lower quantization of 0.0128 ft/sec yields reductions in the standard deviation of the estimated angular rate which are most significant when the measured

attitude has the highest quantization of 110 arcsec. As seen in the table, when the attitude quantization has its highest value, the standard deviation drops from 0.0249 deg/sec to 0.020 deg/sec.

It is most important to bear in mind that the above conclusions were for a control sampling period of 0.1 seconds used in the simulation studies. Possibly one-third to one-half of this sampling period may be required to provide adequate compensation of the vehicle bending modes, in which case the standard deviations of the derived rate would be scaled up by a factor of two to three. Fortunately, the standard deviation of the estimated rate would not be scaled up nearly as much, so that the use of the estimated rate becomes desirable for the strapdown IMU as well as the stabilized-platform IMU.

The effects of quantization on the two angular acceleration estimates, $\hat{\dot{\omega}}_1$ and $\hat{\dot{\omega}}_2$, employed in the angular rate estimator are of particular interest because of their potential use in the angle of attack estimator, which must correct the IMU ΔV signal for the effects of angular acceleration. The statistical properties of the two estimated angular acceleration signals were determined by the same simulation runs used to determine the properties of the angular rate signals. The estimated angular acceleration signal statistics are shown in Tables 4.3 and 4.4 along with the standard deviation of the derived angular acceleration. The following relationship was used to compute the standard deviation σ of the derived angular acceleration:

$$\sigma = \frac{\sqrt{2}}{T}\left[\frac{\sqrt{2}}{T}\left(\frac{\text{Quant.}}{\sqrt{12}}\right)\right] = \frac{0.577}{T^2}(\text{Quant.}) = 57.74\,(\text{Quant.})$$

As in the case of the angular rate signal, it would appear from Tables 4.3 and 4.4 that derived rather than estimated angular acceleration signals would suffice for the quantization levels of a strapdown IMU, provided the sampling period is 0.1 sec. However, it should be pointed out that a reduction in the sampling period by a factor of two or three would increase the standard deviation of the derived angular acceleration by a factor of 4 to 9, in which case the use of estimated angular acceleration might be necessary for the strapdown

IMU. In addition, the use of estimated angular acceleration definitely appears necessary for the large attitude quantization of the stabilized-platform IMU. Although the standard deviations of the two alternative angular acceleration estimates $\hat{\dot{\omega}}_1$ and $\hat{\dot{\omega}}_2$ in Tables 4.3 and 4.4 are comparable for low attitude signal quantizations, the standard deviation of $\hat{\dot{\omega}}_2$ is considerably lower for the largest attitude signal quantization of 110 arcsec. The effects of quantization levels on the angle of attack estimator as well as the choice between $\hat{\dot{\omega}}_1$ and $\hat{\dot{\omega}}_2$ will be examined in Chapter 5.

QUANTIZATION		$\omega_{True} - \hat{\omega}$			σ
θ (arc sec)	V (ft/s)	Mean (deg/sec)	σ (deg/sec)	σ^2 (deg/sec)^2	for the derived angular rate (deg/sec)
0	0.0000	-3.5×10^{-3}	3.72×10^{-3}	1.38×10^{-5}	0
3	0.0128	-3.6×10^{-3}	6.21×10^{-3}	3.86×10^{-5}	3.40×10^{-3}
11	0.0128	-2.7×10^{-3}	7.71×10^{-3}	5.94×10^{-5}	1.25×10^{-2}
11	0.0320	-3.6×10^{-3}	1.10×10^{-2}	1.22×10^{-4}	1.25×10^{-2}
110	0.0320	-2.2×10^{-3}	2.49×10^{-2}	6.19×10^{-4}	1.25×10^{-1}
110	0.0128	-3.6×10^{-3}	2.00×10^{-2}	4.00×10^{-4}	1.25×10^{-1}

Table 4.2 Effects of quantization on error in estimated pitch rate.

4.8.6 Simulation Results

For the sake of completeness, plots of some of the estimated angular rate and estimated angular acceleration variables whose statistics are given in Tables 4.2 to 4.4 are presented below.

QUANTIZATION		$\dot{\omega}_{True} - \hat{\dot{\omega}}_1$			σ for the derived angular accel. (deg/sec)
θ (arc sec)	V (ft/s)	Mean (deg/sec^2)	σ (deg/sec^2)	σ^2 $(deg/sec^2)^2$	
0	0.0000	-3.0×10^{-3}	1.13×10^{-3}	1.27×10^{-6}	0
3	0.0128	-2.6×10^{-3}	6.37×10^{-2}	4.06×10^{-3}	4.81×10^{-2}
11	0.0128	-4.4×10^{-3}	7.20×10^{-2}	5.18×10^{-3}	1.76×10^{-1}
11	0.0320	-3.1×10^{-3}	1.77×10^{-1}	3.14×10^{-2}	1.76×10^{-1}
110	0.0128	-4.1×10^{-3}	2.4×10^{-1}	5.72×10^{-2}	1.76×10^{0}

Table 4.3 Effects of quantization on error in estimated angular acceleration.

QUANTIZATION		$\dot{\omega}_{True} - \hat{\dot{\omega}}_2$			σ for the derived angular accel. (deg/sec)
θ (arc sec)	V (ft/s)	Mean (deg/sec^2)	σ (deg/sec^2)	σ^2 $(deg/sec^2)^2$	
0	0.0000	-1.7×10^{-2}	1.44×10^{-2}	2.06×10^{-4}	0
3	0.0128	-1.7×10^{-2}	6.61×10^{-2}	4.37×10^{-3}	4.81×10^{-2}
11	0.0128	-1.5×10^{-3}	7.40×10^{-2}	5.48×10^{-3}	1.76×10^{-1}
11	0.0320	-1.7×10^{-2}	1.77×10^{-1}	3.13×10^{-2}	1.76×10^{-1}
110	0.0128	-1.7×10^{-2}	6.61×10^{-2}	4.37×10^{-3}	1.76×10^{0}

Table 4.4 Effects of quantization on error in estimated angular acceleration.

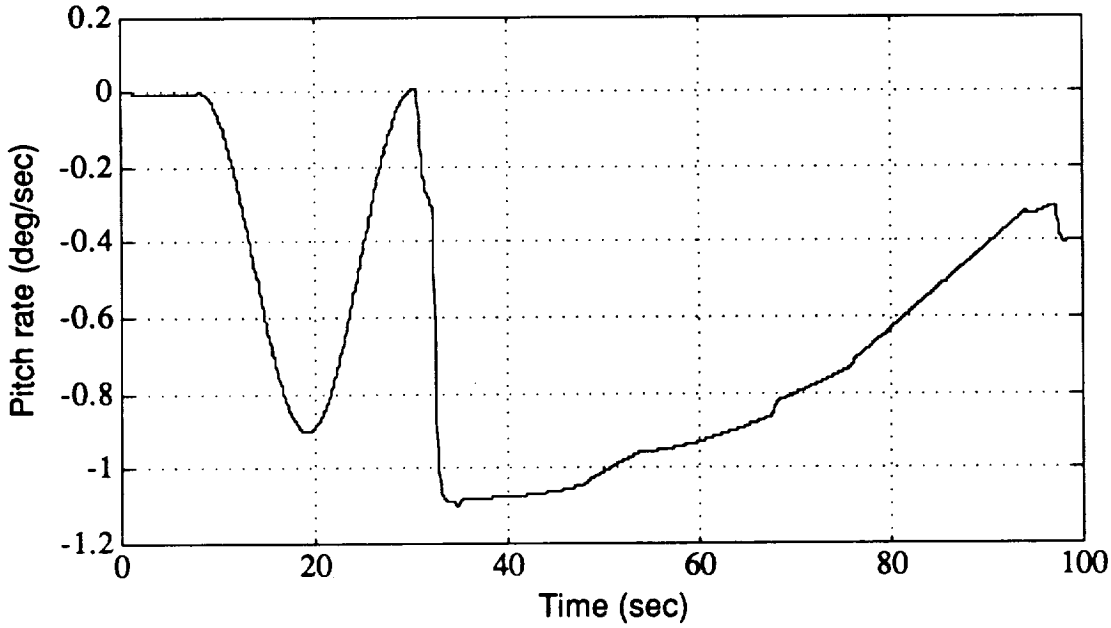

Figure 4.14 True pitchrate (ω)

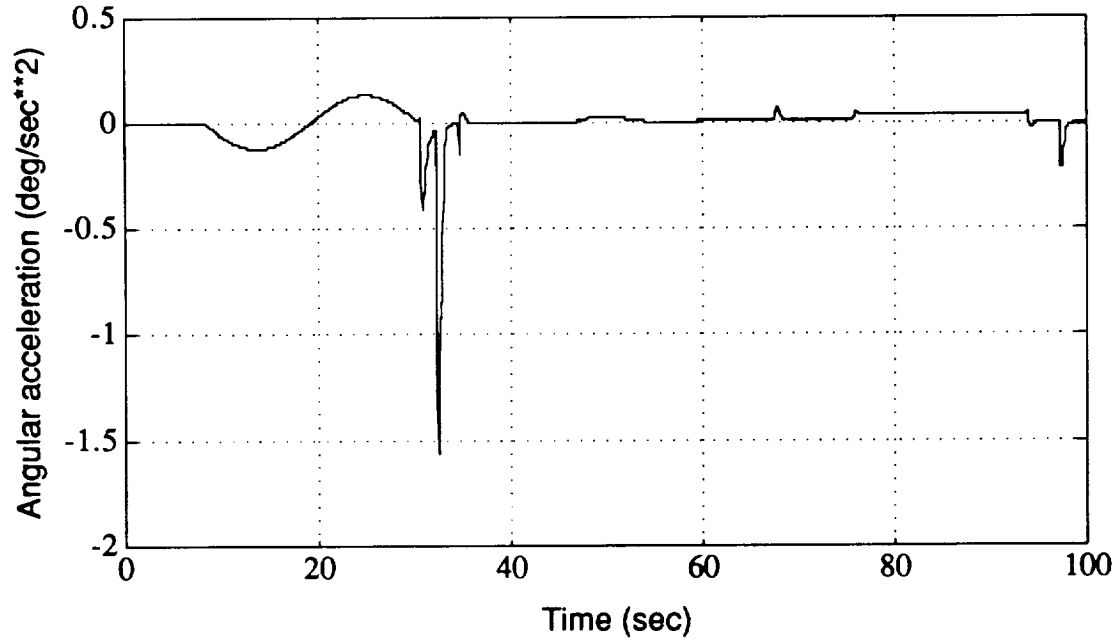

Figure 4.15 True angular acceleration $(\dot{\omega})$.

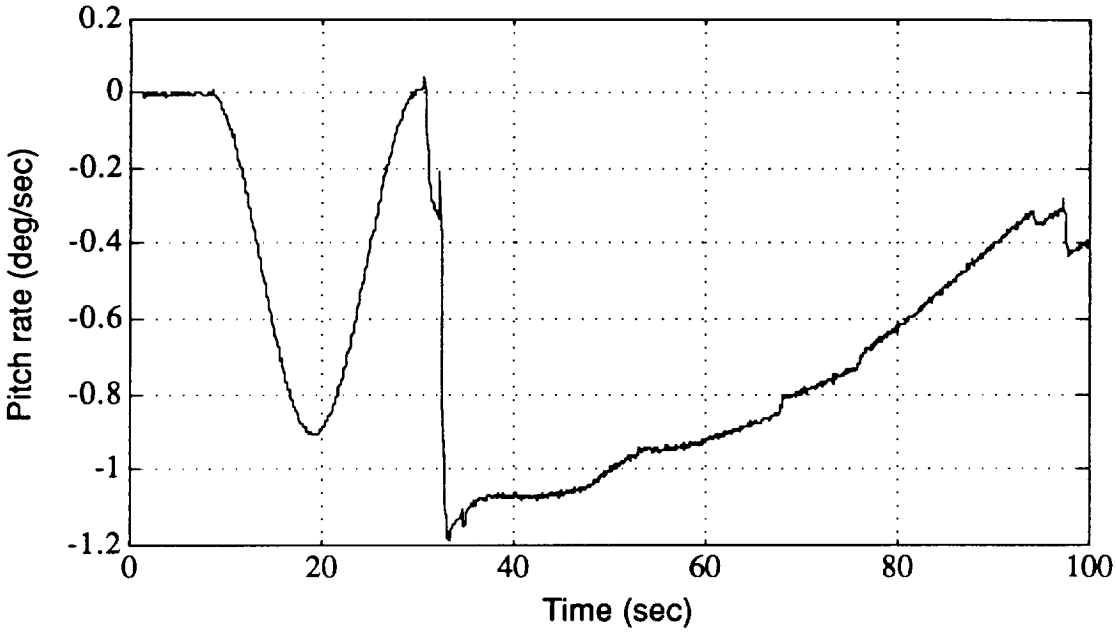

Figure 4.16 Pitch rate $(\hat{\omega})$ with 3 arcsec and 0.0128 ft/s quantization.

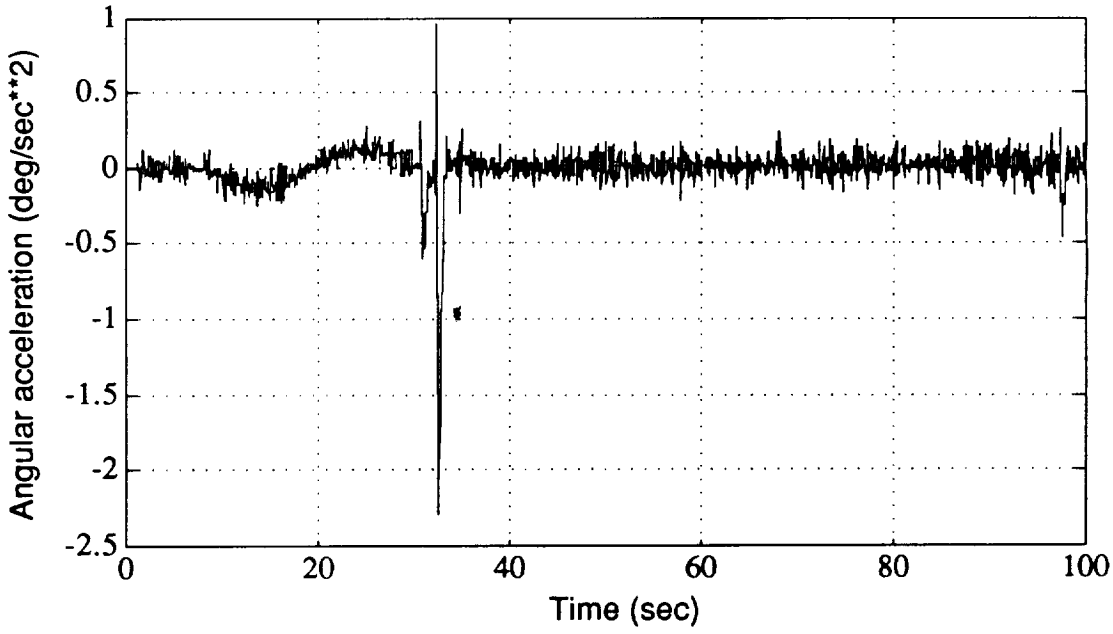

Figure 4.17 Angular acceleration $(\hat{\dot{\omega}}_1)$ with 3 arcsec and 0.0128 ft/s quantization.

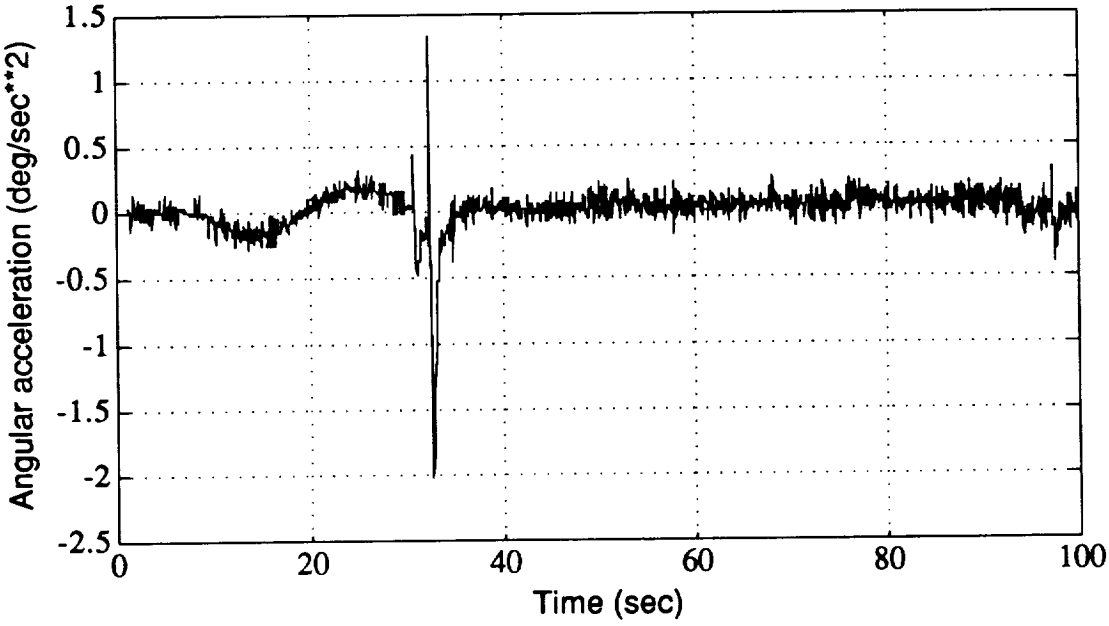

Figure 4.18 Angular acceleration $(\hat{\dot{\omega}}_2)$ with 3 arcsec and 0.0128 ft/s quantization.

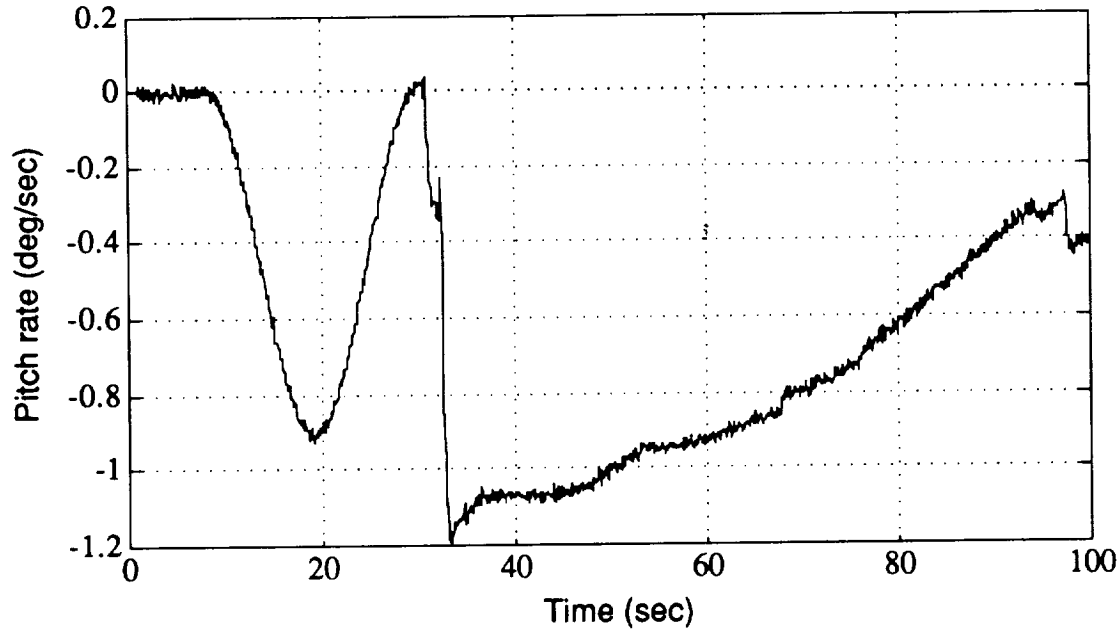

Figure 4.19 Pitch rate $\hat{\omega}$ with 11 arcsec and 0.032 ft/s quantization.

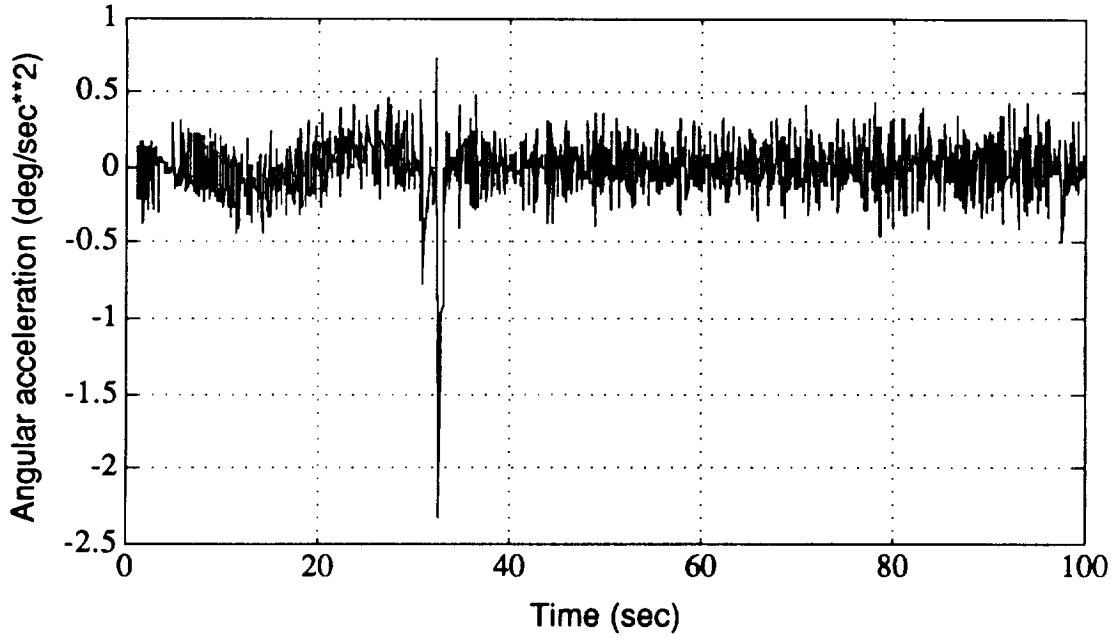

Figure 4.20 Angular acceleration $(\hat{\dot{\omega}}_1)$ with 11 arcsec and 0.032 ft/s quantization.

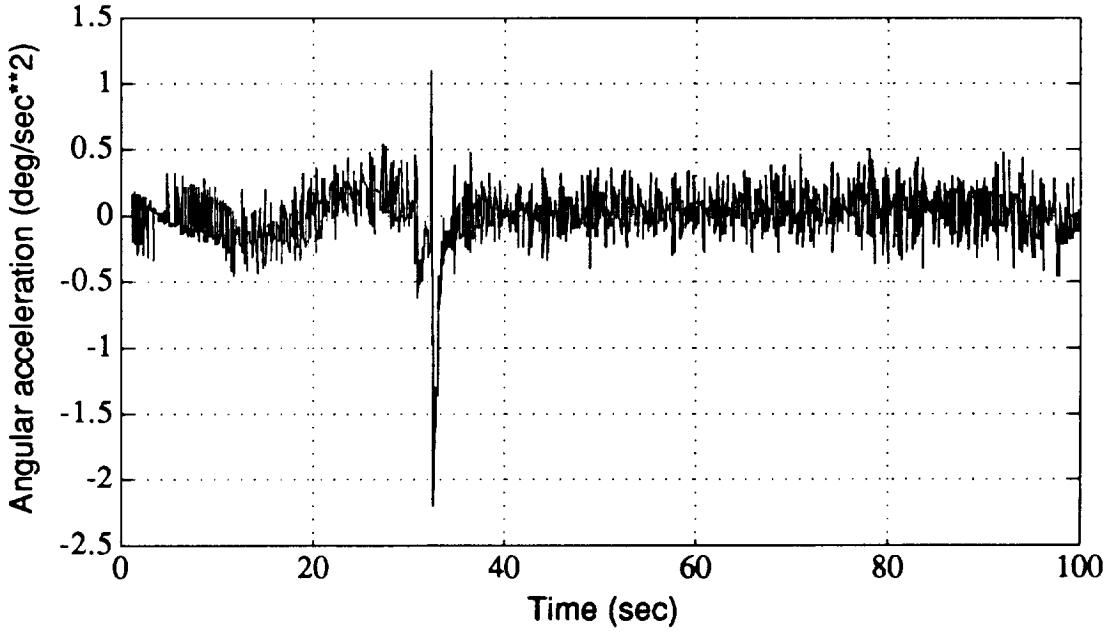

Figure 4.21 Angular acceleration $(\hat{\dot{\omega}}_2)$ with 11 arcsec and 0.032 ft/s quantization.

Chapter Five

ANGLE OF ATTACK ESTIMATION

5.1 Introduction

The estimated angle of attack plays two key roles in the implementation of the dual mode concept of an acceleration-direction control with a Qα-limit override. First, it is employed in the logic for switching between the acceleration-direction and Qα-limit modes of this concept and second, it is employed as the primary control feedback variable when in the Qα-limit mode. In both cases the accuracy of the estimation of the angle of attack has an important effect on system performance.

It is assumed that aerodynamic sensors will not be provided in the ALS for the direct measurement of the angle of attack, but that the angle of attack must be estimated from the IMU measured effects of vehicle motion. The estimation of angle of attack can be achieved by the following procedure:

(1) Compute the normal acceleration at the cg by using the estimated angular acceleration and estimated angular rate to adjust the IMU measured normal ΔV component for the effects of extraneous tangential and centripital acceleration at the IMU.

(2) Subtract the effects of the normal component of thrust as determined from the measured δ to determine the normal acceleration at the cg produced by the normal aerodynamic force.

(3) Determine the magnitude of the normal aerodynamic force by dividing the vehicle mass into the estimated normal acceleration produced by this force at the cg.

(4) Compute the normal aerodynamic force coefficient by dividing the estimated force magnitude by the product of the aerodynamic reference area and the estimated dynamic pressure.

(5) Employ the estimated Mach number in combination with the estimated normal aerodynamic force coefficient to compute the angle of attack from the computer stored relationship between these quantities.

The accuracy of this estimation procedure is limited by the accuracy of the measured and estimated quantities employed as inputs, and also by the accuracy of the aerodynamic relationships that are employed to determine the angle of attack from the Mach number and the normal aerodynamic coefficient. Although errors in angle of attack estimation appear to be manageable in the logic of the Qα-limit mode , their effects on the stability of the controls in the Qα-limit mode could be of greater concern. This concern centers on possible uncertainties in the gain between estimated and true angle of attack resulting from uncertainties in the aerodynamic relationships.

To ensure adequate stability of the Qα-limit mode it was decided to employ a complementary filter that (1) uses the above estimation procedure to compute only a low frequency input to the complementary filter and (2) employs a high frequency input to the complementary filter that is based on the attitude. However, to avoid the adverse effects on stability margins of the aerodynamic uncertainties in the low-frequency input it is desirable to chose a filter break frequency that is lower than the 0 dB crossover frequency of the open loop control transfer function. This results in the open loop characteristics in the vicinity of the critical 0 dB crossover frequency being dependent primarily on the measured attitude which produces no gain uncertainties in the open loop characteristics.

It can be shown that the use of attitude alone for the high frequency input can result in an appreciable constant or slowly-varying bias in the estimated α. This error comes from neglecting the effects of a constant or slowly varying rate of rotation of the earth-relative velocity vector. Although it is possible to estimate this velocity vector rotation rate as done by Bushnell, it is also possible to effectively eliminate this bias by employing a second order complementary filter. This latter approach was chosen for the ALS application. The rationale for selecting a second order complementary filter will be described subsequently in this chapter.

5.2 The Complementary Filter

A simple continuous signal second order complementary filter is illustrated in Figures 5.1. In a manner similar to the first order complementary filter described in Chapter Three, the state estimate, $\hat{\mathbf{x}}$, is computed from the filtered sum of two separate low and high frequency state estimates. The high frequency estimate, $\hat{\mathbf{x}}_{\text{high frequency}}$, is passed through a high pass filter while the low frequency estimate, $\hat{\mathbf{x}}_{\text{low frequency}}$, is passed through a low pass filter. The transfer function of the second order complementary filter has unity gain with no phase shift. Consequently, in the ideal case where both the high and low frequency signals are exact over the whole frequency range, the filter acts as a unity block.

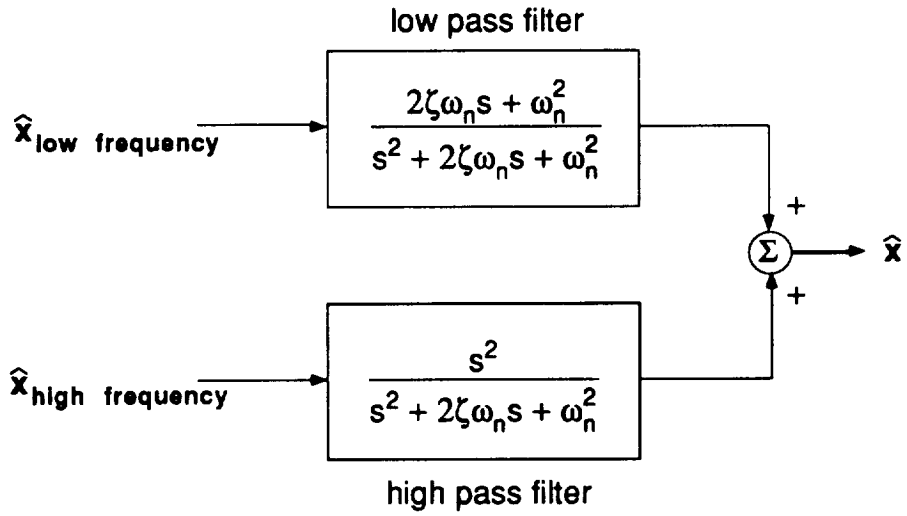

Figure 5.1 Second order complimentary filter.

5.3 The Digital Complementary Filter

In the angle of attack estimator, the second order complementary filter is implemented as a discrete filter. Using the bilinear transformation the complex frequency, s, can be approximated in the discrete z-domain by the relationship:

$$s \cong \frac{2}{T}\left(\frac{1 - z^{-1}}{1 + z^{-1}}\right)$$

where T is the sampling time of the discrete filter. Substituting this expression for s into the transfer function in Figure 5.1 results in the digital filter illustrated in Figure 5.2. Noting that $(1 - z^{-1})$ times the high frequency input is equivalent to supplying an incremental input to a filter in which $(1 - z^{-1})$ is deleted, the angle of attack estimator shown in Figure 5.3 may be derived from Figure 5.2.

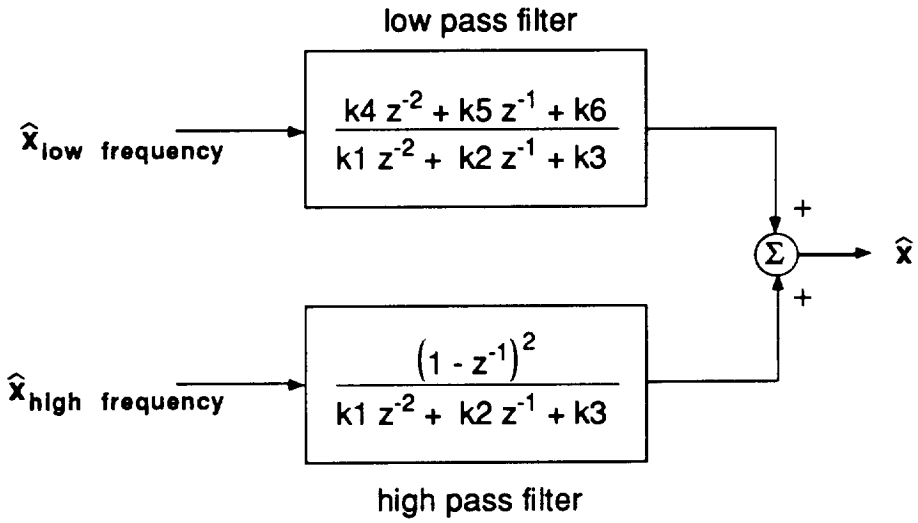

Figure 5.2 Digital second order complimentary filter.

The coefficients in Figure 5.2 and 5.3 are defined as follows in terms of the sampling period, T, the natural frequency, ω_n, and the damping ratio, ζ, of the complementary filter.

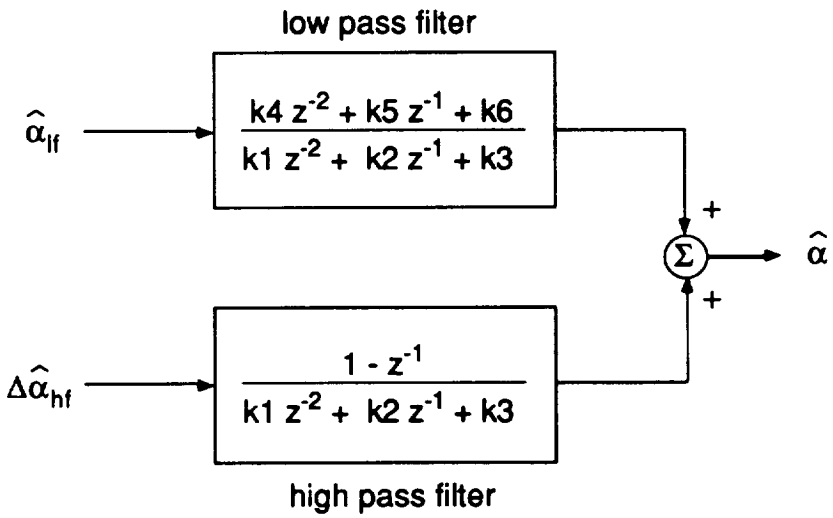

Figure 5.3 Digital angle of attack complementary filter.

$$K1 = 1 - T\zeta\omega_n + \frac{T^2}{4}\omega_n^2$$

$$K2 = \frac{T^2}{2}\omega_n^2 - 2$$

$$K3 = 1 + T\zeta\omega_n + \frac{T^2}{4}\omega_n^2$$

$$K4 = \frac{T^2}{4}\omega_n^2 - T\zeta\omega_n$$

$$K5 = \frac{T^2}{2}\omega_n^2$$

$$K6 = T\zeta\omega_n + \frac{T^2}{4}\omega_n^2$$

5.4 High Frequency Angle of Attack Estimate

As illustrated in Figure 5.4 the angle of attack of the vehicle can be expressed by the relationship

$$\alpha = \theta - \gamma + \alpha_w \tag{5.1}$$

Ideally, the incremental change in angle of attack, shown as the high frequency input in Figure 5.3, should be based on the taking the incremental variation of Equation 5.1:

$$\Delta\alpha = \Delta\theta - \Delta\gamma + \Delta\alpha_w \tag{5.2}$$

However, as explained previously, $\Delta\alpha$ is approximated in the ALS implementation by $\Delta\theta$. The effects of this approximation is discussed below in terms of the two contributions to $\Delta\alpha$ that are omitted.

First, the incremental change $\Delta\alpha_w$ is due to the variation in winds normal to the velocity vector. This quantity, however, is not measured and its effect is neglected in the computation of α. As a result, the estimators response to winds is dependent on only its low frequency channel which is subject to low pass filtering. However, by choosing a break frequency, ω_n, which is close to the 0 dB crossover frequency of the open loop control transfer function, the effects of the lag in the load relief response to winds will be reduced. The value of this break frequency selected for the ALS is 2 rad/sec, which is only a factor of two below the crossover frequency in the Qα-limit mode.

Second, the effect of neglecting the contribution of $\Delta\gamma$ to $\Delta\alpha$ can be expressed in terms of

$$\Delta\hat{\gamma} \cong T\,\dot{\gamma} \tag{5.3}$$

where T is the control sampling period. The rotation rate of the velocity vector, $\dot{\gamma}$, is determined as follows (see Appendix D): First the linear acceleration of the vehicle normal to the earth relative velocity vector is expressed as

$$\sum F_{uvz} = -M\dot{\gamma}V = T_b \sin(\delta - \alpha) + T_c \sin(\delta - \alpha) + Mg\cos(\gamma) - SQC_n \cos(\alpha) + SQC_a \sin(\alpha) \tag{5.4}$$

Then, solving for $\dot{\gamma}$ yields

$$\dot{\gamma} = \frac{(T_b + T_c)\sin(\alpha - \delta)}{MV} + \frac{SQC_n \cos(\alpha)}{MV} - \frac{SQC_a \sin(\alpha)}{MV} - \frac{g \cos(\gamma)}{V} \qquad (5.5)$$

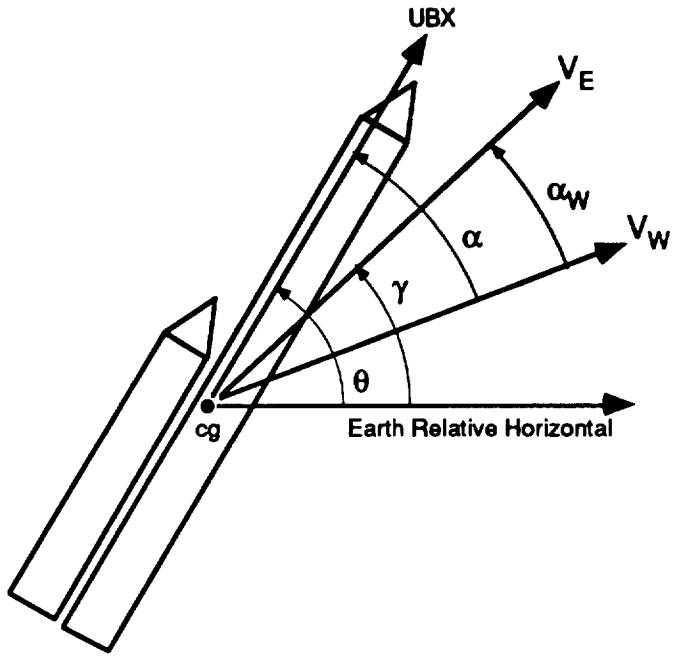

Figure 5.4 Vehicle orientation parameters.

The flight path angle rate is typically small and does not vary rapidly in Phase Three. This is shown in Figure 5.5 where the back difference of gamma is used to calculate a typical $\dot{\gamma}$ profile for a no-wind trajectory. The effect of $\dot{\gamma}$ is to introduce a small-time varying bias in the estimation of $\Delta\alpha_{HF}$. If the complementary filter were a first order filter this $\dot{\gamma}$-produced bias would be transmitted to the estimator output, subject to the low pass filtering. In that case it might be advisable to employ an approximate computation of $\dot{\gamma}$ to correct the high frequency input. However, in the case of the ALS where the computation of $\dot{\gamma}$ is more complicated it appears that a more attractive alternative is to employ a second order complementary filter which attenuates a slowly varying $\dot{\gamma}$ and eliminates the effects of a constant $\dot{\gamma}$. Thus, it is seen that the response of the estimated angle of attack in Figure 5.3 to a constant $\Delta\hat{\alpha}_{hf}$, as might be produced

by a constant $\dot{\gamma}$, is obtained by letting z=1, producing a zero contribution to the estimated angle of attack, $\hat{\alpha}$. Also a constant $\Delta\hat{\alpha}_{hf}$ in the discrete signal implementation corresponds to a constant $\dot{\alpha}_{lf}$ in the continuous signal representation, in which case the effect of a constant $\dot{\alpha}_{lf}$ on the estimated angle of attack is given by

$$\hat{\alpha}(s) = \frac{s}{s^2 + 2\zeta\omega_n s + \omega_n^2}\dot{\alpha}_{hf}(s) \tag{5.7}$$

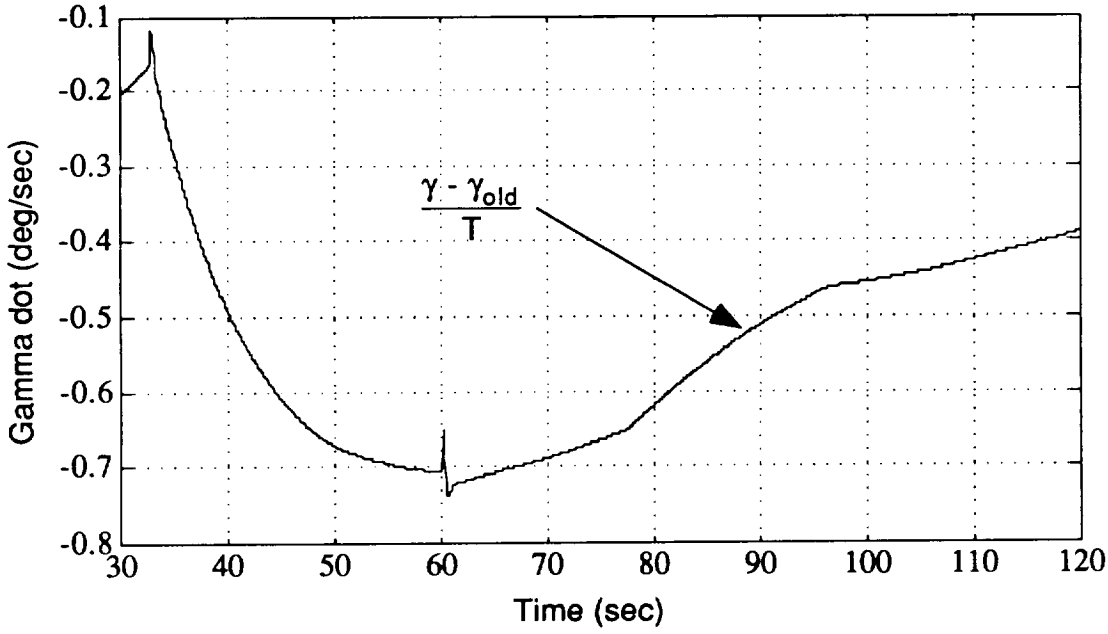

Figure 5.5 Typical $\dot{\gamma}$ profile for Phase Three.

which indicates that the contribution to the estimated angle of attack is well attenuated for frequencies that are well below the break frequency ω_n, and that the contribution is zero for an input frequency of zero.

In summary, it has been shown that for the second order complementary filter with the selected break frequency of 2 rad/sec it is possible to employ a high frequency input of

$$\Delta\alpha_{hf} = \Delta\theta$$

It will be recalled that a primary reason for employing the complementary filter was to make the estimator characteristics primarily dependent on the high frequency, attitude based input signal in the vicinity of the critical 0 dB crossover frequency of the Qα–limit mode listed in Table 3.1.

The method of computing the low frequency input to the angle of attack estimator will now be considered.

5.5 Low Frequency Angle of Attack Estimate

As shown in the flow chart of Figure 5.6, the five step procedure for computing the low frequency input to the α estimator first involves determining an estimate of the acceleration of the vehicle along the yaw axis (**UBZ**) based on measurements from the IMU as well as estimates of angular rate and angular acceleration. The estimated cg acceleration is then employed as an input to estimating the normal aerodynamic force, F_n. Following this, the normal aerodynamic force coefficient, C_n, is determined from the quotient of the estimated normal force and the product of the cross-sectional area of the vehicle, S, and the estimated dynamic pressure, $\hat{Q}$. (An improved method for determining the dynamic pressure based on an air-relative velocity estimate instead of the usual earth-relative velocity is described in Chapter Six.) The low frequency estimate of angle of attack is then found by performing a table look-up procedure, (See Appendix B) based on a table containing pre-calculated aero-coefficients (C_n) as a function of Mach number and angle of attack. The resulting low frequency estimate is then passed through a low pass filter to attenuate unwanted high frequency components and summed with the corresponding filtered high frequency estimate to yield an estimate of angle of attack that is valid over a wide range of frequencies.

The derivation for the low frequency estimate of angle of attack in the pitch plane defined by the body-axis vectors, **UBX** and **UBZ**, is as follows. From Figure 5.7 the acceleration of the center of gravity along the body negative z axis is given by the equation

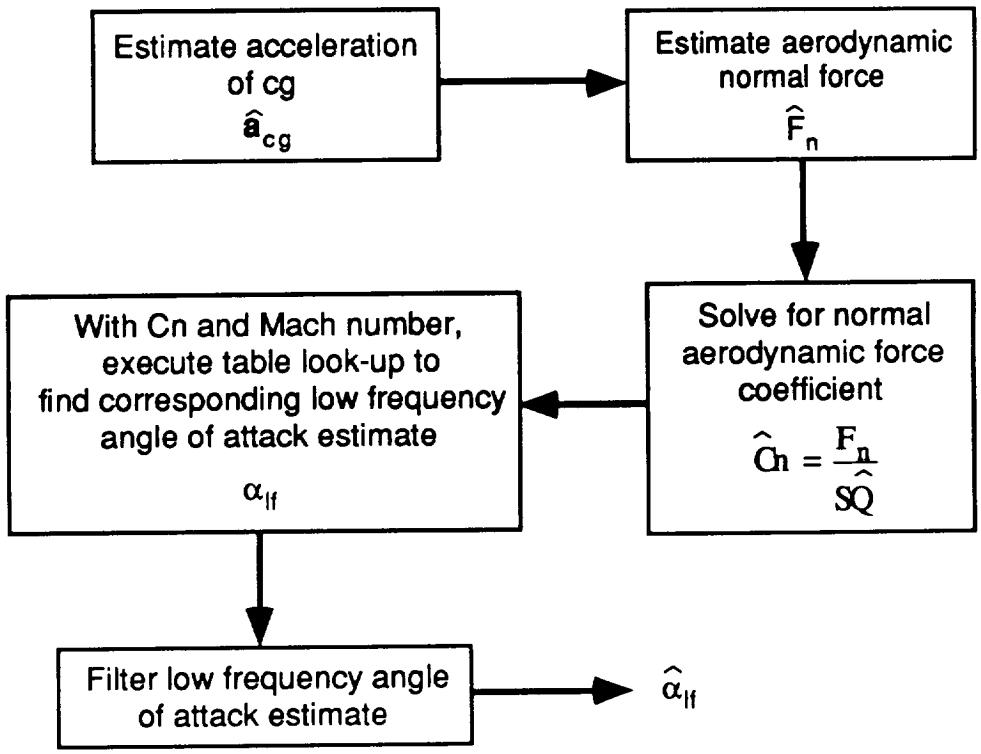

Figure 5.6 Low frequency angle of attack flow chart.

$$m\ a_{cg} = F_n - T_b \sin(\delta_b) + T_c \sin(\delta_c) \tag{5.12}$$

The acceleration of the center of gravity in the body frame is further related to the acceleration sensed at the IMU (also body frame) by the relationship

$$\vec{a}_{cg} = \vec{a}_{imu} + \left(\left(\vec{l}_{imu} \times \vec{\omega}\right) \times \vec{\omega}\right) + \left(\dot{\vec{\omega}} \times \vec{l}_{imu}\right) \tag{5.13}$$

where

$\vec{l}_{imu}$ = vector from the IMU to the center of gravity.

$\vec{\omega} = \omega$ **UBY** = average angular velocity vector over one control cycle.

$\vec{\dot{\omega}} = \dot{\omega}\,\mathbf{UBY}$ = average angular acceleration vector.over one control cycle.

The acceleration, $\vec{a}_{imu}$, corresponds to the translation of the vehicle, while the relative accelerations $\left(\left(\vec{l}_{imu} \times \vec{\omega}\right) \times \vec{\omega}\right)$ and $\left(\vec{\dot{\omega}} \times \vec{l}_{imu}\right)$ are associated with the rotation of the vehicle about the center of gravity. The component of a_{cg} along the body negative z axis can be expressed as

$$a_{cg} = a_{imu} + l_{imu}\,\omega^2 \sin(\beta) - l_{imu}\,\dot{\omega}\cos(\beta) \qquad (5.14)$$

The angle, β, defining the location of the IMU as shown in Figure 5.7 is typically less than 8°. Therefore, using small angle approximations ($\sin\beta=\beta$, $\cos\beta=1$), Equation (5.14) is simplified to

$$\hat{a}_{cg} = a_{imu} + l_{imu}\,\omega^2\,\beta - l_{imu}\,\dot{\omega} \qquad (5.15)$$

Therefore, the estimated acceleration of the center of gravity along the body negative z axis is a function of the IMU to cg vector (l_{imu}, β) as well as the angular rate and angular acceleration of the vehicle (ω, $\dot{\omega}$). As discussed in Chapter Four, the angular rate and angular acceleration of the vehicle are estimated quantities. From Figure (4.9) it can be seen that the angular acceleration of the vehicle is available from two separate signal paths. The first estimate, $\hat{\dot{\omega}}_1$, is derived from the back difference of the estimated angular rate, and the second, $\hat{\dot{\omega}}_2$, is the average angular acceleration (over a control cycle) based on an assumed dynamic model of the vehicle. Both angular acceleration estimates are corrupted by quantization noise in the measurements of ΔV and $\Delta\theta$. The effects of this noise upon the accuracy of $\hat{\dot{\omega}}_1$ and $\hat{\dot{\omega}}_2$ is dependent upon the filter coefficients chosen for the angular estimation loop. The estimated average normal aerodynamic force over one control cycle is then obtained by substituting Equation (5.15) into Equation (5.12).

$$\hat{F}_n = m\left(a_{imu} + l_{imu}\,\omega^2\,\beta - l_{imu}\,\dot{\omega}\right) + T_b \sin(\delta) - T_c \sin(\delta) \qquad (5.16)$$

The normal aerodynamic force is also related to the coefficient of normal force, C_n, by the relationship

$$\hat{C}_n = \frac{\hat{F}_n}{S\hat{Q}} \qquad (5.17)$$

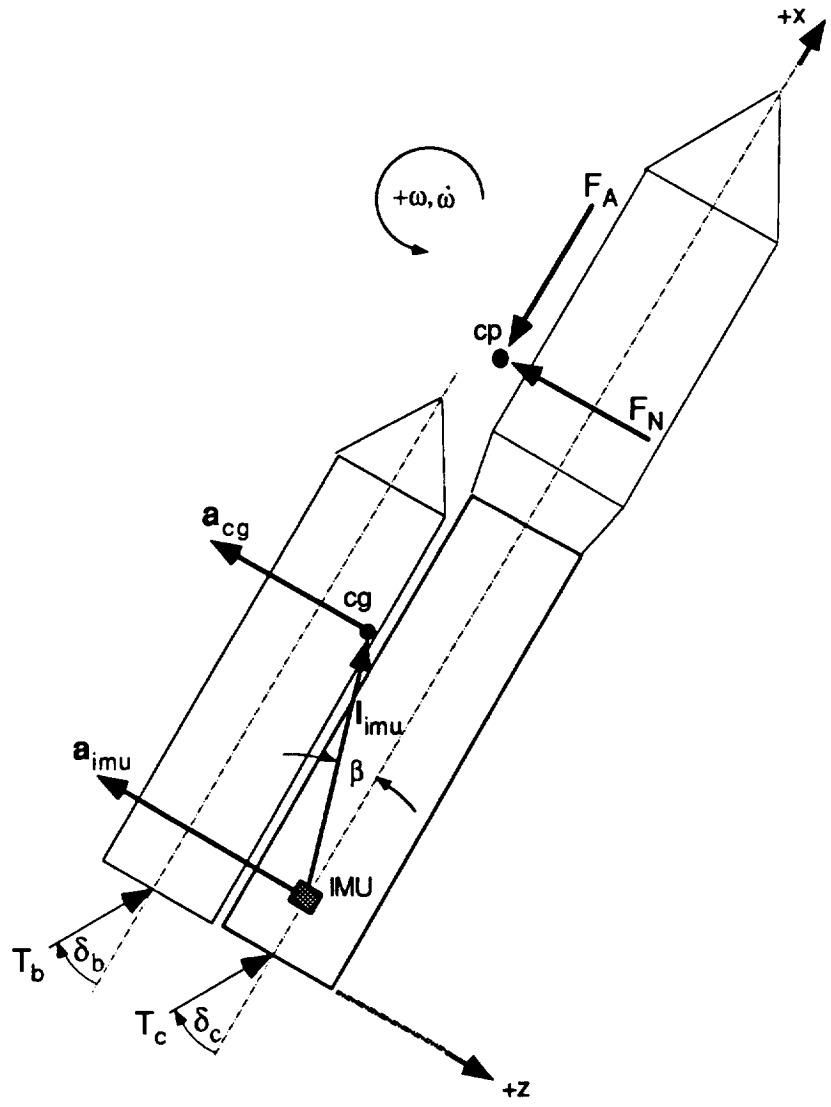

Figure 5.7 Vehicle Free Body Diagram for determination of F_n.

where S is the cross-sectional area of the vehicle, and $\hat{Q}$ is the estimated dynamic pressure. Following the estimation of Cn, an aerodynamic table look-up procedure is employed for estimating the low frequency angle of attack. These tables list the coefficients of normal and axial force as a function of Mach number and angle of attack. To determine α_{lf} the estimated coefficient of normal force and the current Mach number are employed in a linear interpolation search. A detailed description of this search procedure is found in Appendix B. Finally, the estimated low frequency angle of attack estimate is passed through a complementary low-pass filter and summed with the corresponding filtered high frequency estimate to produce an estimate of angle of attack that is valid over a wide range of frequencies.

5.6 Angle of Attack Filter Coefficients

The angle of attack estimator sums a high frequency estimate based on attitude measurements and a low frequency estimate based on measured δ, ΔV, and estimated ω and $\dot{\omega}$ through a complementary filter. The high and low pass filters of the complementary filter are second order. The natural frequency of both filters, ω_n, and damping ratio, ζ, are important in determining the accuracy of the angle of attack estimator as well as the control loop stability of the system. For a system with perfect high and low frequency estimates the complementary filter would reduce to a unity transfer function. In reality, however, both high and low frequency estimates contain errors. The extent that these errors effect the accuracy of the angle of attack estimator and the stability of the control loop depends in large part to the chosen filter parameters ω_n and ζ. In determining the appropriate values for these coefficients several conflicting issues must be considered.

5.6.1 Issues Effecting Choice of Filter Coefficients

For the high frequency path of the angle of attack estimator the issues are:

(1) The attitude signal quantization produces fluctuations in the measured incremental change in attitude over a control period. This produces corresponding fluctuations in the estimated angle of attack, depending on the filter characteristics.

(2) As previously mentioned, the high frequency estimate of angle of attack does not incorporate the effect of the rotation of the velocity vector ($\dot{\gamma}$). As a result, the prefiltered high frequency angle of attack estimate may contain a slowly varying bias. To help eliminate this bias and its effect upon the accuracy of the angle of attack estimate a second order high pass filter was employed. Increasing the crossover frequency of the complementary filter, reduces the effects of the slowly-varying bias. However, as will be shown below, increasing this frequency also magnifies the effects of quantization and modelling errors on the low-frequency estimate.

For the low frequency path of the angle of attack estimator the issues are:

(1) The low-frequency estimate is a function of the estimated angular rate and angular acceleration (see Chapter Four). Both of these signals are effected by quantization errors in measured $\Delta\theta$, and ΔV signals. The extent to which these errors effect the low frequency estimate is a function of the amount of attenuation present in the low-pass filter. This attenuation level of the filter is a function of its parameters (ω_n, ζ).

(2) The choice of ω_n is dependent upon the need to minimize the adverse effects of uncertainties in the parameters used to estimate the angle of attack. These uncertainties are not as yet defined for the ALS. However, it is assumed for the purposes of this thesis that because of these uncertainties it is desirable to select a ω_n value that is lower than the 0 dB crossover frequency of the control

loop. This choice of ω_n prevents the uncertainties from adversely affecting the frequency response in the critical range near and above the 0 dB crossover frequency.

The statistical properties of the error in estimated angle of attack are listed in Tables 5.1 and 5.2 for various quantization levels, assuming that the angular acceleration estimates employed in the angle of attack estimation are based on $\hat{\dot{\omega}}_1$ and $\hat{\dot{\omega}}_2$,respectively. The values of $\hat{\dot{\omega}}_1$ and $\hat{\dot{\omega}}_2$ and corresponding α estimates were computed from the variables generated in a no-wind simulation in which true values of feedback variables were employed. The values of the second order complementary filter parameters used were $\omega n=2$ rad/sec and $\zeta=0.8$. It will be recalled that

$\hat{\dot{\omega}}_1$ = angular acceleration estimated based on the back difference in estimated angular rate.

$\hat{\dot{\omega}}_2$ = angular acceleration estimate based on the measured ΔV and δ, with a correction for the bias produced by mismodeling.

Comparing tabulated values of the standard deviation, σ, it is seen that the use of $\hat{\dot{\omega}}_2$ yields better statistical performance for the largest attitude signal quantization. However, there is not a drastic difference between the standard deviations either between the tables or within each table. For the angle of attack estimator presented in Chapter 8 it was decided to employ $\hat{\dot{\omega}}_2$ for the simulation runs.

QUANTIZATION		$\hat{\alpha} - \alpha_{True}$		
θ (arc sec)	V (ft/s)	Mean (deg)	σ (deg)	σ^2 (deg^2)
0	0.0000	7.6×10^{-2}	3.83×10^{-2}	1.47×10^{-3}
3	0.0128	8.9×10^{-2}	1.03×10^{-1}	1.08×10^{-2}
3	0.0320	1.2×10^{-2}	1.62×10^{-1}	2.63×10^{-2}
11	0.0128	9.5×10^{-2}	1.26×10^{-1}	1.59×10^{-2}
11	0.0320	1.3×10^{-1}	1.65×10^{-1}	2.75×10^{-2}
110	0.0128	4.8×10^{-1}	6.97×10^{-1}	4.85×10^{-1}

Table 5.1 Effects of quantization in angle of attack error using $\hat{\dot{\omega}}_1$.

QUANTIZATION		$\hat{\alpha} - \alpha_{True}$		
θ (arc sec)	V (ft/s)	Mean (deg)	σ (deg)	σ^2 (deg^2)
0	0.0000	1.3×10^{-1}	5.63×10^{-2}	3.17×10^{-3}
3	0.0128	1.2×10^{-1}	1.12×10^{-1}	1.25×10^{-2}
3	0.0320	1.5×10^{-1}	1.63×10^{-1}	2.67×10^{-2}
11	0.0128	1.2×10^{-1}	1.12×10^{-1}	1.25×10^{-2}
11	0.0320	1.5×10^{-1}	1.63×10^{-1}	2.67×10^{-2}
110	0.0128	1.2×10^{-1}	1.13×10^{-1}	1.27×10^{-2}

Table 5.2 Effects of quantization in angle of attack error using $\hat{\dot{\omega}}_2$.

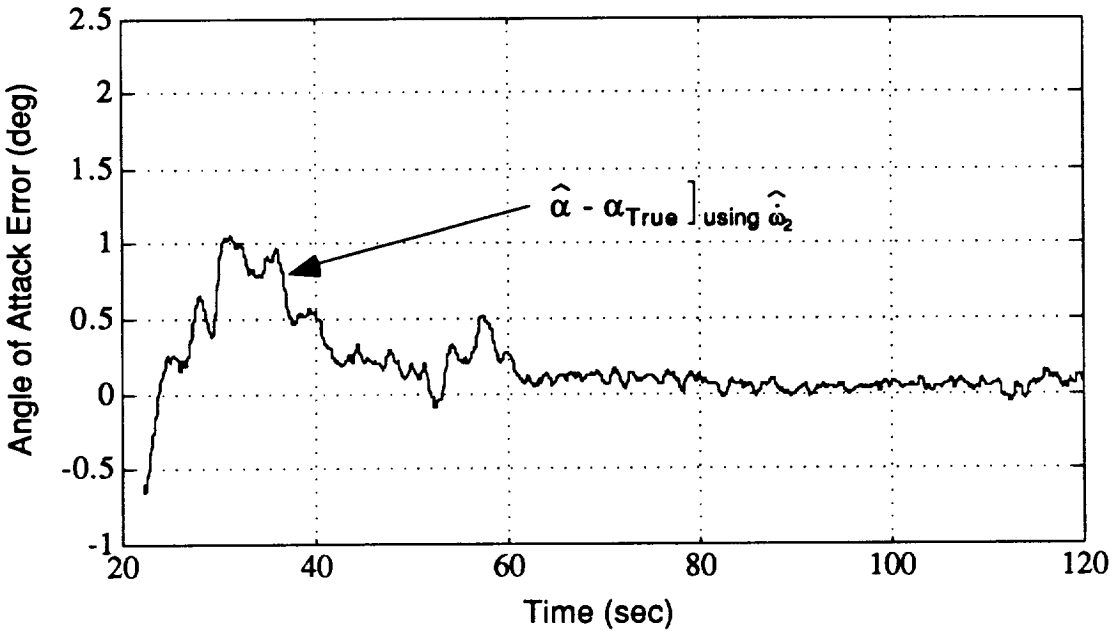

Figure 5.8 Angle of attack error using $\hat{\dot{\omega}}_2$ with quantization of 3 arcsec and 0.0128 ft/sec.

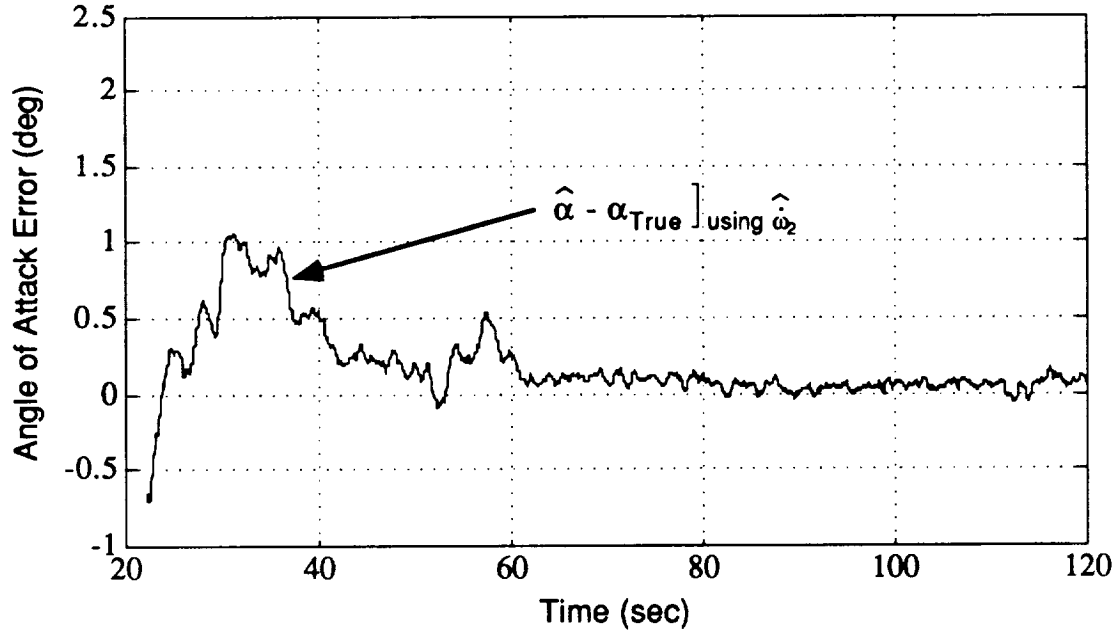

Figure 5.9 Angle of attack error using $\hat{\dot{\omega}}_2$ with quantization levels of 110 arcsec. and 0.0128 ft/sec.

Chapter Six

DYNAMIC PRESSURE ESTIMATION

6.1 Introduction

The dynamic pressure Q is defined as

$$Q = \frac{1}{2} \rho V_A^2$$

where ρ is the air density and V_A is the air-relative velocity. Current practice in estimating Q from inertial measurements neglects the effects of winds to assume that the magnitude of the air-relative velocity equals that of the earth-relative velocity. This approach can result in errors as high as 10 percent in Q being caused by high velocity winds, as shown in Figure 6.1.

In the implementation of the ALS guidance and control system examined in this thesis, these Q errors are of potential concern because of the use of estimated Q in the estimation of angle of attack and in the computation of the limit on angle of attack. The resulting errors in the estimated angle of attack can reduce the effective stability margins when in the $Q\alpha$-limit mode, and the errors in both the estimated angle of attack and its limit can adversely affect the limitation of $Q\alpha$.

Although these effects might be tolerable for some ALS vehicle designs and ALS launch conditions, there is a simple approach that might be employed to reduce the errors in estimated Q produced by the largest wind velocities. This approach employs the estimated angle of attack in combination with the estimated earth-relative velocity to generate an estimate of the magnitude of the air-relative velocity, which in turn is used in the estimation of Q. This approach assumes that the winds contributing to the estimated angle of attack are horizontal in the local geographic reference frame -- an assumption that should

be most accurate for the very large wind velocities. This assumption limits the extent to which the Q errors can be reduced, but the possibility of reducing the largest of the errors makes this approach worthwhile.

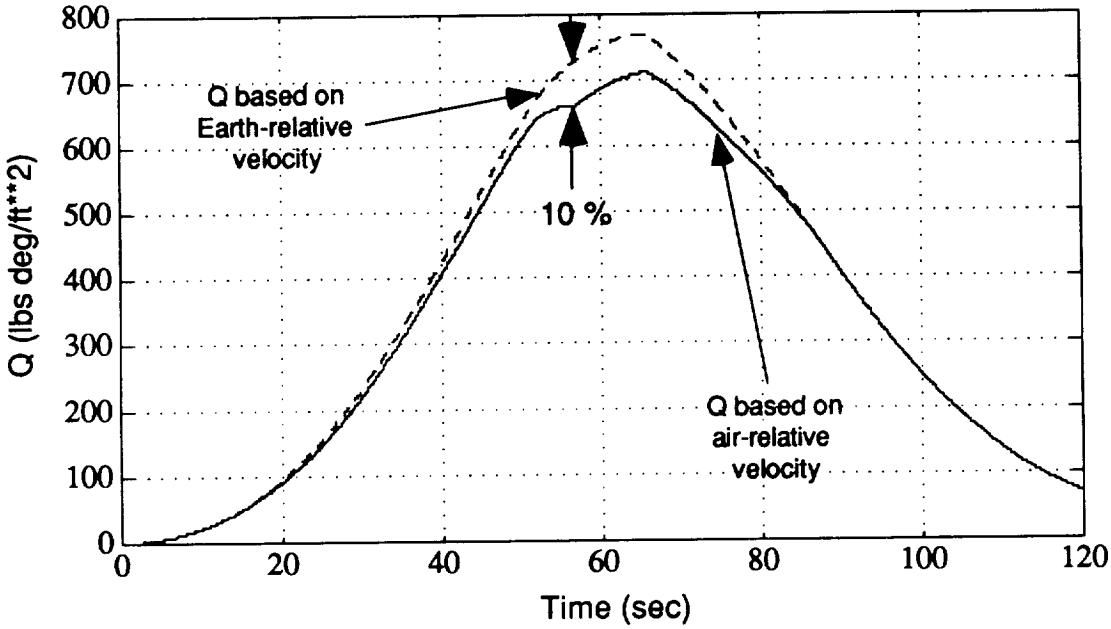

Figure 6.1 Q based on Earth -relative and air-relative velocities using tail wind Vandenberg #69 wind profile.

6.2 Estimation Procedure

The estimation of Q in this thesis is based (1) on a function of the density ρ in terms of the estimated altitude based on a standard atmospheric model and (2) on the use of the estimated angle of attack to improve the estimation of Q based on the earth-relative velocity. The relationships employed in (2) are derived below.

The quantities used to estimate the air-relative velocity are:

$\hat{\alpha} = (0, \hat{\alpha}_{pitch}, \hat{\alpha}_{yaw})$ = estimated angle of attack. For this thesis $\hat{\alpha}_{yaw}$ is assumed to be zero.

$\mathbf{V_E}$ = inertial earth relative velocity.

C_I^B = body to inertial transformation matrix

C_{LG}^I = inertial to local geographic reference frame transformation matrix.

An illustration of the vector relationships used to estimate $\mathbf{V_A}$ is shown in Figure 6.2. The estimation procedure is as follows:

1. Determine the vector $\hat{\mathbf{U}}_\alpha$, by the relationship:

$$\hat{\mathbf{U}}_\alpha = \text{unit } (0, \hat{\alpha}_{pitch}, \hat{\alpha}_{yaw}) \tag{6.2}$$

$\hat{\mathbf{U}}_\alpha$ is a unit vector normal to the plane formed by the roll axis of the vehicle and the air-relative velocity vector. For this thesis there is no yaw plane motion, therefore

$$\hat{\mathbf{U}}_\alpha = (0, 1, 0) \tag{6.3}$$

2. Using small angle approximations compute the total angle of attack from the relationship

$$\hat{\alpha}_{tot} = \sqrt{\hat{\alpha}_{pitch}^2 + \hat{\alpha}_{yaw}^2} \tag{6.4}$$

3. Determine the unit vector which defines the orientation of the air-relative velocity vector in the body frame using the following relationship based on Equations (6.2) and (6.4):

$$\hat{\mathbf{U}}_{A_{Body}} = \mathbf{X} \cos \hat{\alpha}_{tot} - \hat{\mathbf{U}}_{\alpha} \times \mathbf{X} \sin \hat{\alpha}_{tot} \tag{6.5}$$

where

$\mathbf{X}$= (1, 0, 0) is the direction of the roll axis in body coordinates.

Since the motion of the vehicle is assumed to be limited to the pitch plane, Equation (6.5) can be reduced to:

$$\hat{\mathbf{U}}_{A_{Body}} = \left(\cos \hat{\alpha}_{tot}, 0 , \sin \hat{\alpha}_{tot} \right) \tag{6.6}$$

4. Transform the unit vector $\hat{\mathbf{U}}_{A_{Body}}$ from the body frame to the local geographic coordinate frame by the relationship:

$$\hat{\mathbf{U}}_{A_{LG}} = C^{I}_{LG} C^{B}_{I} \hat{\mathbf{U}}_{A_{Body}} \tag{6.7}$$

where

C^{B}_{I} = a body frame to inertial frame transformation matrix and

C^{I}_{LG} = an inertial frame to local geographic frame transformation matrix.

The product of $C_{LG}^{I} C_{I}^{B}$ is equivalent to a single transformation from the body frame to the local geographic frame.

5. Transform the earth relative velocity vector, $\mathbf{V_E}$, from the body frame to the local geographic frame and unitize the resulting vector.

$$\widehat{V}_{E_{LG}} = C_{LG}^{I} C_{I}^{B} \widehat{V}_{E_{Body}} \tag{6.8}$$

$$\widehat{U}_{E_{LG}} = \frac{\widehat{V}_{E_{LG}}}{\left|\widehat{V}_{E_{LG}}\right|} \tag{6.9}$$

6. Assuming that the wind velocity is horizontal so that the difference between the vertical components of $\widehat{V}_E$ and $\widehat{V}_A$ is zero, determine the magnitude of $\widehat{V}_A$ using the relationship below:

$$\text{z component of} \left[\widehat{V}_E \widehat{U}_{E_{LG}} - \widehat{V}_A \widehat{U}_{A_{LG}}\right]^{\substack{\text{Local Geographic} \\ \text{Frame}}} =$$

$$(\text{z component of wind}) = 0 \tag{6.10}$$

Solving for $\widehat{V}_A$ in Equation (6.10) yields the final result:

$$\widehat{V}_a = \widehat{V}_E \left[\frac{\widehat{U}_{E_{LG}}}{\widehat{U}_{A_{LG}}}\right]_{\text{z component}} \tag{6.11}$$

This estimate of air-relative velocity magnitude is then used to compute dynamic pressure by the relationship

$$\hat{Q} = \frac{1}{2} \rho \hat{V}_A^2 \qquad (6.12)$$

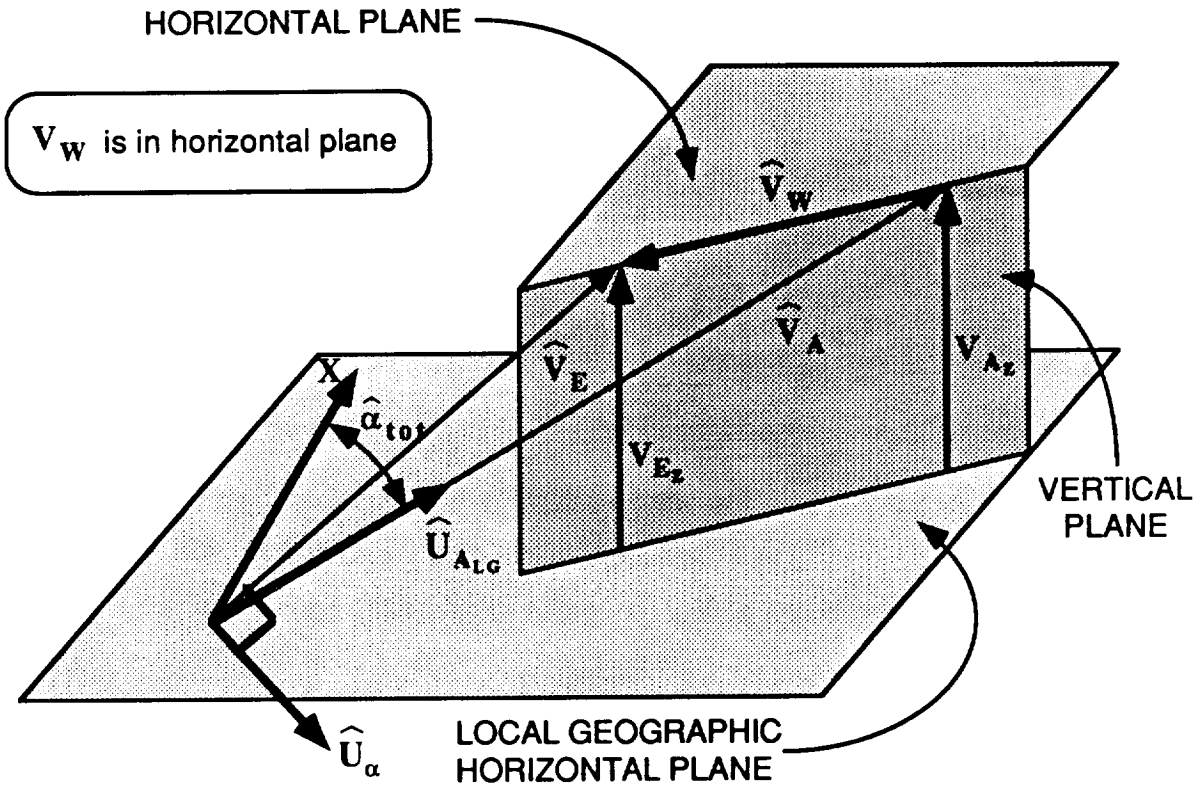

Figure 6.2 Vector relationships for air-relative velocity estimator.

6.3 Effects of Improved Air-Relative Velocity Estimation

Using the derivation from the previous section, two simulations were run to test the accuracy of the Q estimation procedure. Each test was begun at the end of Phase Two which corresponds to the point when acceleration direction/angle of attack steering begins. Two tail wind profiles, Vandenberg

#70 and Vandenberg #69, were chosen as worst cases. A discussion of the characteristics of each profile is presented in Appendix G.

Since dynamic pressure is proportional to the square of air-relative velocity, a measure of the effects of the air-relative velocity estimation on the estimated dynamic pressure can be obtained by computing a ratio (r) between the error in the square of estimated air-relative velocity, $e(\hat{V}_A^2)$, and the square of the true air-relative velocity, V_A^2. ie.

$$r = \frac{e\left(V_A^2\right)}{V_A^2} = \frac{\hat{V}_A^2 - V_A^2}{V_A^2} = \frac{\hat{V}_A^2}{V_A^2} - 1 \qquad (6.13)$$

A plot of the ratio, r, is given in Figures 6.3 and 6.4 for the two wind profiles.

The shape of both curves is very similar. Both show a large initial transient excursion followed by a "tailoff" period after 100 sec. in which the error in Q increases exponentially. The peak error in Q for both trials is approximately 2.25%. This error occurs at the beginning of the estimation procedure and is due to the initial transient errors associated with the angle of attack estimator. The reduction in accuracy in the estimate of dynamic pressure shown in the tailoff portion of the curves is a result of the degradation in the angle of attack estimate as the dynamic pressure approaches zero.

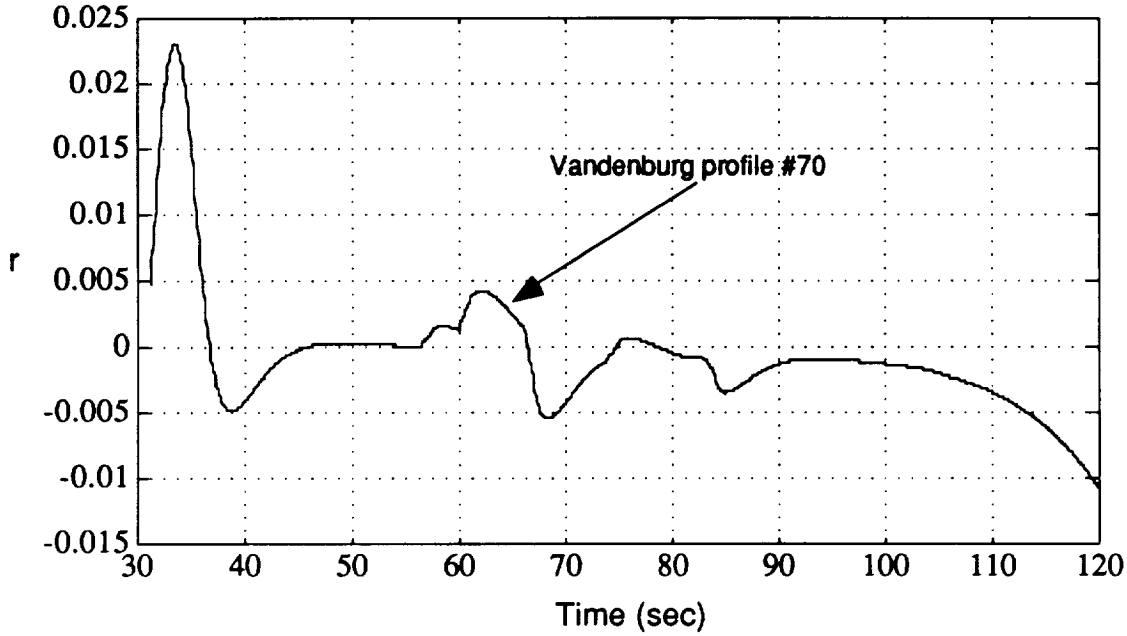

Figure 6.3 Error ratio relating estimated and true air-relative velocities for Vandenberg wind profile #70.

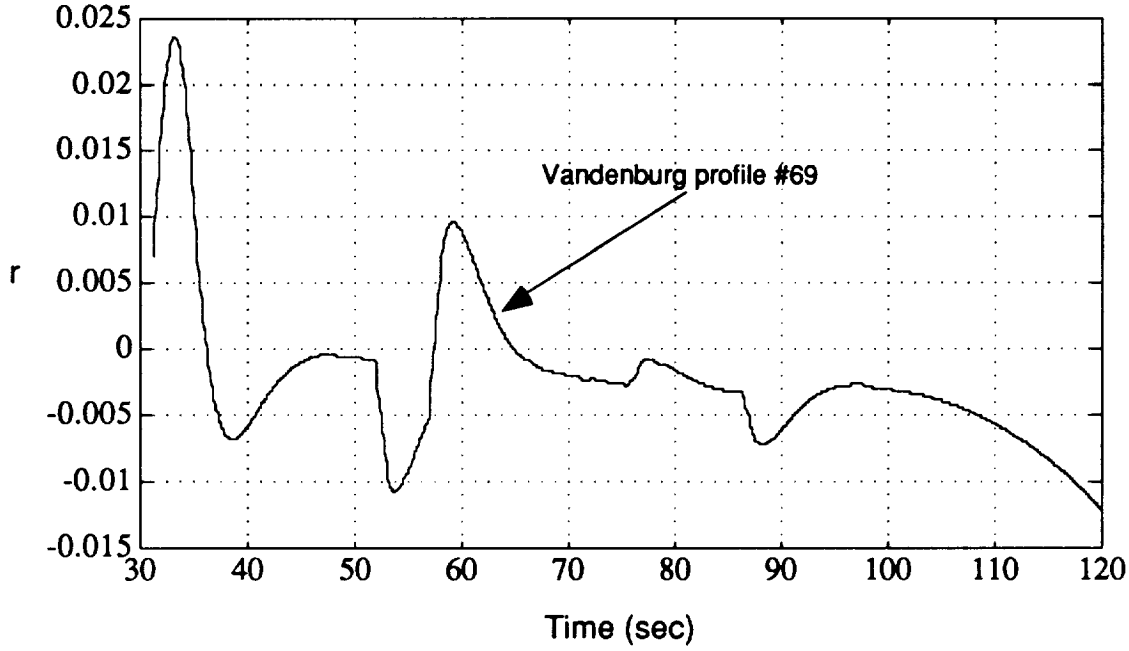

Figure 6.4 Error ratio relating estimated and true air-relative velocities for Vandenberg wind profile #69.

Chapter Seven

TRAJECTORY DESIGN

7.1 Introduction

The guidance commands issued for the first three phases of flight are specified prior to launch. These commands are functions of time and determine the desired path or trajectory that the vehicle will follow until the predictive-adaptive powered explicit guidance takes over. Deciding which trajectory is most appropriate for the given mission is the objective of the trajectory design process. The shape of the trajectory is determined by specified objectives and constraints. In general, the objective is an end condition and represents some desired terminal state. The constraint is a boundary that limits and/or restricts the shape of the trajectory. The $Q\alpha_{limit}$, for example, is one physical constraint on the trajectory.

In previous work by Michael Corvin for the single-stage-to-orbit (SSTO) Shuttle II vehicle, the primary mission objective was to maximize the terminal mass of the vehicle. By maximizing the terminal mass more fuel was available for any post boost maneuvers. In addition, by minimizing the required fuel needed to achieve orbit, payloads of higher weight could be lifted. This objective of maximizing the terminal mass is also assumed as the primary mission objective in this thesis.

As previously mentioned in Chapter 2, the trajectory of the vehicle is divided into four phases. The trajectory design program is employed to determine the parameters which define the shape of the trajectory in the first three phases. Phase Four employs a close to optimal predictive-adaptive guidance whose trajectory depends on the initial conditions provided by the combined effects of the first three phases.

The design program defines the trajectory shape in the first three phases in terms of

(1) The altitude the vehicle is to reach at the end of the vertical rise from the launch pad in Phase One.

(2) The function describing the desired attitude rate versus time in Phase Two.

(3) The parameters of an angle of attack profile defining the shape of the trajectory in Phase Three for the initial conditions provided by Phase Two.

Although the altitude required for the vertical rise of (1) can be varied to optimize the shape of the boost trajectory, it was decided to clamp this required altitude at 400 ft.

Two alternative time functions will be considered for the rapid pitchover of (2). These functions differ in their ability to determine the end conditions for this flight phase. The functions and their effects on end conditions will be discussed in Section 7.2.

Three parameters used to define the angle of attack profile of (3) will be described in Section 7.3. It should be noted that although it is convenient to design this portion of the trajectory for Phase Three in terms of the angle of attack profile, the in-flight guidance for this flight phase employs an estimated-acceleration-direction profile corresponding to the angle of attack profile as the command signal.

The trajectory design process involves iteratively adjusting the parameters and functions for the three initial phases to produce a maximum mass at the end of Phase Four. These adjustments must pay particular attention to (a) the need to produce final conditions for Phase Two that are consistent with the initial angle of attack and attitude rate desired at the beginning of Phase Three and (b) the need to have an acceleration direction at the end of Phase Three that approximately matches the acceleration direction that will be commanded by the predictive-adaptive guidance in Phase Four.

Section 7.4 provides a brief description of the predictive-adaptive guidance employed in Phase Four and of the orbital goals employed in the application of this guidance. The acceleration direction command supplied by this guidance is generated as a function of time by a "linear tangent guidance

law". The parameters of this law are automatically adjusted in flight by predictive-adaptive calculations which are designed to maximize the on-orbit mass.

Following the descriptions in Sections 7.2 to 7.4 of the selected parameters and Phase Four guidance that must be selected to define the trajectory, the potential sensitivities of overall trajectory characteristics to changes in selected parameters are explored in Section 7.5. These sensitivities are shown for a close to optimal no-wind trajectory based on the flight configuration in which the booster stage rides on top of the core stage.

The effects of winds upon the performance of the trajectory design process is then analyzed in Section 7.6. Six different head and tail wind cases are presented and compared on the basis of their respective on-orbit mass performance.

Employing the no-wind trajectory simulation of Section 7.5 it is shown in Section 7.7 that the in-flight guidance gives a closer fit to the prelaunch design trajectory if the acceleration-direction command stored for in-flight use is not based on the actual acceleration direction determined in the trajectory design simulation, but rather on the filtered estimate of this direction as determined in the design simulation.

Finally, in Section 7.8 the details of the automated computer routines that determine the parameters of the Phase Two trajectory functions for specified end conditions are presented.

It is important to bear in mind that although the trajectory design procedures are illustrated in terms of no-wind conditions in this chapter the actual prelaunch design computations must be based on the wind conditions that are measured just prior to launch. Simulation results presented in Chapter 8 employ an assumed wind profile for the prelaunch design simulation and employ another wind profile for the in-flight simulation. These two profiles are based on an actual pair of wind profiles measured at a potential launch sight by Jimspheres over an interval of 3 1/2 hours. The simulation results include consideration of a flight configuration in which the booster is under the core stage, which offers significant advantages for the case of a strong head wind.

The trajectory design process also requires the iterative adjustment of the Phase Two launch maneuver. This iterative adjustment ensures that the

transition from Phase Two, to Phase Three is "smooth". Two different launch profiles are presented, both of which are based on time functions of commanded pitch rate. A launch design program was written to automate the iterative launch design process.

The trajectory design technique is implemented using the main 6 DOF simulation. Although the parameters of the angle of attack profile were optimized, no attempt was made to show that this particular formulation of an alpha based trajectory was the best choice.

7.2 Phase Two Functionalization

The choice of the functionalization to generate the commanded attitude rate in Phase Two is a crucial part of the trajectory design process because of (1) the major role played by the rapid pitchover in Phase Two in determining the overall trajectory shape and (2) the importance of achieving a smooth transition from the rapid pitchover of Phase Two. This functionalization must provide the flexibility needed to achieve at the end of Phase Two the value of angle of attack required at the beginning of Phase Three, with a final attitude that is compatible with the rate required initially in Phase Three.

This thesis investigates two different launch profiles of commanded attitude versus time for Phase Two. Both algorithms employ a smooth sinusoidal pitch rate command. The first launch profile was developed by Michael Corvin for the single-stage-to-orbit Shuttle II launch system. This method is shown in Figure 7.1. The second launch profile illustrated in Figure 7.2 is similar to the first except that the commanded pitch rate is held constant throughout the second half of the maneuver. Two parameters are necessary to define the launch profiles. The first, T_{kick}, is the desired duration of Phase Two, and the second, Ω, is a rate equal to half the maximum pitch rate. Determination of these parameters is achieved by a launch design program which iteratively adjusts T_{kick} to obtain the desired end-of-maneuver state necessary for a smooth transition to Phase Three. A discussion of the automated launch design process is found in section 7.6.

The initial trajectory shaping studies were performed successfully using only the sinusoidal launch maneuver. However, although the profile provided a

smooth transition in angle of attack it was observed that during the transition from Phase Two to Phase Three the flight controller would command a large step in commanded nozzle deflection which produced a large increase in attitude rate. This large increase in pitch rate was required so that the vehicle could follow the initial constant angle of attack profile ($\alpha 1$) commanded in Phase Three. This sudden increase in pitch rate is undesirable for the following reasons:

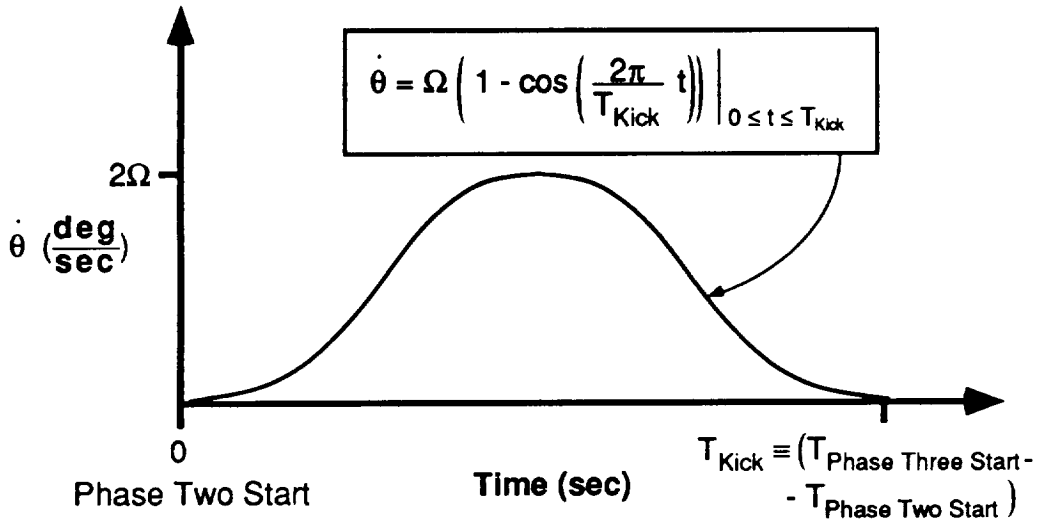

Figure 7.1 Phase Two command profile with sinusoidal pitch rate

(1) First, any large increases in commanded attitude rate could cause the core and booster nozzles to rate limit. (For the ALS it was decided to limit the nozzle rate to 10°/sec).

(2) Any large changes in the attitude of the vehicle adversely affects the performance of not only the angular rate and angular acceleration estimates, but also the angle of attack estimate.

To help remove the effects caused by the large change in commanded angular velocity, the new Phase Two launch profile described in Figure 7.3 was developed. This launch profile involves an initial sinusoidal pitch rate launch maneuver followed by a non-zero terminal pitch rate. The shape of this profile enables the launch designer to specify not only the terminal attitude and duration of Phase Two, but also the desired terminal attitude rate. Although this

adds a degree of freedom to the launch design process it does not further complicate the procedure for determining the suitable launch design parameters. A detailed description of this launch maneuver is found in section 7.6.

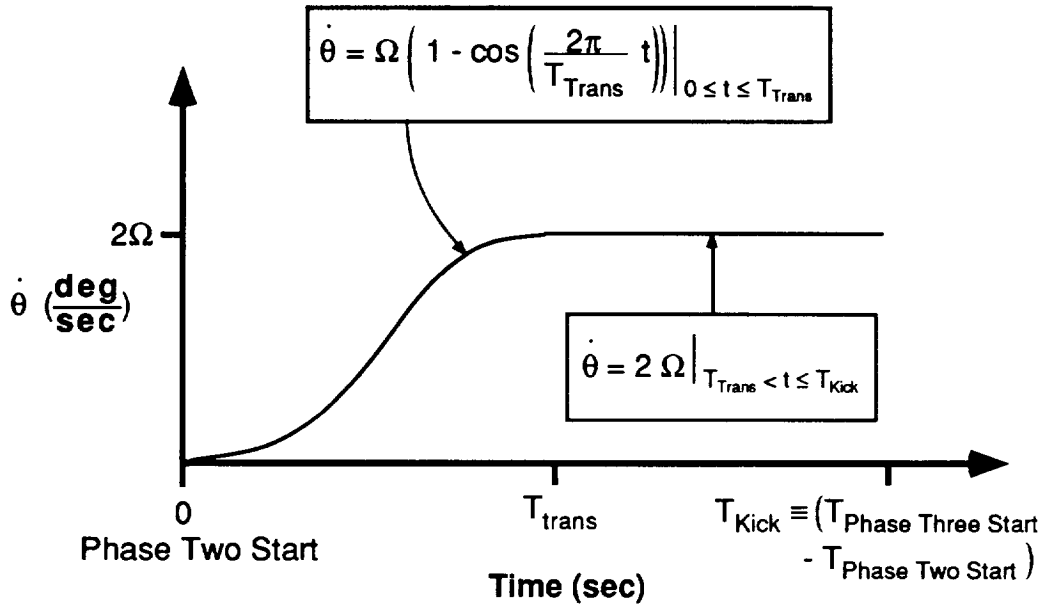

Figure 7.2 Phase Two command profile with constant terminal pitch rate.

7.3 Phase Three Functionalization

As illustrated in Figure 7.3 the angle of attack profile for Phase Three is defined in terms of the following three parameters that may be adjusted within vehicle design constraints to maximize the on-orbit mass:

(1) An initial angle of attack, α_1, which is maintained until the product $Q\alpha_1$ reaches a specified limit.

(2) A $Q\alpha_{limit}$ which is followed until the resulting α (with decreasing Q) increases to a specified final value.

(3) A final value of angle of attack, $\alpha 2$.

The degree to which these three parameters can be varied to optimize the boost trajectory is limited by

(1) The degree of flexibility in Phase Two to produce the desired initial conditions in Phase Three

(2) The required margin of safety between the $Q\alpha_{limit}$ and the vehicle structural limit on $Q\alpha$.

(3) The need to produce a terminal α that is compatible with the initial guidance commands generated in Phase Four.

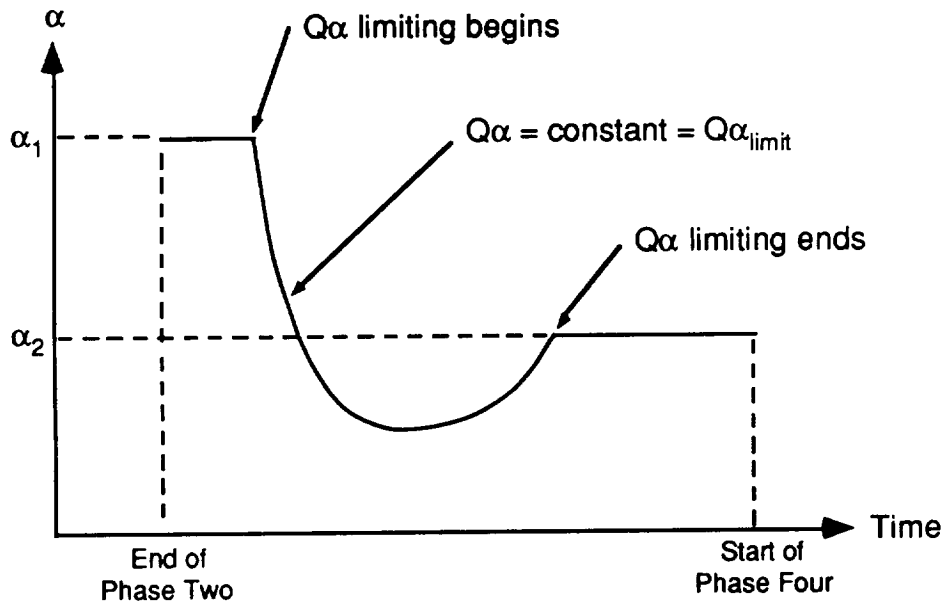

Figure 7.3 Trajectory shaping angle of attack profile.

The trajectory shape in and beyond Phase Three is strongly influenced by the depth of the $Q\alpha$ bucket in Figure 7.3, as determined by the selection of the $Q\alpha_{limit}$ for the trajectory design. The value of this limit must be well below the assumed structural limit of 3,500 lbs deg/ft^2. For the ALS vehicle a margin between this structural limit and the trajectory design limit is required so that the vehicle will have the ability to tolerate transient excursions in $Q\alpha$ during periods of $Q\alpha$ limiting. Even in no-wind simulations, $Q\alpha$ typically exceeds the $Q\alpha_{limit}$ by as much as 80 lbs deg/ft^2. Consequently, to provide a safe design margin it was decided to set $Q\alpha_{limit}$ at 3,000 lbs deg/ft^2.

7.4 Predictive-Adaptive Guidance for Phase Four

The predictive-adaptive Powered Explicit Guidance (PEG) program is employed both in flight and in the trajectory design calculations for Phase Four. In both cases the guidance program is employed every six seconds to adjust the parameters of a "linear tangent guidance law" that generates the commanded acceleration direction as a function of time. This guidance law is expressed as

$$\tan \theta_{Ac} = K_o + (t - t_o) K_1$$

where θ_{Ac} is the commanded acceleration angle and K_o, K_1, and t_0 are the adjusted parameters. The guidance program solves analytical relationships to predict the amount of propellant required to reach specified orbital conditions from the current vehicle state. Using this analytical prediction the program adjusts the linear tangent function parameters to minimize the propellent required, and thereby maximize the on-orbit mass.

In both the trajectory design calculations and the in-flight guidance calculations the analytical predictions of PEG are simplified by neglecting the effects of the aerodynamic forces. Since Phase Four is initiated in the upper atmosphere this simplifying assumption results in small prediction errors in the beginning of Phase Four which steadily reduce as the vehicle emerges from the atmosphere. For the purposes of this thesis investigation it was decided to simulate the response of the vehicle to PEG only up to the point of staging in both the cut-and-try design simulations and the final in-flight simulations for performance evaluation. The analytical relationships of PEG are then used to predict the on-orbit mass resulting from the post-staging boost trajectory. In his Shuttle II studies, Corvin found that the use of such analytical predictions, in lieu of actual simulations to the end of boost, did not significantly degrade the trajectory optimization.

Along with the predicted on-orbit mass the PEG algorithm also calculates the commanded attitude change at the transition to Phase Four. This variable was useful since it provided insight into the shape of the trajectory. Based on experience, the magnitude of the commanded attitude change indicated whether the trajectory was too low or high with respect to the sought after optimal one. Generally, those trajectories which had minimum commanded attitude changes at PEG also had correspondingly high values of terminal on-orbit mass.

The orbital objective used in all PEG calculations in this thesis is based on the following two conditions

(1) The perigee of the vehicle is 80 Nmi. and

(2) The velocity (horizontal) of the vehicle is large enough to achieve an apogee of 150 Nmi. This velocity is determined from the relationship

$$V_{orbit} = \left[\frac{2\mu \left(\frac{r_{ap}}{r_{pe}} \right)}{r_{ap} + r_{pe}} \right]^{1/2}$$

where μ is the gravitational constant , r_{ap} is the apogee, and r_{pr} is the perigee.[1]

7.5 Trajectory Parameter Sensitivity Analysis

The effects of adjusting the various design parameters for both Phase Two and Three are illustrated in Figures 7.4 through 7.19. For each design parameter, plots of flight path angle (γ) and attitude (θ) are provided. Each plot contains three curves. A solid line represents the launch design profile for the

---

[1] Battin, Richard H., An Introduction to the Mathematics and Methods of Astrodynamics.1987. New York: AIAA Educational Series. (pp 116).

selected "optimal" value of the given launch design parameter. Dashed curves represent the the response of the vehicle to small perturbations in each of the launch design parameters. The results of this perturbation analysis are also shown in Table 7.1. For each separate launch maneuver an "optimal" set of trajectory design parameters was first obtained. These results are presented in italics and are listed as "Nominal" in the Run Number column. In Table 7.1 Launch Profile #1 corresponds to the sinusoidal launch maneuver illustrated in Figure 7.1, while Launch Profile #2 represents the non-zero terminal pitch rate launch maneuver shown in Figure 7.2. For each simulation the terminal on-orbit mass (as predicted by the PEG algorithm), as well as the pitch attitude change at PEG was also recorded. In addition, a sensitivity quotient which measured the effect of perturbations in the launch design parameters to losses in the predicted optimal on-orbit mass was also calculated. This performance measure was obtained by using the general expression

$$S.Q. = \frac{[\text{On-orbit Mass}]_{\text{Nominal}} - [\text{On-orbit Mass}]_{\text{Perturbation}}}{[\text{Trajectory Parameter}]_{\text{Nominal}} - [\text{Trajectory Parameter}]_{\text{Perturbation}}} \qquad (7.1)$$

where the Trajectory Parameter is either θ_f, $\dot{\theta}_f$, $\alpha 1$, $\alpha 2$, or the $Q\alpha_{limit}$.

The Nominal run for each launch profile was based on a minimization of the change in pitch attitude at transition to PEG. As shown in Table 7.1 most trials which had larger values of "Δ pitch" at PEG also had smaller predicted terminal on-orbit masses. The process of minimizing Δ pitch at PEG, however, did not always guarantee an optimal on-orbit mass. In one case (Run Number 14) an additional 6 slugs of mass was achieved despite a larger transitional value of Δ pitch.

For both launch profiles the variation of the $Q\alpha_{limit}$ had little effect upon the shape and predicted on-orbit mass of the trajectory. This was also true for variations in $\alpha 1$. For $\alpha 2$ it was noted that small negative deviations from the nominal case caused the vehicle to pitch over rapidly towards the latter half of Phase Three. Consequently, the required attitude change at transition to PEG was quite large for both launch maneuvers (14.1° for Launch Phase 1 and 15.2° for Launch Phase 2) and the resulting terminal mass was less than optimal as demonstrated by the high sensitivity quotients.

In addition to the variables responsible for defining the angle of attack profile ($\alpha 1$, $\alpha 2$, $Q\alpha_{limit}$), the effects caused by perturbations in the launch maneuver parameters (θ_f, $\dot{\theta}_f$) was also investigated. For the sinusoidal launch maneuver, the desired terminal launch attitude proved to be the most sensitive variable. For run 4, for example, a variation of only -0.06° from the nominal case caused the vehicle to pitch over rapidly prior to entering Phase Four.

For launch profile 2, the desired terminal attitude rate provided the largest changes in the terminal mass. In one instance a variation of only -0.1°/sec caused the predicted terminal mass to decrease by 97 slugs from the nominal case. However, despite this large sensitivity quotient the effect on the shape of the trajectory was minimal as evidenced by the small commanded change in pitch attitude at PEG transition.

7.5.1 Sensitivity Analysis Plots

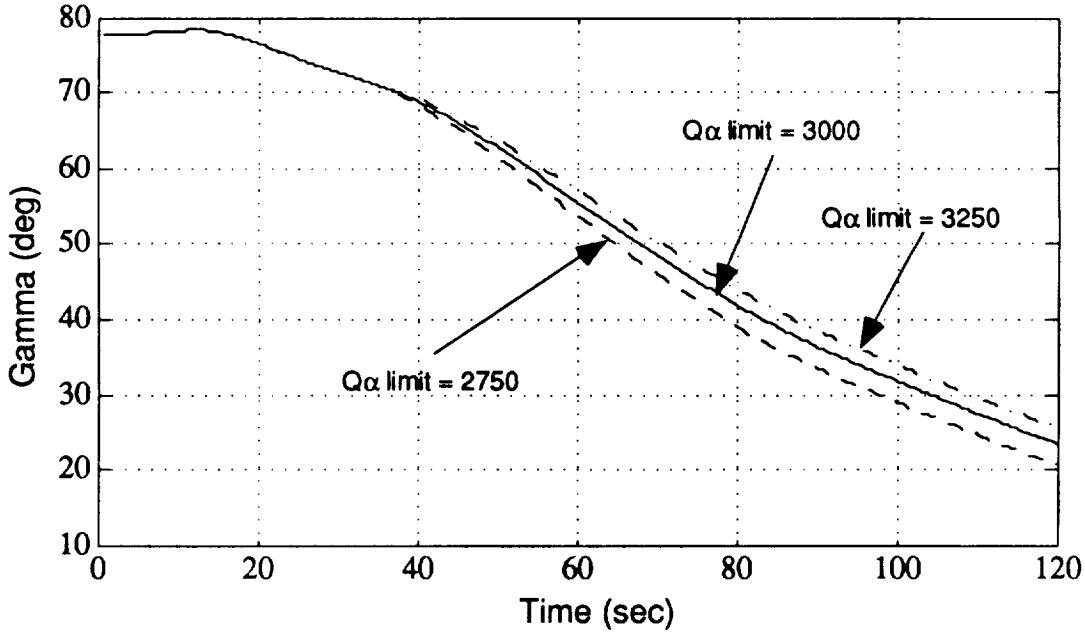

Figure 7.4 Sensitivity of gamma to Qα limit for a non-zero terminal pitch rate maneuver.

Run Number	Launch Profile	θ_f (deg)	$\dot{\theta}_f$ (deg / sec)	α_1 (deg)	α_2 (deg)	$Q\alpha_{limit}$ (lb deg/ ft^2)	Terminal Mass (slugs)	Δ pitch at PEG (deg)	Sensitivity Quotient S.Q.
Nominal	*1*	*80*	-	*11.1*	*4.5*	*3000*	*12167*	*0.48*	-
1	1	80	-	11.1	4.5	2750	12164	4.72	.012
2	1	80	-	11.1	4.5	3250	12153	-3.46	-.056
3	1	83	-	11.1	4.5	3000	12122	-6.95	-15.0
4	1	79.94	-	11.1	4.5	3000	*	*	*
5	1	80	-	10.9	4.5	3000	12143	-4.48	120.0
6	1	80	-	11.3	4.5	3000	12153	7.93	-70.0
7	1	80	-	11.1	2.5	3000	12039	14.05	64.0
8	1	80	-	11.1	6.5	3000	12156	-6.60	-5.5
Nominal	*2*	*84.5*	*-0.5*	*9.5*	*4.0*	*3000*	*12159*	*0.32*	-
9	2	84.5	-0.5	9.5	4.0	2750	12159	5.33	-
10	2	84.5	-0.5	9.5	4.0	3250	12141	-3.48	-.072
11	2	81.5	-0.5	9.5	4.0	3000	12160	6.59	-.333
12	2	87.5	-0.5	9.5	4.0	3000	12114	-6.42	-15.0
13	2	84.5	-0.5	9.3	4.0	3000	12142	-3.06	85.0
14	2	84.5	-0.5	9.7	4.0	3000	12165	4.08	30.0
15	2	84.5	-0.5	9.5	2.0	3000	12000	15.21	79.5
16	2	84.5	-0.5	9.5	6.0	3000	12139	-8.06	-10.0
17	2	84.5	-0.4	9.5	4.0	3000	12062	-10.87	-970.0
18	2	84.5	-0.6	9.5	4.0	3000	12100	-7.82	590.0

Table 7.1 Trajectory shaping results. * Trajectory did not reach PEG.

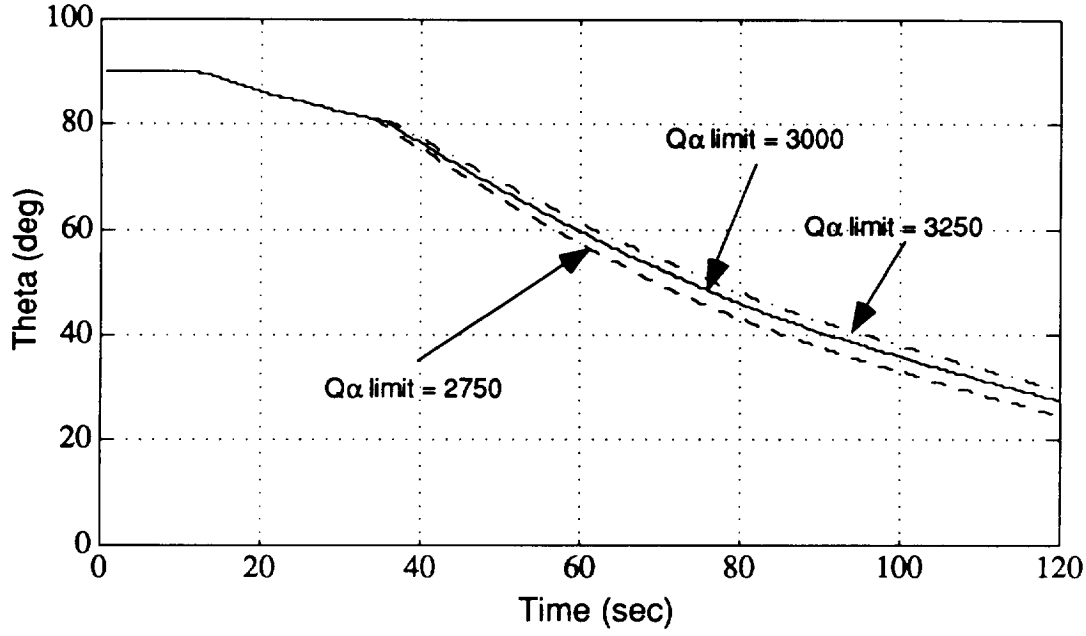

Figure 7.5 Sensitivity of theta to Qα limit for a non-zero terminal pitch rate maneuver.

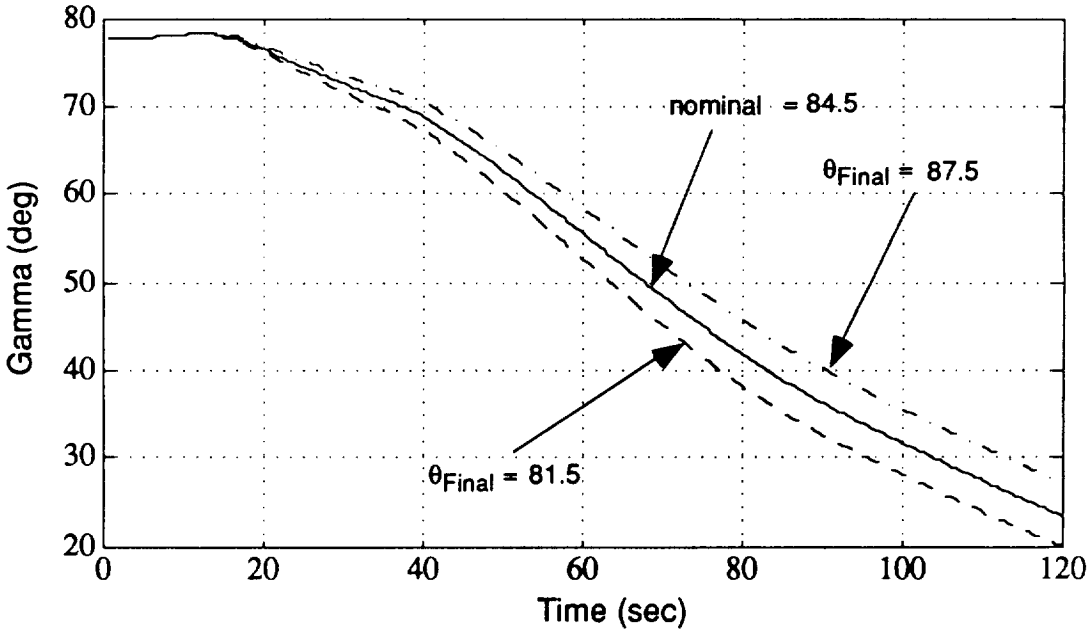

Figure 7.6 Sensitivity of gamma to terminal launch theta for a non-zero terminal pitch rate maneuver.

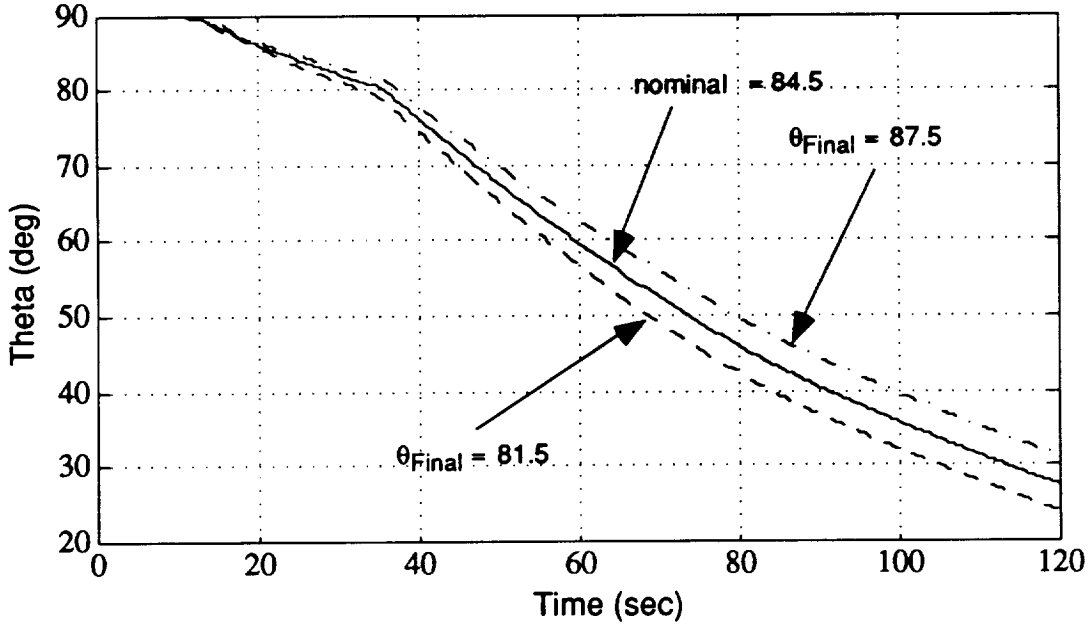

Figure 7.7 Sensitivity of theta to terminal launch theta for a non-zero terminal pitch rate maneuver.

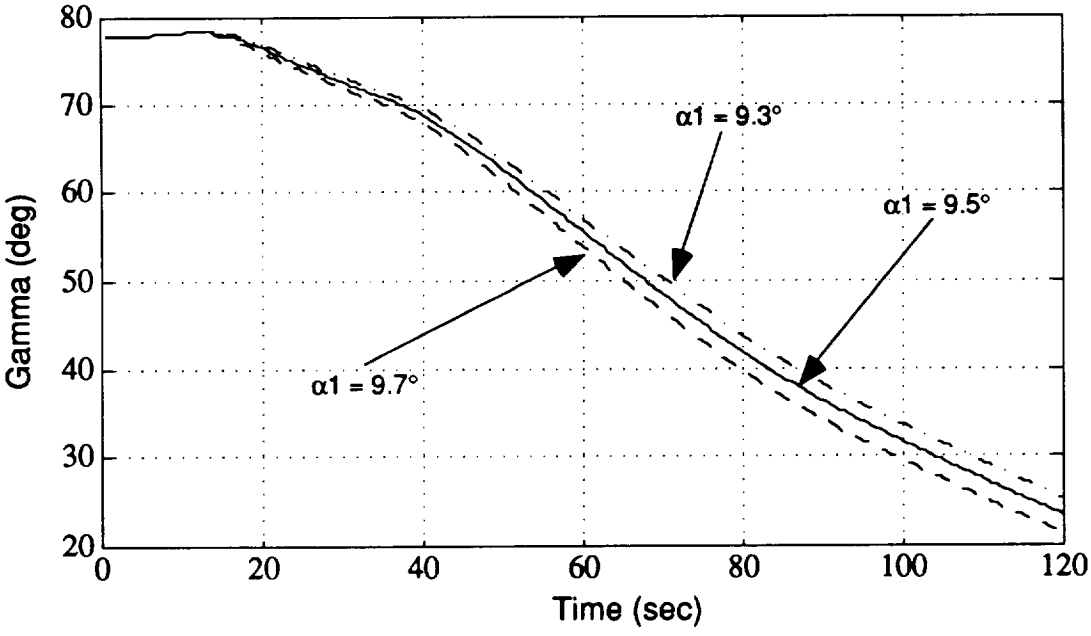

Figure 7.8 Sensitivity of gamma to α1 for a non-zero terminal pitch rate launch maneuver.

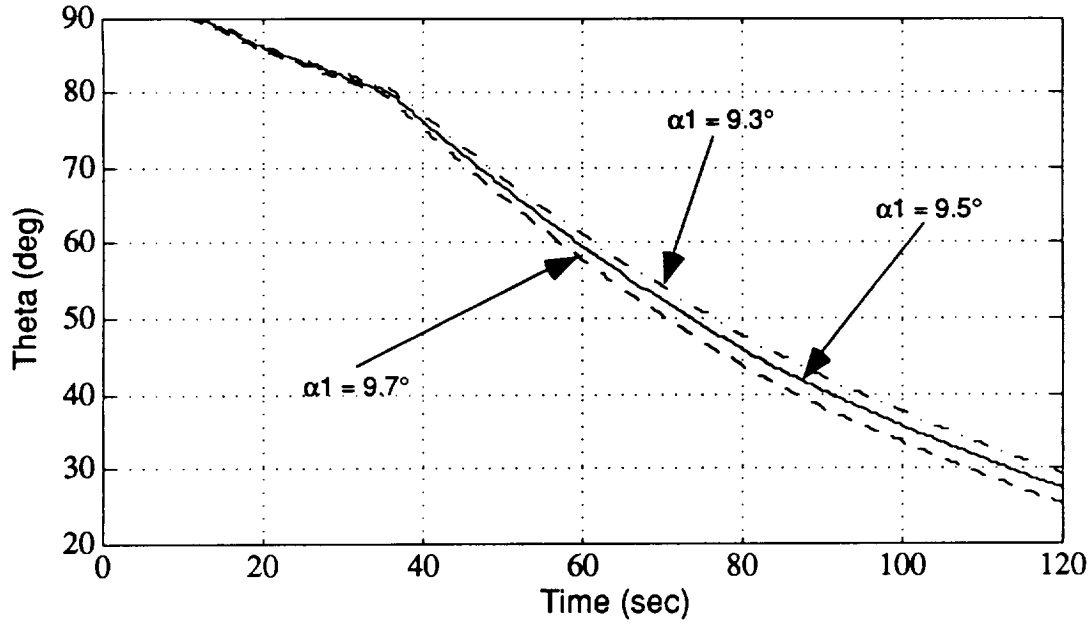

Figure 7.9 Sensitivity of theta to α1 for a non-zero terminal pitch rate launch maneuver.

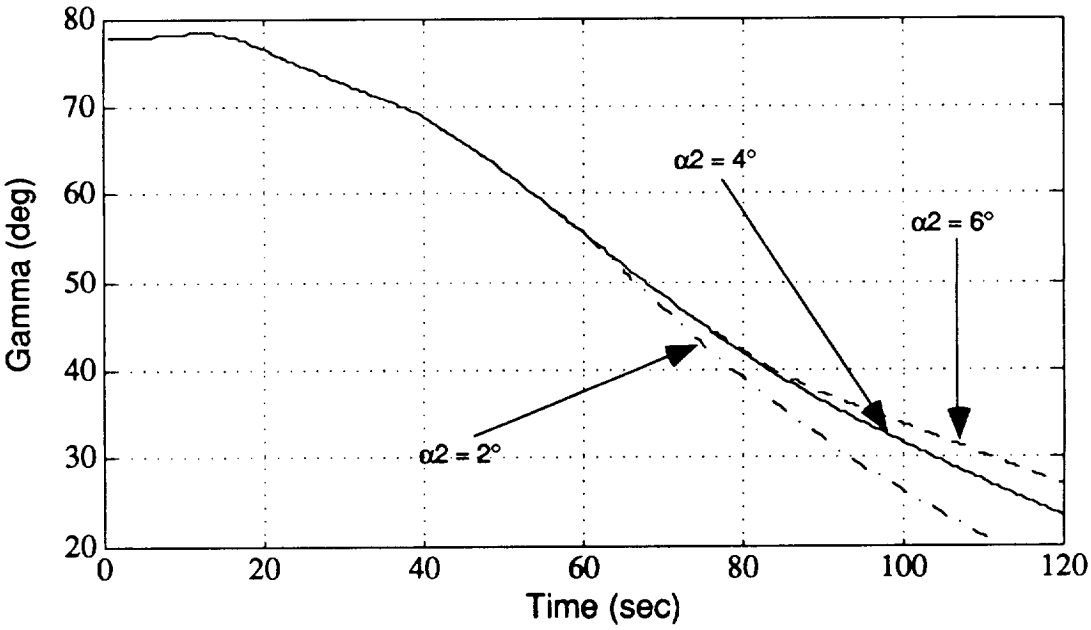

Figure 7.10 Sensitivity of gamma to variations in α2 for a non-zero terminal pitch rate launch maneuver.

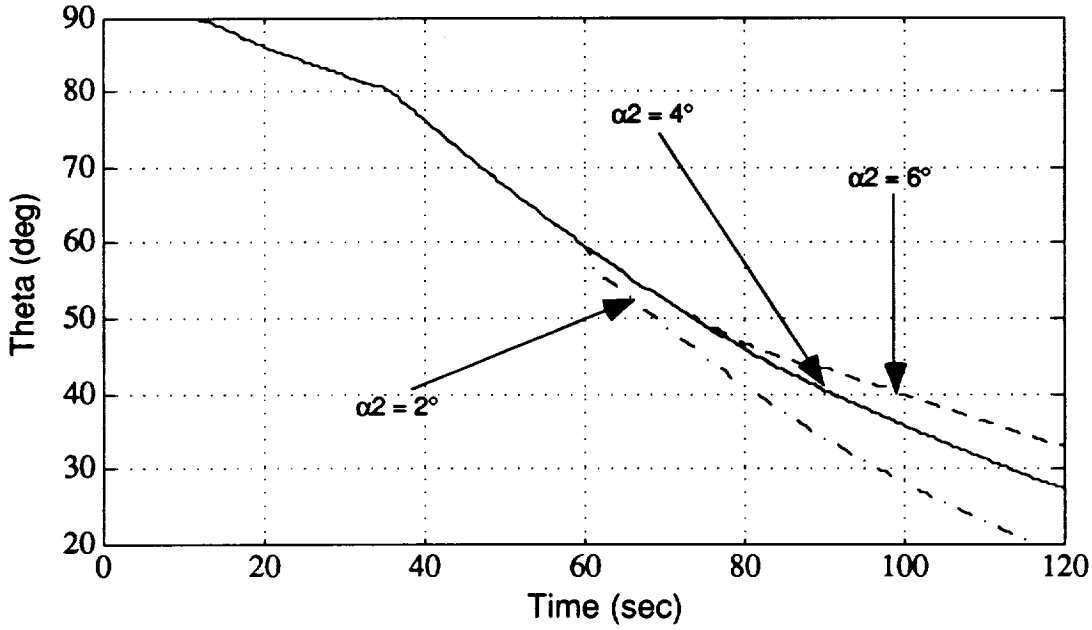

Figure 7.11 Sensitivity of theta to variations in $\alpha 2$ for a non-zero terminal pitch rate maneuver.

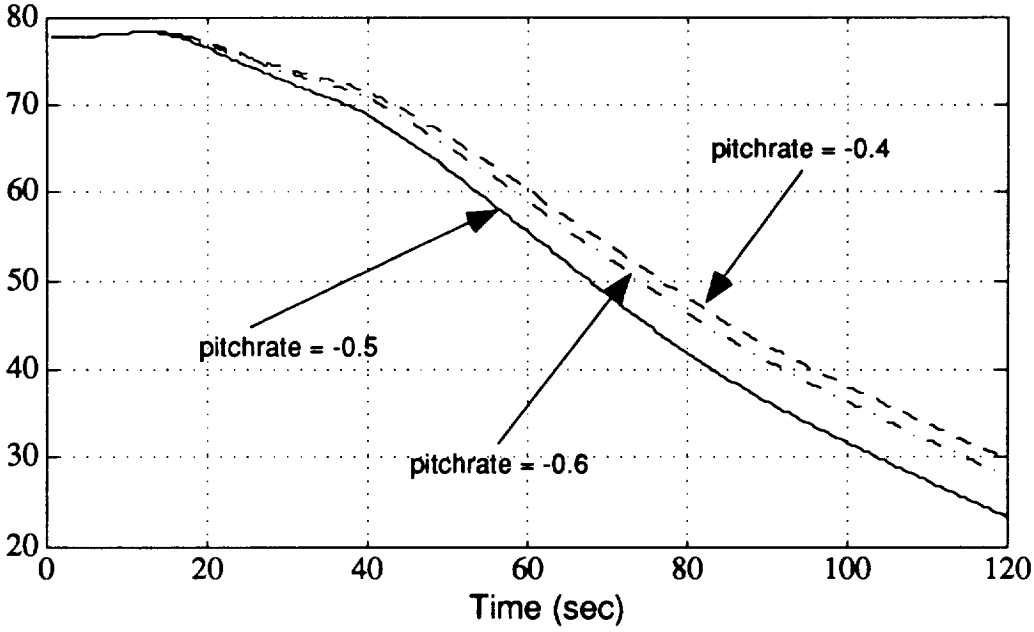

Figure 7.12 Sensitivity of gamma to variations in terminal pitch rate for a non-zero terminal pitch rate maneuver.

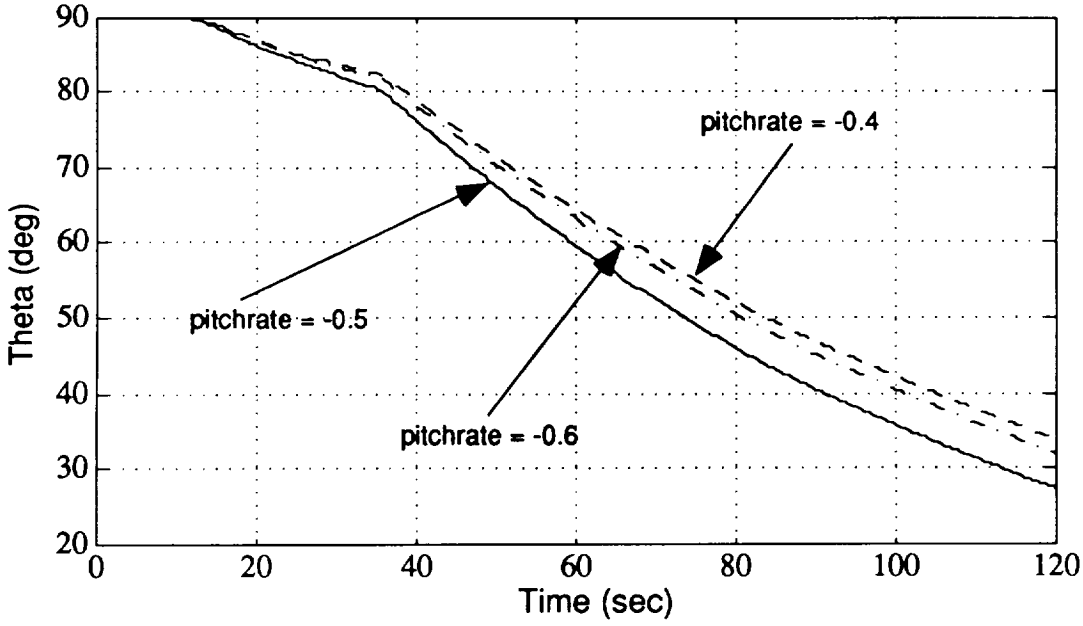

Figure 7.13 Sensitivity of theta to variations in terminal pitch rate for a non-zero terminal pitch rate maneuver.

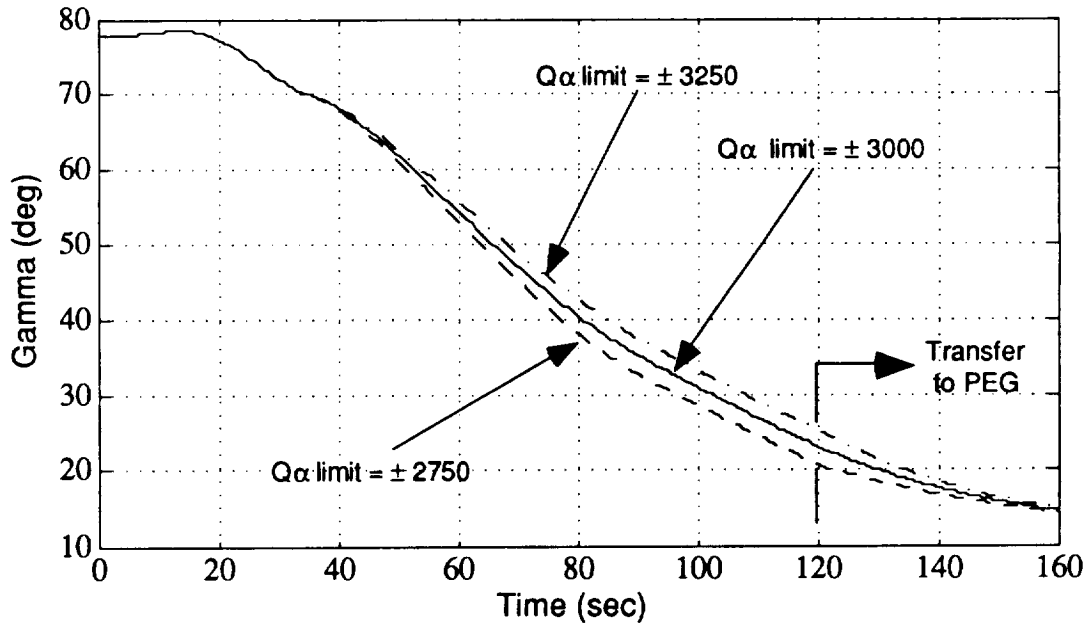

Figure 7.14 Sensitivity of gamma to Qα limit for a sinusoidal pitch rate maneuver.

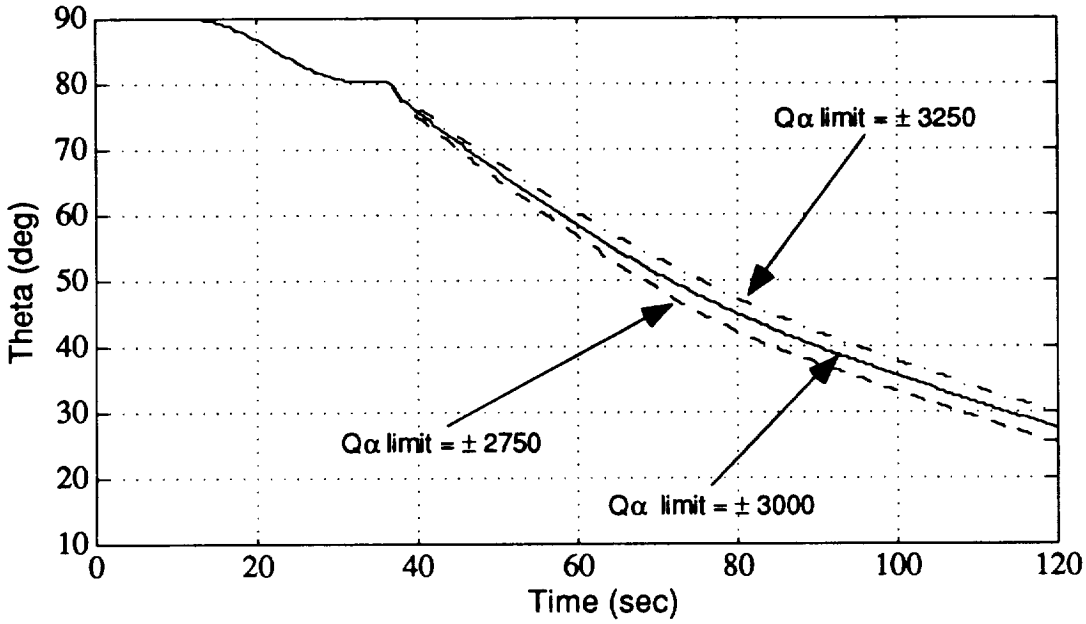

Figure 7.15 Sensitivity of theta to Qα limit for a sinusoidal pitch rate maneuver.

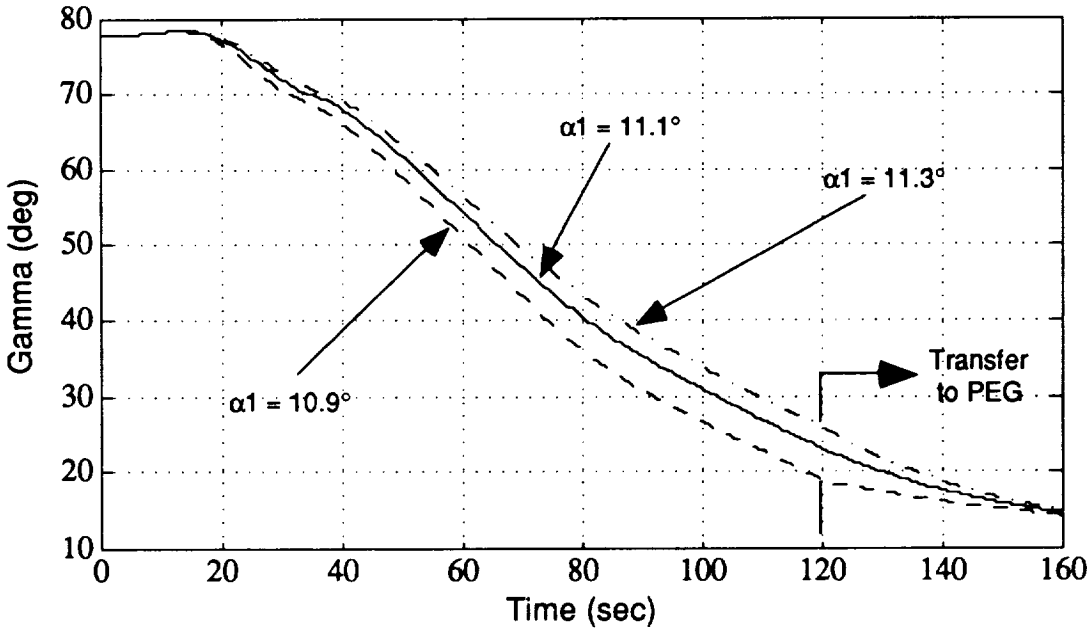

Figure 7.16 Sensitivity of gamma to α1 for a sinusoidal pitch rate launch profile.

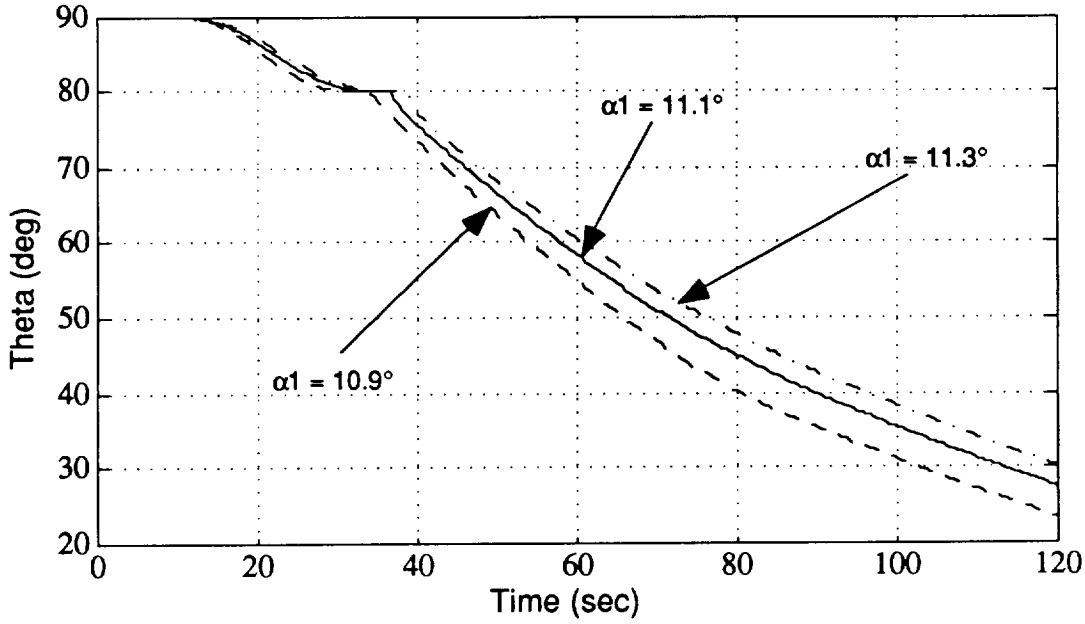

Figure 7.17 Sensitivity of theta to α1 for a sinusoidal pitch rate launch profile.

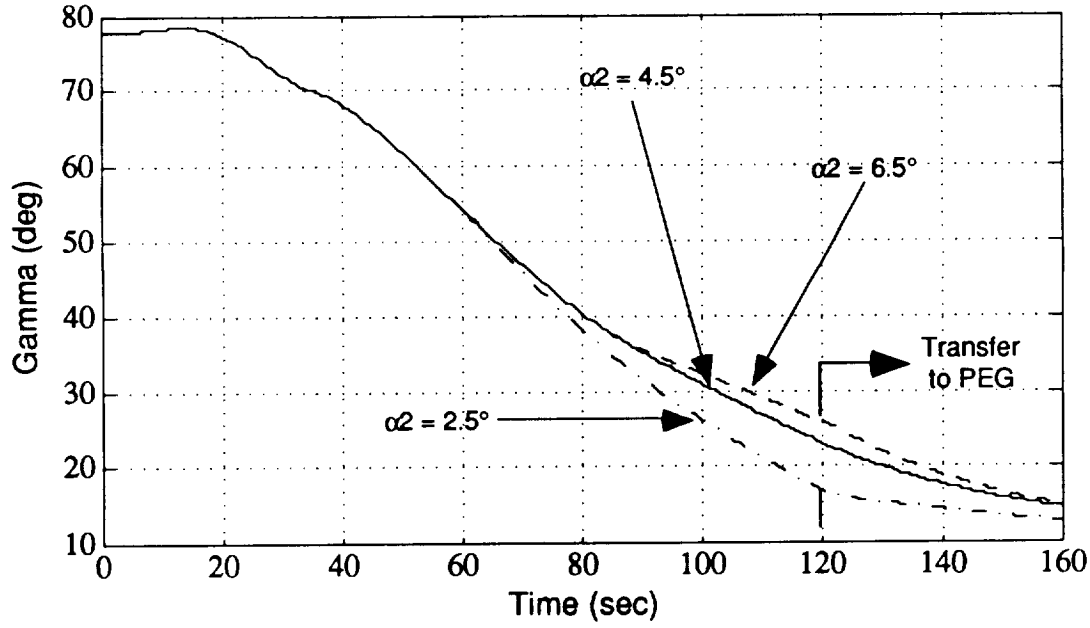

Figure 7.18 Sensitivity of gamma to α2 for a sinusoidal pitch rate launch maneuver.

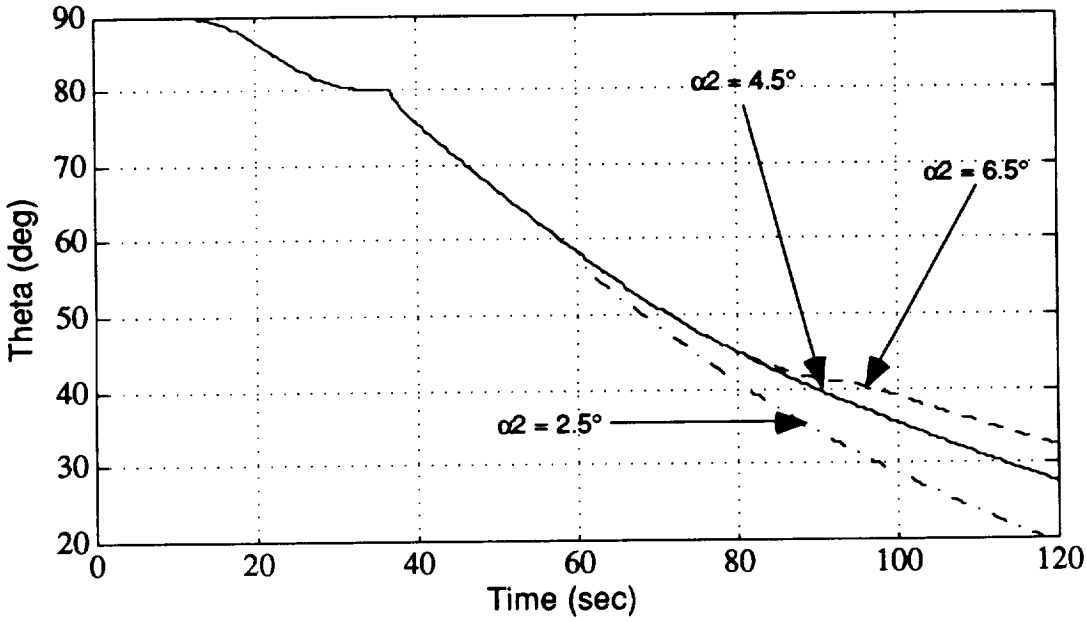

Figure 7.19 Sensitivity of theta to α2 for a sinusoidal pitch rate launch maneuver.

7.6 Effect of Winds on Trajectory Design

In Section 7.5 the effects of adjusting the launch design parameters upon the shape and performance of the trajectory in a no-wind environment was analyzed. In order to better understand the effects of winds upon the trajectory design, a different study was conducted in which the on-orbit mass of the vehicle was optimized in a wind environment. As shown in Table 7.2, six different cases were simulated for trajectories ending at staging (≅ 160 sec after ignition). For each case a different combination of wind speed and direction was employed. The wind speed was determined by scaling the stored wind magnitude of the Vandenberg #69 profile (see Appendix G). In Table 7.2 the scaling is represented as a percentage of the total wind magnitude. Because this thesis study is limited to the pitch plane, only head and tail wind directions were simulated.

For each case a separate set of optimal launch design parameters corresponding to the sinusoidal launch maneuver was first obtained. The on-

orbit mass of the vehicle was optimized by adjusting the launch design parameters such that the change in pitch attitude at the transition to PEG was minimized. The prediction of on-orbit mass was determined by the PEG algorithm at staging. As shown in Table 7.2 the required attitude, θ_f, and angle of attack, $\alpha 1$, are larger for the head wind cases. The larger angle of attack values are primarily due the contribution of winds, while the higher attitude values are necessary to provide the vehicle with a loftier initial trajectory since at later times (during $Q\alpha$ limiting) the trajectory of the vehicle is depressed.

In addition to having a significant impact upon the chosen optimal launch design parameters, the magnitude and direction of winds also effects the on-orbit mass of the vehicle. As shown in Table 7.20 larger tail winds increased the on-orbit mass of the vehicle. Comparing the two 100% head and tail wind cases it can be seen that the on-orbit mass of the vehicle increased by 71.4 slugs when flying with a tail wind. In addition, the on-orbit mass is linearly correlated to the wind magnitude. This is illustrated in Figure 7.20 where the on-orbit mass is plotted against the scaled wind magnitude.

Wind Profile Magnitude (% of #69)	Wind Profile Direction	θ_f (deg)	$\alpha 1$ (deg)	$\alpha 2$ (deg)	Δ pitch @ PEG (deg)	Mass On-orbit (slugs)
100	Head Wind	87.95	15.30	4.0	0.12	12121.1
60	Head Wind	85.60	13.70	4.0	0.27	12137.9
40	Head Wind	84.90	12.80	4.0	0.13	12145.1
100	Tail Wind	82.75	5.75	4.2	0.00	12192.5
60	Tail Wind	82.75	8.00	4.2	0.04	12182.3
40	Tail Wind	82.95	9.00	4.2	-0.09	12175.7

Table 7.2 Effect of winds on trajectory parameters and on-orbit mass.

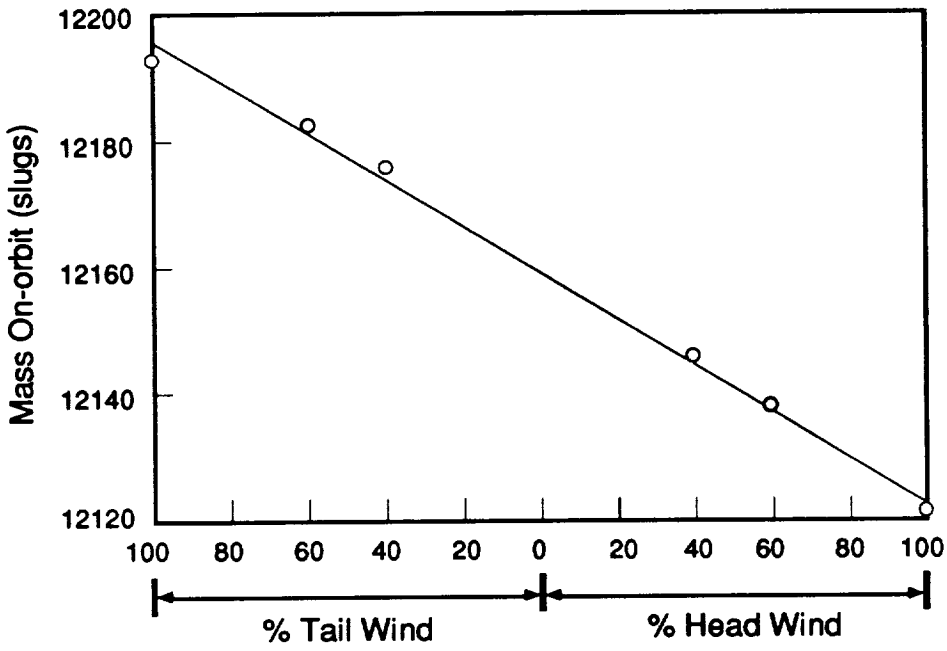

Figure 7.20 Effect of tail and head winds on the predicted on-orbit mass.

7.7 Stored Acceleration-Direction

The trajectory design process is used to generate and store acceleration-direction profiles which are then followed in simulations of the actual ascent. These profiles are stored as functions of time. Early in this study, the inertial acceleration of the vehicle (neglecting gravity) as calculated by the environment program, was the stored parameter. During actual simulations this stored inertial acceleration direction was compared to the filtered acceleration direction estimate to produce an acceleration direction error. The filtering present in the estimated acceleration direction feedback loop is necessary not only to reduce the effects of quantization in the IMU signals, but also to improve the control stability of the system caused by the regenerative feedback of estimated acceleration direction. A disadvantage of the filtering process, however, is the additional lag that is introduced into the steering loop. As a result of this lag, the trajectory followed by the acceleration-direction algorithm is different than the trajectory stored by the trajectory design simulation. This difference is illustrated in Figure 7.21 where the commanded acceleration

direction is plotted along with the filtered acceleration direction estimate as well as the actual acceleration direction of the vehicle. As shown the filtered acceleration-direction lags the commanded acceleration-direction by a considerable amount. To eliminate the errors associated with the additional lag, it was decided to store the filtered acceleration-direction during the trajectory design simulations instead of the actual inertial acceleration-direction.

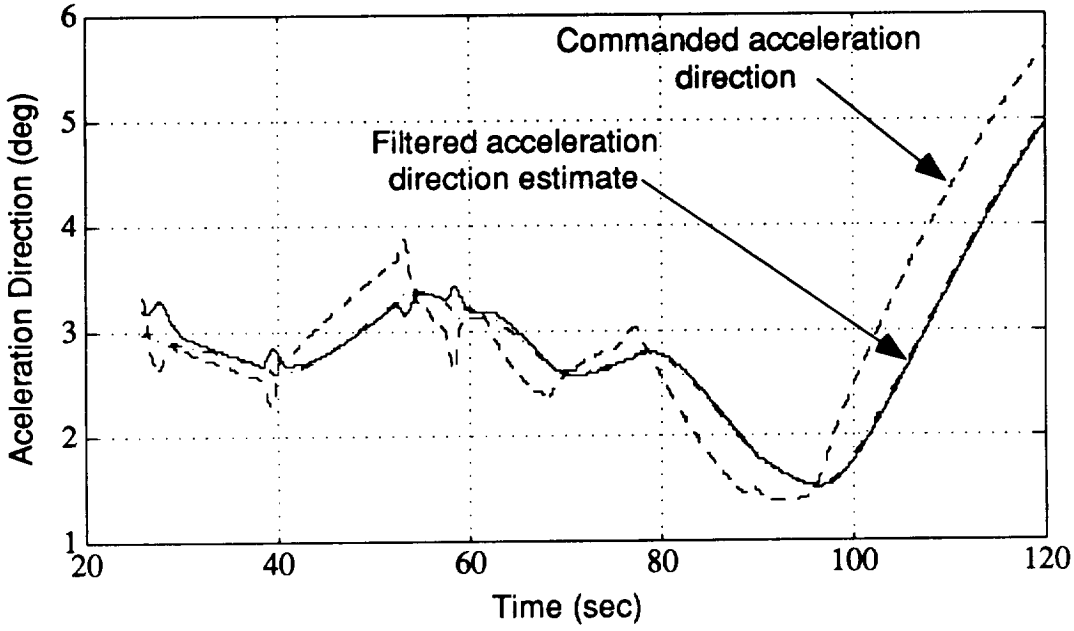

Figure 7.21 Commanded and filtered acceleration direction profile in body coordinates.

7.8 Launch Maneuver Design

7.8.1 General Description

The goal of Phase Two is to orient the vehicle to the correct state for a smooth transition to Phase Three. During the pitchover maneuver the vehicle is commanded according to a time varying pitch rate schedule. The objective of the launch phase is to orient the vehicle to the correct attitude and velocity

vector direction for Phase Three steering. For the sinusoidal launch maneuver the two parameters, T_{kick} and Ω, are used to define the maneuver. These variables, with the addition of T_{trans}, also define the sinusoidal launch maneuver with non-zero terminal pitch rate (see Figures 7.2 and 7.3). The desired end of launch state is described either in terms of θ and α, or in terms of θ, α and $\dot{\theta}$. To determine the values of T_{kick}, Ω, and T_{trans}, the launch maneuver design routine conducts a series of simplified launch simulations. These simulations are based on a simplified two degree of freedom model which is summarized in section 7.4.2.

The launch design program employs a numerical minimization of the error between the desired angle of attack, and the angle of attack estimated by the launch design simulation. The length of the launch maneuver, T_{kick}, is used as the free variable. The launch maneuver algorithm iteratively adjusts the length of the maneuver, T_{kick}, to minimize the error in the angle of attack at the end of launch. The minimization process uses a bisection search based on the "golden ratio" bisection factor[1]. The other launch parameters Ω, and T_{trans}, are analytically related to the chosen T_{kick} and $\dot{\theta}$.

7.8.2 Launch Maneuver Simulation

A vehicle description of the quantities used to define the launch design simulation is illustrated in Figure 7.22. The initial conditions used for the launch simulation are based on the true terminal state of the vehicle at the end of Phase One. For this model it is assumed that the rate of mass loss is a constant. An accurate functionalization of thrust versus time for the thrust developed by the core and booster is obtained by a second order curve fit . The curve fit is based on average thrust rates experienced from a series of nominal runs. For added simplicity it is also assumed that the normal force stability derivative, $C_{n\alpha}$, is constant throughout the launch phase. A mean value of 0.096 deg^{-1} was selected for $C_{n\alpha}$. The air density is obtained from a functionalization of height

---

[1] Press, W.H., Flannery, B.P, Teukolsky, S.A., Vetterling, W.T., Numerical Recipes. 1986. Cambridge: Cambridge University Press. (pp 274).

based on data obtained from standard US atmosphere tables. The effect of the axial aerodynamic force is neglected. The launch program uses the design wind profile to obtain the value of the wind velocity throughout flight, as does the main simulation program. This enables the calculation of the air-relative velocity of the vehicle and hence the angle of attack. For the calculation of Q, however, the earth relative velocity is used instead of the air-relative velocity. The error associated with this assumption is negligible. The location of the center of gravity as well as the center of pressure is assumed to be known accurately.

From Figure 7.22 it is possible to derive the following simplified dynamic equations to describe the motion of the vehicle during the launch phase. Wherever possible small angle approximation are used (ie., $\sin(\theta) = \theta$ and $\cos(\theta) = 1$).

For the sinusoidal launch maneuver, the attitude rate is described by

$$\dot{\theta} = \Omega \left(1 - \cos\left(\frac{2\pi}{T_{Kick}} t \right) \right) \Big|_{0 \le t \le T_{Kick}} \tag{7.2}$$

For the sinusoidal launch maneuver with a non-zero terminal pitch rate the first half of the launch profile is described by

$$\dot{\theta} = \Omega \left(1 - \cos\left(\frac{2\pi}{T_{Kick}} t \right) \right) \Big|_{0 \le t \le T_{Trans}} \tag{7.3}$$

and

$$\dot{\theta} = 2\,\Omega \Big|_{T_{Trans} < t \le T_{Kick}} \tag{7.4}$$

The angular momentum of the vehicle can be described by the equation

$$\begin{aligned} I\ddot{\theta} = & -T_B \left(D + z_{cg}\right) - T_C z_{cg} + SQC_{n\alpha}\alpha \left(l_{cpx} - x_{cg}\right) \\ & + T_C\, x_{cg}\, \delta + T_B\, x_{cg}\, \delta \end{aligned} \tag{7.5}$$

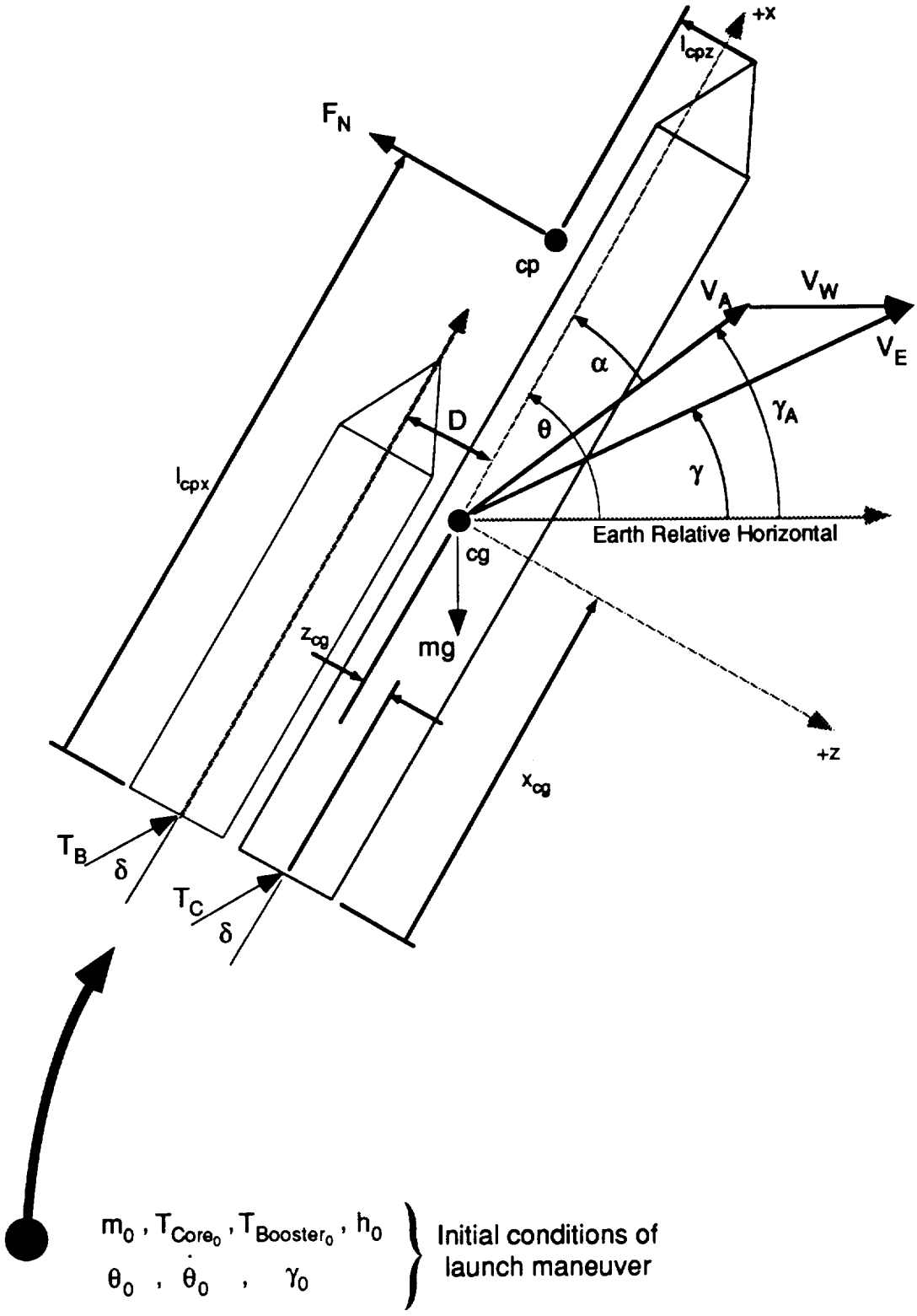

Figure 7.22 Simplified dynamic model for launch maneuver design.

Solving for δ yields

$$\delta = \frac{T_B (D + z_{cg}) + T_C z_{cg} + I\ddot{\theta} - SQC_{n\alpha}\alpha (l_{cpx} - x_{cg})}{(T_B + T_C) x_{cg}} \qquad (7.6)$$

The acceleration of the vehicle along the Earth relative velocity vector can be expressed as

$$\dot{V} = \frac{(T_B + T_C) \cos(\theta - \gamma - \delta) - g \sin(\gamma) - SQC_{n\alpha}\alpha \sin(\alpha)}{m} \qquad (7.7)$$

The sum of forces on the vehicle perpendicular to the velocity vector can be expressed as

$$mV\dot{\gamma} = (T_B + T_C) \sin(\theta - \gamma - \delta) - mg \cos(\gamma) + SQC_{n\alpha}\alpha \cos(\alpha) \qquad (7.8)$$

Solving Equation (7.8) for $\dot{\gamma}$ yields

$$\dot{\gamma} = \frac{(T_B + T_C) \sin(\theta - \gamma - \delta)}{mV} - \frac{g \cos(\gamma)}{V} + \frac{SQC_{n\alpha}\alpha \cos(\alpha)}{mV} \qquad (7.9)$$

The height of the vehicle during flight is given by the differential equation

$$\dot{h} = V \sin(\gamma) \qquad (7.10)$$

7.8.3 Launch Maneuver Correlation Results

Equations (7.2) through (7.10) form a simplified description of the dynamic behavior of the vehicle during Phase Two. The launch design simulation employed a fourth order Runge-Kutta integration technique with an integration step size of 0.1 sec. To evaluate the accuracy of these simplified equations the Phase Two trajectory was determined both with the simplified simulation and a more accurate 6 degree of freedom (6 DOF) simulation. A first simulation comparison used the sinusoidal pitch rate maneuver described in section 7.2. A no-wind environment was used. Results from the first trial are illustrated in Figures 7.23 and 7.24, where all solid lines represent results generated from the 6 DOF simulation and all dashed lines are the predicted values calculated from the launch design simulation. As seen the peak errors between the predicted values of alpha and gamma, and the true values are minimal.

A second simulation comparison was also conducted using the sinusoidal launch maneuver with non-zero terminal pitch rate. These results are illustrated in Figures 7.26 and 7.27. Again the errors between the predicted and actual values of gamma and alpha are minimal. The peak errors resulting from both comparisons is shown in Table 7.3.

Figure Number	Time (sec)	Error (deg)
7.20	30.3	0.241
7.21	30.3	0.172
7.23	23.0	0.172
7.24	23.0	0.150

Table 7.3 Peak errors in launch design simulation.

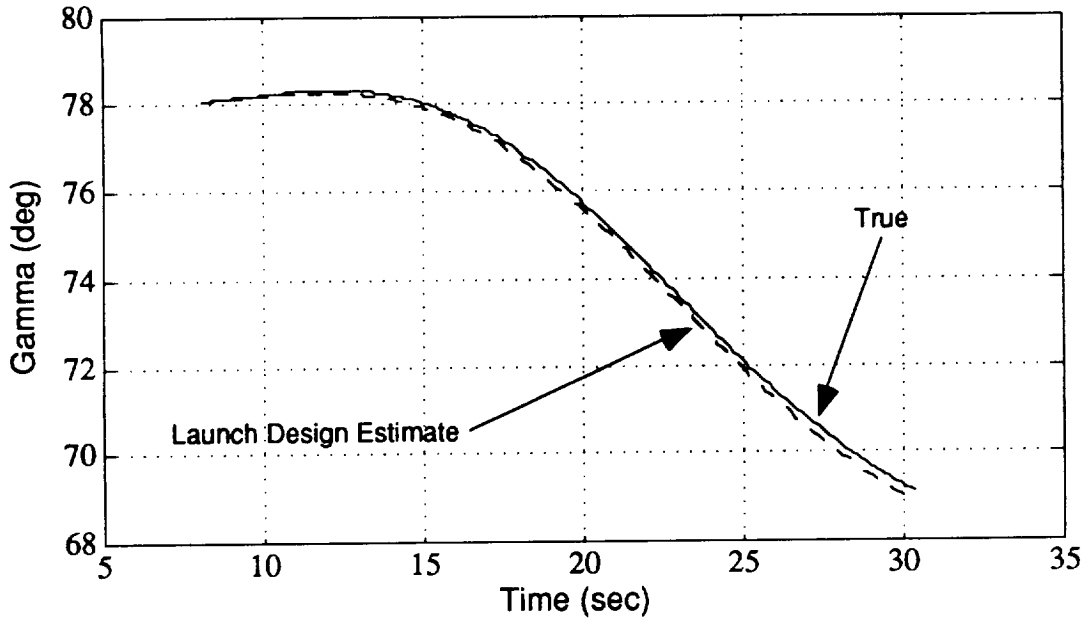

Figure 7.23 Sinusoidal launch maneuver correlation between true and estimated γ.

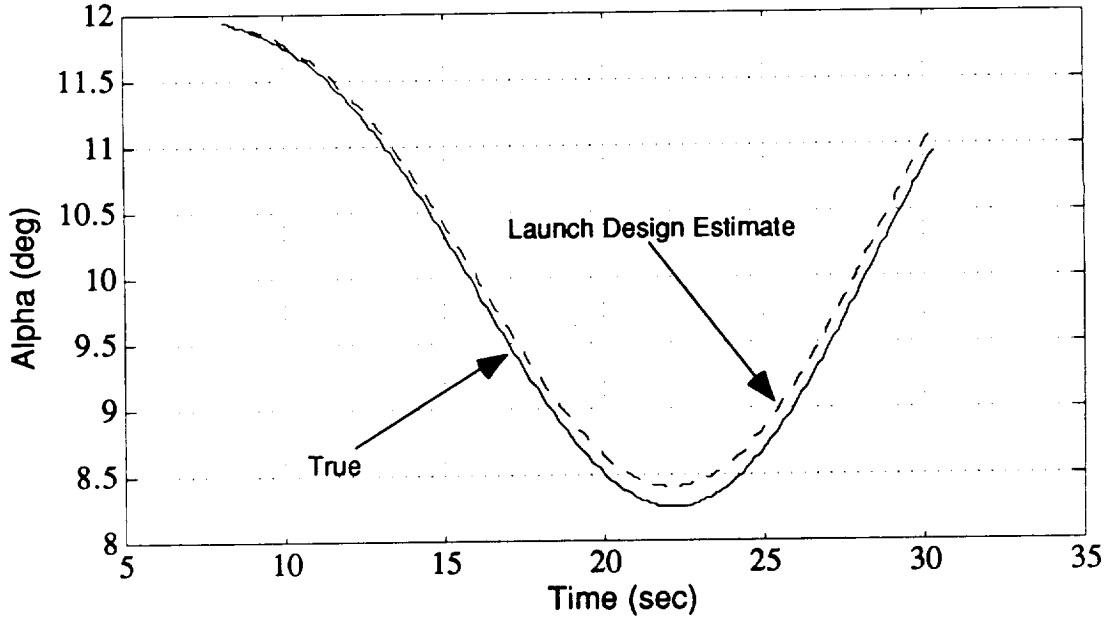

Figure 7.24 Sinusoidal launch maneuver correlation between true and estimated α.

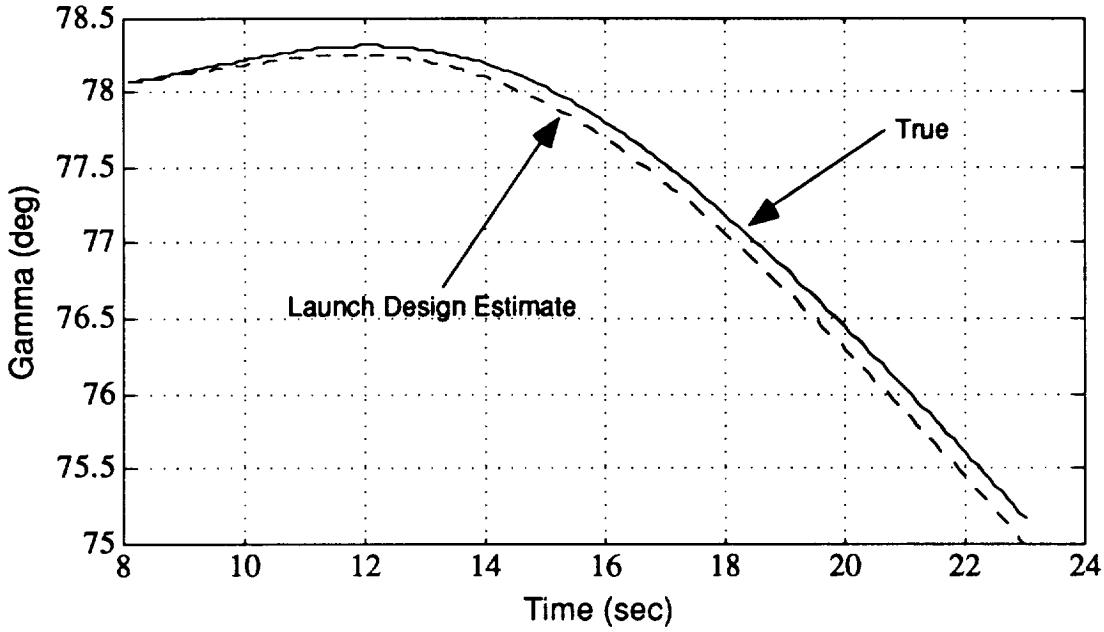

Figure 7.25 Sinusoidal launch maneuver with non-zero terminal pitch rate: correlation between true and estimated γ.

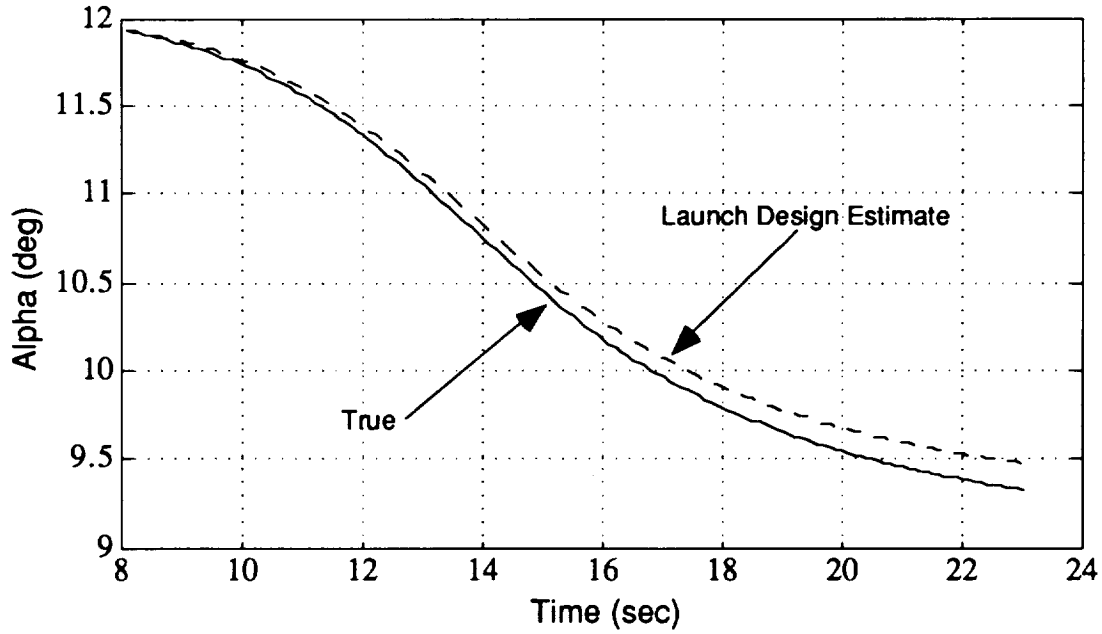

Figure 7.26 Sinusoidal launch maneuver with non-zero terminal pitch rate: correlation between true and estimated α.

7.8.4 Sinusoidal Launch Maneuver Parameter Adjustment

The sinusoidal launch maneuver is a function of two parameters, T_{kick}, and , Ω. As shown in Figure 7.1, T_{kick} represents the length of the maneuver and Ω is a value equal to half the maximum commanded pitch rate. During the launch design process, the user specifies the desired θ and α at the end of Phase Two. The process of then choosing the correct combination of T_{kick} and Ω to ensure a "smooth" transition to Phase Three is an iterative procedure. That procedure involves minimizing the error between the estimated α, as computed by the launch design simulation, and the desired α at the end of launch. The other terminal launch state, θ, is a function of Ω, T_{kick}, and $\theta_{initial}$. This is demonstrated by integrating the equation of the sinusoidal launch profile, which is:

$$\dot{\theta} = \Omega \left(1 - \cos\left(\frac{2\pi}{T_{Kick}} t\right)\right) \tag{7.11}$$

Integrating the left side of Equation (7.11) results in

$$\int_{t=0}^{t=T_{Kick}} \dot{\theta}\, dt = \theta_{Final} - \theta_{Initial} \tag{7.12}$$

Similarly for the right side of Equation (7.11):

$$\int_{t=0}^{t=T_{Kick}} \Omega \left(1 - \cos\left(\frac{2\pi}{T_{Kick}} t\right)\right) dt = \Omega\, T_{Kick} \tag{7.13}$$

Combining Equations (7.12) and (7.13), and solving for Ω yields

$$\Omega = \frac{\theta_{Final} - \theta_{Initial}}{T_{Kick}} \tag{7.14}$$

Initially, the minimization algorithm selects a value of T_{kick} with which to estimate the terminal launch states. Ω is then calculated based on Equation (7.14) and a simulated launch is performed. The results from the simulated launch are then compared to the desired terminal launch states. If the estimated terminal states and the desired states are not identical, then a new value of T_{kick} is chosen using a golden search bisection. A new Ω is then re-calculated and the launch simulation is re-run until the error in terminal states is minimized. The complete procedure is shown in Figure 7.27. The values of T_{kick} chosen by the launch design algorithm are always rounded to the nearest 0.1 sec to conform to the integration step time of both the simplified launch simulation and the full 6 DOF simulation. In addition, the launch design algorithm continually adjusts T_{kick} until the predicted error in alpha final is less than 0.05° or the value of T_{kick} yielding the minimum error in alpha has been located within 0.1 seconds.

7.8.5 Parameter Adjustment for the Sinusoidal Launch Maneuver with a Non-zero Terminal Pitch Rate

The second launch profile employing a non-zero terminal pitch rate is illustrated in Figure 7.2, and is characterized by two different phases. During the first half of the maneuver the vehicle is commanded to follow a sinusoidal pitch rate command. When the commanded pitch rate has reached its maximum value at $t = T_{trans}$, the commanded pitch rate is held constant until the end of the maneuver. Termination of the launch profile occurs at $t = T_{kick}$. A non-zero terminal pitch rate means that one extra variable is necessary to define the launch profile. This allows the user to match not only the desired attitude and angle of attack at the beginning of Phase Three, but also the attitude rate.

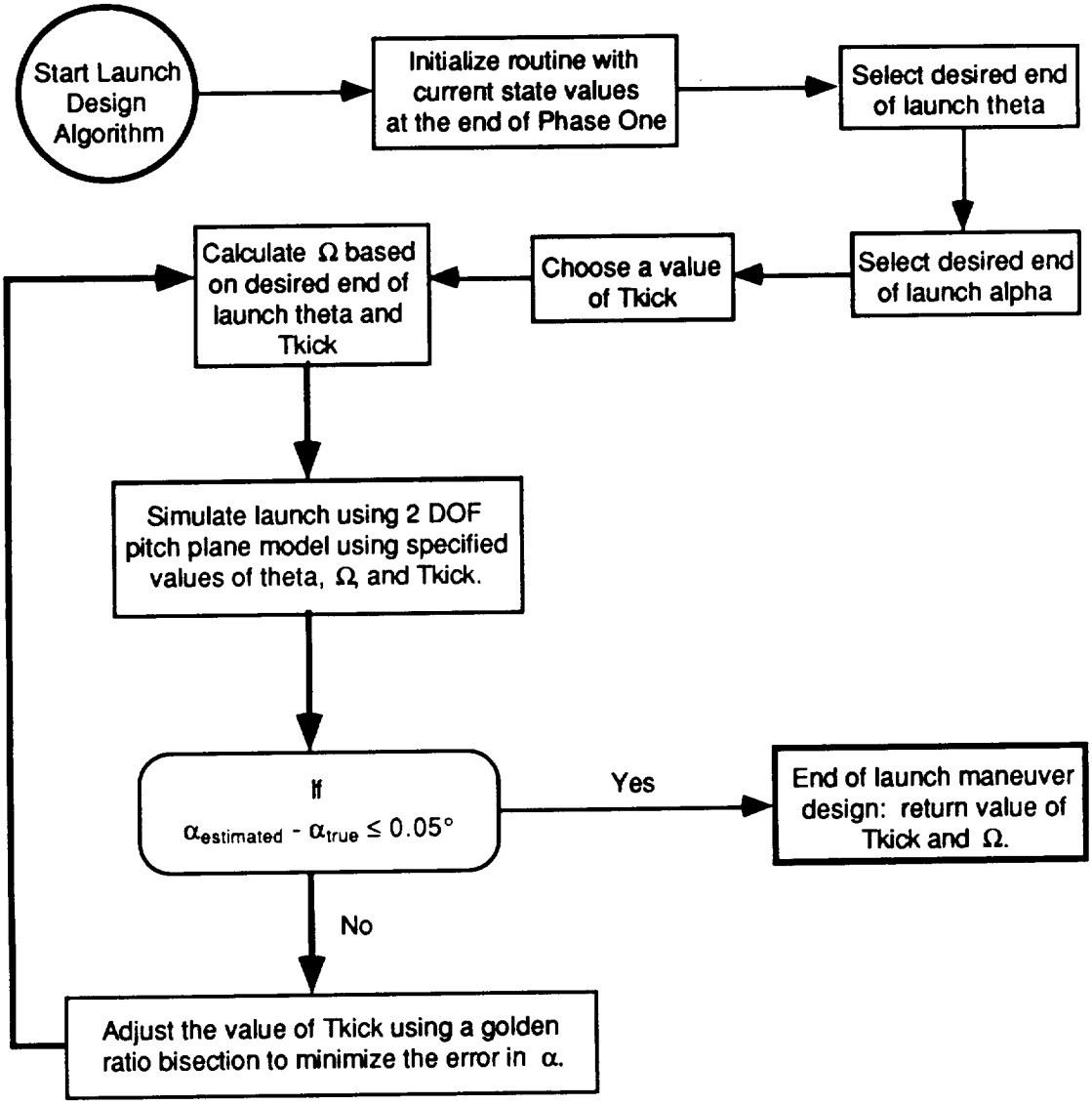

Figure 7.27 Sinusoidal launch maneuver design flow chart.

The process of determining the launch design parameters for the non-zero terminal pitch rate maneuver again involves a minimization of α with T_{kick} as the free variable. The end of launch states θ, and $\dot{\theta}$ are further related to the launch maneuver transition time, T_{trans}. This is proven by first integrating the launch profile.

$$\int_{t=0}^{t=T_{Kick}} \dot{\theta}\, dt = \int_{t=0}^{t=T_{Trans}} \Omega\left(1 - \cos\left(\frac{\pi}{T_{Trans}}\, t\right)\right) dt + \int_{t=T_{Trans}}^{t=T_{Kick}} 2\,\Omega\, dt \qquad (7.15)$$

From Equation (7.15), the change in attitude over the length of the maneuver can therefore be written as:

$$\theta_{Final} - \theta_{Initial} = -\Omega\ T_{Trans} + 2\Omega\ T_{Kick}$$
$$\text{or } \Delta\theta = -\Omega T_{Trans} + 2\Omega T_{Kick} \qquad (7.16)$$

Solving Equation (7.16) for T_{trans} yields:

$$T_{Trans} = \frac{\Delta\theta - 2\Omega T_{Kick}}{-\Omega} \qquad (7.17)$$

A necessary condition is that the right side of Equation (7.17) is always positive. This restricts the value of Tkick chosen for the launch simulation by the relationship:

$$T_{Kick} \geq \frac{\Delta\theta}{2\Omega} \qquad (7.18)$$

The flow chart shown in Figure 7.27 for the sinusoidal launch maneuver, is also applicable to the sinusoidal launch maneuver with a non-zero terminal pitch rate. The only additional calculation performed by the sinusoidal launch maneuver with a non-zero terminal pitch rate is the calculation of T_{trans}.

Chapter Eight

SIMULATION RESULTS

8.1 Introduction

Two different sets of simulation runs with and without the effects of signal quantization were made. The first set was made to evaluate the acceleration-direction guidance, steering and control concept for ideal feedback variables. The second set was made to evaluate the performance of the rate, angle of attack, and dynamic pressure estimators. The runs in the first set, listed in Table 8.1, are based on the feedback of true angular rate, angle of attack, and dynamic pressure. Plotted results of these runs are shown in Figures 8.1 through 8.11. The maximum Q and $Q\alpha$ values for each of the runs are tabulated in Table 8.2. The runs in the second set, listed in Table 8.3, were made using different combinations of true and estimated angular rate, angle of attack, and dynamic pressure. Plots showing the effectiveness of the estimators are illustrated in Figures 8.12 through 8.25. The maximum values of Q and $Q\alpha$ for each of these runs are shown in Table 8.4.

The results presented in this chapter are preliminary. The effects of bending and fuel slosh are omitted. The engine nozzle actuators are assumed to provide perfect instantaneous response to the nozzle command subject only to the limitation that the change in nozzle deflection not exceed 1° from one sampling instant to the next (this is equivalent to a nozzle rate limit of 10°/sec). The tail-wags-dog effect is also omitted. The effects of varying the levels of IMU quantization on the angular rate and angle of attack estimators are examined in Chapters Four and Five.

For each run in Table 8.1, a separate trajectory design was first carried out to optimize the predicted on-orbit mass of the vehicle and minimize the change in pitch attitude at the transition to PEG. For the first four runs the trajectory design was done for a variety of winds with the design $Q\alpha$ limit set at 3000 lbs deg/ft^2. For run number 5, the vehicle was oriented differently with the

core stage on top of the booster during flight. To take advantage of the improved performance offered by this alternative orientation the design $Q\alpha$ limit for this configuration was reduced to 2800 lbs deg/ft^2. For each optimal trajectory design the filtered acceleration-direction was stored as a function of time so that it could be later employed in an actual flight employing the acceleration-direction concept. The trajectory design simulations were run using the Vandenberg #69 wind profile exclusively in either a tail or head wind direction. The magnitude of the winds was determined by scaling the stored wind profile by a fixed percentage.

To test the performance of the acceleration-direction concept each stored acceleration-direction profile was employed in an actual in-flight simulation employing a different wind profile. For each acceleration-direction flight simulation the Vandenberg #70 wind profile was employed at different magnitude levels in either a head or tail wind direction. In addition to having a slightly different wind profile shape, the Vandenberg #70 profile has wind magnitudes that are approximately twice those of the Vandenberg #69 profile. By flying the acceleration-direction concept in a wind profile that was different than the wind profile used during the trajectory design, the effectiveness of the acceleration-direction concept in providing adequate load relief as well as accurate trajectory following was tested.

For all of the runs listed in Table 8.1 an in-flight $Q\alpha$ limit of 3350 lbs deg/ft^2 was employed during the acceleration-direction simulations. This $Q\alpha$ limit was higher than the trajectory design $Q\alpha$ limit of 3000 lbs deg/ft^2 used for the first four runs and also higher than the 2800 lbs deg/ft^2 used for run number 5. The larger in-flight $Q\alpha$ limit values are necessary so that when variations from the pre-launch winds are encountered, there is enough latitude within the $Q\alpha$ limit to adjust the trajectory.

As mentioned above, the performance of the angular rate, angle of attack, and dynamic pressure estimators was tested by employing a second category of runs. For each run listed in Tables 8.3 and 8.4 (runs 6-10) a quantization level of 3 arcsec was assumed in the measurement of $\Delta\theta$ and a quantization level of 0.0128 ft/sec was assumed in the measurement of ΔV. For the sake of comparison, each run was made using the worst-case flight conditions listed under "run # 1" in Table 8.1. As shown in Table 8.4 all of the acceleration-direction runs with estimators and signal quantization were made

with the Qα limit increased to 3500 lbs deg/ft^2. This higher limit was required to accommodate the increased errors in the estimated Qα resulting from quantization. (This includes run #10 which represents the alternative vehicle configuration in which the core stage rides on top of the booster stage.) The trajectory design Qα limit was set at 3000 lbs deg/ft^2 for runs #6 through #9, and 2800 lbs deg/ft^2 for run # 10.

Run #	Trajectory Design			Simulation			Δ pitch @ PEG (deg)	On-orbit Mass (slugs)	Figure #
	Wind Direction	Magnitude	Wind Profile #	Wind Direction	Magnitude	Wind Profile #			
1	Head	60%	69	Head	60%	70	4.04	12130	8.1-8.3
2	Head	40%	69	Head	40%	70	1.40	12147	8.4-8.5
3	Tail	60%	69	Tail	60%	70	-0.11	12191	8.6-8.7
4	Tail	40%	69	Tail	40%	70	-0.05	12182	8.8-8.9
5*	Head	60%	69	Head	60%	70	1.31	12212	8.10-8.11

Table 8.1 Simulation results for acceleration-direction concept with the true feedback variables.

Run #	Maximum Q	Maximum Qα	Qα limit Trajectory Design	Qα limit Simulation
1	849.5	3431	3000	3350
2	862.1	3404	3000	3350
3	768.8	3272	3000	3350
4	772.8	3169	3000	3350
5*	927.9	3570	2800	3350

Table 8.2 Maximum Q and Qα values for acceleration-direction concept simulations with true feedback variables. (* Core on top of booster.)

Run #	Feedback Variable						Δ Pitch @ PEG (deg)	On-orbit Mass (slugs)	Figure #
	α		ω		Q				
	α_{True}	$\hat{\alpha}$	ω_{True}	$\hat{\omega}$	Q_{True}	$\hat{Q}$			
6	Yes	-	-	Yes	Yes	-	2.46	12136	8.12-8.13
7	-	Yes	Yes	-	Yes	-	5.06	12134	8.14-8.15
8	-	Yes	-	Yes	Yes	-	4.46	12118	8.16-8.17
9	-	Yes	-	Yes	-	Yes	4.57	12128	8.18-8.21
10*	-	Yes	-	Yes	-	Yes	1.90	12210	8.22-8.25

Table 8.3 Simulation results for acceleration-direction concept using estimated angle of attack, angular rate, and dynamic pressure. (* Core on top of booster.)

Run #	Maximum Q	Maximum Qα	Qα limit Trajectory Design	Qα limit Simulation
6	837.2	3583	3000	3500
7	862.1	3603	3000	3500
8	855.8	3579	3000	3500
9	857.4	3592	3000	3500
10*	940.6	3692	2800	3500

Table 8.4 Maximum Q and Qα values for acceleration-direction concept simulations using estimated feedback variables. (* Core on top of booster.)

8.2 Discussion of Results

For the first run tabulated in Table 8.1 the vehicle was flown in a head wind corresponding to 60% of the Vandenberg #70 profile. This head wind had wind velocities which were greater than the 60% Vandenberg #69 wind profile used during the trajectory design process. As shown in Figure 8.1, this increased level of head winds caused the flight control system to switch to the Qα limiting mode to prevent the angle of attack of the vehicle from exceeding the angle of attack limit, α_{limit}. As shown in Figure 8.2 this resulted in the vehicle closely following the Qα limit of 3350 lbs deg/ft^2. By switching from acceleration-direction steering to angle of attack feedback the flight control system was able to provide quick load relief performance.

In Figure 8.3 it can be seen that the vehicle spent approximately one half of Phase Three flying in the Qα limit mode. The effect of this long period of Qα–limiting load relief is to cause the attitude of the acceleration vector to be slightly lower than the attitude for the corresponding nominal trajectory design case.

Despite this effect on the trajectory, only a 4.02° change in attitude was commanded at the transition to PEG. As shown in Table 8.1, this also resulted in a predicted on-orbit mass of 12130 slugs which is slightly lower than the corresponding trajectory design prediction of 12136 slugs -- a decrease of only 6 slugs.

Run #2 was also a head wind case, but the magnitudes of winds employed in both the trajectory design and the actual in-flight simulation were only 40% of the full Vandenberg #69 and #70 wind profiles. In the presence of lighter winds the performance of the vehicle improved. The predicted on-orbit mass of 12147 slugs for the in-flight simulation was higher than that predicted for run #1, and the change in commanded attitude at the transition to PEG was only 1.40°. This improvement in performance was at least in part due to the fact that the vehicle spent a shorter time period in the $Q\alpha$ limit mode. This can be seen by comparing Figure 8.5 and Figure 8.2. As shown in Figure 8.5 the vehicle again closely follows the $Q\alpha$ limit of 3350 lbs deg/ft^2 but its duration at that limit is much shorter than that of Figure 8.2. As a result the vehicle spends a larger portion of time in the latter stages of Phase Three flying in the acceleration-direction mode. The decrease in on-orbit mass from the trajectory design to the subsequent flight is only 3 slugs. This smaller decrease in mass can be attributed to the fact that the reduced-magnitude winds result in smaller differences between prelaunch (design) winds and flight winds which in turn result in less of a trajectory change being produced by wind produced $Q\alpha$-limiting.

For runs #3 and #4 the vehicle was subjected to tail winds of the same magnitudes as in runs #1 and #2, respectively. As shown in Figures 8.6 and 8.7 the angle of attack of the vehicle in both tail wind runs remained below the angle of attack limit at all times. As a result the vehicle did not enter the $Q\alpha$ limit mode at any time during Phase Three. This is illustrated in Figures 8.7 and 8.9 where it can be seen that the $Q\alpha$ of the vehicle remains below the $Q\alpha$ limit of 3350 lbs deg/ft^2.

As shown in Table 8.1, the effects of the tail winds for both run #3 and run #4 improved the in-flight predicted on-orbit mass performance of the vehicle compared to the head wind in-flight simulations. In comparing run #3 (60% tail wind) to run #1(60% head wind) it can be seen that the on-orbit mass improved by 61 slugs (from 12130 slugs to 12191 slugs). An improvement in on-orbit

mass can also be seen when comparing the trajectory design simulations of runs #3 and #4 with their corresponding in-flight simulations. For run #3, the in-flight simulation yielded an improvement of 10 slugs over the trajectory design simulation, and for run #4, the improvement from trajectory design to in-flight was 6 slugs. For both tail wind cases the change in commanded attitude at the transition to PEG was no different than that seen in the corresponding trajectory design simulations. As shown in Table 8.1, the change in pitch attitude at PEG for both run #3 and run #4 was less than 0.2°.

As previously mentioned run #5 was made with the alternative configuration of the core stage riding on-top of the booster. For the sake of comparison the trajectory design and in-flight simulations were run in the same wind profiles as in run#1. As shown in Table 8.2, the trajectory design for this alternative configuration was carried out with the slightly lower $Q\alpha$ limit of 2800 lbs deg/ft^2. This decrease in the $Q\alpha$ limit provided the vehicle with some added latitude in adjusting the trajectory in the presence of off-nominal winds. In comparing Figure 8.10 and Figure 8.1 it can be seen that with the alternative configuration the vehicle spent less time flying in the $Q\alpha$–limiting mode. Consequently, the load relief was applied for a shorter time in run #5 compared to run #1 and this helped reduce the trajectory deviations throughout Phase Three. This improvement in design-trajectory following is evidenced by the lower commanded attitude change at PEG (1.31° for run #5 vs. 4.04° for run #1). In addition to this performance improvement there was also a significant improvement in the predicted on-orbit mass of the vehicle. As shown in Table 8.1 the predicted on-orbit mass of 12212 slugs for run #5 was 82 slugs more than that predicted for run #1. Such an improvement is significant, especially since the predicted on-orbit mass for both tail wind simulations was also less than that predicted for the alternative configuration.

With the utilization of perfect feedback the performance of the acceleration-direction steering concept with $Q\alpha$–limiting load relief provides excellent trajectory shaping capability as well as accurate and fast load relief performance in the presence of off-nominal winds. For the first four trials in Table 8.1 the difference between the trajectory design $Q\alpha$ limit and the selected in-flight $Q\alpha$ limit was only 350 lbs deg/ft^2. For run #5 a larger difference of 550 lbs deg/ft^2 was available because of the improved trajectory shaping capabilities offered by this orientation. Both margins, while quite small,

provided enough latitude to allow the flight controller to maintain the desired trajectory in the presence of small wind disturbances.

To study the effects that estimated feedback quantities would have on the performance of the acceleration-direction steering concept, two additional runs were made. These runs, which are tabulated in Table 8.5, were made with the same flight conditions as run #1. The first line of the table is a duplication of the results presented for run #1, which was made using true values of the feedback variables. The first of the two additional runs was made with estimated angular rate and angle of attack feedback but without any quantization in the signals processed by the estimators. For the final run quantization was added to the signals processed by the estimators.

Comparing the first of the additional runs with the run using true feedback variables it can be seen that the utilization of estimated feedback variables degraded the performance. The predicted on-orbit mass of the vehicle decreased by 15 slugs (from 12130 slugs to 12115 slugs) and the attitude change at PEG increased by 1.89° (from 4.04° to 5.93°). In addition, although the maximum value of $Q\alpha$ decreased, it will be shown that this reduction is due to errors associated with estimating the angle of attack.

For the second of the additional runs quantization levels of 3 arcsec and 0.0128 ft/sec respectively were assumed in the measurements of $\Delta\theta$ and ΔV. As shown in the last row of Table 8.5 this added effect further degraded the performance of the system. Compared to the results tabulated for true variable feedback, the predicted on-orbit mass of the vehicle decreased by 27 slugs (from 12130 slugs to 12103 slugs) and the attitude change at PEG increased by 3.05° (from 4.04° to 7.09°). In addition, the added effect of quantization increased the maximum value of $Q\alpha$ to 3513 lbs deg/ft^2, or 163 lbs deg/ft^2 above the in-flight $Q\alpha$ limit. This loss in performance is partly due to the combined effects of lags associated with estimating the feedback quantities, and the quantization introduced into the measurements of $\Delta\theta$ and ΔV. As a result of this loss in performance it was decided to increase the in-flight $Q\alpha$ limit to 3500 lbs deg/ft^2 for the runs (6-10) listed in Tables 8.3 and 8.4.

For run #6, the estimated angular rate (see Chapter 4), the true angle of attack and the true dynamic pressure were employed. As shown in Figure 8.12,

Flight Condition		Δ pitch @ PEG	On-orbit Mass	Maximum Qα
Feedback	Quantization	(deg)	(slugs)	(lbs deg/ft^2)
α, ω	No	4.04	12130	3431
$\hat{\alpha}, \hat{\omega}$	No	5.93	12115	3407
$\hat{\alpha}, \hat{\omega}$	Yes	7.09	12103	3513

Table 8.5 Effects of estimators and quantization on performance of run #1.

the larger head wind magnitudes encountered in-flight forced the vehicle to enter the Qα–limiting mode to prevent the angle of attack from exceeding the angle of attack limit, α_{limit}. As shown in Figure 8.13 this resulted in the vehicle closely following the larger in-flight Qα limit of 3500 lbs deg/ft^2. The effect of increasing the Qα limit upon the predicted on-orbit mass can be seen by comparing run #1 and run #6. Despite feeding back estimated angular rate (which in theory should degrade the performance), the on-orbit mass of the vehicle improved by 6 slugs -- from 12130 slugs to 12136 slugs. Increasing the Qα limit also improved the trajectory-following capability of run #6 which is demonstrated by the lower attitude change at PEG.

For run #7, the estimated angle of attack (see Chapter 5), the true angular rate and the true dynamic pressure were employed. As shown in Table 8.3 the use of estimated angle of attack alone had a larger impact upon the performance of the system than the estimated angular rate alone (run #6). Although the loss in predicted on-orbit mass was only 2 slugs the attitude change at the transition to PEG increased to 5.06°. As illustrated in Figure 8.14 the true angle of attack of the vehicle tended to lead the angle of attack limit throughout most of Phase Three. As a result, the Qα of the vehicle tended to be below the in-flight Qα limit of 3500 lbs deg/ft^2. This effect is illustrated in Figure 8.15.

The combined effect of estimated angular rate and angle of attack feedback on system performance are shown in Figures 8.16 and 8.17 (run #8).

It can be seen that the angle of attack and Qα of the vehicle throughout Phase Three were very similar to those illustrated in Figures 8.14 and 8.15 for run #7. As shown in Table 8.3 the predicted on-orbit mass for run #8 was 12118 slugs. This prediction of on-orbit mass was 16 slugs less than that predicted for run #7 and 18 slugs less than that predicted for run #6. This loss in performance is expected since run #8 employs two estimated feedback variables while run #6 and run #7 employ only one.

For run #9 The angle of attack, the angular rate, and the dynamic pressure estimators were all employed in the in-flight simulation. As shown in Figures 8.18 and 8.19 the performance of the system was very similar to the results presented for run #8. As shown in Table 8.3, the change in commanded attitude at the transition to PEG was 0.11° greater than that reported for run #8. In addition, the predicted on-orbit mass was 12128 slugs, which is an increase of 10 slugs over the previous run.

For run #10 the alternative orientation of the core riding on top of the booster was employed. For the sake of comparison the in-flight simulation was made using estimated angle of attack, estimated angular rate, and estimated dynamic pressure, as in run #9. As shown in Table 8.4, the trajectory design for this alternative configuration was carried out with a slightly lower Qα limit of 2800 lbs/deg ft^2. In comparing Figure 8.21 and 8.18 it can be seen that with the alternative configuration the vehicle spent less time flying in the Qα-limiting mode. Consequently, the vehicle spent more time in the acceleration-direction mode and this improved the trajectory following throughout Phase Three. This improvement is evidenced by the lower commanded attitude change at PEG (1.90°). In addition, there was also a significant increase in the predicted on-orbit mass. As shown in Table 8.3 the predicted on-orbit mass was 12210 slugs, or 82 slugs higher than that predicted for run #9. In comparing run #5 to run #10, it can be seen that the use of estimated feedback quantities only slightly degraded the performance in the case of the core riding on top of the booster. For both the commanded attitude change at PEG as well as the predicted on-orbit mass the difference between the two runs was minimal.

The effect of feeding back both the estimated angular rate and the estimated angle of attack upon the commanded nozzle deflection is illustrated in Figure 8.20. As shown the nozzle command fluctuates more during the initial portions of the Qα limit mode. In addition, these fluctuations are less during

periods where the vehicle is in the acceleration-direction mode and the angle of attack is no longer being employed as a feedback variable. These fluctuations are due in part to the effects of quantization as well as the transient behavior of the angle of attack and angular rate estimators. The amplitude of these nozzle command variations illustrated in Figure 8.20 do not exceed the rate limit of the nozzle actuators at any time.

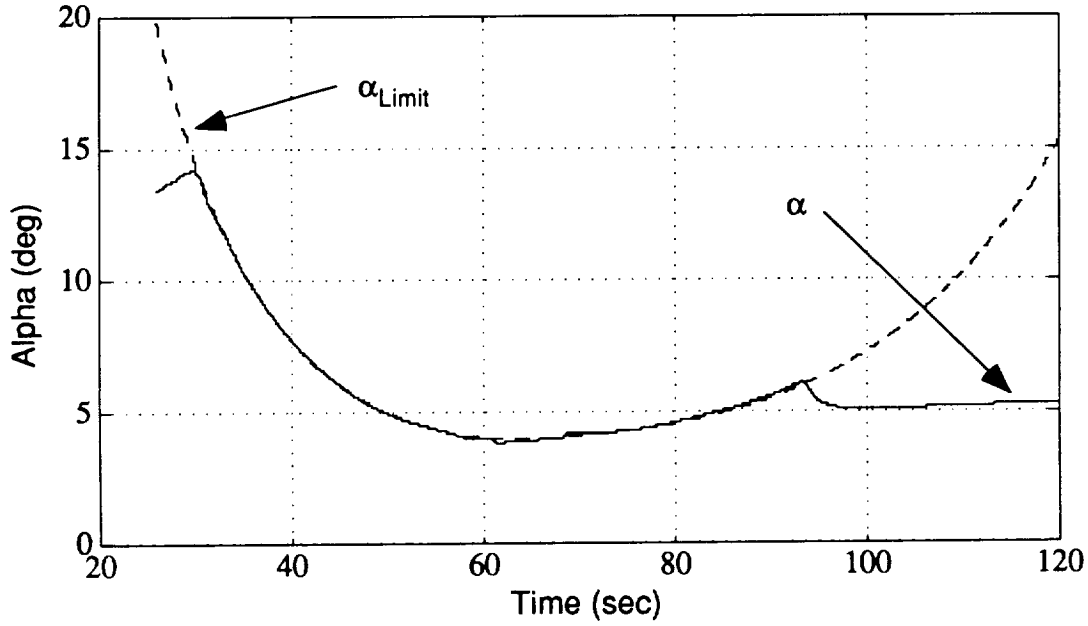

Figure 8.1 Angle of attack and angle of attack limit with perfect feedback in 60% Vandenburg #70 head wind.

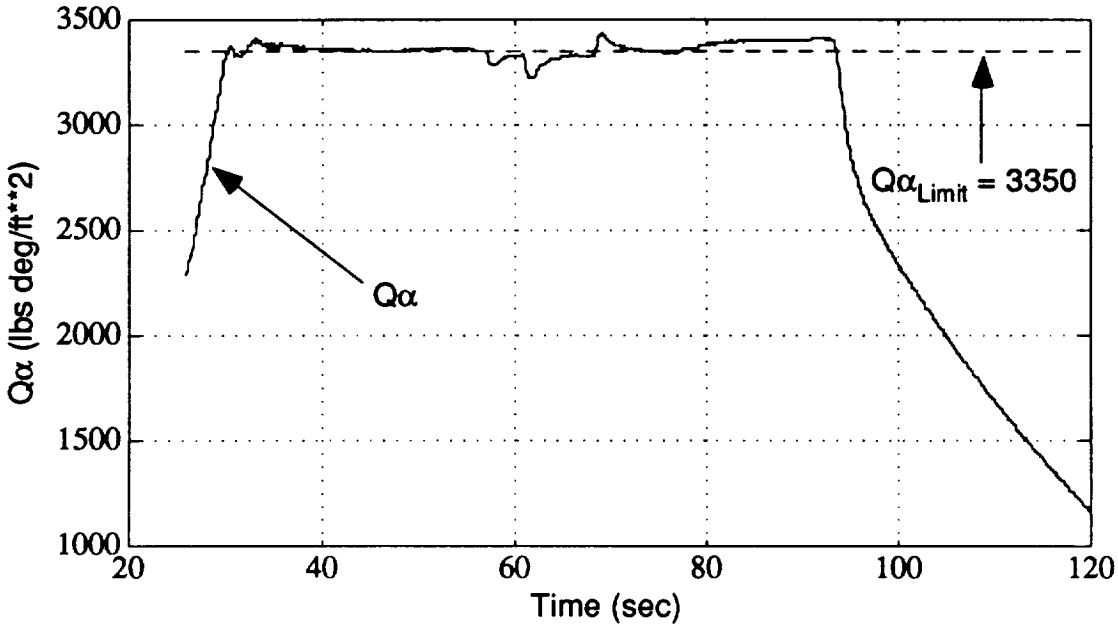

Figure 8.2 Qα and Qα limit with perfect feedback in 60% Vandenburg #70 head wind.

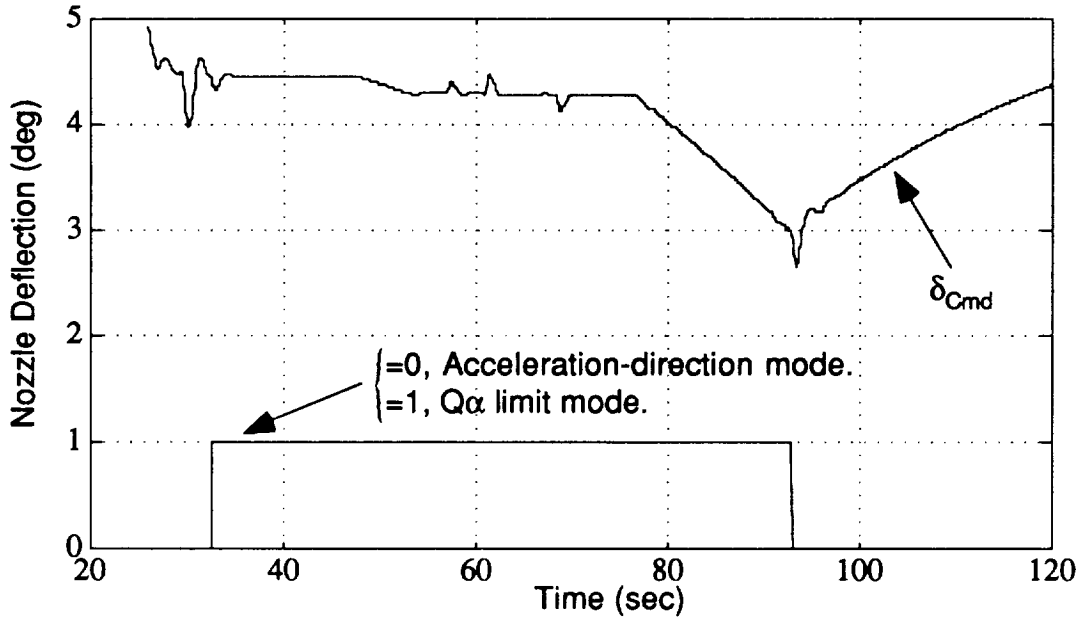

Figure 8.3 Commanded nozzle deflection for Angle of attack and angle of attack limit with perfect feedback in 60% Vandenburg #70 head wind.

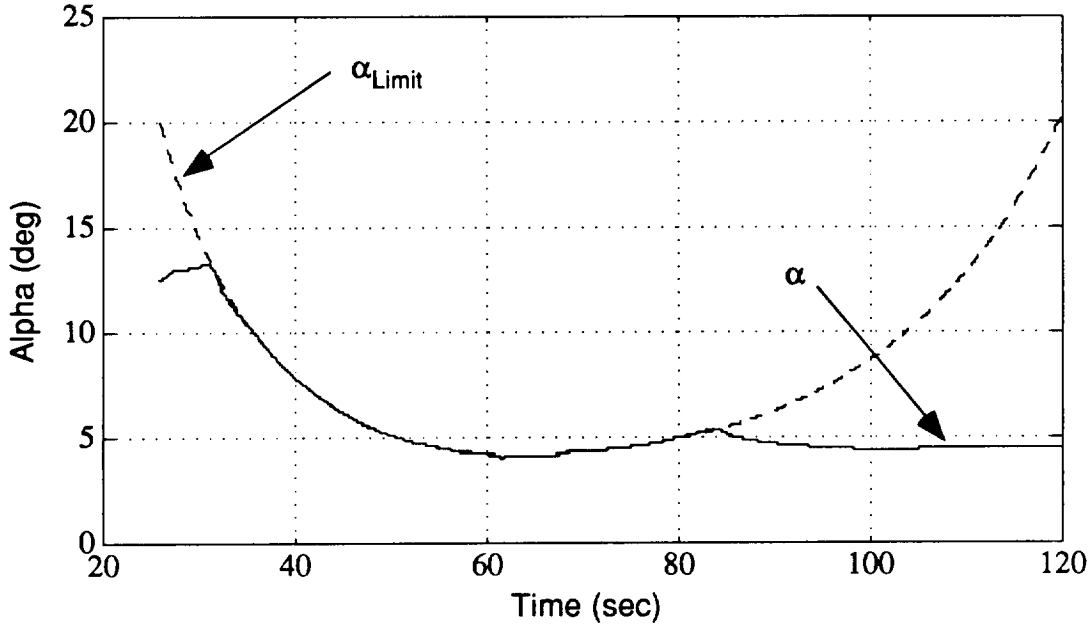

Figure 8.4 Angle of attack and angle of attack limit with perfect feedback in 40% Vandenburg #70 head wind.

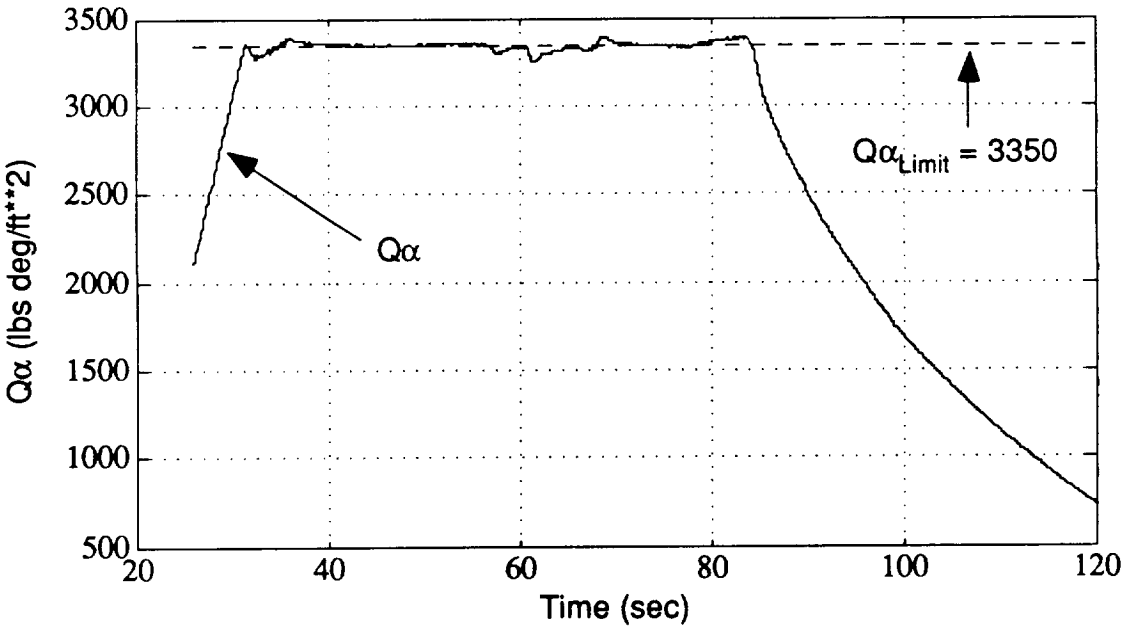

Figure 8.5 Qα and Qα limit with perfect feedback in a 40% Vandenburg #70 head wind.

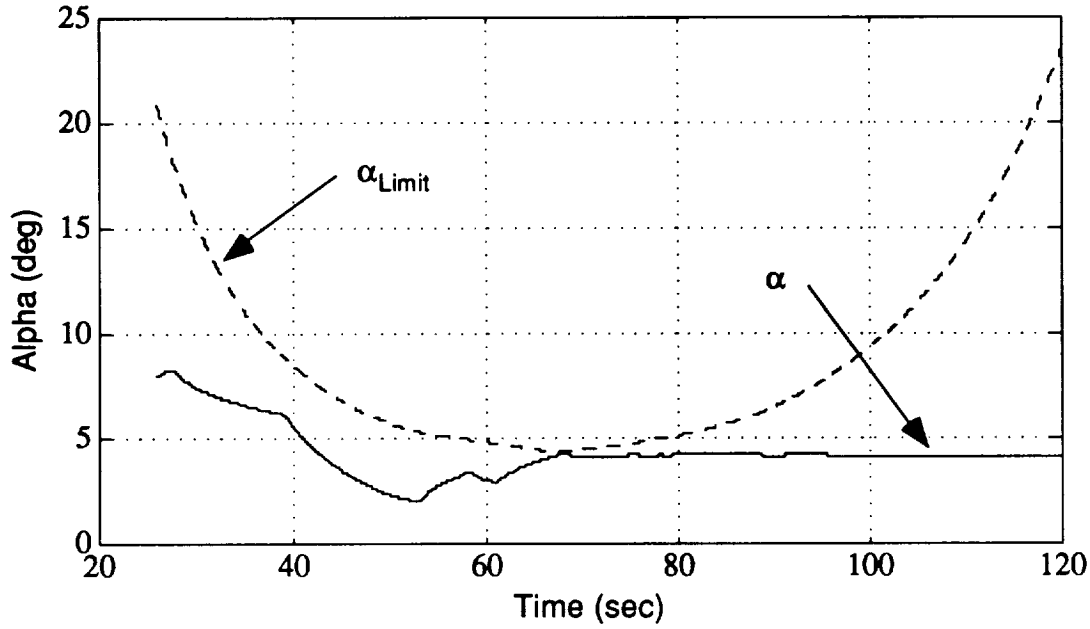

Figure 8.6 Angle of attack and angle of attack limit with perfect feedback in 60% Vandenburg #70 tail wind.

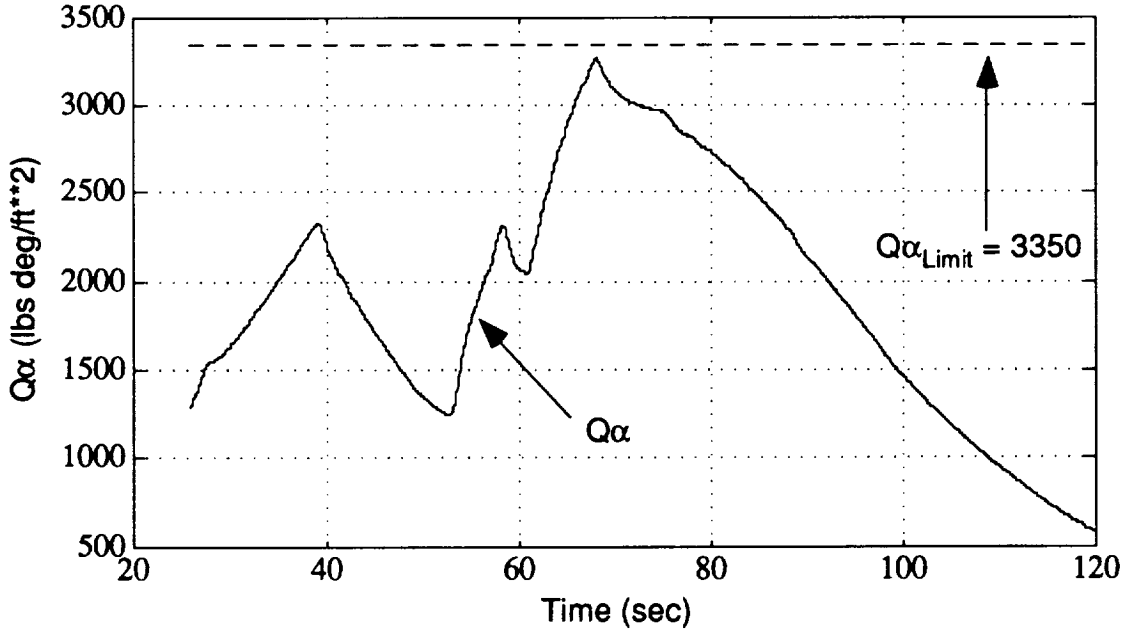

Figure 8.7 Qα and Qα limit with perfect feedback in a 40% Vandenburg #70 tail wind.

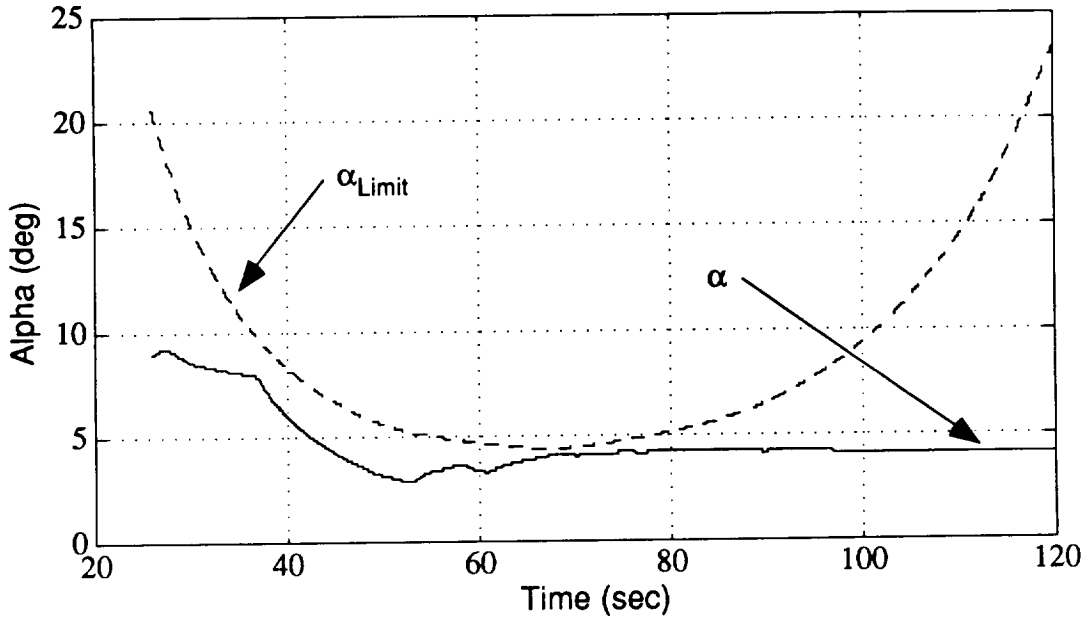

Figure 8.8 Angle of attack and angle of attack limit with perfect feedback in 40% Vandenburg #70 tail wind.

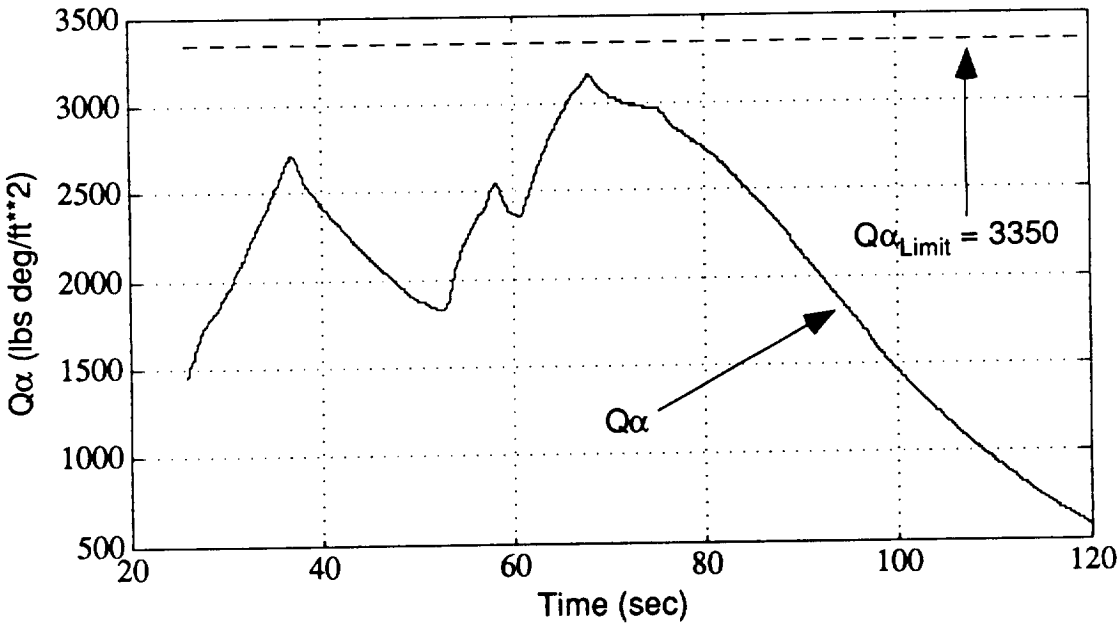

Figure 8.9 Qα and Qα limit with perfect feedback in a 40% Vandenburg #70 tail wind.

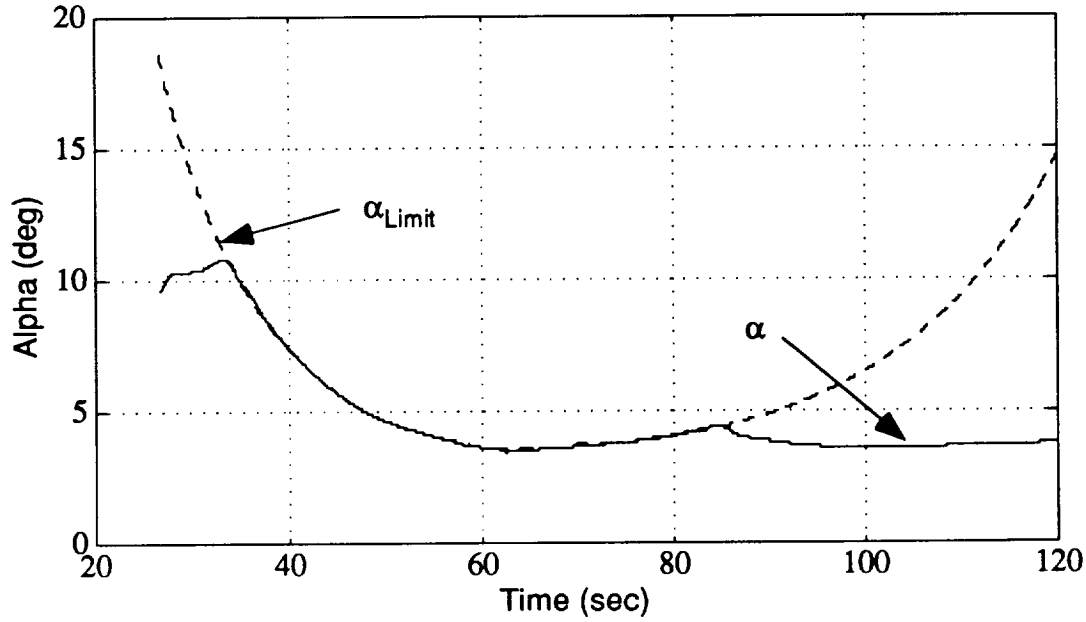

Figure 8.10 Angle of attack and angle of attack limit with perfect feedback in a 40% Vandenburg #70 tail wind with the core stage riding on top of the booster stage.

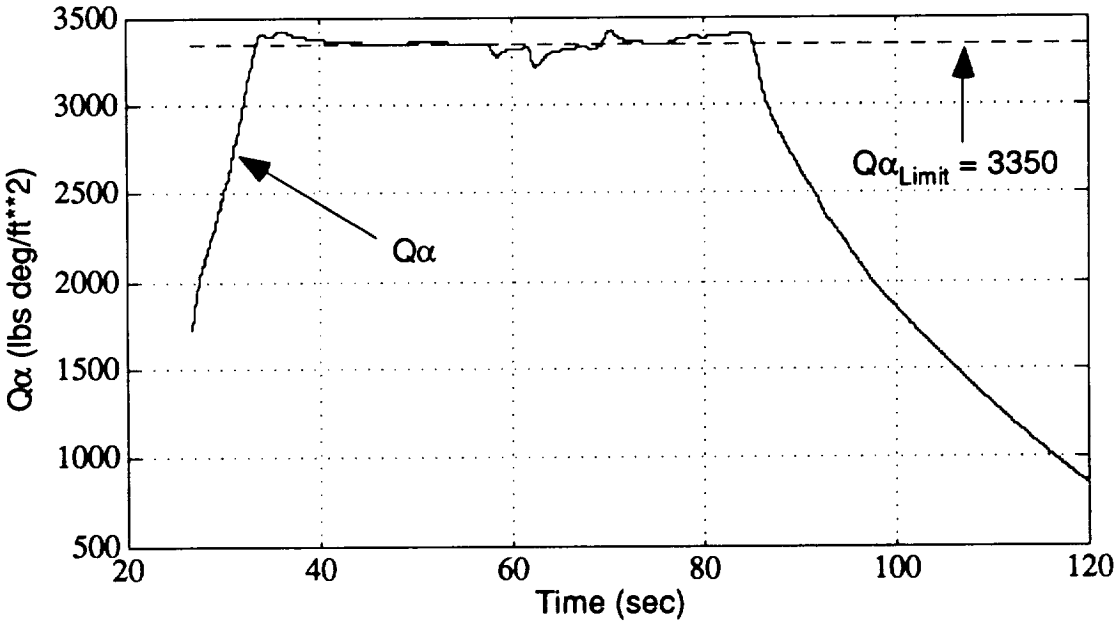

Figure 8.11 Q α and Qα limit with perfect feedback in a 60% Vandenburg #70 head wind with the core stage riding on top of the booster stage.

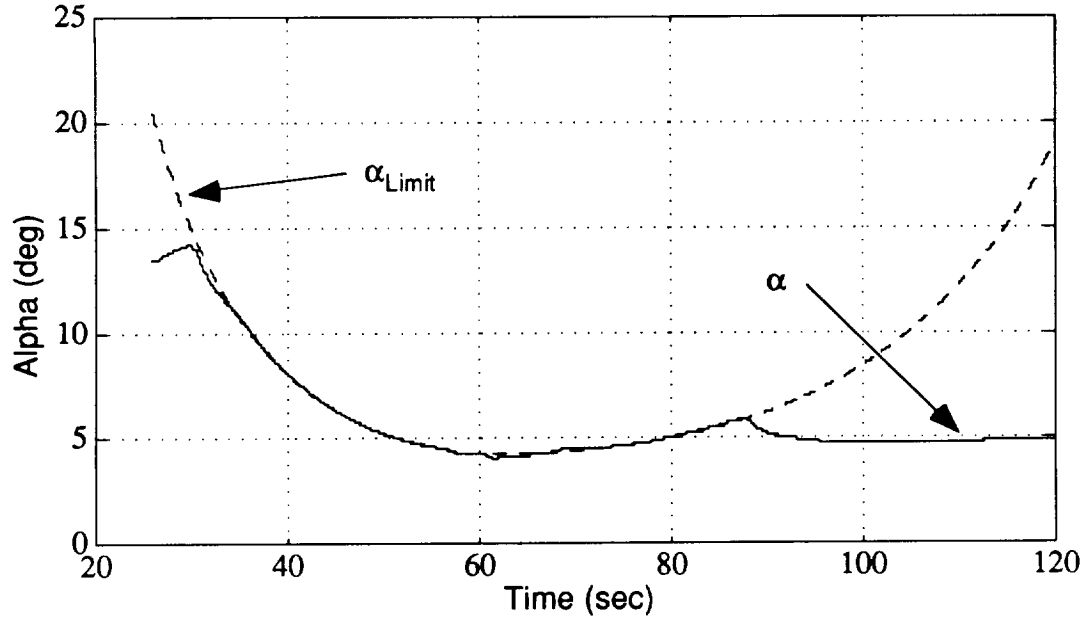

Figure 8.12 Angle of attack and angle of attack limit with estimated feedback of angular rate in a 60% Vandenburg #70 head wind.

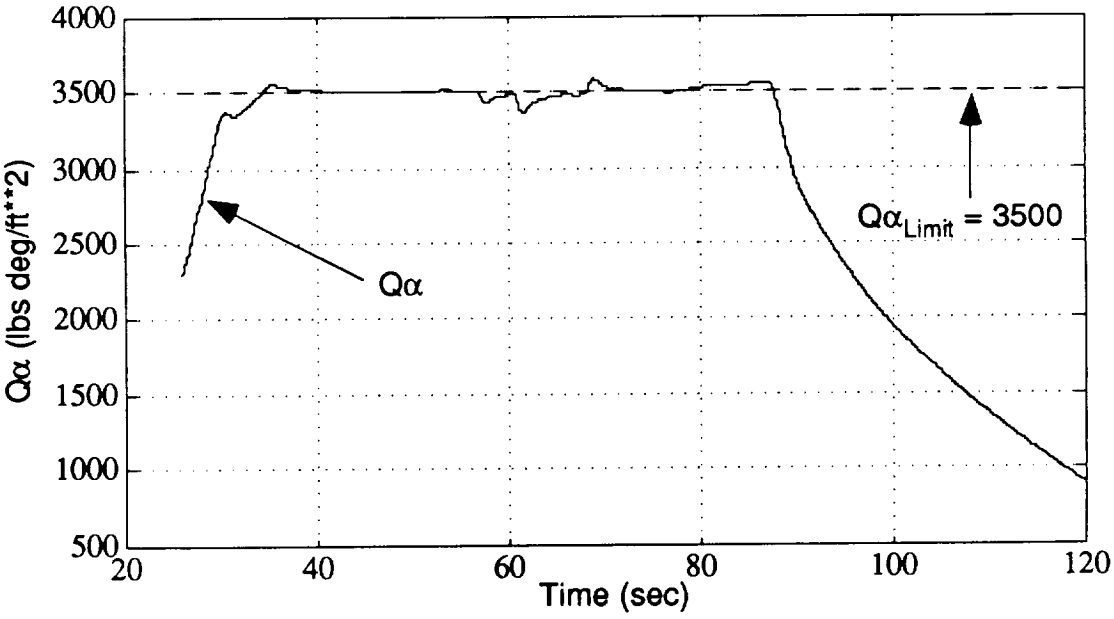

Figure 8.13 Qα and Qα limit with estimated angular rate feedback in a 60% Vandenburg #70 head wind.

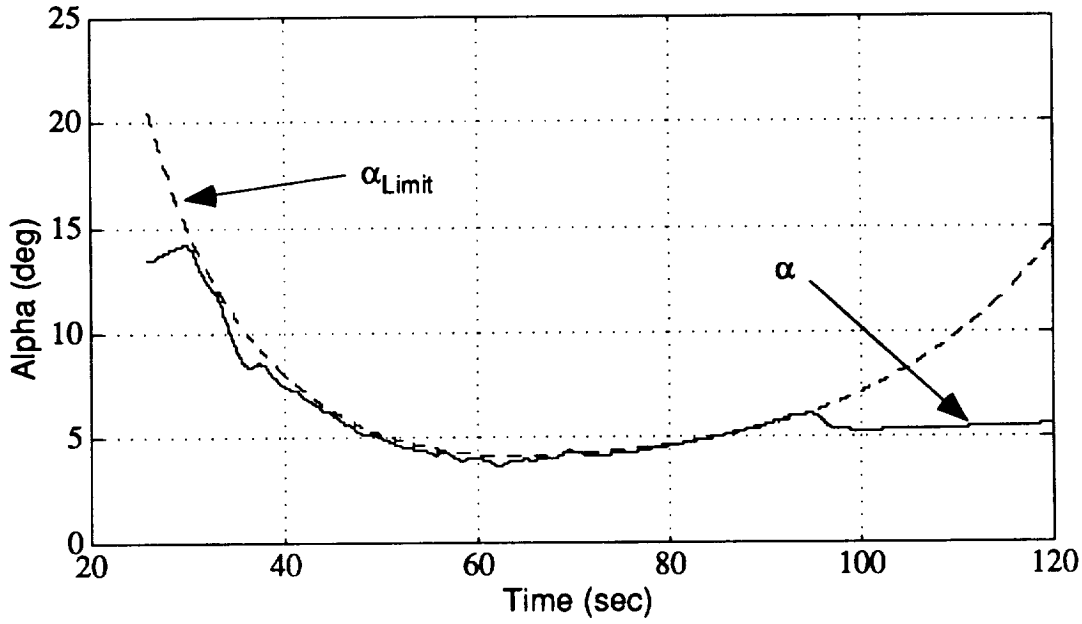

Figure 8.14 Angle of attack and angle of attack limit with estimated feedback of angle of attack in a 60% Vandenburg #70 head wind.

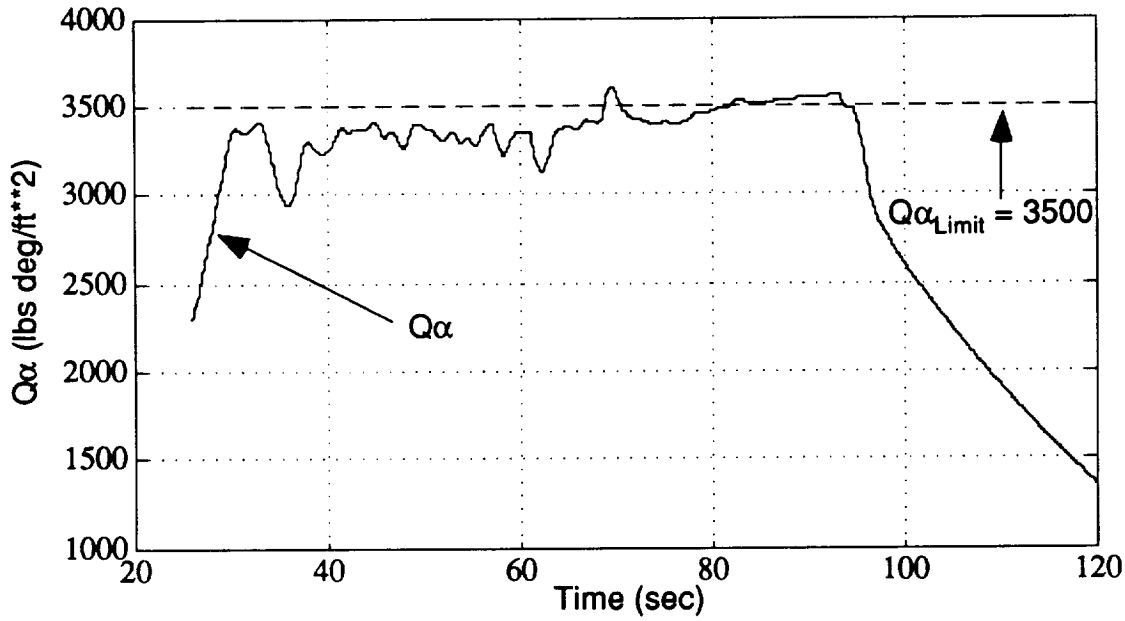

Figure 8.15 Qα and Qα limit with estimated angle of attack feedback in a 60% Vandenburg #70 head wind.

C-3

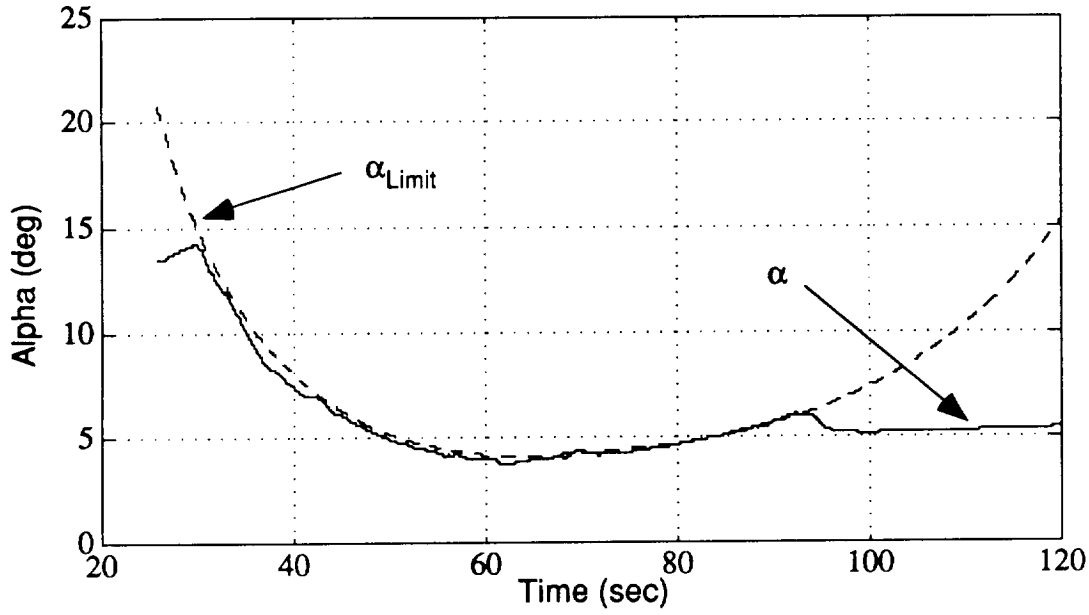

Figure 8.16 Angle of attack and angle of attack limit with estimated feedback of angle of attack and angular rate in a 60% Vandenburg #70 head wind.

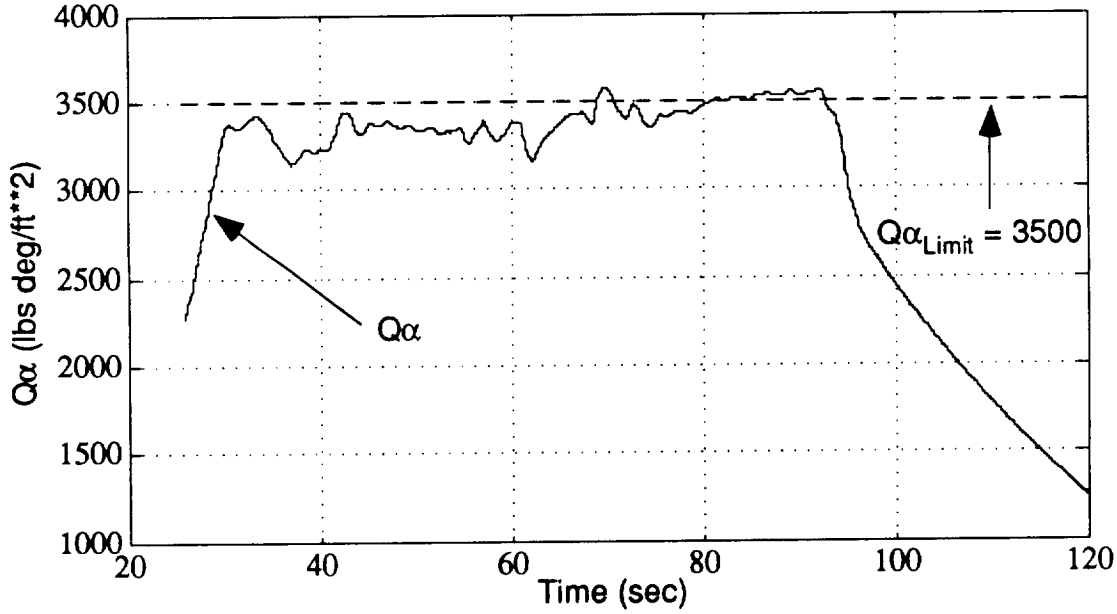

Figure 8.17 Qα and Qα limit with estimated angle of attack and angular rate feedback in a 60% Vandenburg #70 head wind.

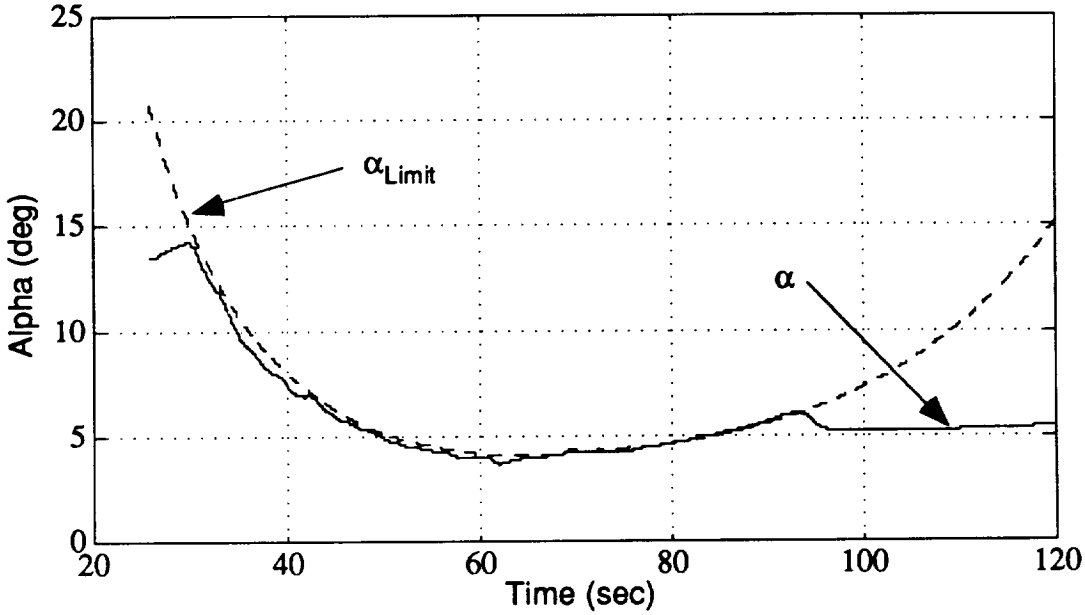

Figure 8.18 Angle of attack and angle of attack limit with estimated feedback of angle of attack, angular rate, and Q in a 60% Vandenburg #70 head wind.

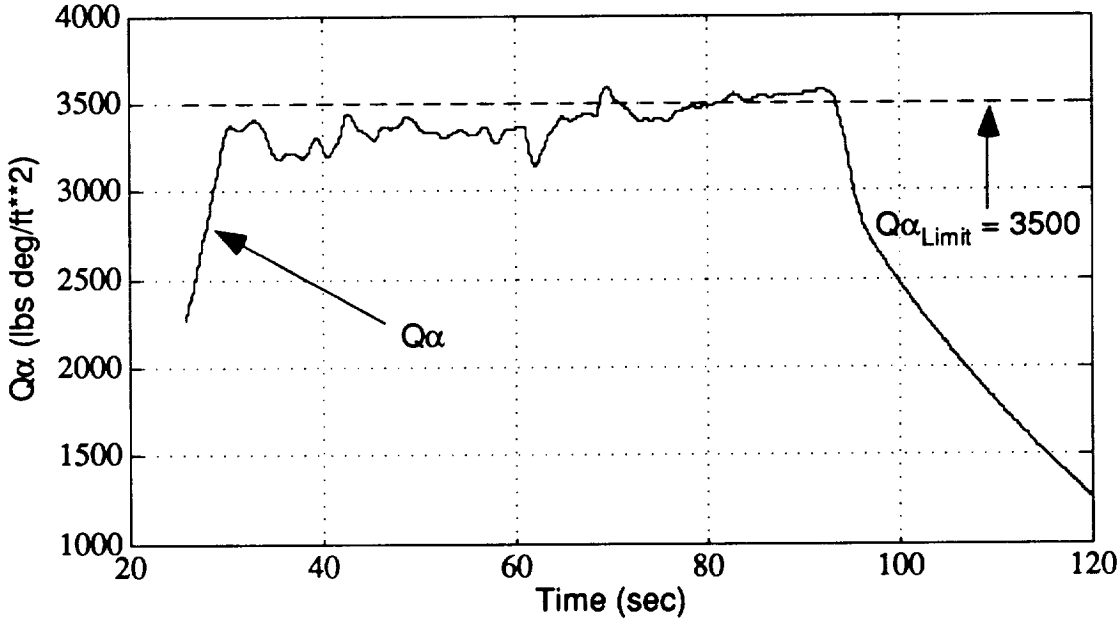

Figure 8.19 Qα and Qα limit with estimated angle of attack, angular rate, and Q feedback in a 60% Vandenburg #70 head wind.

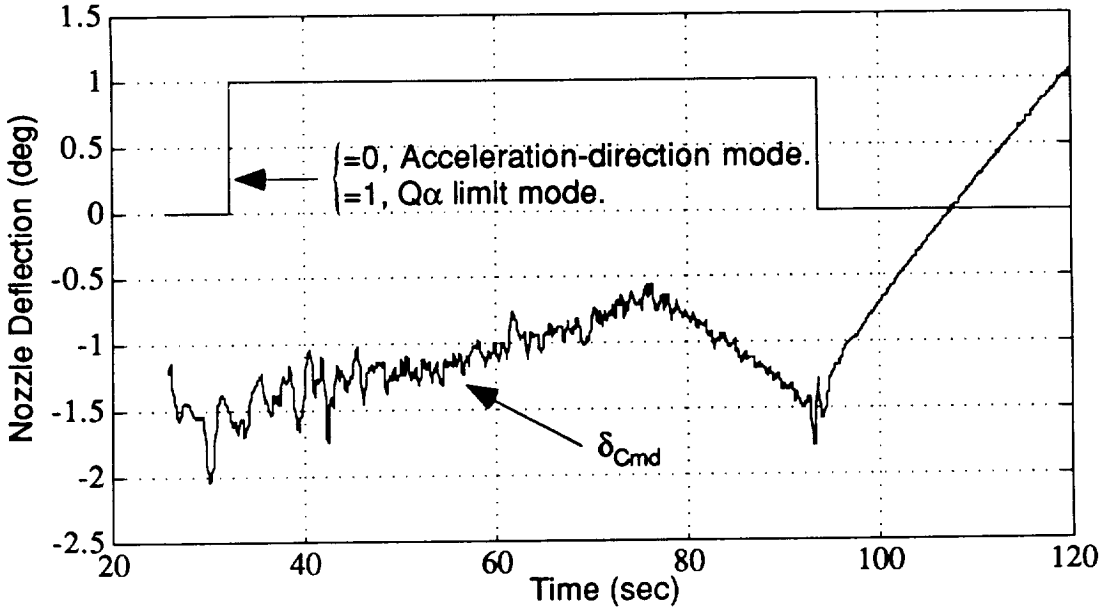

Figure 8.20 Commanded nozzle deflection with estimated angle of attack, angular rate, and Q feedback in a 60% Vandenburg #70 head wind.

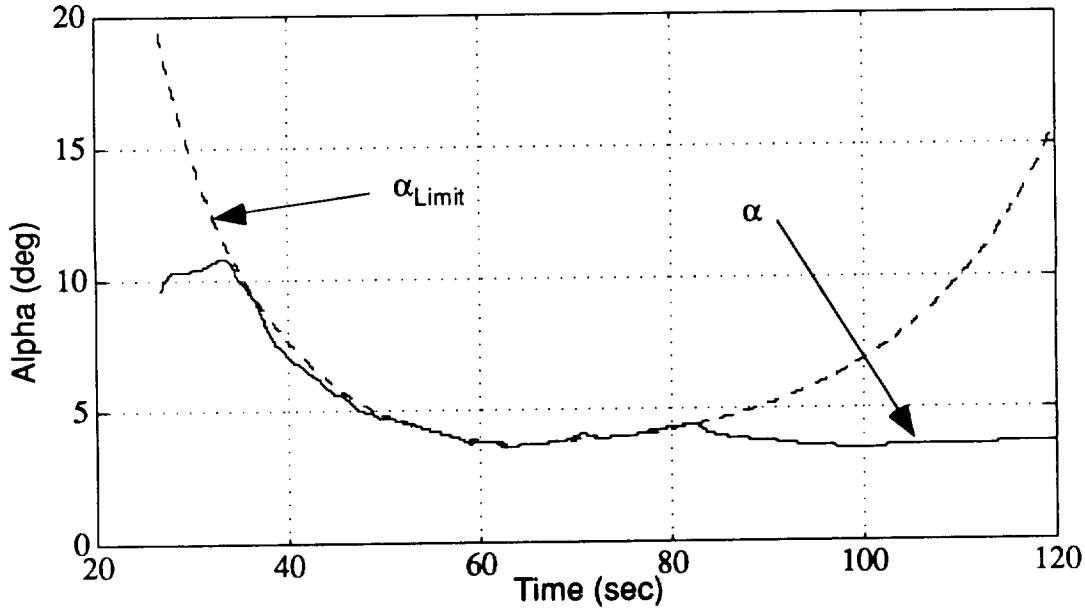

Figure 8.21 Angle of attack and angle of attack limit with estimated feedback of angle of attack, angular rate, and Q in a 60% Vandenburg #70 head wind. (Core on top of booster).

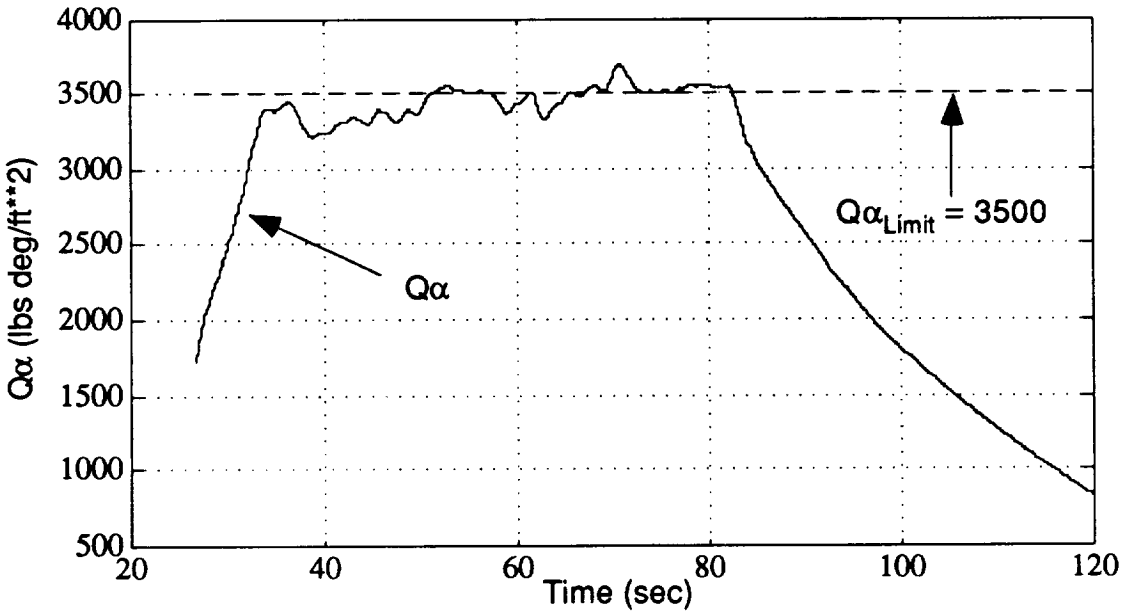

Figure 8.22 Qα and Qα limit with estimated angle of attack, angular rate, and Q feedback in a 60% Vandenburg #70 head wind. (Core on top of booster).

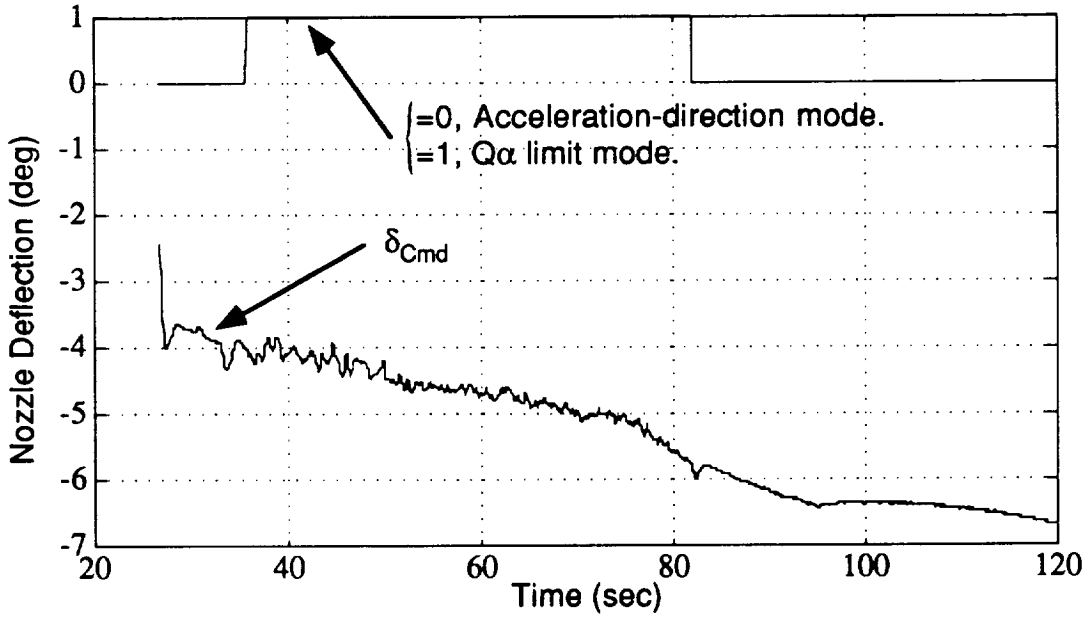

Figure 8.23 Commanded nozzle deflection with estimated angle of attack, angular rate, and Q feedback in a 60% Vandenburg #70 head wind. (Core on top of booster)

Chapter Nine

CONCLUSIONS AND RECOMMENDATIONS

9.1 Conclusions

The primary purpose of this thesis was to develop and evaluate an integrated concept of guidance, steering, control, load relief and estimation for application to the asymmetrical configuration of the Advanced Launch Vehicle (ALS). This concept is preliminary in that it was developed for an early ALS design for which comprehensive aerodynamic data, bending and slosh data, engine nozzle actuator data and IMU characteristics were not available. As a result, certain details had to be omitted from the system models and from the designs of the control and estimator systems. It is also preliminary in that much remains to be done in exploring predictive-adaptive concepts in guidance and control that might give the ALS greater flexibility and better performance in dealing with the effects of last-minute changes in payload, vehicle configuration, mission objectives and winds as well as in-flight changes in the wind environment. Nevertheless, there are a number of new component concepts and features embodied in this integrated concept that could provide a considerable advancement over present methods, with or without predictive-adaptive features.

The integrated concept that has been explored in this thesis centers on the use of acceleration-direction guidance and control in combination with an override control mode that limits the product of the dynamic pressure Q and the angle of attack α. This guidance and control approach has been studied for the case of an acceleration direction command that is stored as a function of time based on trajectory design computations that are carried out just prior to launch. These prelaunch design computations shape the trajectory for winds that are measured prior to launch with a specified $Q\alpha$ limit that is less than the limit employed in flight. The difference between in-flight and prelaunch limits on $Q\alpha$

provides some leeway to adjust the in-flight trajectory to compensate for the effects of changes in the winds from their prelaunch values.

As previously mentioned, the acceleration-direction guidance and control approach and the associated trajectory design program build upon concepts that were investigated earlier by Bushnell and Corvin, respectively. The acceleration-direction guidance and control with the $Q\alpha$-limit override was studied by Bushnell for the case of a symmetrical solid-propellant boost vehicle whose ideal post-launch endoatmospheric trajectory was a zero-α trajectory. The employment of this approach in the case of a liquid-propellant asymmetrical ALS with large angle of attack values and different vehicle properties requires some modifications. The trajectory design program developed by Corvin was for a guidance/steering system based on the flight path angle and a control system based on the angle of attack. Corvin's program generated a commanded flight path angle which was stored for in-flight use. The ALS version of Corvin's program generates a commanded acceleration direction for in-flight employment. In addition to these and other revisions in the design program and the basic guidance and control approach, the ALS system examined in this thesis includes new concepts in estimation of the angular rate, angular acceleration, angle of attack and dynamic pressure.

The innovations which have been considered in this thesis for the ALS application are:

(1) Alternative pitch rate profile for the launch maneuver which has a constant pitch rate in the latter half of the maneuver.

(2) Utilization of the trajectory design simulation to compute an acceleration-direction command for Phase Three by passing the simulation-determined acceleration-direction through the same low-pass filter that is employed in the in-flight acceleration direction estimator: This command is stored for in-flight use.

(3) Employment of a different set of compensation gains for each of the two control modes of Phase Three.

(4) Reinitialization of the forward-path control integral when switching control modes in Phase Three so as to prevent the gain changes from producing a step change in the engine nozzle command.

(5) Utilization of a first order complementary filter estimator to provide the rate feedback, employing an estimated acceleration input that relies on a feedback loop to estimate the angular acceleration produced by the aerodynamic axial force in combination with the offset of the center of pressure normal to the longitudinal axis.

(6) Employment of a second order complementary filter estimator to provide the angle of attack feedback, taking advantage of the properties of the second order estimator to minimize low-frequency errors produced by neglecting the effects of the slowly varying flight path angle.

(7) Use of the estimated angle of attack in combination with the estimated earth-relative velocity to estimate the dynamic pressure, approximating the effects of winds by assuming they are horizontal.

Other elements of the flight and ground software system that was tested in combination with the above features were based on the previous studies of a Shuttle 2 SSTO system by Corvin which shaped the design trajectory for Phase Three in terms of α and $q\alpha$ profiles and which employed the predictive-adaptive Powered Explicit Guidance in Phase Four. The simulation results, which were based on a rigid -body vehicle model with ideal actuators and other approximations, indicate reasonable overall performance with and without the effects of quantization in the attitude and velocity signals.

9.2 Recommendations

The basic approach of acceleration-direction guidance and control with a $Q\alpha$ override control mode , and the various features developed to implement and accompany this approach, provide a good starting point for studies of predictive-adaptive techniques for Phase Three in combination with improvements of the methods employed in this thesis for the other flight phases. More specifically, the following studies are recommended for future consideration:

(1) Improve and automate the program for trajectory design (including the possibilities of last-minute changes in the payload or the mission objectives).

(2) Effectively eliminate the adverse effects of errors in aerodynamic modeling, dynamic pressure estimation and Mach number estimation on the limiting of the angle of attack by defining the trajectory limit in terms of the normal aerodynamic force rather than the $Q\alpha$ product. (This procedure should result in a more accurate limiting of the normal aerodynamic force than is possible for the $Q\alpha$ product.)

(3) Consider the possibility of including a variable roll attitude in the trajectory design computations and also the possibility of changing the roll attitude in flight in a predetermined or adaptive fashion.

(4) Develop a predictive-adaptive guidance that adjusts an added rate bias in the acceleration-direction command in the same way as Corvin has adjusted a rate bias in a flight path angle command.[1]

(5) Compare the performance of the predictive-adaptive methods applied to the acceleration-direction guidance-and-control approach and the Corvin approach of guidance-steering based on the flight path angle in combination with an inner angle of attack control loop.

(6) Investigate other more complex predictive-adaptive techniques as applied to the more appropriate form of guidance and control.

(7) Utilize an updated simulation model of the ALS vehicle, including more comprehensive aerodynamic data, nozzle actuator dynamics, tail-wags-dog effects, bending modes, and ultimately including propellant slosh modes and possibly the detailed engine nozzle command logic.

(8) Study the problem of bending mode compensation, possibly considering adaptive techniques to deal with bending effects in the various estimators.

---

[1] Corvin, op cit.

Appendix A

Derivation of Equations of Motion

The angular momentum of a rigid body with respect to a fixed reference frame, **i**, in inertial space can be written as:

$$\mathbf{H}^{\mathbf{i}} = \int_m \mathbf{r} \times \mathbf{V}\, dm = \int_m \mathbf{r} \times \dot{\mathbf{r}}^{\mathbf{i}}\, dm \tag{A.1}$$

where

$\mathbf{r}$ = a position vector from q to a differential element dm.

$\dot{\mathbf{r}}^{\mathbf{i}} = \frac{d}{dt}^{\mathbf{i}} \mathbf{r}$ = the derivative of $\mathbf{r}$ taken relative to the inertial frame **i**.

The derivative of $\mathbf{r}$ relative to the inertial frame **i** can be expressed as the derivative relative to an arbitrary frame **f** by the relationship

$$\frac{d}{dt}^{\mathbf{i}} \mathbf{r} = \frac{d}{dt}^{\mathbf{f}} \mathbf{r} + \omega^{fi} \times \mathbf{r} \tag{A.2}$$

or simply

$$\dot{\mathbf{r}}^{\mathbf{i}} = \dot{\mathbf{r}}^{\mathbf{f}} + \omega \times \mathbf{r} \tag{A.3}$$

Substituting (A.3) into (A.1) yields:

$$\mathbf{H}^{\mathbf{i}} = \int_m \mathbf{r} \times \dot{\mathbf{r}}^{\mathbf{f}}\, dm + \int_m \mathbf{r} \times (\omega \times \mathbf{r})\, dm \tag{A.4}$$

If we then require that frame **f** be fixed with respect to the rigid body, and the origin of **f** coincide with the mass center of the body, then $\dot{\mathbf{r}}^{\mathbf{f}} = 0$ and equation (A.4) reduces to:

$$\mathbf{H}^{\mathbf{i}} = \int_{m} \mathbf{r} \times (\omega \times \mathbf{r})\, dm \tag{A.5}$$

By introducing a set of body fixed orthogonal unit vectors ($\mathbf{u}_1$, $\mathbf{u}_2$, $\mathbf{u}_3$) to establish the orientation of frame **f** at the mass center, ω and **r** can be expressed as

$$\mathbf{r} = r_1\mathbf{u}_1 + r_2\mathbf{u}_2 + r_3\mathbf{u}_3 \tag{A.6}$$

$$\omega = \omega_1\mathbf{u}_1 + \omega_2\mathbf{u}_2 + \omega_3\mathbf{u}_3 \tag{A.7}$$

Substituting these expressions into equation (A.5)

$$\begin{aligned}\mathbf{H} = &\left[\int (r_2^2 + r_3^2)\,\omega_1\, dm - \int r_1 r_2\, \omega_2\, dm - \int r_1 r_3\, \omega_3\, dm\right]\mathbf{u}_1 \\ &+\left[-\int r_2 r_1\, \omega_1\, dm + \int (r_3^2 + r_1^2)\,\omega_2\, dm - \int r_2 r_3\, \omega_3\, dm\right]\mathbf{u}_2 \\ &+\left[-\int r_3 r_1\, \omega_1\, dm - \int r_3 r_2\, \omega_2\, dm + \int (r_1^2 + r_2^2)\,\omega_3\, dm\right]\mathbf{u}_3\end{aligned} \tag{A.8}$$

Or in matrix form

$$\mathbf{H} \equiv \begin{bmatrix} H_1 \\ H_2 \\ H_3 \end{bmatrix} = \begin{bmatrix} I_{11} & I_{12} & I_{13} \\ I_{21} & I_{22} & I_{23} \\ I_{31} & I_{32} & I_{33} \end{bmatrix} \begin{bmatrix} \omega_1 \\ \omega_2 \\ \omega_3 \end{bmatrix} \tag{A.9}$$

Where the diagonal terms I_{11}, I_{22}, I_{33} are called the principal moments of inertia, and the off-diagonal terms are called the products of inertia.

It is assumed that for the ALS vehicle the body pitch, yaw and roll axes ($\mathbf{u}_1$, $\mathbf{u}_2$, $\mathbf{u}_3$) form a principal axes vector basis. Therefore, all of the off-diagonal terms in Equation (A.9) are equal to zero. Equation (A.9) can then be reduced to

$$\mathbf{H}^{\mathbf{b}} = I_{11}\omega_1\mathbf{u}_1 + I_{22}\omega_2\mathbf{u}_2 + I_{33}\omega_3\mathbf{u}_3 \qquad \text{(A.10)}$$

The rate of change of the angular momentum relative to an inertially fixed frame is equal to the vector sum, $\mathbf{M}$, of all external torques on the system:

$$\mathbf{M} = \dot{\mathbf{H}}^{\mathbf{i}} \qquad \text{(A.11)}$$

It is convenient to express $\dot{\mathbf{H}}^{\mathbf{i}}$ in term of the derivative relative to the body fixed system $\mathbf{b}$:

$$\mathbf{M} = \dot{\mathbf{H}}^{\mathbf{i}} = \dot{\mathbf{H}}^{\mathbf{b}} + \omega \times \mathbf{H} \qquad \text{(A.12)}$$

Substituting (A.10) into (A.12) yields

$$\begin{aligned}\mathbf{M} = {} & (I_{11}\dot{\omega}_1\mathbf{u}_1 + I_{22}\dot{\omega}_2\mathbf{u}_2 + I_{33}\dot{\omega}_3\mathbf{u}_3) \\ & + (\omega_1\mathbf{u}_1 + \omega_2\mathbf{u}_2 + \omega_3\mathbf{u}_3) \\ & \times (I_{11}\omega_1\mathbf{u}_1 + I_{22}\omega_2\mathbf{u}_2 + I_{33}\omega_3\mathbf{u}_3)\end{aligned} \qquad \text{(A.13)}$$

$$\begin{aligned}\mathbf{M} = {} & [I_{11}\dot{\omega}_1 - \omega_2\omega_3(I_{22} - I_{33})]\,\mathbf{u}_1 \\ & + [I_{22}\dot{\omega}_2 - \omega_3\omega_1(I_{33} - I_{11})]\,\mathbf{u}_2 \\ & + [I_{33}\dot{\omega}_3 - \omega_1\omega_2(I_{11} - I_{22})]\,\mathbf{u}_3\end{aligned} \qquad \text{(A.14)}$$

Equivalently, the vector $\mathbf{M}$ in body coordinates is given by

$$\mathbf{M} = \begin{bmatrix} I_{11}\,\dot{\omega}_1 - \omega_2\,\omega_3\,(I_{22} - I_{33}) \\ I_{22}\,\dot{\omega}_2 - \omega_3\,\omega_1\,(I_{33} - I_{11}) \\ I_{33}\,\dot{\omega}_3 - \omega_1\,\omega_2\,(I_{11} - I_{22}) \end{bmatrix} \qquad \text{(A.15)}$$

The expressions for the three components of $\mathbf{M}$ in (A.15) represent Euler's Equation's of Motion.

Appendix B

Determination of Aero-Coefficients

Figure B.1 is a three dimensional sketch of a procedure for determining the coefficient of normal force, Cn, given a Mach number and angle of attack. The aero-data for the ALS was provided in a matrix format where each row of data corresponds to a constant Mach number, and each column corresponds to a constant angle of attack. The curves shown in Figure B.1 represent curve fits of two adjacent rows from the aero data matrix. A total of fourteen such curves comprise the matrix. Each curve is calculated by splicing together several third order curves. Each third order curve spans two adjacent discrete Mach points and its slope is continous from point to point. The "Low Mach" and "High Mach" curves were found by determining which adjacent rows of the matrix bound the current Mach number of the vehicle. The procedure for computing Cn from a given Mach number and angle of attack is outlined in Table B.1. The same procedure is used for determining the coefficient of axial force, Ca.

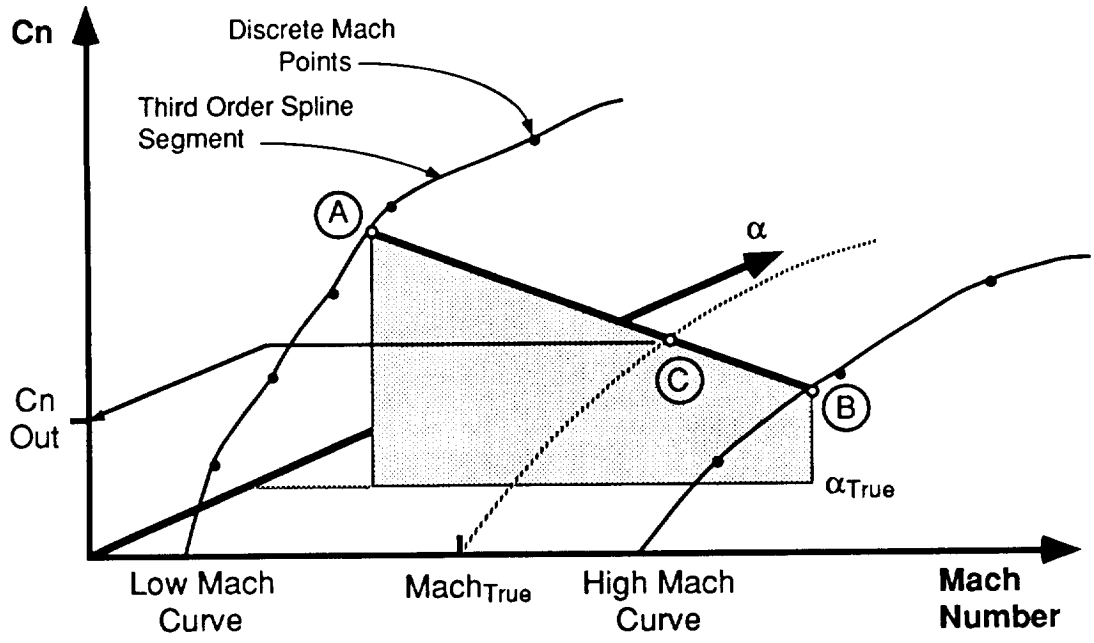

Figure B.1 Determination of Cn by Linear Interpolation.

1) Select the two 3^d order Cn vs α curves that correspond to the consecutive Mach numbers ($Mach_{Low}$ and $Mach_{High}$) that bound the given Mach number, $Mach_{True}$. These curves are designated as the Low Mach and High Mach curves.

2) For the given value of angle of attack, α_{True}, compute the value of Cn on both the Low Mach and High Mach curves. - Points Ⓐ and Ⓑ in Figure C.1.

3) Linearly interpolate in Mach number between points Ⓐ and Ⓑ to determine the value of Cn for $Mach_{True}$. - Point Ⓒ in Figure C.1. This value is the desired value of Cn as a function of α_{True} and $Mach_{True}$.

Table B.1 Procedure for Determining Cn.

Appendix C

Determination of Mass Properties

In order to simulate the ALS vehicle, a simple model was constructed to approximate the time varying mass, center of gravity location, and pitch moment of inertia. The distribution of the total dry weight for each stage among all the components was based on the percentage of volume that each component occupied. In addition, because only the total height and width of each stage was provided, all other dimensions such as the thickness of each fuel tank was estimated. The data was provided by the General Dynamics Corportation, Space Systems Division.

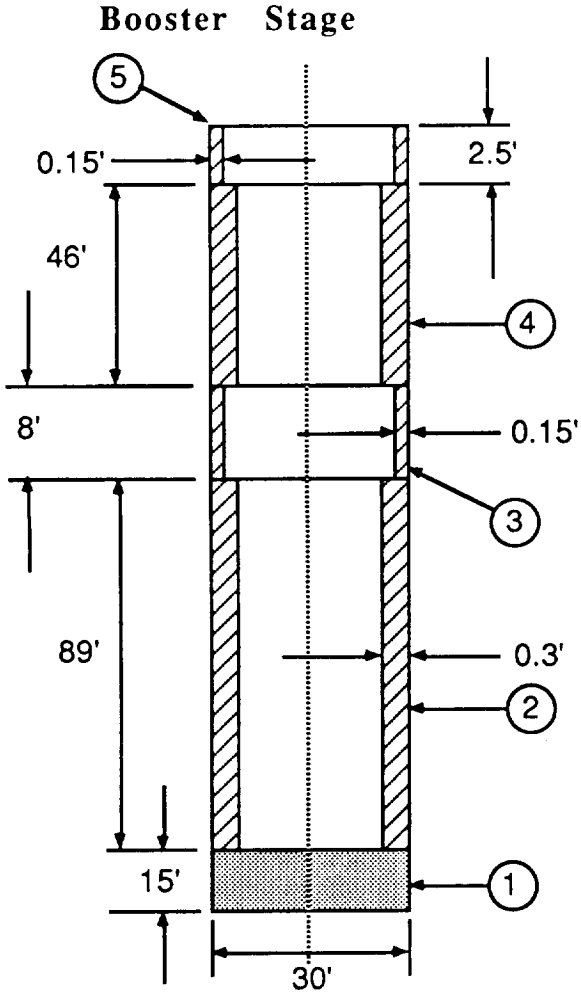

Component	Mass (Slugs)
1 - Engine Module	1688
2 - Hydrogen Tank	2597
3 - Inter-Tank Adapter	117
4 - Oxygen Tank	1342
5 - Nose Cone	37
TOTAL	**5781**

Figure C.1 Booster Stage Component Masses and Dimensions.

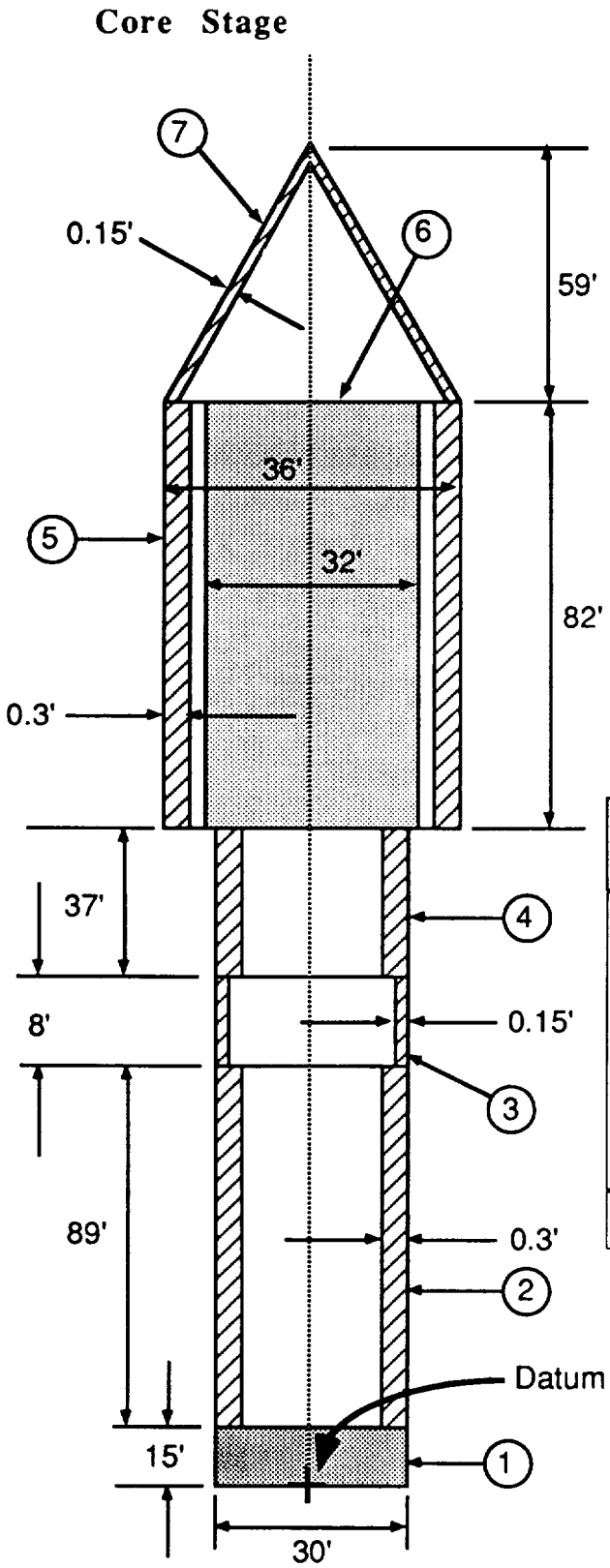

Component	Mass (Slugs)
1 - Engine Module	723
2 - Hydrogen Tank	2782
3 - Inter-Tank Adapter	125
4 - Oxygen Tank	1156
5 - Payload Container	1010
6 - Payload	4973
7 - Nose Cone	155
TOTAL	**10924**

Figure C.2 Core Stage Component Masses and Dimensions.

Propulsion Module

Propulsion Module	Booster	Core
Mass of Engines Number of Engines	209.6 7	209.6 3
Total Engine Mass	1467.3	628.8
Common Structure @ 15% Total Mass	220.1	94.3
TOTAL MASS (Slugs)	**1687.4**	**723.1**

Table C.1 Core and Booster Propulsion Masses.

Appendix D

Vehicle Rigid Body Equations of Motion

The scope of this thesis is limited to the evaluation and study of flight software concepts in the pitch plane. With this assumption, the trajectory pitch plane motion of the vehicle can be defined by three differential equations. The free body diagram of the vehicle in the pitch plane is shown in Figure D1. The acceleration of the center of mass can be expressed in the earth relative velocity direction frame (UVX, UVY, UVZ) by the relationship:

$$\left[\dot{\mathbf{V}}_E\right]_{\substack{\text{relative to the local}\\ \text{geographic frame}}} = \left[\dot{\mathbf{V}}_E\right]_{\substack{\text{relative to the}\\ \text{velocity frame}}} + \left(\omega \times \mathbf{V}_E\right) \tag{D.1}$$

where ω is the angular velocity of the velocity reference frame with respect to the local geographic frame. Since the velocity is along the x axis of the velocity direction vector,

$$\left[\dot{\mathbf{V}}_E\right]_{\substack{\text{relative to the}\\ \text{velocity frame}}} = \dot{V}_E\,\mathbf{UVX} \tag{D.2}$$

The rotation rate of the velocity coordinate system is the flight path angle rate so that

$$\omega \times \mathbf{V}_E = \dot{\gamma}\,\mathbf{UVY} \times V\,\mathbf{UVX} = -V\dot{\gamma}\,\mathbf{UVZ} \tag{D.3}$$

Substituting Equations (D.2) and (D.3) into Equation (D.1),

$$\dot{\mathbf{V}}_E = \dot{V}_E\,\mathbf{UVX} - V\dot{\gamma}\,\mathbf{UVZ} \tag{D.4}$$

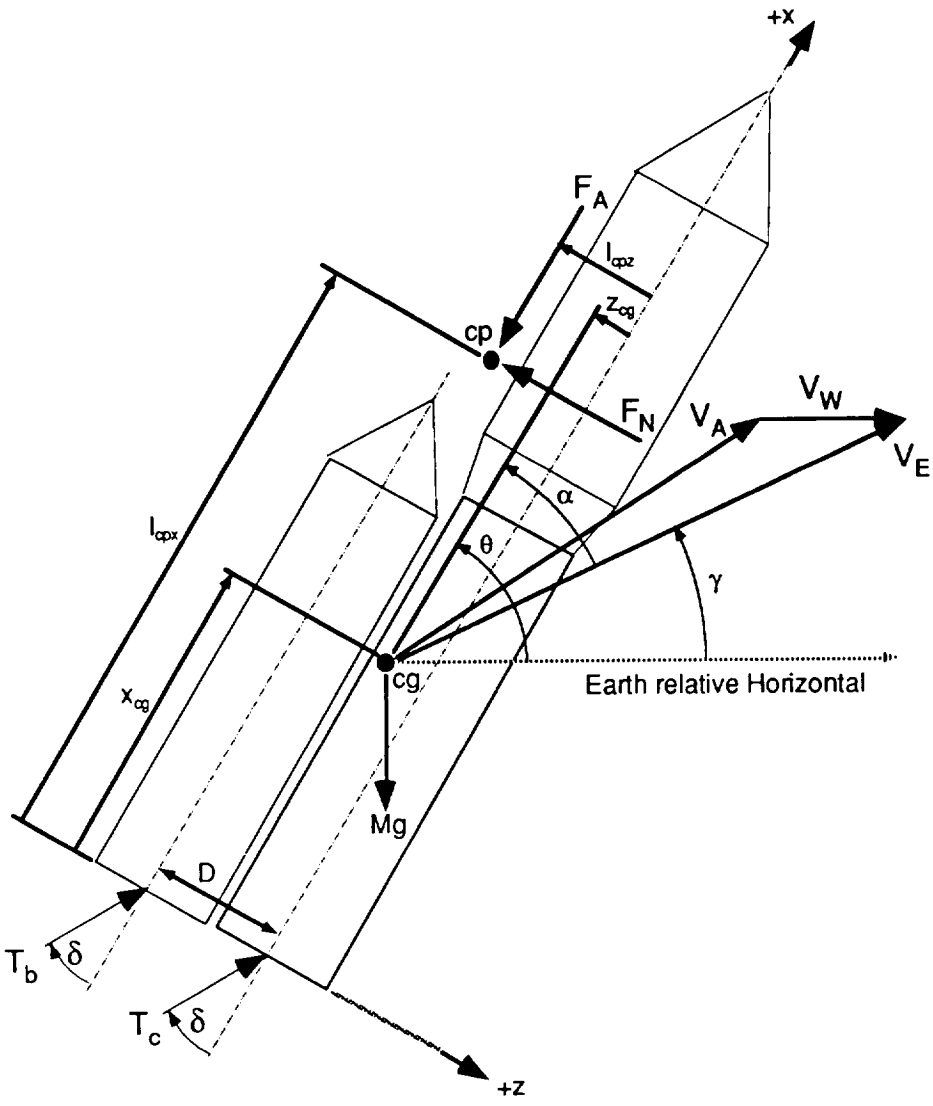

Figure D.1 Vehicle Free Body Diagram.

The corresponding equation of motion is given by

$$M \dot{V}_E = \sum [F]_{\text{Velocity frame}} \qquad \text{(D.5)}$$

Summing the forces in the **UVX**, and **UVZ** directions yields the first two equations of motion.

$$\sum F_{uvz} = -M\dot{\gamma}V = T_b \sin(\delta - \alpha) + T_c \sin(\delta - \alpha) + Mg \cos(\gamma) - SQC_n \cos(\alpha) + SQC_a \sin(\alpha) \quad \text{(D.6)}$$

$$\sum F_{uvx} = M\dot{V} = T_b \cos(\delta - \alpha) + T_c \cos(\delta - \alpha) - Mg \sin(\gamma) - SQC_a \cos(\alpha) - SQC_n \sin(\alpha) \quad \text{(D.7)}$$

Summing the torque about the **UVY** axis yields the third equation of motion,

$$\sum T_{uvy} = I_{yy}\ddot{\theta} = T_b \sin(\delta)\, x_{cg} + T_c \sin(\delta)\, x_{cg} - T_b \cos(\delta)(D + z_{cg}) - T_c \cos(\delta)\, z_{cg} + SQC_n(l_{cpx} - x_{cg}) + SQC_a(-l_{cpz} + z_{cg}) \quad \text{(D.8)}$$

where

I_{yy} = The inertia about the pitch axis.

M = The mass of the vehicle

$SQC_a = (F_a)$ = the axial component of the aerodynamic force.

$SQC_n = (F_n)$ = the normal component of the aerodynamic force.

g = gravity

Solving Equation (D.8) for $\ddot{\theta}$ yields:

$$\ddot{\theta} = \frac{(T_b + T_c)\sin(\delta)\, x_{cg}}{I_{yy}} - \frac{T_b \cos(\delta)(D + z_{cg})}{I_{yy}} - \frac{T_c \cos(\delta)\, z_{cg}}{I_{yy}} + \frac{SQC_n(l_{cpx} - x_{cg})}{I_{yy}} + \frac{SQC_a(-l_{cpz} + z_{cg})}{I_{yy}} \quad \text{(D.9)}$$

Solving Equation (D.6) for $\dot{\gamma}$ yields

$$\dot{\gamma} = \frac{(T_b+T_c)\sin(\delta - \alpha) - SQC_n\cos(\alpha) + SQC_a\sin(\alpha) + Mg\cos(\theta - \alpha)}{-MV} \tag{D.10}$$

Since $\dot{\gamma} = \dot{\theta} - \dot{\alpha}$, Equation (D.10) can be solved for $\dot{\alpha}$ to give

$$\dot{\alpha} = \dot{\theta} + \frac{(T_b+T_c)\sin(\delta - \alpha) - SQC_n\cos(\alpha) + SQC_a\sin(\alpha) + Mg\cos(\theta - \alpha)}{MV} \tag{D.11}$$

Linearized Equations of Motion

Equation (D.9) can be linearized by the following approximation:

$$\Delta\ddot{\theta} \cong \frac{\partial\ddot{\theta}}{\partial\delta}\Delta\delta + \frac{\partial\ddot{\theta}}{\partial\alpha}\Delta\alpha \tag{D.12}$$

where Δ denotes a perturbation of the state variable from its nominal value along the trajectory. The derivatives on the right side of Equation (D.12) can be approximated by:

$$\frac{\partial\ddot{\theta}}{\partial\delta} = \frac{(T_b+T_c)\,x_{cg}\cos(\delta_{ss}) + T_b(D+z_{cg})\sin(\delta_{ss}) + T_c\,z_{cg}\sin(\delta_{ss})}{I_{yy}} \tag{D.13}$$

$$\frac{\partial\ddot{\theta}}{\partial\alpha} = \frac{SQ\left(\frac{\partial C_n}{\partial\alpha}(l_{cpx} - x_{cg}) + \frac{\partial(l_{cpx} - x_{cg})}{\partial\alpha}C_n\right)}{I_{yy}}$$

$$+\frac{SQ\left(\frac{\partial C_a}{\partial \alpha}\left(-l_{cpz}+z_{cg}\right)+\frac{\partial\left(-l_{cpz}+z_{cg}\right)}{\partial \alpha}C_a\right)}{I_{yy}} \tag{D.14}$$

The derivatives of $\left(l_{cpx}-x_{cg}\right)$ and $\left(-l_{cpz}+z_{cg}\right)$ with respect to α are assumed to be negligible for this thesis study. Substituting Equations (D.13) and (D.14) into Equation (D.12) yields the following rigid body state equation

$$\Delta\ddot{\theta}=\frac{\left(T_b+T_c\right)x_{cg}\cos\left(\delta_{ss}\right)+T_b\left(D+z_{cg}\right)\sin\left(\delta_{ss}\right)+T_c\,z_{cg}\sin\left(\delta_{ss}\right)}{I_{yy}}\Delta\delta$$
$$+\frac{SQC_{n\alpha}\left(l_{cpx}-x_{cg}\right)+SQC_{a\alpha}\left(-l_{cpz}+z_{cg}\right)}{I_{yy}}\Delta\alpha \tag{D.15}$$

Equation (D.11) can be linearized by the following approximation.

$$\Delta\dot{\alpha}\cong\frac{\partial\dot{\alpha}}{\partial\theta}\Delta\theta+\frac{\partial\dot{\alpha}}{\partial\delta}\Delta\delta+\frac{\partial\dot{\alpha}}{\partial\dot{\theta}}\Delta\dot{\theta}+\frac{\partial\dot{\alpha}}{\partial\alpha}\Delta\alpha \tag{D.16}$$

The derivatives on the right side of Equation (D.16) can be expressed as:

$$\frac{\partial\dot{\alpha}}{\partial\theta}=\frac{-g}{V}\sin\left(\gamma_{ss}\right) \tag{D.17}$$

$$\frac{\partial\dot{\alpha}}{\partial\delta}=\frac{\left(T_b+T_c\right)\cos\left(\delta_{ss}-\alpha_{ss}\right)}{MV} \tag{D.18}$$

$$\frac{\partial\dot{\alpha}}{\partial\dot{\theta}}=1 \tag{D.19}$$

$$\frac{\partial \dot{\alpha}}{\partial \alpha} = \left\{ \frac{-(T_b+T_c)\cos(\delta_{ss} - \alpha_{ss}) - SQ\left(\frac{\partial C_n}{\partial \alpha}\cos(\alpha_{ss}) - C_n \sin(\alpha_{ss})\right)}{MV} + \frac{SQ\left(\frac{\partial C_a}{\partial \alpha}\sin(\alpha_{ss}) + C_a \cos(\alpha_{ss})\right)}{MV} + \frac{g \sin(\gamma_{ss})}{V} \right\} \quad \text{(D.20)}$$

Substituting Equations (D.17) through (D.20) into Equation (D.16) yields the following state equation

$$\Delta\dot{\alpha} = \frac{-g}{V}\sin(\gamma_{ss})\Delta\theta + \Delta\dot{\theta} + \frac{(T_b+T_c)\cos(\delta_{ss} - \alpha_{ss})}{MV}\Delta\delta + \left\{ \frac{g \sin(\gamma_{ss})}{V} - \frac{(T_b+T_c)\cos(\delta_{ss} - \alpha_{ss})}{MV} - \frac{SQ(C_{n\alpha}\cos(\alpha_{ss}) - C_n \sin(\alpha_{ss}))}{MV} + \frac{SQ(C_{a\alpha}\sin(\alpha_{ss}) + C_a \cos(\alpha_{ss}))}{MV} \right\} \Delta\alpha \quad \text{(D.21)}$$

Rigid Body Poles

Given the linearized state equations in (D.15) and (D.21) define

$$C1 = \frac{1}{MV}\left\{-(T_b+T_c)\cos(\delta_{ss} - \alpha_{ss}) - SQ(C_{n\alpha}\cos(\alpha_{ss}) - C_n \sin(\alpha_{ss})) + SQ(C_{a\alpha}\sin(\alpha_{ss}) + C_a \cos(\alpha_{ss}))\right\} \quad \text{(D.22)}$$

$$C2 = \frac{g \sin(\gamma_{ss})}{V} \quad \text{(D.23)}$$

$$C3 = \frac{(T_b+T_c)\cos(\delta_{ss} - \alpha_{ss})}{MV} \quad \text{(D.24)}$$

$$C4 = \frac{SQC_{n\alpha}\left(l_{cpx} - x_{cg}\right)}{I_{yy}} + \frac{SQC_{a\alpha}\left(-l_{cpz} + z_{cg}\right)}{I_{yy}} \qquad (D.25)$$

$$C5 = \frac{\left(T_b + T_c\right) x_{cg} \cos\left(\delta_{ss}\right)}{I_{yy}} + \frac{T_b\left(D+z_{cg}\right) \sin\left(\delta_{ss}\right)}{I_{yy}} + \frac{T_c\, z_{cg} \sin\left(\delta_{ss}\right)}{I_{yy}} \qquad (D.26)$$

Equations (D.15) and (D.21) can then be expressed as

$$\Delta\dot{\alpha} = -C2\ \Delta\theta + \Delta\dot{\theta} + C3\ \Delta\delta + \left(C2 + C1\right)\Delta\alpha \qquad (D.27)$$

$$\Delta\ddot{\theta} = C5\ \Delta\delta + C4\ \Delta\alpha \qquad (D.28)$$

Typical values for C1, C2, C3, C4, and C5 at 8, 60, and 120 seconds from ignition are shown in Table I.1. C5, which is inversely proportional to the inertia of the vehicle, increases during flight. The values of C1, C2, and C3 decrease as the vehicle velocity increases. In Laplace notation Equations (D.27) and (D.28) can be expressed as

$$\left(s - \left(C1 + C2\right)\right)\Delta\alpha = \left(s - C2\right)\Delta\theta + C3\ \Delta\delta \qquad (D.29)$$

$$s^2\Delta\theta = C5\ \Delta\delta + C4\ \Delta\alpha \qquad (D.30)$$

By solving for $\Delta\alpha$ in Equation (D.29) and substituting the result into Equation (D.30), the rigid body transfer function relating the commanded nozzle deflection to the resulting vehicle attitude can be expressed as

$$\frac{\Delta\theta\,(s)}{\Delta\delta\,(s)} = \frac{C5\left\{s + \left\{\frac{C3\ C4}{C5} - \left(C2 + C1\right)\right\}\right\}}{\left\{s^3 - \left(C1 + C2\right)s^2 - C4\ s + C2\ C4\right\}} \qquad (D.31)$$

Time (sec)	C1	C2	C3	C4	C5
8	-.4192	.2928	.4161	.0060	3.022
66	-.0625	.0171	.0452	.5909	3.746
90	-.0505	.0074	.0304	1.000	4.046
120	-.0248	.0027	.0206	.3426	4.449

Table D.1 Typical rigid body dynamic coefficients.

The characteristic equation of the system is therefore,

$$s^3 - (C1 + C2)\, s^2 - C4\, s + C2C4 = 0 \qquad \text{(D.32)}$$

Equation (D.32) has three roots one of which is small compared to the other two. To obtain an approximation for the larger two roots of this characteristic equation first set the input nozzle deflection in Equations (D.29) and (I.30) to zero. The state equations can then be expressed as

$$\Delta\alpha\,(s - (C1 + C2)) = \Delta\theta\,(s - C2) \qquad \text{(D.33)}$$

and

$$\Delta\theta\, s^2 = C4\, \Delta\alpha \qquad \text{(D.34)}$$

Since C2 is small compared to s Equation (D.33) can be approximated by

$$\Delta\alpha\,(s - C1) = \Delta\theta\, s \qquad \text{(D.35)}$$

Solving for $\Delta\alpha$ in Equation (D.35) and substituting the result into Equation (D.34) results in the simplified equation

$$s^2 - C1s - C4 \cong 0 \tag{D.36}$$

Assuming that $(0.25\ C1^{2)} << C4$ then the solution to (D.36) is

$$s \cong \frac{C1}{2} \pm \sqrt{C4} \tag{D.37}$$

The remaining unstable root is very close to zero. To find an approximation for this root Equation (D.32) can be written as

$$\left[\left(s^2 - (C1 + C2)\ s - C4\right)\right] s + C2C4 = 0 \tag{D.38}$$

For small values of s, the terms s^2 and (C1 + C2)s are small compared to C4. Eliminating these terms results in

$$-C4s + C2\ C4 \cong 0 \tag{D.39}$$

and the solution is

$$s \cong C2 \tag{D.40}$$

Appendix E

Continuous Rate Estimator Transfer Functions

From the block diagram of the simplified continuous rate estimator illustrated in Figure 4.10, a set of transfer functions relating the state variables $\hat{\omega}$, $\dot{\hat{\omega}}_1$, and $\dot{\hat{\omega}}_b$ to the inputs ω and $\dot{\omega}_b$ can be written in matrix form as:

$$\begin{bmatrix} 1 & \dfrac{-\tau}{\tau s + 1} & 0 \\ 0 & 1 & -1 \\ \dfrac{-K}{\tau_1 s + 1} & \dfrac{K}{s(\tau_1 s + 1)} & 1 \end{bmatrix} \begin{bmatrix} \hat{\omega} \\ \dot{\hat{\omega}}_1 \\ \dot{\hat{\omega}}_b \end{bmatrix} = \begin{bmatrix} \dfrac{1}{\tau s + 1} \\ s \\ 0 \end{bmatrix} \omega - \begin{bmatrix} 0 \\ 1 \\ 0 \end{bmatrix} \dot{\omega}_b \qquad \text{(E.1)}$$

Algebraically Equation (E.1) can also be expressed as:

$$A\,\mathbf{x} = B\,\omega - C\,\dot{\omega}_b \qquad \text{(E.2)}$$

By treating each input separately, transfer functions relating ω and $\dot{\omega}_b$ to each of the state quantities $\hat{\omega}$, $\dot{\hat{\omega}}_1$, and $\dot{\hat{\omega}}_b$ can be obtained by solving the following two matrix equations using Cramer's Rule. That is:

$$x_j = \frac{\det D_j}{\det A}\,\omega \qquad \text{(E.3)}$$

and

$$x_j = \frac{\det E_j}{\det A}\,\dot{\omega}_b \qquad \text{(E.4)}$$

where

$\det A$ = the determinant of the A matrix.

x_j = the j th component of the **x** vector.

$\det D_j$ = the determinant of the matrix formed by replacing the jth column of the A matrix by the column vector B.

$\det E_j$ = the determinant of the matrix formed by replacing the jth column of the A matrix by the column vector C.

Using Equation (E.3) the transfer function relating the estimated angular rate, $\hat{\omega}$, to the true rate, ω, is given by:

$$\hat{\omega} = \frac{\det \begin{bmatrix} \frac{1}{\tau s + 1} & \frac{-\tau}{\tau s + 1} & 0 \\ s & 1 & -1 \\ 0 & \frac{K}{s(\tau_1 s + 1)} & 1 \end{bmatrix}}{\det A} \omega \qquad \text{(E.5)}$$

Therefore,

$$\frac{\hat{\omega}}{\omega} = \frac{1 + \frac{K}{s(\tau_1 s + 1)(\tau s + 1)}}{1 + \frac{K}{s(\tau_1 s + 1)(\tau s + 1)}} = 1 \qquad \text{(E.6)}$$

The effect of an unmodelled angular acceleration disturbance upon the estimate of angular rate can be found by utilizing Equation (E.4). The transfer function relating $\hat{\omega}$ to $\dot{\omega}_b$ can then be expressed as:

$$\hat{\omega} = \frac{\det \begin{bmatrix} 0 & \frac{-\tau}{\tau s + 1} & 0 \\ -1 & 1 & -1 \\ 0 & \frac{K}{s(\tau_1 s + 1)} & 1 \end{bmatrix}}{\det A} \dot{\omega}_b \qquad \text{(E.7)}$$

Therefore,

$$\frac{\hat{\omega}}{\dot{\omega}_b} = \frac{-\tau\, s(\tau_1 s + 1)}{s(\tau_1 s + 1)(\tau s + 1) + K} \qquad \text{(E.8)}$$

The response of the estimate of unmodelled angular acceleration estimate to an angular acceleration disturbance input can also be determined using Equation (E.4). Again, applying Cramer's rule:

$$\hat{\dot{\omega}}_b = \frac{\det \begin{bmatrix} 1 & \frac{-\tau}{\tau s + 1} & 0 \\ 0 & 1 & -1 \\ \frac{-K}{\tau_1 s + 1} & \frac{K}{s(\tau_1 s + 1)} & 0 \end{bmatrix}}{\det A} \dot{\omega}_b \qquad \text{(E.9)}$$

Therefore,

$$\frac{\hat{\dot{\omega}}_b}{\dot{\omega}_b} = \frac{K}{s(\tau_1 s + 1)(\tau s + 1) + K} \qquad \text{(E.10)}$$

Similarly, the response of the high frequency estimate of angular acceleration, $\hat{\dot{\omega}}_1$, to an angular acceleration disturbance input is given by:

$$\hat{\dot{\omega}}_1 = \frac{\det \begin{bmatrix} 1 & 0 & 0 \\ 0 & -1 & -1 \\ \frac{-K}{\tau_1 s + 1} & 0 & 1 \end{bmatrix}}{\det A} \dot{\omega}_b \qquad \text{(E.11)}$$

Therefore,

$$\frac{\hat{\dot{\omega}}_1}{\dot{\omega}_b} = \frac{-s(\tau_1 s + 1)(\tau s + 1)}{s(\tau_1 s + 1)(\tau s + 1) + K} \qquad \text{(E.12)}$$

Appendix F

Relationships Between Continuous and Discrete Rate Estimator Coefficients

In Chapter 3, a continuous representation of the complementary low-pass and high-pass filters was given in Figure 4.5. The corresponding discrete representation was developed in that chapter and was shown in Figure 4.6. The time constant, τ, in the discrete case is the same as that shown in the continous case.

A similar approach can be used to develop a discrete representation of the angular acceleration loop from the simplified continuous model. The continuous loop is shown in Figure F.1 and contains an integrator in series with a low pass filter. The continuous LaPlace operator, s, can be approximated in the discrete z-domain by the bilinear transformation.

$$s \cong \frac{2}{T}\frac{\left(1 - z^{-1}\right)}{\left(1 + z^{-1}\right)} \tag{F.1}$$

where T is the sampling time of the discrete filter. Substituting this expression for s in the low pass filter block of Figure F.1 results in a digital filter of the form:

$$\frac{\hat{\dot{\omega}}_b}{\hat{\dot{\omega}}_{Error_{Int}}} = \frac{\left(1 + z^{-1}\right)\dfrac{1}{\left(\dfrac{2\tau_1}{T} + 1\right)}}{1 - \left(\dfrac{\dfrac{2\tau_1}{T} - 1}{\dfrac{2\tau_1}{T} + 1}\right) z^{-1}} \tag{F.2}$$

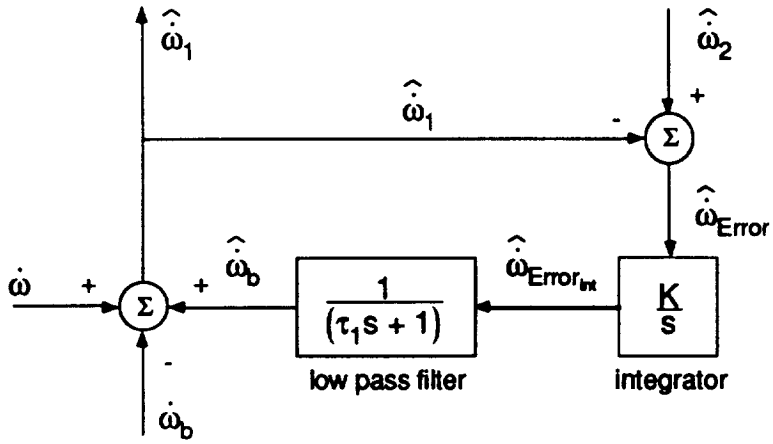

Figure F.1 Unmodelled angular acceleration estimator loop.

Define

$$cb3 = \frac{1}{\left(\frac{2\tau_1}{T} + 1\right)} \tag{F.3}$$

and

$$cb2 = \left(\frac{\frac{2\tau_1}{T} - 1}{\frac{2\tau_1}{T} + 1}\right) \tag{F.4}$$

Then Equation (F.2) can be written as

$$\frac{\hat{\dot{\omega}}_b}{\hat{\dot{\omega}}_{Error_{Int}}} = \frac{\left(1 + z^{-1}\right)\ cb3}{1 - cb2\ z^{-1}} \tag{F.5}$$

This is the discrete filter used in Figure 4.9. The integrator, K/s, in Figure F.1 can also be transformed to the z domain by the bilinear transformation (F.1). However, in the present design the simpler relationship

$$s \cong \frac{1 - z^{-1}}{T} \tag{F.6}$$

was used. The digital integrator can then be represented as

$$\frac{\hat{\dot{\omega}}_{Error_{Int}}}{\hat{\dot{\omega}}_{Error}} = \frac{K T}{1 - z^{-1}} \tag{F.7}$$

Define

$$cb1 = K T \tag{F.8}$$

Then

$$\frac{\hat{\dot{\omega}}_{Error_{Int}}}{\hat{\dot{\omega}}_{Error}} = \frac{cb1}{1 - z^{-1}} \tag{F.9}$$

This is the integrator transfer function used in Figure 4.9.

Appendix G

Wind Profiles

The wind profiles that were used for the ALS study were provided by the NASA Langley Research Center. Each profile was based on actual wind measurements using the Jimsphere radar-tracked balloon system at KSC and Vandenberg AFB. The data was provided in a graphical format with wind speed plotted as a function of altitude. Each profile consisted of two curves representing separate wind measurements taken at three and a half hour intervals. The magnitude differences between the measured profiles is of particular interest since it represents the possible differences that might exist between the prelaunch estimate and that actually encountered during flight. The worst case Jimsphere models studied in this study was a pair of profiles made at Vandenberg AFB, designated "Vandenberg #69" and "Vandenberg #70". These profiles are illustrated in Figure G.1. Azimuth data was provided in conjunction with the magnitude data however it was ignored in this thesis. Consequently, it was assumed that the winds were directed in the trajectory plane and parallel to the Earth-relative horizontal reference frame. Figure G.2 shows the simplified linearized profiles which were used in place of the more complex profiles shown in Figure G.1.

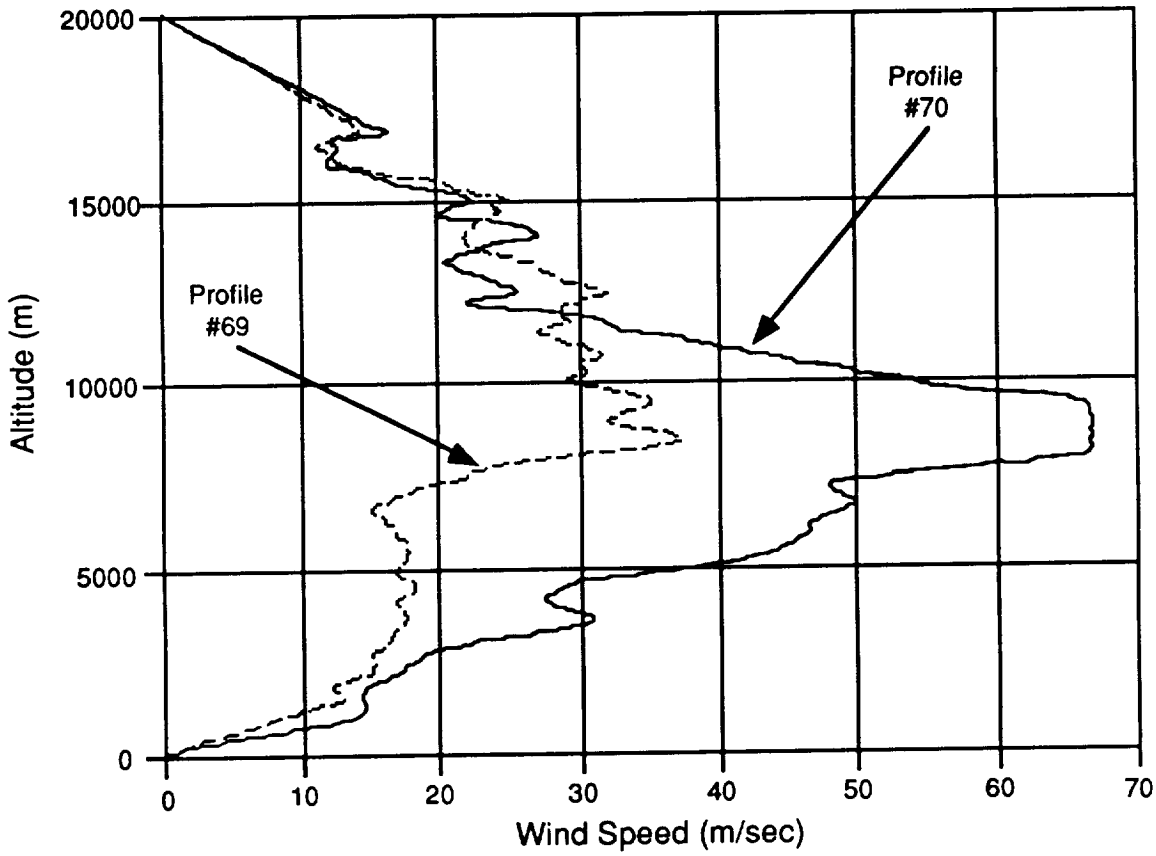

Figure G.1 Vandenberg #69 an #70 wind profiles.

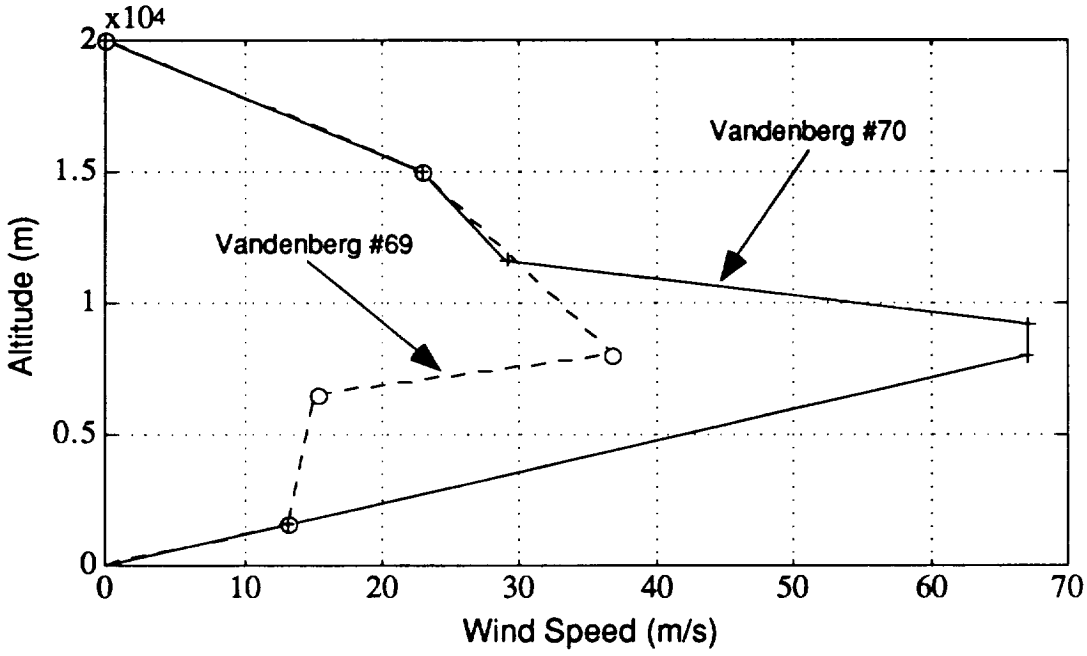

Figure G.2 Linearized Vandenberg #69 and #70 wind profiles.

List of References

[1] Press, W.H., Flannery, B.P., Teukolsky, S.A., Vetterling, W.T., Numerical Recipes. 1986. Cambridge: Cambridge University Press.

[2] Bonnice, W.F., "Steering of a Boost Vehicle to a Desired Flight Path Angle Trajectory using Angle of Attack Control". 1983. Massachusetts Institute of Technology Master of Science Thesis, published as CSDL Report T-802. Charles Stark Draper Laboratory, Inc., Cambridge.

[3] Corvin, M.A., "Ascent Guidance for a Winged Boost Vehicle". 1988. Massachusetts Institute of Technology Master of Science Thesis, published as CSDL Report T-1002. Charles Stark Draper Laboratory, Inc., Cambridge.

[4] Bushnell, G.S., "Guidance, Steering and Control of a Three Stage Solid Propellant Boost Vehicle". 1989. Massachusetts Institute of Technology Master of Science Thesis, published as CSDL Report T-1012. Charles Stark Draper Laboratory, Inc., Cambridge.

[5] Likins, P.W., Elements of Engineering Mechanics. 1973. New York: McGraw-Hill Book Company.

[6] Etkin,B., Dynamics of Flight - Stability and Control. 2nd Edition. 1982. New York: John Wiley & Sons, Inc.

[7] Stubbs, G.S., "Final Report, Fiscal Year 1974 Advanced Targeting Software Design Studies." 1974. Published as CSDL Report R-838. Charles Stark Draper Laboratory, Inc., Cambridge.